

ANISOTROPY IN THE INFRARED, OPTICAL
AND TRANSPORT PROPERTIES OF HIGH
TEMPERATURE SUPERCONDUCTORS

By

MANUEL ALBERTO QUIJADA

A DISSERTATION PRESENTED TO THE GRADUATE SCHOOL
OF THE UNIVERSITY OF FLORIDA IN PARTIAL FULFILLMENT
OF THE REQUIREMENTS FOR THE DEGREE OF
DOCTOR OF PHILOSOPHY

UNIVERSITY OF FLORIDA

1994

ACKNOWLEDGMENTS

It is with great pleasure that I thank my advisor, Professor David B. Tanner, for his advice, patience and encouragement throughout my graduate career here at the University of Florida. I feel fortunate to be part of his research group. I also thank Professors J. Graybeal, P.J. Hirschfeld, C. Hooper, N. Sullivan, and J.H. Simmons for their interests in serving on my supervisory committee and for reading this dissertation.

Thanks also go to all my past and present colleagues in Tanner's group for their friendship, useful conversations and cooperation. In particular, I would like to thank C.D. Porter for his assistance with computer software. I am also indebted to Drs. G.L. Carr, D.B. Romero, and V. Železný for many enlightening and useful discussions.

I would like to express my gratitude to Drs. J.P. Rice, D.M. Ginsberg, M. Kelley, M. Onellion, F.C. Chou and D.C. Johnston for providing good quality single crystals that were essential to the completion of this work.

The technical support of the staff members in the physics department machine shop and engineers in the cryogenic group is appreciated greatly.

I would also like to take this opportunity to thank my wife, Zunilda, and my daughter, Melissa, for their support and understanding during the countless nights they stayed alone while I was working in the laboratory.

Finally, I also thank my parents for giving me their support throughout my academic life.

Financial support from the NSF (grant number DMR 9101676) and from a U.S. Department of Education fellowship are gratefully acknowledged.

TABLE OF CONTENTS

	<u>Page</u>
ACKNOWLEDGMENTS	ii
ABSTRACT	vii
CHAPTERS	
I. INTRODUCTION	1
II. REVIEW OF PREVIOUS EXPERIMENTAL WORK	5
Crystal Structure of Copper-Oxide Materials	5
$\text{La}_2\text{CuO}_{4+\delta}$	5
$\text{YBa}_2\text{Cu}_3\text{O}_{7-\delta}$	8
$\text{Bi}_2\text{Sr}_2\text{CaCu}_2\text{O}_8$	10
Review of Optical Properties Copper-Oxide Materials	12
<i>c</i> -Axis Response	13
Midinfrared Absorption in the CuO_2 Planes	15
Anisotropy in the <i>ab</i> Plane	19
$\text{YBa}_2\text{Cu}_3\text{O}_{7-\delta}$	19
$\text{Bi}_2\text{Sr}_2\text{CaCu}_2\text{O}_8$	22
III. THEORY	25
Models for Carriers in the CuO_2 Planes: Normal State	25
Three-Band Hubbard Model	25
<i>t</i> – <i>J</i> Model	28
Models for $\sigma_1(\omega)$	30
Numerical Results	30
Two-Component Model	33
One-Component Model	35

Superconducting State Models	37
Symmetry of the Order Parameter	38
Evidence for Proposed Pairing States	40
Determination of Gap by Optical Spectroscopy	43
IV. EXPERIMENTAL TECHNIQUES	45
Fourier Transform Infrared Spectroscopy	45
Optical Spectrometers	48
Bruker Fourier Transform Spectrometer	48
Bolometer Detector	49
The Perkin-Elmer Monochromator	50
Polarizers	54
Sample Mounting and Low Temperature Measurements	56
Normalization Procedure of the Reflectance	58
Data Analysis of the Spectra: The Kramers-Kronig Transformations	59
High-Frequency and Low-Frequency Extrapolations	60
Optical Constants	61
Sample Preparation Techniques	62
YBa ₂ Cu ₃ O _{7-δ} Single-Domain Crystal	63
Bi ₂ Sr ₂ CaCu ₂ O ₈ Single-Domain Crystals	65
La ₂ CuO _{4+δ} Single Crystal	67
V. OPTICAL STUDY OF La ₂ CuO _{4+δ} SINGLE CRYSTAL	69
<i>c</i> -Axis Reflectance of La ₂ CuO _{4+δ}	72
Room Temperature Spectra	72
Low Temperature <i>c</i> -Axis Reflectance	74
Assignment <i>c</i> -Axis Phonons	76
Effective Charge	80
<i>ab</i> -Plane Reflectance	82
Assignment <i>ab</i> -Plane Phonons	82
Low Temperature <i>ab</i> -Plane Reflectance	84
Results of <i>ab</i> -Plane Optical Constants	86
Loss Function	87
<i>ab</i> -Plane Optical Conductivity	89

Midinfrared Component	90
Comparison of ab -Plane Reflectance: $\mathbf{q} \parallel c$ and $\mathbf{q} \perp c$	93
Concluding Remarks	97
VI. ANISOTROPY IN THE AB -PLANE OPTICAL PROPERTIES	
OF $\text{YBa}_2\text{Cu}_3\text{O}_{7-\delta}$	99
Room Temperature Spectra	99
Temperature Dependent Reflectance	103
Effect of the Chains	107
ab -Plane Anisotropy in the London Penetration Depth	109
VII. ANISOTROPY IN THE AB -PLANE OPTICAL PROPERTIES	
OF $\text{Bi}_2\text{Sr}_2\text{CaCu}_2\text{O}_8$	111
Results of the Optical Reflectance	113
Room Temperature Spectra	113
Temperature Dependent Spectra	114
Discussion of Optical Constants	116
Temperature Dependent Optical Conductivity	121
One-Component Analysis	125
Two-Component Analysis	127
Drude Component	129
Midinfrared Absorption	134
Superconducting Condensate	139
ab -Plane Anisotropy in the London Penetration Depth	141
Optical Conductivity and Symmetry of the Order Parameter	143
VIII. RESISTIVITY TENSOR OF $\text{Bi}_2\text{Sr}_2\text{CaCu}_2\text{O}_8$ SINGLE-DOMAIN	
CRYSTALS	147
Sample Preparation and Measurement Method	148
Resistivity Analysis for Anisotropic Materials	152
Resistivity Tensor	158
c -Axis Results	158
Anisotropy in the ab -Plane Resistivity	159
Temperature Dependent ab -Plane Resistivity	160

Closer Look to the Transition Temperature	161
Results and Discussion	163
Review of Flux-Flow Resistance and Kosterlitz-Thouless Transition .	165
Concluding Remarks	168
IX. CONCLUSIONS	170
APPENDICES	
A OPTICAL STUDY OF BEDT-TTF(ClO ₄) ₂	173
B MICROWAVE CAVITY APPARATUS	186
REFERENCES	200
BIOGRAPHICAL SKETCH	214

Abstract of Dissertation Presented to the Graduate School
of the University of Florida in Partial Fulfillment of the
Requirements for the Degree of Doctor of Philosophy

ANISOTROPY IN THE INFRARED, OPTICAL
AND TRANSPORT PROPERTIES OF HIGH
TEMPERATURE SUPERCONDUCTORS

By

Manuel Alberto Quijada

April 1994

Chairman: David B. Tanner

Major Department: Physics

The optical properties of the high-temperature superconductors are extremely unusual. We have extensively studied superconducting high-quality single crystals of $\text{YBa}_2\text{Cu}_3\text{O}_{7-\delta}$, $\text{Bi}_2\text{Sr}_2\text{CaCu}_2\text{O}_8$, and $\text{La}_2\text{CuO}_{4+\delta}$. All these materials have CuO_2 planes as the entities responsible for the metallic behavior and superconductivity. Polarized optical reflectance measurements were taken both above and below the superconducting state on a wide frequency range.

All these materials display interesting anisotropy in their optical properties. In particular, optical investigations of the oxygen-doped $\text{La}_2\text{CuO}_{4+\delta}$ reveal the out-of-plane (c axis) spectrum of this material is typical of an insulator with the optical conductivity dominated by optical phonons. In contrast, the ab -plane optical spectrum is characterized by a metallic conductivity in the far infrared. We also find evidence of electron-phonon interaction that is enhanced when the ab -plane optical

response is measured on the face of the crystal that has the c axis parallel to the propagation vector of the light.

The normal-state infrared conductivity of the CuO_2 planes shows a strong, nearly temperature-independent, broad band in the midinfrared in addition to a strong temperature-dependent narrow Drude-like band in the far infrared. There is also anisotropy in the infrared conductivities between the a and b axes of both $\text{YBa}_2\text{Cu}_3\text{O}_{7-\delta}$ and $\text{Bi}_2\text{Sr}_2\text{CaCu}_2\text{O}_8$. In the case of $\text{YBa}_2\text{Cu}_3\text{O}_{7-\delta}$, the strong anisotropy can be mostly attributed to the presence of CuO chains along the b axis.

One striking result is that in spite of the fact that $\text{Bi}_2\text{Sr}_2\text{CaCu}_2\text{O}_8$ does not have the CuO chains, we observed anisotropy between the a and b axes infrared conductivity of this compound as well. The presence of this anisotropy even in the superconducting state suggests two possibilities. One possibility could be an anisotropic superconducting order parameter. A second explanation is that the overall conductivity is composed of a simple Drude term combined with a more broad midinfrared component. The observed higher absorption in the low-frequency region along the b axis could be explained by an anisotropic second midinfrared component in the optical conductivity.

CHAPTER I

INTRODUCTION

The discovery of superconductivity in the copper oxides by Bednorz and Müller¹ in 1986 has revolutionized the field of condensed matter physics. The importance of this remarkable discovery can not be overstated. On the one hand, it offers promising technological applications for materials that lose their resistance to the flow of electrical current above liquid nitrogen temperatures. On the other hand, many experiments have provided ample evidence of the exciting new phenomena present in these materials. Early measurements were designed to learn if the superconducting properties of these materials could be explained in the context of the Bardeen-Cooper-Schrieffer (BCS) theory² for conventional superconductors. Some of those initial results supported a BCS-like theory. Among these, flux quantization³ and the AC Josephson effect⁴ show that the elementary charge in the superconducting state is $2e$ rather than e . In addition, photoemission⁵⁻⁷ and tunneling^{8,9} experiments suggest the presence of a superconducting energy gap. At the same time, there has been an accumulation of evidence for an unconventional nature of the high- T_c materials. Some of the most important results that have emerged are high superconducting transition temperature,^{1,10,11} linear dc resistivity in the normal state,^{12,13} and extremely small coherence lengths.^{14,15} Perhaps the second most striking property in these materials, beside their high- T_c value, is the anisotropy in their physical properties.¹⁶⁻²¹

As soon as these materials were discovered, there began an intense effort to study their optical properties.²²⁻²⁴ Soon, it was realized that the strong anisotropy that is observed in the electrical properties is continued in the infrared where the optical properties are also very anisotropic.²⁵⁻²⁹ The study of this anisotropy by optical

means has provided some important results but at the same time has raised some unresolved questions. As it is well known, superconductivity in these materials is associated with the quasi-two dimensional CuO_2 planes. Most optical studies related to the anisotropy in these materials have concentrated in the anisotropy between the directions perpendicular to (c axis) and parallel to the CuO_2 planes. Research of the anisotropy within the CuO_2 (ab) planes has been studied to a lesser degree. In view of the orthorhombic distortion that exists in these planes there are two important questions that must be addressed: (1) how this structural anisotropy affects the anisotropy of the 2-d electronic structure in the normal state and (2) what if any is the anisotropy of the superconducting order parameter?

Since the energy gap plays a central role in the BCS theory, substantial efforts have been devoted to observing this gap by optical methods.^{30,31} One of the advantage of the optical methods compared to, for example, tunneling is that direct electrical contact to the sample surface is not necessary. This is especially important since crystals and films may have dead layers near the surface that make it nearly impossible for current to tunnel between an electrode and the superconductor. In an optical experiment, by contrast, the probing radiation can penetrate a few thousand Å into the sample so the presence of dead layers becomes less of an issue. This technique, which has been used with great success in the past to study energy gaps in conventional superconductors, has also given valuable information in solids about lattice vibrations, electron-phonon coupling, low-lying excitations, and electronic band structures. In the context of the BCS theory, the presence of a gap means that for photon energies less than 2Δ , the bulk properties of the superconductor at $T \ll T_c$ show only an inductive part, with the real or absorptive part being zero. So, in order for there to be absorption in the material, the photon energy must be larger than 2Δ . Only at energies above 2Δ , it is possible to break up Cooper pairs to produce

quasiparticles in the sample. At photon energies well above the gap, the material behaves as if it was in the normal state.

This thesis is concerned with the subject of anisotropy in the optical properties of the high- T_c materials. The materials investigated are single-domain crystals of $\text{YBa}_2\text{Cu}_3\text{O}_{7-\delta}$ ($T_c = 90$ K), $\text{Bi}_2\text{Sr}_2\text{CaCu}_2\text{O}_8$ ($T_c = 85$ K), and an oxygen-doped single crystal of $\text{La}_2\text{CuO}_{4+\delta}$ ($T_c = 40$ K). There are two important issues that will be considered. The first one is the anisotropy in the optical properties of the ab plane *vs.* the c axis. A large surface area containing the c axis in the $\text{La}_2\text{CuO}_{4+\delta}$ sample allowed the study of the c -axis polarization as well as the ab -plane response in this material. This also allowed us to examine the ab -plane response in this material when the propagation vector (\mathbf{q}) of the light is parallel and perpendicular to the CuO_2 planes. The second issue is the anisotropy in the optical response along the two principal axes in the ab plane, and how this is related to the crystal structure anisotropy in single-domain crystals of $\text{Bi}_2\text{Sr}_2\text{CaCu}_2\text{O}_8$ and $\text{YBa}_2\text{Cu}_3\text{O}_{7-\delta}$. One important observation is the presence of a larger absorption in the superconducting-state optical conductivity along the b axis below the frequency where a superconducting energy gap should be observed. Explanation for this larger absorption in the framework of the models that have been proposed will be discussed in addition to its possible connection with the symmetry of the superconducting order parameter in the copper-oxide superconductors.

The organization of this thesis is as follows. Chapter II presents a review of experimental works that have been done related to the crystal structure and optical properties of the high- T_c superconductors. A brief theoretical background for the understanding of the physical properties will be presented in Chapter III. A description of the experimental techniques along with the instrumentation used in this investigation will be done in Chapter IV. The results and discussion pertaining

to anisotropy between the ab -plane and c -axis optical measurements of $\text{La}_2\text{CuO}_{4+\delta}$ crystal are presented in Chapter V. The presentation of results and discussion related to the measurements on $\text{YBa}_2\text{Cu}_3\text{O}_{7-\delta}$ and $\text{Bi}_2\text{Sr}_2\text{CaCu}_2\text{O}_8$ single-domain crystals, with emphasis of the anisotropy within the ab plane, is done in Chapters VI and VII respectively. Chapter VIII is for presentation of results regarding dc-transport measurements of the resistivity tensor of $\text{Bi}_2\text{Sr}_2\text{CaCu}_2\text{O}_8$ samples. Finally, Chapter IX contains concluding remarks.

CHAPTER II

REVIEW OF PREVIOUS EXPERIMENTAL WORK

This chapter will be devoted to a survey of previous experimental works related to the physical properties of the copper-oxide superconductors. It will be divided in two major sections. The first one is related to investigations of the crystal structures of the three kind of materials studied in this study. Information about the lattice parameters that are relevant to an optical experiment will be given here. The second major section is a brief review of relevant previous work of the optical properties in the copper-oxide superconductors.

Crystal Structure of Copper-Oxide Materials

Good knowledge of the crystallographic structure in single-crystal materials is essential to the understanding of the optical properties. This is certainly true in the case of the copper-oxide materials. These materials are considered by many as a good example of a 2-dimensional system. The reason for this point of view is that the charge transport and superconductivity occur mainly in a 2-dimensional arrangement of copper atoms that are strongly bonded to oxygen atoms with an interatomic distance of 1.9 Å. This distance hardly changes from structure to structure. Above and below the CuO₂ layers, there are other layers of atoms that are believed to provide the carriers necessary for conductance in these planes, as well as to provide overall charge neutrality. The identity of these atoms depends on the system under study.

La₂CuO_{4+δ}

The first superconducting material reported by Bednorz and Müller in their pioneering work¹ had composition La-Ba-Cu-O. Their suggestion that this system has

the tetragonal K_2NiF_4 structure was soon corroborated by Takagi *et al.*³² Further research indicated the nearly stoichiometric La_2CuO_4 is an antiferromagnetic insulator that can be hole doped by partially substituting the lanthanum site with some of the alkaline earths Ca, Sr, or Ba to produce superconducting materials with T_c in the 30–40 K range. Later, it was also realized that superconducting samples in this system can be obtained by producing samples where the oxygen stoichiometry is higher than four.^{33,34} Figure 1 shows the crystal structure of the undoped La_2CuO_4 compound. In this nearly stoichiometric material, the oxidation state of the individual species is La^{3+} , Cu^{2+} , and O^{2-} in order to have charge neutrality. The oxidation state of copper leaves this atom with one unpaired electron in the d-shell; therefore, the net spin at the copper site is $1/2$.

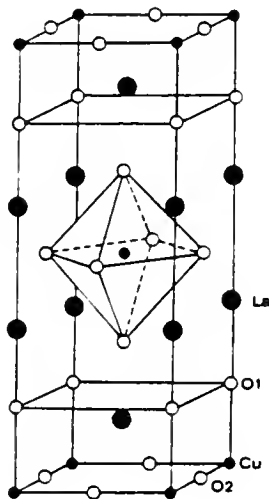


Fig. 1. Crystal structure of La_2CuO_4 material (After Ref. 33).

Each copper atom is coordinated to four oxygen atoms in the plane (1.9 \AA). In addition, there are two more distant apical oxygens above and below the copper (2.4 \AA). Hence, each copper atom is surrounded by an octahedron of oxygens. The larger distance for the out-of-plane oxygens suggests that the dominant bonds are

those in the plane. The Cu ion and its octahedral oxygen configuration would imply a tetragonal $I4/mmm$ space group in the structure. However, neutron scattering data for this compound indicate that below a characteristic temperature there is a lowering of the symmetry due to a slight tilt of the apical oxygens from their high symmetry points. This tilting produces a tetragonal to orthorhombic transformation at a temperature that is close to 500 °C for the nearly stoichiometric material and decreases with increasing doping, reaching 240 K at a Sr concentration of around 15%.

As mentioned above, superconductivity in this material can be achieved by intercalating additional oxygen atoms in the structure. This excess oxygen is thought to provide hole carriers in the CuO_2 planes. The first report on the structure of oxygen-enriched samples was done by Chaillout *et al.*³⁵ They reported neutron diffraction results on a sample that had 3% extra oxygen. First, they reported that at this doping level the material will phase separate into a superconducting (oxygen-rich) phase and a near stoichiometric region, just as happens in $\text{La}_2\text{NiO}_{4+\delta}$.³⁶ Based in a two-phase model, the conclusion was reached that the superconducting phase has the $Bmab$ space group from the observation of peaks in the neutron scattering data that are forbidden in $Fmmm$ symmetry. They created a model where one apical oxygen is replaced by two oxygen sites that form a peroxide with a short O–O bond distance of 1.64 Å.

Most recently, Radaelli *et al.*³⁷ pointed out the need to perform such experiments on samples with oxygen concentration well beyond the phase separation regime. They reported neutron diffraction data on three electrochemically-oxidized samples: two ceramics ($\delta = 0.08$, with $T_c = 32$ K, and $\delta = 0.12$, with $T_c = 42$ K) and one single crystal ($\delta = 0.10$, with $T_c = 38$ K). Normal and superconducting state susceptibility measurements indicated the absence of two-phase material in these samples.

After a carefully analysis of the neutron scattering data, they concluded the basic crystal structure of all samples corresponds to the $Fm\bar{3}m$ symmetry. This was obtained from the absence of small diffraction peaks that would be allowed in a $Bm\bar{2}$ symmetry. They argued the $Bm\bar{2}$ symmetry would be frustrated by the presence of interstitial oxygen in the structure. Following up on their conclusion, they carried out a refinement of the structural parameters for the single-crystal data in the $Fm\bar{3}m$ space group symmetry. In the analysis, they relaxed the apical oxygen position slightly from the high-symmetry points and introduced an additional oxygen site located nearby and adjacent to a LaO layer (see Fig. 2). The lattice parameters obtained from analysis of the neutron scattering data on the single crystal at 18 K are $a \approx b = 5.34 \text{ \AA}$ and $c = 13.22 \text{ \AA}$.

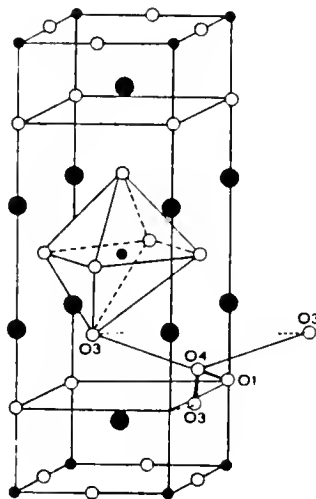


Fig. 2. Model for the crystal structure of $\text{La}_2\text{CuO}_{4+\delta}$ (After Ref. 33).

$\text{YBa}_2\text{Cu}_3\text{O}_{7-\delta}$

$\text{YBa}_2\text{Cu}_3\text{O}_{7-\delta}$ was the first copper-oxygen-based material that showed superconductivity above liquid nitrogen temperature.¹⁰ This discovery triggered a lot of research to determine its crystal structure after its announcement in 1987. In the 1-2-3

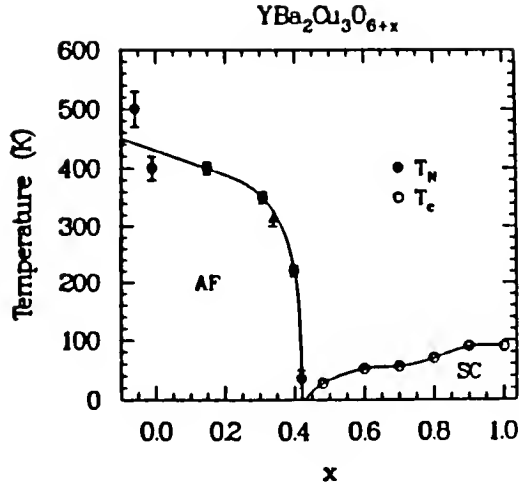


Fig. 3. Phase diagram for $\text{YBa}_2\text{Cu}_3\text{O}_{7-\delta}$ as a function oxygen concentration. AF: antiferromagnet, SC: superconductor (after Ref. 38).

system, the parent compound $\text{YBa}_2\text{Cu}_3\text{O}_6$ crystallizes in tetragonal form at high temperatures, but converts by oxygen ordering to an orthorhombic form ($\text{YBa}_2\text{Cu}_3\text{O}_{7-\delta}$) on cooling down at room temperatures. There is also a tetragonal to orthorhombic transition driven by the oxygen content in the material at $x_c = 0.3$, which also determines the T_c in the sample as shown in the phase diagram of Fig. 3. Figure 4 shows the essential features of the crystal structure of the orthorhombic phase that have been gathered based on x-ray and neutron diffraction data. In this material, each copper atom in the plane is linked to four oxygens atoms at about 1.94 Å, and a fifth weakly bonded apical oxygen at 2.3 Å as in the 2-1-4 compounds. This arrangement of the oxygen atoms in the planes gives a perovskite-like structure with the space group $Pmmm$.¹² There are two CuO_2 planes per unit cell. Unlike the tetragonal compound, the orthorhombic phase contains an additional CuO containing layer that consists of a 1-dimensional network of CuO chains along the b axis in the unit cell. Doping of carriers in the CuO_2 planes is controlled by the amount of oxygen vacancies along the chains in this material (it is widely accepted that one oxygen atom

contributes 0.25 hole per copper for each of the two planes). There is a difference between the a - and b -axis dimensions in the order of 2%, with the b axis being the larger on account of the CuO chains present along this direction. The unit cell has lattice dimensions of $a = 3.82 \text{ \AA}$, $b = 3.88 \text{ \AA}$, and $c = 11.65 \text{ \AA}$. Effects of the chains on the superconducting properties of the material have been difficult to clarify because the as-grown samples are usually twinned in the ab plane with alternating strip-like domains of a - and b -axis oriented material.

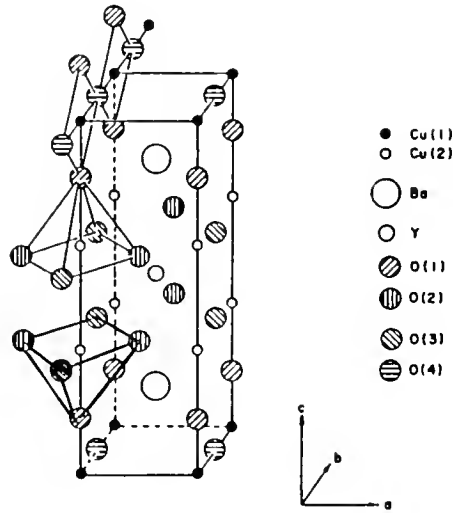


Fig. 4. Crystal structure of $\text{YBa}_2\text{Cu}_3\text{O}_{7-\delta}$ material (after Ref. 39).

Special growing techniques⁴⁰ in recent years have provided large enough single-domain crystals, that have made possible the study of this issue in more detail. More discussion about this will be given later when discussing sample preparation techniques.

$\text{Bi}_2\text{Sr}_2\text{CaCu}_2\text{O}_8$

The discovery of 20 K superconductivity in $\text{Bi}_2\text{Sr}_2\text{CuO}_6$ ⁴² opened up the race to produce higher T_c material in the bismuth based superconductors. Soon after this, superconductivity above 80 K was reported in the Bi-Sr-Ca-Cu-O compound.¹¹

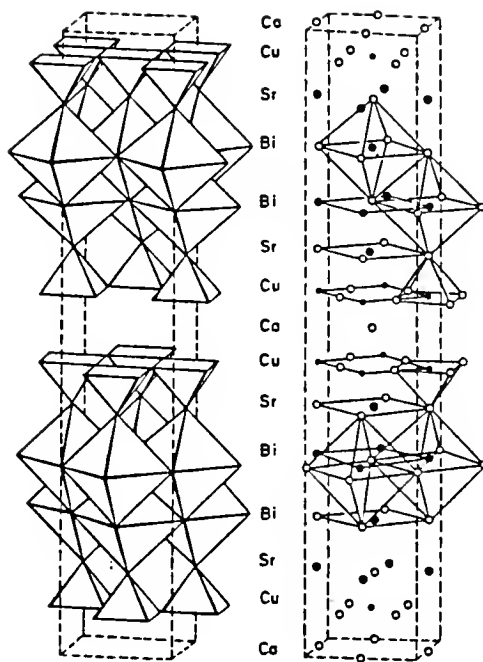


Fig. 5. Crystallographic structure of $\text{Bi}_2\text{Sr}_2\text{CaCu}_2\text{O}_8$ sample (after Ref. 41).

The structure of this material was quickly identified as $\text{Bi}_2\text{Sr}_2\text{CaCu}_2\text{O}_8$ or “2-2-1-2”.⁴³ The Bi-based compounds form a series of layered material where the CuO_2 planes are separated by alkaline-earth cations and sheets of Bi_2O_2 . The general formula is $(\text{BiO})_2\text{Sr}_2\text{Ca}_{n-1}\text{Cu}_n\text{O}_{2+2n}$ where n is the number of consecutively stacked CuO_2 sheets. It is found that T_c increases with the number n , reaching a maximum value of 110 K when $n = 3$ and decreasing again as n increases further. Figure 5 shows the ideal crystal structure for the case when $n = 2$. In this structure the $\text{CuO}/\text{Ca}/\text{CuO}$ layers are seen to be separated by sheets of Bi_2O_2 and SrO . The crystal lattice parameters of the orthorhombic unit cell are $a = 5.41 \text{ \AA}$, $b = 5.44 \text{ \AA}$, and $c = 30.78 \text{ \AA}$. In spite of the relatively simple arrangement of the many atoms, a full understanding of the structure is complicated because of deviation from the ideal 2212 cationic stoichiometry. The position of the oxygen atoms in the Bi_2O_2 layers

is not well defined; cation disorder also contributes to this problem. In contrast to the Bi_2O_2 disorder, the CuO_2 sheets appear to be free of defects as determined from x-ray and neutron scattering experiments.⁴⁴ In addition, the oxygen content varies for any fixed cation composition, affecting the transition temperature in the material. In general, T_c increases as oxygen is removed. It is still unclear however how doping of the CuO_2 planes occurs in this structure. It is generally assumed that doping of the CuO_2 planes in this material comes from excess oxygen in the Bi_2O_2 planes. X-ray⁴⁵ and neutron scattering⁴⁶ experiments have shown the existence of a superlattice modulation or distortion that resides mostly on the Bi_2O_2 layers. It is incommensurate^{13,47,48} with the b -axis unit cell parameter given above (period $\sim 4.7b$). There have been many attempts to explain this superlattice by modeling defects that are observed in the structure of this compound.^{41,48-51} In one of those models, the superstructure is claimed⁴⁸ to be the result of the addition of one in ten oxygen atoms in the Bi_2O_2 layers, that would also cause a displacement of the surrounding atoms. Final verification of this or any model must await further work.

Review of Optical Properties Copper-Oxide Materials

This section is devoted to a review of the work related to the status of the infrared response in the copper-oxide superconductors. Investigation of the optical properties in these materials has been very vigorous since their discovery in 1986.^{23,24} In spite of this, understanding of the infrared properties in these materials remain a controversial issue. As mentioned before, the feature common to these materials is the CuO_2 plane structure. Since the optical properties of these materials are very different for directions parallel and perpendicular to the CuO_2 planes and even show substantial anisotropy within these planes, the availability of ab -plane oriented films and high quality single crystals in recent years have made possible certain advances in the field. The first section treats the subject of the out-of-plane optical response

(c axis) mainly on $\text{La}_{2-x}\text{Sr}_x\text{CuO}_4$ single crystals. The second section will touch the subject of the midinfrared absorption that starts off as soon as a few carriers are introduced in the CuO_2 planes of these materials. In the third section, the subject of the anisotropy within the ab plane will be reviewed in the context of the work done with single-domain crystals of $\text{YBa}_2\text{Cu}_3\text{O}_{7-\delta}$ and $\text{Bi}_2\text{Sr}_2\text{CaCu}_2\text{O}_8$.

c -Axis Response

As a result of the layered nature of the materials, the in-plane and out-of-plane optical properties of the copper-oxide superconductors show a remarkable anisotropy. This became evident as soon as the first polarized studies were reported on single crystals of these compounds.^{28,52-54} In one of the earlier reports,⁵⁴ the reflectivity of insulating La_2CuO_4 and of 8% Sr-doped samples were compared for polarizations parallel and perpendicular to the CuO_2 planes. The results showed that the c -axis reflectance in both cases was virtually unchanged suggesting that doping did not affect the c -axis response in the system. The spectra were typical of an insulating material with phonon-like structures due to infrared-active modes (A_{2u} symmetry). In contrast, the reflectance parallel to the ab planes showed substantial differences. In the undoped sample, the reflectance is dominated by the presence of infrared allowed phonons (E_u symmetry) with the reflectance approaching a constant value at low frequencies indicative of insulating behavior in the CuO_2 planes as well. On the other hand, the doped sample showed a rising reflectivity at low frequencies with the phonons visibility greatly reduced due to screening by the free carriers in the material. This rising reflectivity implies a metallic conductivity in the CuO_2 planes of this doped material, although at this concentration the material is not yet superconducting. It became clear from this study that the anisotropy between the ab -plane and the c -axis optical conductivity of doped sample would make very difficult to interpret the results that were first observed in unaligned samples.^{55,56}

A more systematic study of the c -axis and ab -plane optical response as function of Sr doping in $\text{La}_{2-x}\text{Sr}_x\text{CuO}_4$ was done by Uchida *et al.*²⁸ Let us first review the c -axis data. Figure 6 displays the reflectivity for three representative doping levels: undoped, superconducting ($x = 0.15$), and the overdoped ($x = 0.34$). These results confirm²⁸ the previous observation about the unchanged character of the c -axis reflectance between the insulating and superconducting phase. The electronic background appears to be very weak from the almost flat slope of the reflectance in the far infrared. The spectrum is dominated by two major optical phonons. Only in the overdoped nonsuperconducting samples do there appear to be qualitative changes in the reflectance. In this case, the spectrum appears to have a free carrier component, although the highest phonon is not completely screened out. This is consistent with an observed metallic behavior in the resistivity as a function of temperature in the c axis at this concentration. In this context, the authors regard the overdoped samples as an example of anisotropic 3-dimensional metals.

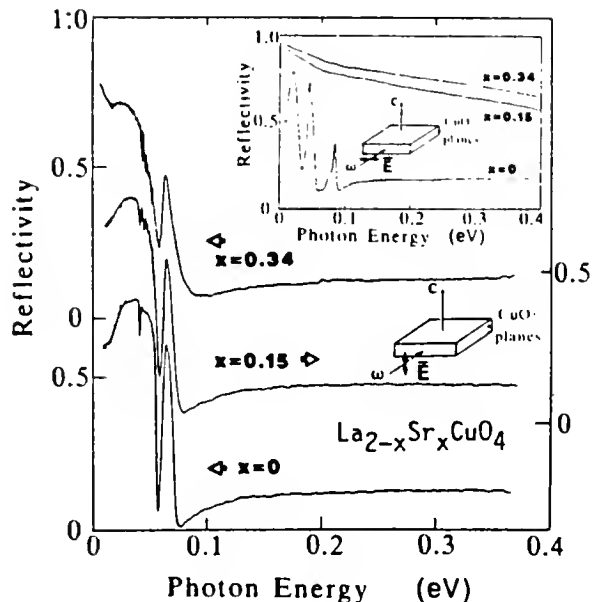


Fig. 6. c -axis reflectance of $\text{La}_{2-x}\text{Sr}_x\text{CuO}_4$ as a function of doping (after Ref. 28).

This semiconducting-like behavior for the c -axis conductivity has also been documented in other cuprate such as $\text{YBa}_2\text{Cu}_3\text{O}_{7-\delta}$ and $\text{Bi}_2\text{Sr}_2\text{CaCu}_2\text{O}_8$.^{25,29,57} In the case $\text{YBa}_2\text{Cu}_3\text{O}_{7-\delta}$ the results show some variation for various oxygen concentrations. It appears that samples with the highest oxygen content show a nearly metallic behavior along the c axis,^{25,29} signaling that coupling between the CuO_2 planes of this compound is somewhat stronger. The temperature dependence of the c -axis optical properties has also been investigated in superconducting samples of $\text{La}_{2-x}\text{Sr}_x\text{CuO}_4$ compound.⁵⁸ The results of the reflectance measured at several temperatures for three doping levels are shown in Fig. 7. Above T_c , the far-infrared reflectance is rather featureless, approaching a constant value at low frequencies for the lowest doping, while it shows a slight negative slope for higher doping indicative of some weak dc transport. Below T_c , a sharp edge develops in the reflectance that signals the onset of superconductivity. In the analysis, the authors find that this edge does not scale with T_c and it is not due to a superconducting gap excitation, but rather to a plasma-edge-like feature associated with the superconducting-state carriers. A direct consequence of this is the appearance of coherent transport of charge across the CuO_2 planes below T_c . Similar results have also been obtained in the superconducting state c -axis response of $\text{YBa}_2\text{Cu}_3\text{O}_{7-\delta}$ single crystals.^{25,29}

Midinfrared Absorption in the CuO_2 Planes

The optical spectrum of undoped parent compounds of the copper-oxide superconductors such as La_2CuO_4 and Nd_2CuO_4 shows that these materials are charge transfer insulators, with a band gap energy in the range 1.7–2.0 eV ($14,000\text{--}16,000\text{ cm}^{-1}$), depending on the material. It is generally accepted that this energy corresponds to transitions in the CuO_2 planes between occupied O $2p$ levels and the lowest unoccupied Cu $3d$ orbitals.⁵⁹ Below this energy, there are other identifiable electronics features; lattice vibrations (phonons) and perhaps weak magnon side bands.^{60,61} As soon as a

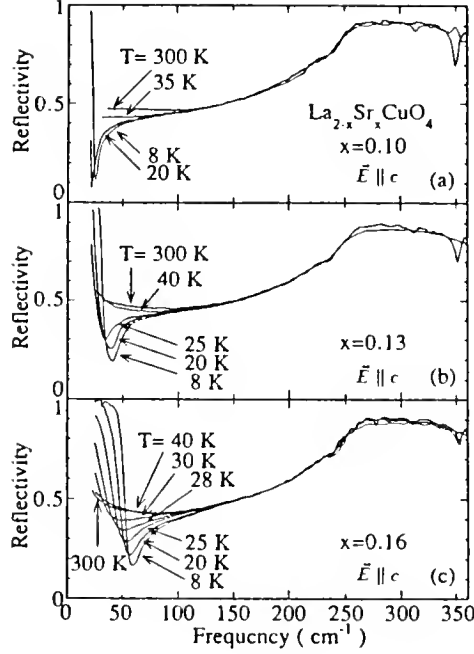


Fig. 7. Temperature dependence in c -axis reflectance of $\text{La}_{2-x}\text{Sr}_x\text{CuO}_4$ as a function of doping (after Ref. 58).

few carriers are introduced in these planes, there is an appearance of excitations in the midinfrared²⁴ that are peaked in an energy range from 0.1 eV to 0.5 eV ($800\text{--}4000\text{ cm}^{-1}$) depending on the material under study. These new excitations are thought to be the result of photon assisted transition of bound holes (electrons) from their ground state to excited states and the continuum. Due to the peak energy of one of these midinfrared modes being approximately equal to the antiferromagnetic exchange energy J ($\sim 0.12\text{eV}$), this band has been attributable to a magnetic origin, *i.e.*, the hopping of a charge from site to site involving the flipping of the nearby spins.⁶² In other works, these excitations have been related to the polaronic binding energy of an impurity to the lattice.^{63,64}

As a function of increased doping these excitations seem to grow and eventually merge with or get washed out by a Drude-like response that occurs in metallic samples.^{28,65} To illustrate this effect, Fig. 8 shows the evolution in the optical

conductivity in $\text{La}_{2-x}\text{Sr}_x\text{CuO}_4$ samples as a function of Sr concentration by Uchida *et al.*²⁸ Doping of the CuO_2 planes in this system can be achieved by partially replacing the lanthanum sites La^{3+} by strontium Sr^{2+} . Depending on the doping level, the properties of the samples change from insulating ($x = 0$), to superconducting ($0.10 < x < 0.20$), to nonsuperconducting metallic ($x > 0.20$). The insulating compound La_2CuO_4 shows the charge transfer (CT) band at 2eV ($16,000 \text{ cm}^{-1}$) and no absorption below this energy. For the lightly doped ($x = 0.02$) sample, there is clear evidence of the maximum that develops in the midinfrared conductivity at 0.5 eV, followed by a reduction of the spectral weight above the CT band. This transfer of spectral weight from energies above the CT band is regarded as evidence of the itinerant nature of the states near the Fermi surface of these materials. The maximum appears to shift to lower energies as a function of doping. For $x = 0.10$, it shows up at 0.14 eV (1100 cm^{-1}); while for $x = 0.15$, it appears as a shoulder at a even lower energy. Other materials such as $\text{YBa}_2\text{Cu}_3\text{O}_{7-\delta}$ and Nd_2CuO_4 show similar evolution of the infrared conductivity as doping proceeds in these systems.²⁴

Photoinduced absorption, a technique that induces doping in the insulating materials by shining light onto them to excite photo carriers, has also shown the presence of this midinfrared absorption in several samples. The samples studied are $\text{La}_{2-x}\text{Sr}_x\text{CuO}_4$ and Nd_2CuO_4 by Kim *et al.*⁶⁶, and in La_2CuO_4 , $\text{YBa}_2\text{Cu}_3\text{O}_{6.25}$ and $\text{Tl}_2\text{Ba}_2\text{Ca}_{1-x}\text{Gd}_x\text{Cu}_2\text{O}_8$ by Foster *et al.*⁶⁷

The optimally-doped samples do not show a discernible maximum in the midinfrared. But even in this case, the conductivity ($\sigma_1(\omega)$) decays more slowly than the typical Drude-type dependence ω^{-2} . Evidence for this non-Drude response in $\sigma_1(\omega)$ has been provided for nearly all the copper-oxide-based superconductors.^{23,24,65,68-70} The explanation for this has been a matter of heated controversy in this field. There are some clear-cut facts about the unconventional nature of this absorption that show

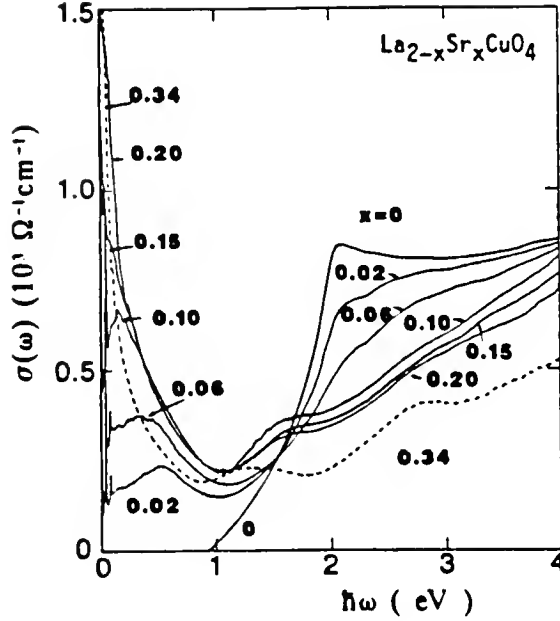


Fig. 8. Evolution of *ab*-plane conductivity as a function of doping in $\text{La}_{2-x}\text{Sr}_x\text{CuO}_4$ (after Ref. 28).

up in optimally-doped samples. In the first place, there is a region ($800\text{--}4000\text{ cm}^{-1}$) where this absorption shows very little temperature dependence. This happens at the same time the dc conductivity in the material changes by a factor of three between 300 and 100 K. Clearly, a Drude formula with a single relaxation rate for the charge carriers will not account for such a behavior. Secondly, there is a definite temperature dependence in the low frequency conductivity that is in good agreement with the measured dc value.^{65,68,69,71,72}

The two most commonly mentioned models for interpretation of this midinfrared absorption have taken two rather divergent approaches. In one approach, there is only one type of carrier which is responsible for both the dc transport and the conductivity in the midinfrared. The reconciliation between the T-dependent dc and the nearly T-independent midinfrared conductivity is throughout a frequency dependent

scattering rate and an effective mass enhancement at low frequencies. These carriers are expected to form a superconducting condensate below T_c .

The second approach is called the two-component model. In this approach, the infrared conductivity in the cuprate is the result of two types of charge carriers. The first type of carriers, which are considered to be Drude-like in nature, are responsible for the dc conductivity in the normal state and form the superfluid density below T_c . The second component, which is formed by bound carriers, has a semiconducting-like band gap. In this model, the Drude component is expected to have a scattering rate that is independent in frequency and linear in temperature. More discussion about this will be done in Chapter III. The following subsection will address the issue of the anisotropy of the midinfrared absorption of single-domain crystals of $\text{YBa}_2\text{Cu}_3\text{O}_{7-\delta}$ and $\text{Bi}_2\text{Sr}_2\text{CaCu}_2\text{O}_8$.

Anisotropy in the ab Plane

$\text{YBa}_2\text{Cu}_3\text{O}_{7-\delta}$

$\text{YBa}_2\text{Cu}_3\text{O}_{7-\delta}$ is one of the most studied high- T_c systems. At the same time, most of the optical studies in this material have been done on samples that show severe twinning in the ab plane. Therefore, these measurements only show an average of the ab -plane optical properties. Since the presence of the CuO chains along the b axis is likely to provide substantial conductivity in the midinfrared, polarized optical measurements of single-domain crystals have become highly desirable. Fortunately, recent developments^{40,73} in making large enough twin-free samples have made possible optical studies along the two principal axes in the ab plane of this material.^{26,31,74,75} The first room temperature measurements done on a wide frequency scale were performed by Koch *et al.*⁷⁴ The samples used in this study were mechanically detwinned single crystals with a transition temperature of 85 K. The reflectance was measured

for linearly polarized light parallel and perpendicular to the chain direction. At low frequencies, the reflectance for R_a and R_b are nearly equal. At higher frequencies, R_a falls off faster than R_b , reaching the plasmon minimum at a lower frequency. This plasma edge minimum, which signals the zero crossing of $\epsilon_1(\omega)$, occurs at 1 eV for the a axis, while it is at 1.5 eV for the b direction. This shows a splitting of the plasma edge minimum observed in twinned samples.⁶⁵ At approximately 3 eV, $R_a = R_b$ and for higher energies $R_a > R_b$. A Kramers-Kronig analysis of this reflectance reveals a spectral weight in the midinfrared that is roughly a factor of 2 larger along the b axis. Koch *et al.* interpret the a -axis conductivity as intrinsic to the CuO_2 planes. To obtain the chain conductivity, they subtract the a -axis conductivity from the total b -axis conductivity. In this analysis, the chain conductivity is then modeled by a broad Drude-like peak with strongly damped carriers. As pointed out by Koch *et al.* the additive nature of the conductivities is violated at higher frequencies ($\omega > 2.0$ eV) where $\sigma_a > \sigma_b$.

Cooper *et al.*⁷⁵ reported optical studies on single-domain crystals of $\text{YBa}_2\text{Cu}_3\text{O}_{6+x}$ as a function of oxygen doping x . The doping levels they studied were $x \simeq 1$ ($T_c = 90$ K), $x \simeq 0.6$ ($T_c = 66$ K), and $x \simeq 0.1$ (insulating). The spectrum of the insulating ($x \simeq 0.1$) phase shows the charge transfer band at $\omega \sim 2.0$ eV. This energy has been associated with a charge transfer across the O $2p$ and the Cu $3d$ levels.^{28,76,77} Upon doping, the strength of this charge transfer transition diminishes. The reduction is accompanied by an enhancement of the conductivity in the midinfrared in both the a and b axes. Moreover, there is a lifting in the degeneracy of the peak at 4.1 eV that is present in the tetragonal insulating phase. The peak becomes weaker and is blueshifted in the a -axis polarization as oxygen doping in the sample is increased.

Schlesinger *et al.*³¹ reported the temperature dependence in the a - and b -axis reflectance of mechanically detwinned single-domain crystals ($T_c = 90$ K). The normal state data show qualitatively similar results as described above for samples of similar T_c . In the superconducting state, the authors reported what appears to be 100% reflectivity (within 0.5% uncertainty) for the a -axis polarization below an energy of 500 cm^{-1} . On the other hand, the b -axis reflectance is 2–3% lower in the same energy range. This apparent threshold in the a -axis reflectance is interpreted as the BCS superconducting energy gap ($2\Delta = 8k_B T_c$) in the CuO_2 planes. The extra absorption observed in the b direction is argued as resulting from the stronger midinfrared absorption due to the presence of the chain excitations in this direction. The doping dependence of this threshold in the a -axis reflectance has also been investigated by Rotter *et al.*⁷⁸ The samples investigated are oxygen reduced single-domain crystals of $\text{YBa}_2\text{Cu}_3\text{O}_{7-\delta}$ with T_c of 56, 82, and 93 K. The results show the structure at 500 cm^{-1} does not shift neither with doping nor with a change in temperature for all three doping levels studied.

The claim that this energy corresponds to a superconducting energy gap is now considered rather questionable. Most recent direct absorption (bolometric) measurements by Pham *et al.*³⁰ show a finite and fairly large conductivity below this energy for polarization along the a -axis direction in 90-K single-domain crystals. The fact that the accuracy in these measurements is rather high compared to typical uncertainties in reflectance experiments (0.02% *vs.* 0.5%) makes the results for the a -axis conductivity shown in Fig. 9 more representative of the real situation. Because of their short coherence length ($\xi \sim 10 \text{ \AA}$), the high- T_c superconductors are considered type II material. In all the analyses of the conductivity,^{68,71,72} the mean free path (l) obtained from the scattering rate of the Drude component just above T_c is long compared to ξ ($\xi < l$). This implies the materials are in the clean limit as first

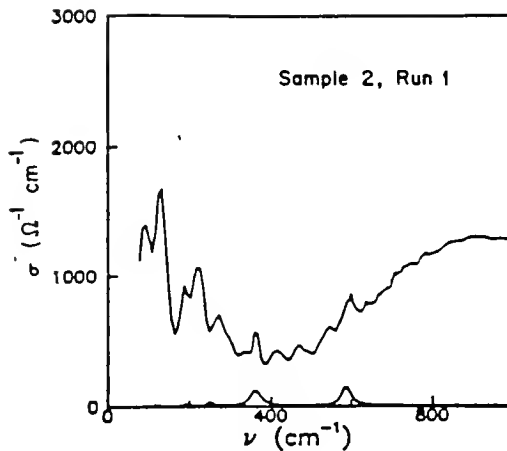


Fig. 9. Superconducting state optical conductivity of single domain of $\text{YBa}_2\text{Cu}_3\text{O}_{7-\delta}$ in the a direction. The weak peaks are calculated phonon contributions. No evidence of a superconducting gap is seen in the spectrum (after Ref. 30).

pointed out by Kamaras *et al.*⁶⁸ Since the width of the free carrier band is smaller than that of the superconducting gap, observation of this gap by optical methods might be difficult because most of the spectral weight of the free carrier part has condensed into a δ -function at zero frequency, leaving a negligible amount of weight for transition across the gap. Notice this argument agrees with a superconducting gap that is large compared to the scattering rate of the Drude component. There have been attempts⁷⁹ to produce dirty enough samples, but still superconducting, that would make $\xi \sim l$ so the gap might be observable using optical methods. So far, these experiments have not been successful.

$\text{Bi}_2\text{Sr}_2\text{CaCu}_2\text{O}_8$

There are many studies concentrating on the optical properties in the $\text{Bi}_2\text{Sr}_2\text{CaCu}_2\text{O}_8$ compound.^{57,80–86} With perhaps a few exceptions most studies have not addressed the anisotropy of the ab plane in this material. Let us first discuss some

of the unpolarized results. Figure 10 displays results of the average reflectance in the ab plane of this system on a wide frequency range for three samples with different doping levels.⁸⁰ Similar results have been reported by other groups.^{81–83} The low frequency reflectance is characterized by the absence of strong phonon lines. At higher frequencies, the reflectance falls off in a quasilinear fashion reaching the plasma edge minimum at around $10,000\text{ cm}^{-1}$ (1.2 eV). The results at high frequency are characterized by a couple of interband transitions. The first peak, which is centered at $16,000\text{ cm}^{-1}$ (2 eV), is attributed to the charge transfer band between the occupied O $2p$ levels and the lowest unoccupied Cu $3d$ orbitals in the CuO_2 planes. The second interband peak, which appears at $30,000\text{ cm}^{-1}$ (3.8 eV), is found to show some sample to sample variation and has been interpreted as an interband transition occurring mostly in the Bi_2O_2 layers. As mentioned previously, this material has no chains. In spite of this, there is an orthorhombic distortion of the ab plane resulting from an incommensurate superlattice modulation presents along the b axis of the material. There have been only a few studies reporting on the anisotropy of the ab -plane optical properties of this system.^{57,85,86} The first of those reports, by Kelly *et al.*,⁸⁵ consisted of ellipsometric measurements that showed a strong anisotropy in the near-infrared region and higher frequencies. In particular, the peak at $30,000\text{ cm}^{-1}$ (3.8 eV) is found to be sharper and stronger along the modulation direction.

The temperature dependence in the far-infrared optical conductivity has been obtained from a Kramers-Kronig analysis of the unpolarized reflectance⁸⁴ and transmittance⁸⁷ studies of free standing single crystals. The micaceous nature of the Bi-based material has made possible the preparation of very thin flakes (1000 \AA) that could be used for transmittance studies without having to worry about substrates. The results for the optical conductivity, obtained from Kramers-Kronig analysis of the transmittance, indicate a far-infrared conductivity that follows closely the T-dependence of the

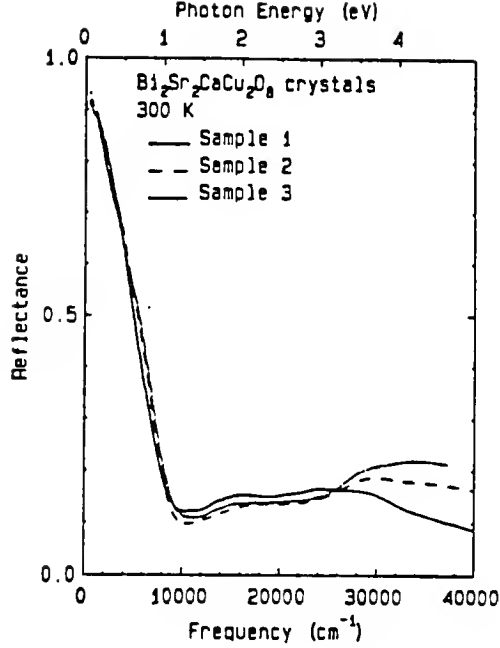


Fig. 10. Room temperature reflectance of $\text{Bi}_2\text{Sr}_2\text{CaCu}_2\text{O}_8$ samples with different oxygen doping (after Ref. 80).

dc value. At the same time, the temperature dependence of $\sigma_1(\omega)$ is less pronounced in the midinfrared.⁸⁸ This is consistent with the non-Drude behavior observed in the infrared properties of the cuprate. In the superconducting state, there is a broad maximum at 1000 cm^{-1} (0.15 eV) followed by some weak phonon structures and a notch-like minimum at $\omega \sim 400 \text{ cm}^{-1}$. In addition, transmittance studies showing *ab*-plane anisotropy in the midinfrared region were reported by Romero *et al.*⁸⁶ The reported anisotropy is quite substantial in spite of the fact the difference in the *a*- and *b*-axis dimensions of the pseudotetragonal unit cell is only 3%. The transmittance in the midinfrared is found to be lower for the *b* direction (more absorbing) than the *a* axis.

CHAPTER III THEORY

Models for Carriers in the CuO₂ Planes: Normal State

Superconductivity in the copper-oxide materials arises through the addition of carriers by hole or electron doping the nearly square CuO₂ planes. The normal-state properties of these doped planes are very unusual, and so far, they have not been fully accounted for. The property that is most frequently mentioned as indicative of unusual normal-state behavior is the linear temperature dependence of the resistivity $\rho(T)$. This behavior is not the case in, for example a Fermi liquid description, where $\rho \propto T^2$ is what is expected due to electron-electron scattering. Other unusual properties are a temperature dependent Hall coefficient, proximity of superconductivity to a magnetic phase, and a very short coherence length. It is widely believed that understanding of the normal-state properties will eventually provide knowledge of the pairing mechanism in the cuprate. Most theoretical models for the normal-state properties start with the so-called three-band Hubbard model. Next sections discuss the underlying issues of this and other models and the implications for the description of electron dynamics in the 2-dimensional CuO₂ planes.

Three-Band Hubbard Model

The unusual properties of the copper-oxide superconductors prompted the need to construct a Hamiltonian that properly describes the motion of carriers in the CuO₂ planes of these materials. People working in the field soon realized that electron correlations were essential to properly describe the physics of the high- T_c superconductors. As an example, let us start with the insulating La₂CuO₄. Charge counting in this

system leaves one hole (or one electron) per unit cell. If one neglects interactions, this material would be expected to be metallic with a half-filled conduction band. In reality, this material is an antiferromagnetic insulator. Band structure calculations⁸⁸ showed the available states for this hole could be in either one of the Cu $3d$ or O $2p$ ($2p_x, 2p_y$) orbitals. As mentioned before, each Cu atom in the structure is surrounded by an octahedron of six O atoms. (This number changes for different materials: 5 for $\text{YBa}_2\text{Cu}_3\text{O}_{7-\delta}$ and 4 for Nd_2CuO_4 .) This configuration removes the degeneracy between the $3d$ orbitals of the Cu atom. It turns out the highest energy level has mainly a $3d_{x^2-y^2}$ character. Therefore, the hole would reside mostly on the Cu site, giving this atom a net spin of $1/2$. Hence, the material can be best described by a model with localized spin- $1/2$ states. An antiparallel arrangement of these spins would seem to explain both the insulating and antiferromagnetic properties of the material as indeed is the case.⁵⁹ A low-lying optical excitation would then be the transfer of one hole from the O $2p$ level to the upper Hubbard band (Cu $3d$). The gap for this excitation is denoted by Δ in Fig. 11. This has been corroborated in optical studies of La_2CuO_4 and other insulating parent compounds, where a charge transfer excitation has been observed in the optical conductivity that is peaked at around $1.7\text{--}2.0$ eV.^{28,77}

Then, the next question to ask is how to construct a Hamiltonian that includes the motion of additional holes introduced by doping? An answer to this has been provided in a 2-dimensional tight-binding model by Emery *et al.*^{89,90} and Varma *et al.*⁹¹ The basic feature of this model is the introduction of an hybridization parameter t_{pd} between the Cu $3d$ and O $2p$ orbitals. Other parameters that are included to account for all possible interactions are site energies ϵ_d and ϵ_p , Coulomb energies U_d and U_p between two holes of opposite spins on the same Cu and O sites respectively, and V_{dp} is the interaction term between holes on neighboring Cu and O sites. The

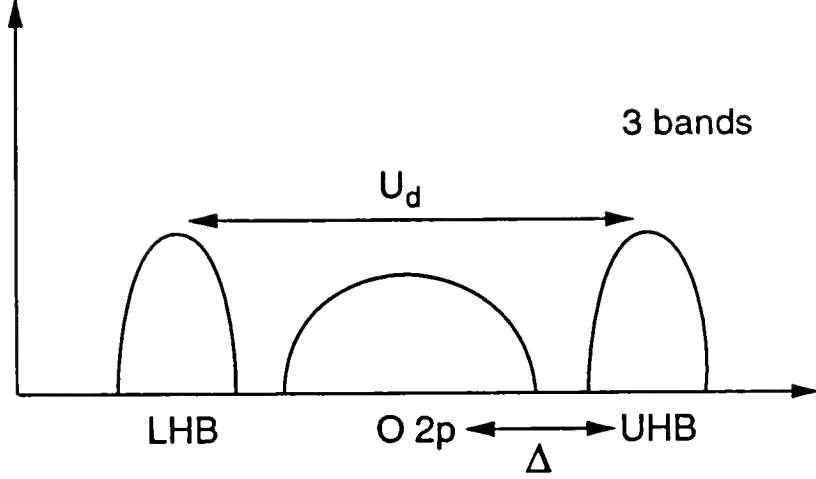


Fig. 11. Energetic position of the three bands in the three-band Hubbard model.

Hamiltonian can be written explicitly as

$$\begin{aligned}
 H = & -t_{pd} \sum_{\langle i,j \rangle} p_j^\dagger (d_i + h.c.) - t_{pp} \sum_{\langle j,j' \rangle} p_j^\dagger (p_{j'} + h.c.) + \epsilon_d \sum_i n_i^d + \epsilon_p \sum_j n_j^p \\
 & + U_d \sum_i n_{i,\sigma}^d n_{i,-\sigma}^d + U_p \sum_i n_{i,\sigma}^p n_{i,-\sigma}^p + V_{dp} \sum_{\langle i,j \rangle} n_i^d n_j^p.
 \end{aligned} \tag{1}$$

The first term is the hybridization or hopping between nearest neighbors on Cu and O atoms. The p_j are Fermionic operators that destroy holes at the O site labeled j , while the d_i correspond to annihilation operators at the Cu site i . Also, $\langle i, j \rangle$ refers to pairs of nearest neighbors on i (Cu) and j (O) sites. A term for direct O–O hopping is also included for completeness. Notice also that only near-neighbor interactions are taken into account. Interactions at larger distances are thought to be screened by a finite density of electrons. In the undoped materials and for $\epsilon_p - \epsilon_d > 0$, the Hamiltonian in Eq. 1 shows there will be one hole on every Cu site as indeed is the case. In the

limit $U_d > \epsilon_p - \epsilon_d$, additional holes produced by doping will go mostly into the O $2p$ orbitals. There have been band structure calculations⁹³ and most recently cluster calculations⁹⁴ that have placed estimates for the parameters in Eq. 1. The results are $\epsilon_p - \epsilon_d \simeq 3.6$ eV, $U_d = 8 - 11$ eV, $U_p \simeq 4$ eV; the remaining terms (t_{pd} , U_{pd} , and t_{pp}) are all in the range 1–2 eV. It is clear from the value of U_d the appropriate limit for the physics of the high temperature superconductors is the intermediate to the strong coupling limit.

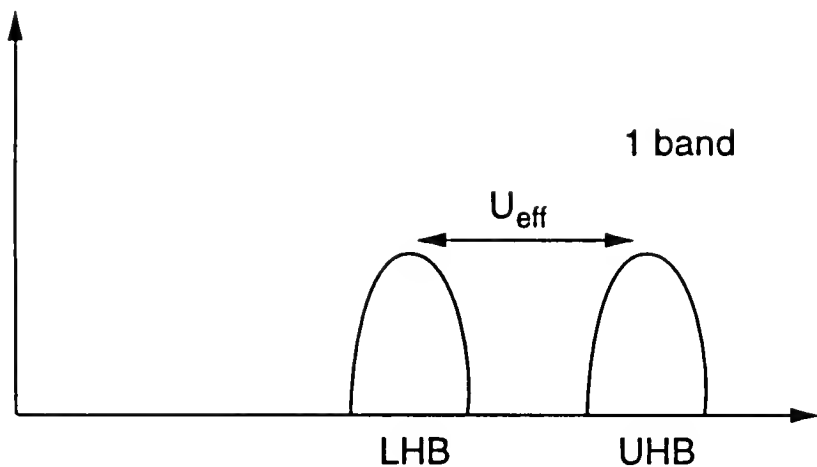


Fig. 12. Simplified picture of the three-band Hubbard model where the Cu $3d$ and O $2p$ levels are hybridized to form the lower and upper Hubbard bands (LHB and UHB respectively).

$t - J$ Model

It is not clear that a model as complex as Eq. 1 is necessary to describe the correct low-energy physics of the high- T_c materials. Early on, it was proposed by Anderson⁹⁵

that the correct effective theory might be reduced to a one-band Hubbard model. In this case the Hamiltonian is defined as

$$H = t \sum_{\langle ij \rangle, \sigma} [d_{i, \sigma}^\dagger d_{j, \sigma} + h.c.] + U \sum_i n_{i, \uparrow} n_{i, \downarrow}, \quad (2)$$

where the $d_{i, \sigma}^\dagger$ are fermionic operators that create holes at site i with spin σ . The hybridization of the Cu $3d_{x^2-y^2}$ and O_{2p} orbitals is denoted by the parameter t . The parameter U is the on-site Coulomb repulsion. Figure 12 shows a schematic in this case where the three bands of the three-band Hubbard model are combined into two bands labeled as the lower Hubbard band (LHB) and the upper Hubbard band (UHB).

In the strong coupling limit ($U \gg t$), the previous model can be transformed into the so called $t - J$ model that was first derived from the Hubbard model by canonical transformations by Hirsch⁹⁵ and Gros *et al.*⁹⁶ In the context of the high- T_c problem, the model was introduced by Anderson⁹⁴ and derived by Zhang and Rice⁹⁷ by canonical transformation from the three-band Hubbard model. In essence, this is a one-band Hubbard model, where the state of the doped hole is only represented by the spin of the Cu site on which it resides, *i.e.*, spin up or down if there is no hole, or the absence of spin if there is one hole at any particular site. Out of possible triplet or singlet mixing states, the latter was found to have the lowest energy for the hybridization of the Cu and doped-hole wavefunctions.⁹⁷ The Hamiltonian is

$$H = J \sum_{\langle ij \rangle} (S_i \cdot S_j - \frac{1}{4} n_i n_j) - t \sum_{\langle ij \rangle, \sigma} [c_{i, \sigma}^\dagger c_{j, \sigma} + h.c.], \quad (3)$$

where J is the antiferromagnetic coupling between nearest neighbors $\langle ij \rangle$ similar to the formalism in the Heisenberg Hamiltonian. The formula for J is defined as

$$J = \frac{4t^2}{U}, \quad (4)$$

where the limit of validity is for $J \ll t$ or $t \ll U$. The S_i are spin-1/2 operators and $c_{i,\sigma}^\dagger$ create electrons of spin σ on site i . Hence, electrons move in a 2-dimensional lattice with hopping amplitude t , constrained such that there are not doubly occupied sites. There have been some controversies in whether the three-band Hubbard and the reduced $t - J$ models will lead to the same low-energy physics on a temperature scale in the order of T_c . There have been some cluster calculations on a small number of atoms that have addressed this issue. In one of those studies,⁹² a cluster of the form Cu_5O_{16} is used with the full three-band Hubbard Hamiltonian and parameters determined *a priori*. For the stoichiometric case, it is found the eigenvalues of the problem map to the corresponding ones of the Heisenberg Hamiltonian for a finite number of spins. This is taken as giving some support to the model, although more work is clearly needed in the area.

Models for $\sigma_1(\omega)$

Numerical Results

The one-band Hubbard and $t - J$ models have been the starting points in many calculations for studying the dynamics of carriers moving in the CuO_2 planes. These include the response of those carriers under the influence of an electromagnetic field. Results pertaining to the anomalous midinfrared absorption observed in $\sigma_1(\omega)$ for nearly all copper-oxide superconductors were discussed in Chapter II. Here, there will be a summary of the theoretical studies related to obtaining $\sigma_1(\omega)$ from numerical solutions to the one-band Hubbard and the $t - J$ models outlined above.

It is generally accepted the one-band Hubbard model is one of the simplest models which may contain the essential features of the CuO_2 planes. The problem that exists is that in the physical region of interest, the strong coupling regime, there are not easily applicable analytic techniques to study, for example, the optical conductivity.

This is the reason why numerical solutions of finite cluster calculations have been found useful to obtain approximate solutions to the problem.^{98–100}

The numerical method commonly used to determine the ground state of the clusters is the Lanczos technique.¹⁰¹ This technique consists in providing an initial guess for the ground state $|\phi_0\rangle$ of the system. The next step is to apply the chosen Hamiltonian to this ground state to obtain a second state

$$|\phi_1\rangle = H|\phi_0\rangle - \frac{\langle\phi_0|H|\phi_0\rangle}{\langle\phi_0|\phi_0\rangle}|\phi_0\rangle, \quad (5)$$

with the constraint that the second state be orthogonal to the first one, *i.e.*, $\langle\phi_0|\phi_1\rangle = 0$. The remaining states corresponding to the Hilbert space of the cluster under study can be constructed in this way to give a matrix of coefficients a_n and b_n that are defined by

$$a_n = \frac{\langle\phi_n|H|\phi_n\rangle}{\langle\phi_n|\phi_n\rangle}, \quad (6)$$

and

$$b_n = \frac{\langle\phi_n|H|\phi_n\rangle}{\langle\phi_{n-1}|\phi_{n-1}\rangle}. \quad (7)$$

These definitions assure the states that form the basis of the Hilbert space are orthogonal to each other. The matrix obtained from these coefficients can be later diagonalized using standard methods.

The conductivity tensor in linear response theory is obtained from the relationship between the current density operator, $j_x(\mathbf{q}, \omega)$, and the electric field vector, $E_x(\mathbf{q}, \omega)$, in the limit of $\mathbf{q} \sim 0$. Hence, it can be shown

$$j_x(0, \omega) = \sigma_{xx} E_x(0, \omega), \quad (8)$$

where σ_{xx} the absorptive part of the optical conductivity at zero temperature might be written as

$$\text{Re } \sigma_{xx} = \frac{1}{\pi\omega} \text{Im}[\langle \phi_0 | j_x \frac{1}{H - E_0 - \omega - i\epsilon} j_x | \phi_0 \rangle], \quad (9)$$

where H is the Hamiltonian whose energy is E_0 , ω is the frequency, and ϵ is a small number that moves the poles of the Green's function into the complex plane. In the Hubbard model, the current operator j_x in the x direction at zero momentum can be written as⁹⁸

$$j_x = it \sum_{l,\sigma} (c_{l,\sigma}^\dagger c_{l+x,\sigma} - h.c.). \quad (10)$$

As discussed previously, the one-band Hubbard Hamiltonian contains three characteristic energies that are expected to give interesting optical excitations; the hopping term t , the on-site repulsion term U , and the exchange interaction J , given by Eq. 4 in the strong coupling limit. Dagotto *et al.*¹⁰⁰ reported numerical solutions for the one-band Hubbard model on a 4×4 cluster, and for a hole concentration in the interval $0 < x < 0.375$. At half filling, the results show accumulation of weight in $\sigma_1(\omega)$ above an energy which is close to $6t$. If previous estimates of t are taken,⁹² this energy can then be correlated with the corresponding charge transfer gap of excitations that is observed in the optical conductivity of the insulating compounds around $\omega \sim 2.0$ eV. If such correlation is made, the weight in $\sigma_1(\omega)$ is the result of charge excitations from the lower to the upper one-band Hubbard model. Figure 13 also shows the results at doping levels away from half filling. It is evident in the figure the redistribution of spectral weight from this charge transfer gap to lower energies as function of doping. In particular, the doping level of $x = 0.125$, which corresponds to 2 holes in the 4×4 cluster, shows two major features that occur below the CT band. In the first place, there is accumulation of weight at $\omega = 0$, that is related to the Drude or free-carrier response in the material. The second accumulation of spectral

weight that occurs half way between zero and the CT band has been associated by Dagotto *et al.* and others^{98–100} as the midinfrared band that shows up in the optical conductivity spectrum of the cuprate. The results also show that, with increased doping, the Drude peak grows considerably, while the midinfrared band only shows a modest increase. Dagotto *et al.*¹⁰⁰ pointed out the results shown in Fig. 13 would correspond to the intermediate coupling regime, *i.e.*, $U \sim 8t$. For large coupling, a gap develops between the CT excitation and the midinfrared band, whereas for small values of U/t both excitations merge, making it difficult to separate them.¹⁰⁰ Similar calculations in the context of the $t - J$ model have been done by Stephan and Horsch⁹⁹ for different values of J . The results show a qualitative agreement with the ones shown in Fig. 13. The Drude and the midinfrared peaks are clearly evident in these calculations. Similar results in the near-half filling case were also obtained by C.-X. Chen and H.-B. Shüttler from solution of the one-band Hubbard model in the strong coupling limit.¹⁰²

Two-Component Model

From the previous discussion, it is quite clear the numerical results obtained from the one-band Hubbard and $t - J$ models favor the approach followed by many researchers regarding the interpretation of the optical conductivity $\sigma_1(\omega)$ obtained in experiments involving the optical properties of the copper-oxide superconductors. In this approach, the infrared conductivity in these materials is considered to be the combination of a Drude-like free-carrier component at $\omega = 0$, with a strongly temperature dependent scattering rate, combined with much broader bound excitations at higher frequencies. In this picture, the free carriers track the temperature dependence of the dc resistivity above T_c , while condensing into the superfluid below T_c .^{24,28,65,68,103} In contrast the “intraband” or bound carriers have an overdamped scattering rate that exhibits very little temperature dependence.

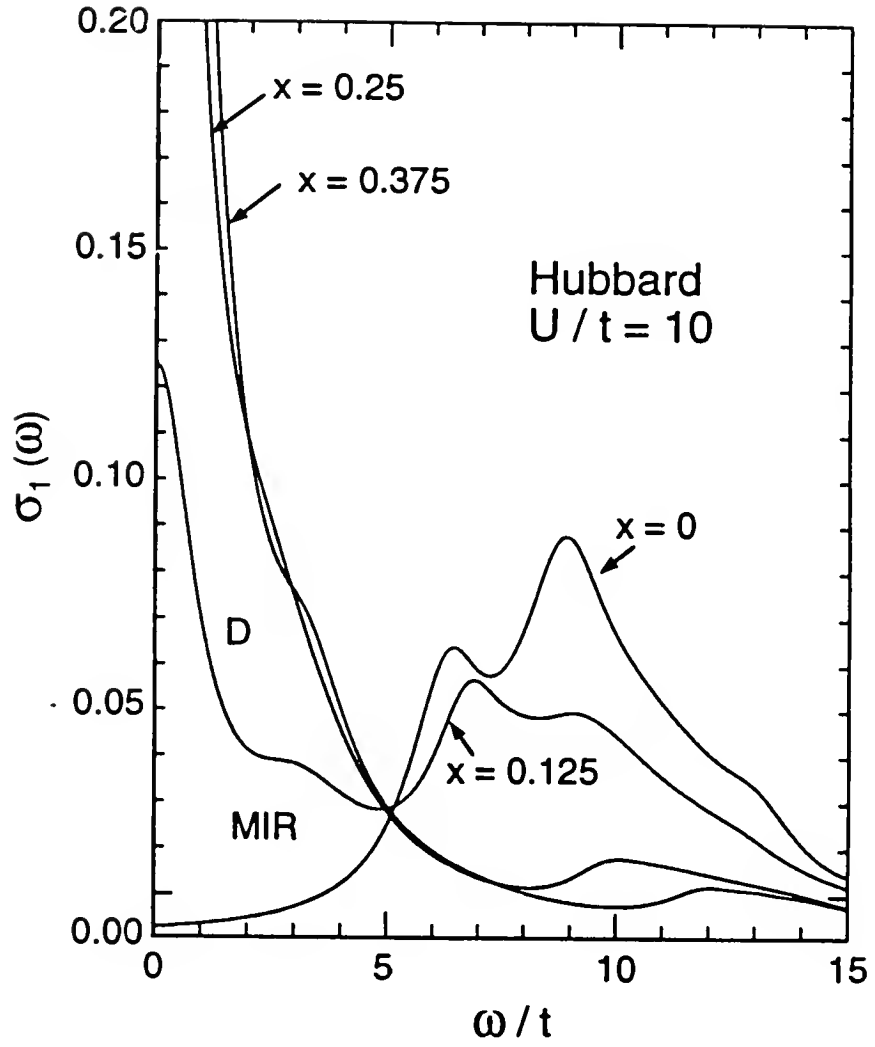


Fig. 13. Optical conductivity obtained from solution of the one-band Hubbard model (After Ref. 101).

The extra component in the infrared has also been argued to be the result of direct transitions from valence band states close to the Fermi level into empty states of the conduction band.¹⁰⁴ In the absence of a clear physical origin for these “intraband” excitations, the natural choice has been to model those absorptions by Drude-Lorentz oscillators. Hence, the dielectric function $\epsilon(\omega)$ is fitted to an equation of the form

$$\epsilon(\omega) = -\frac{\omega_{pD}^2}{\omega^2 + i\omega 1/\tau} + \sum_{j=1}^N \frac{\omega_{pj}^2}{\omega_j^2 - \omega^2 - i\omega\gamma_j} + \epsilon_\infty. \quad (11)$$

In Eq. 11, the first term represents the Drude component described by a plasma frequency ω_{pD} and scattering rate $1/\tau$; the second term is a sum of midinfrared and interband oscillators with ω_j , ω_{pj} , and γ_j being the resonant frequency, oscillator strength, and the width of the j^{th} Lorentz oscillator respectively. The last term, ϵ_∞ , is the high frequency limit of $\epsilon(\omega)$, which includes higher interband transitions.

One-Component Model

An alternative approach that has been proposed to explain the anomalous non-Drude behavior in the infrared conductivity of the copper-oxide materials is to model $\sigma_1(\omega)$ using a generalized Drude model with a frequency dependent scattering rate $1/\tau(\omega)$.^{31,75,78} In this model, there is only one type of charge carriers. Hence, the dielectric function can be written as¹⁰⁵

$$\epsilon(\omega) = \epsilon_\infty - \frac{\omega_p^2}{\omega[\omega - \Sigma(\omega)]}, \quad (12)$$

where ω_p is the bare plasma frequency for the charge carriers in the far and midinfrared, defined by $4\pi Ne^2/m_b$, and ϵ_∞ is a constant that includes contributions from interband transitions. The term $\Sigma(\omega)$ represents the self-energy of the quasiparticles, as will be defined below. Since the real and imaginary part of $\epsilon(\omega)$ are related

through the Kramers-Kronig relations, they must obey causality. Then, to ensure this causality condition, $\Sigma(\omega)$ is taken to be complex, *i.e.*, $\Sigma(\omega) = \Sigma_1(\omega) + i\Sigma_2(\omega)$ with $\Sigma_2(\omega) < 0$. Hence, the model requires the introduction of a modified functional form for both the effective mass and the scattering rate. By decomposing the real and imaginary part of $\Sigma(\omega)$, we arrive at

$$\frac{m^*(\omega)}{m_b} = 1 - \frac{\Sigma_1(\omega)}{\omega}$$

and

$$1/\tau^*(\omega) = -\Sigma_2(\omega) \frac{m_b}{m^*(\omega)}$$

where now $1/\tau^*(\omega)$ is called the “renormalized” scattering rate, m_b is the band mass, and m^* is the frequency dependent effective mass. Two models that provide a phenomenological justification for this approach are the “marginal Fermi liquid” (MFL) theory of Varma *et al.*^{106,107} and the “nested Fermi liquid” (NFL) theory of Virosztek and Ruvalds.¹⁰⁸ For example, the imaginary part of the one-particle self-energy in the MFL model, is written as

$$-\text{Im } \Sigma(\omega) \sim \begin{cases} \pi^2 \lambda T, & \omega < T \\ \pi \lambda \omega, & \omega > T \end{cases} \quad (13)$$

where λ is a dimensionless coupling constant. Hence, for $\omega < T$ the model predicts a renormalized scattering rate that is linear in temperature, which is expected from the linear temperature dependence in the resistivity that is observed in nearly all copper-oxide superconductors. As ω increases, reaching a magnitude of order of T or higher, a new spectrum of excitations arises. This causes $1/\tau^*(\omega)$ to grow linearly with frequency up to a cutoff frequency ω_c that is introduced in the model.

The physical explanation for this behavior is due to coupling of the charge carriers with a spectrum of charge and/or spin-density fluctuations that would lead to an

effective mass enhancement at low frequencies. This enhancement is expected to be proportional to the coupling constant λ . Finally, the model requires the presence of an energy gap that opens up at the Fermi surface as the material enters in the superconducting state. This gap should show up in the spectrum of $\sigma_1(\omega)$. As it will be discussed later, observation of this gap by optical means is still an open question.

When data obtained by different groups^{72,75,87} using different high- T_c materials are analyzed in the context of this model, there seems to be a qualitative agreement with the predictions of the model. In first place, the dc resistivity obtained from the model agrees with the experiment. Secondly, $-\text{Im}\Sigma(\omega)$ is nearly constant for $\omega < T$, while it increases linearly with ω for $\omega > T$. Thirdly, there is an effective mass enhancement at low frequencies that is larger at low temperatures.

One important argument against the model is that the cutoff frequency determined by the agreement between the data and the model is rather low, *i.e.*, ω_c is below 1000 cm^{-1} . This is in conflict with the high cutoff frequency suggested by Raman¹⁰⁹ experiments where $\omega_c \approx 7000 \text{ cm}^{-1}$. In addition, the coupling constant determined for samples with lower T_c is actually larger when compared with the value obtained with higher T_c samples.⁷⁵ The problem arises because the T_c is supposed to be determined by λ .

Superconducting State Models

Experimental evidence for the unconventional nature of the normal-state properties in the copper-oxide superconductors has been established without a doubt. At the same time, there is no unambiguous evidence that the properties in the superconducting state show anomalous behavior as well. It was established early on that pairing of electrons (holes) was indeed present in the superconducting state of these materials. A series of experiments on $\text{YBa}_2\text{Cu}_3\text{O}_{7-\delta}$ were performed that showed the elementary charge in the superconducting state is $2e$ rather than e .^{3,4} There are two

questions that one can ask about the nature of this pairing. The first one is what is the force that mediates the attractive interactions? In ordinary superconductors, the pairing is mediated by phonons interacting with free carriers in the material.² The second question is whether the pairing is accompanied by an energy gap that opens up on the Fermi surface as happens in conventional superconductors.¹¹⁰ Evidence against the conventional nature of this pairing could then be, for example, the presence of nodes or states within this gap.

While answer to the pairing mechanism must await the development of a successful theory to explain superconductivity in the high- T_c materials, experiments could, in principle, provide answer to the presence of a gap. In fact, many experimental techniques, such as tunneling, infrared spectroscopy, photoemission and penetration depth measurements, have tried to demonstrate the existence of the superconducting gap and its symmetry. Unfortunately, there have been contradictions in some of the results. The following section will review the many ideas, both theoretical and experimental, that have been discussed related to the possible symmetry of the pairing in the superconducting state of the copper-oxide materials.

Symmetry of the Order Parameter

Superconductivity in general is regarded as evidence of a broken symmetry. This transformation involves a change that allows the description of the system, in the thermodynamic limit, by a macroscopic wavefunction Ψ and a phase. In group-theoretical calculations, the symmetry of the superconducting state corresponds to one of the irreducible representations of the total symmetry group of the normal state.^{111,112} The possible broken symmetries considered are spin and point group rotations as well as global gauge symmetries. In the high- T_c materials, such as $\text{YBa}_2\text{Cu}_3\text{O}_{7-\delta}$ and $\text{Bi}_2\text{Sr}_2\text{CaCu}_2\text{O}_8$ the symmetry of the crystal lattice is known to be almost tetragonal with the orthorhombic distortion of the CuO_2 planes being relatively small. Inclusion

of this distortion may lead to different conclusions regarding the possible symmetry classifications of the order parameter in the superconducting state. In addition, since in BCS theory superconductivity results from pairing of electrons, the coupling of the electron spins could lead to singlet ($S=0$) or triplet ($S=1$) states for the spin part of the pairing wavefunctions.

In the following discussion spin-orbit coupling is not considered for brevity. Also, the assumed crystal symmetry in the normal state will be the one of the lattice,¹¹³ although others have been proposed in the literature.¹¹⁴ For example, if a tetragonal point group symmetry is considered for the crystal, the possible superconducting state symmetry can be derived from the irreducible representations of the group $SO(3) \times D_{4h}$, where $SO(3)$ is the group rotation in spin space and D_{4h} is the point group symmetry of the lattice. In a singlet state with tetragonal point group symmetry, there are 1- and 2-dimensional irreducible representations corresponding to the D_{4h} group in the system. Based on experimental grounds, the two most quoted possibilities for the high- T_c are the A_{1g} and B_{1g} . The first one, the A_{1g} , is the only singlet state with a gap function that is nonzero everywhere on the Fermi surface. This symmetry corresponds to the so-called s-wave symmetry in the BCS theory for conventional superconductors. The gap function has the form $\Delta(k) = \Delta_0$, up to a function with the symmetry of the lattice. The second possibility that has arisen in some theoretical models,¹¹⁵ as well as from some recent experimental results^{5,116} that will be discussed later, corresponds to the B_{1g} point group symmetry. This representation gives a gap function that can be represented with the $d_{x^2-y^2}$ orbital and that is usually written as $\Delta(k) = \Delta_0(\cos k_x - \cos k_y)$. On a spherical Fermi surface, this gap function would have nodes at 45° angles with respect to the lobe maxima.

If the point group symmetry of the lattice has orthorhombic (D_{2h}) symmetry, there will be 4 possible singlet-state alternatives. The first one corresponds to the

A_{1g} point group and has s-wave symmetry. The rests have the B_{1g} , B_{2g} , and B_{3g} irreducible representations, having single-state gap symmetries of the following d-wave like orbitals: d_{xy} , d_{xz} , and d_{yz} respectively. It should be pointed out that the $d_{x^2-y^2}$ will not be realized in this case.

There are many other possibilities that include triplet state spin wave functions in both orthorhombic and tetragonal point group symmetries. The p-wave states, for example, are important in superfluid ^3He . The interested reader is referred to the literature for more details.¹¹³

Evidence for Proposed Pairing States

In the context of the $t - J$ model, there have been numerical results on finite clusters that suggest an attractive channel for binding of two holes in an antiferromagnetic background with $d_{x^2-y^2}$ symmetry.^{115,117,118} The results show the average distance between the two holes decreases as the ratio J/t increases. It has been proposed this provides evidence that the strong coupling limit is a necessary condition for the binding of holes in the $t - J$ model and that it eventually leads to phase separation in the system, *i.e.*, the material separates in hole-rich and hole-poor regions.^{115,119-121} Dagotto *et al.*¹¹⁵ extended the calculations to include higher doping in a 4×4 cluster as a function of the ratio J/t . The numerical results also suggest in this case a signal for superconductivity that is stronger in the $d_{x^2-y^2}$ channel. For this channel, the pairing correlation function shows a maximum at $J/t \approx 3$. Of course, these results are not enough evidence to prove a condensate in the bulk of the system. Finite size effect studies should be carried out before a definite conclusion could be reached. On the other hand, finite cluster calculations in the three- and one-band Hubbard models have not given evidence for binding of holes in the $d_{x^2-y^2}$ channel, although the results are only for small cluster sizes.^{122,123} When more powerful computers become available, this issue could be address with larger clusters.

Let us turn our attention to the experimental data. The electromagnetic London penetration length $\lambda_L(T)$ is considered one of the basic lengths in superconductivity. This is because its temperature dependence can give information about the pairing state in a superconductor. Earlier *ab*-plane penetration depth measurements on $\text{YBa}_2\text{Cu}_3\text{O}_{7-\delta}$ single crystals and films by Harshman *et al.*^{124,125} and Kruisin-Elbaum *et al.*¹²⁶ suggested the gap was nodeless, *i.e.*, the low temperature behavior of $\lambda_L(T)$ was thought to be exponential as in an ordinary BCS superconductor with isotropic gap. Most recently, a reanalysis of these and more recent kinetic inductance data by Fiory *et al.*¹²⁷ have yielded a quadratic variation of $\Delta\lambda_L(T)$ from its zero temperature value.^{55,128} Most available results are best fitted¹²⁹ by using the empirical Gorter-Casimir formula

$$\lambda_L(T) = \frac{\lambda_L(0)}{(1 - t^2)^{1/2}}, \quad (14)$$

where $t = T/T_c$. Likewise, in more recent penetration depth experiments on single crystals of $\text{YBa}_2\text{Cu}_3\text{O}_{7-\delta}$ using a stable microwave cavity, it has been found the very low temperature dependence of $\lambda_L(T)$ is linear rather than quadratic in T .¹¹⁶ The results have been explained as consistent with an order parameter that has $d_{x^2-y^2}$ symmetry, since this symmetry would introduce a linear power-law variation in $\Delta\lambda_L(T)$ of the form

$$\frac{\lambda_L(T)}{\lambda_L(0)} - 1 = \left(\frac{k_B T}{\Delta_{max}} \right), \quad (15)$$

where Δ_{max} is the maximum gap value over the Fermi surface. Moreover, the temperature dependence of the penetration depth in $\text{Bi}_2\text{Sr}_2\text{CaCu}_2\text{O}_8$ single crystals and $\text{YBa}_2\text{Cu}_3\text{O}_{7-\delta}$ films have been done by Ma *et al.*¹³⁰ In this study, it is found that in both cases $\Delta\lambda_L(T) \propto T^2$ for $T \ll T_c$. Thus far, there has been little progress in the understanding of the observed differences. The problem that exists is that any physical model based on some sort of disorder in some of the samples would imply a significant reduction in T_c contrary to what has been observed. There have been

attempts to model the effect of impurities that could change the linear T dependence to T^2 in less than ideal samples.^{131,132} It is shown in one of those calculations that strong resonant scattering could account for the differences that are observed in the temperature dependence of $\Delta\lambda_L(T)$ in films and single crystals that have an order parameter with a $d_{x^2-y^2}$ symmetry.¹³¹ Perhaps, other more subtle mechanisms such as the CuO chains in $\text{YBa}_2\text{Cu}_3\text{O}_{7-\delta}$ and the superlattice modulation in $\text{Bi}_2\text{Sr}_2\text{CaCu}_2\text{O}_8$ could have some effect in the electrodynamics response of these materials.

Using $\text{Bi}_2\text{Sr}_2\text{CaCu}_2\text{O}_8$ samples from the same batch as the one that showed $\Delta\lambda_L(T) \propto T^2$, Shen *et al.*⁵ performed angular resolved photoemission spectroscopy (ARPES) measurements and found a condensate peak that is larger and more pronounced along the symmetry line $\Gamma - X$, *i.e.*, from center of the Brillouin zone to the x -direction in momentum space, and seems to vanish (within the experimental resolution of 10 meV) 45° away from the previous direction ($\Gamma - M$). Based on this observation, they conclude the symmetry of the order parameter is compatible with $d_{x^2-y^2}$ symmetry pairing.⁵ This conclusion is strongly dependent on two assumptions. The first is that the gap is zero in the direction where it is undetectable in the experiment. The second is the point group symmetry of the crystal is tetragonal rather than orthorhombic, *i.e.*, a rotation of 90° or 180° in the plane would give the same magnitude of the gap with just a change of the phase. From the results presented, it is not clear whether these checks were made. Moreover, such data do not seem incompatible with similar measurements done by Kelley *et al.*⁷ where another singlet d -wave symmetry (d_{xz}) is proposed as an allowed possibility. This is concluded from symmetry analysis of the condensate peak observed in photoemission experiments as function of photon polarization and photoelectron collection directions. The authors also pointed out that other possibilities such as mixing of d -wave with either s - or p -wave symmetries cannot be excluded based on the results of the experiment.

Finally, the authors concluded that the point group symmetries of both the normal and superconducting states of this compound show a D_{2h} instead of a D_{4h} character.

Other probes of the pairing state in the high- T_c , such as tunneling, do not reveal clear evidence of a gap, but rather show substantial density of states in the range where a gap might be expected.^{8,9}

Determination of Gap by Optical Spectroscopy

As is well known, a superconductor is a good reflector of light for energies below 2Δ , where 2Δ is the optical energy gap for quasiparticle excitations in the superconducting state. This means that in a reflectance experiment a signature of the gap will be when $R = 1$ for photon energies less than 2Δ . At higher energies, since there is enough energy to break a Cooper pair, the material will start absorbing light and the reflectance will show deviation from unity. A Kramers-Kronig analysis will then show an optical conductivity $\sigma_1(\omega)$ that is zero for $\omega = 2\Delta$, and finite for $\omega > 2\Delta$. This has indeed been confirmed in the experiment, where 2Δ is very close to the value predicted by the BCS theory for most conventional superconductors.¹¹⁰

There have been attempts in many optical studies to associate features in the superconducting state reflectivity of the high- T_c materials with superconducting energy gaps.^{31,65,78,133,134} Values in the quantity $2\Delta/k_b T_c$ reported in the literature have ranged between 2.5 and 8. However, these claims must be taken with certain caution for two reasons. In the first place, there is a stringent requirement that R must be unity below the threshold for quasiparticle excitations. With the typical uncertainties ΔR in the order $\pm 0.5\%$, it is not possible to rule out any small but finite absorption when the reflectance is very close to 100%. This is important in view of the fact that such uncertainties in R will introduce errors in $\sigma_1(\omega)$ in the order of

$$\frac{\Delta\sigma_1(\omega)}{\sigma_1(\omega)} = \frac{\Delta R}{R(1-R)}. \quad (16)$$

It is clear that the S/N ratio in $\sigma_1(\omega)$ diminishes as R approaches one. Secondly, there have been reports of direct absorption measurements³⁰ that show a nonzero value for the a -axis absorptivity of single domain crystals of $\text{YBa}_2\text{Cu}_3\text{O}_{7-\delta}$ down to 100 cm^{-1} or so. Such energy falls well below the range of values of $2\Delta/k_b T_c$ reported in the literature. To reconcile these results, it has been proposed the extra absorption observed in $\sigma_1(\omega)$ below T_c is part of a second component in the midinfrared conductivity.^{68,71,72,103,116,135} To explain the absence of a gap feature, it has been argued that since the high- T_c materials are in the clean limit,⁶⁸ because of the short coherence length and long mean free path, the rising reflectance in the far infrared is not due to a superconducting gap but rather to a scattering rate that approaches zero as the sample enters in the superconducting state.⁷¹ This picture is consistent with a Drude-term conductivity that condenses into a delta function at zero frequency. This leaves very little spectral weight for transitions across the gap that might still be present in the superconducting state. Furthermore, it has been argued that some of these features might be associated with interaction involving longitudinal c -axis phonons with the ab -plane bound carriers.^{135,136} An apparent justification for this is due to the fact that some of these features are still present above T_c . This issue will be addressed in Chapter V with results obtained on a $\text{La}_2\text{CuO}_{4+\delta}$ single crystal.

CHAPTER IV

EXPERIMENTAL TECHNIQUES

An optical experiment involves the measurement of the transmittance or the reflectance of a sample as a function of the incident light frequency. When this is done over a very wide frequency range, typically between the far infrared and the ultraviolet (UV) regions of the optical spectrum, it is necessary to use different combinations of spectrometers, light sources, and detectors. This chapter describes the experimental techniques used in this work. The first section in the chapter includes discussion of the Fourier transform spectroscopy technique that was used to cover the spectral regions in the far and midinfrared. There is also a discussion on the Perkin-Elmer monochromator that was used to cover from the midinfrared up to the UV. Descriptions of the kind of detectors, polarization control, sample mounting, and data analysis procedures will also be presented. A final section will briefly describe the preparation techniques of the high- T_c materials that were studied in this work.

Fourier Transform Infrared Spectroscopy

The far infrared is one of the less accessible spectral regions. The reason for this is the reduced available power from radiant sources at those low frequencies. For any given source, the total blackbody power spectrum is given by

$$P_0 = \sigma T^4 A, \tag{17}$$

where A and T are the area and temperature of the source respectively, and σ is the Stefan-Boltzmann constant. For a typical mercury arc lamp the radiated power

available from zero up to a frequency ω can be estimated by using the Rayleigh-Jeans law¹³⁷

$$p(\omega) = \frac{k_B T}{12\pi^2 c^2} A \omega^2, \quad (18)$$

where k_B and c are the Boltzmann's constant and speed of light respectively. Then, the ratio of the emitted to the total power up to frequency ω is given by

$$\eta = \frac{P(\omega)}{P_0} = \frac{5}{\pi^4} \left(\frac{\hbar \omega}{k_B T} \right)^3. \quad (19)$$

For $\omega = 100 \text{ cm}^{-1}$ and $T = 5000 \text{ K}$ the fraction is $\eta = 1.2 \times 10^{-6}$, *i.e.*, if the total power of the source is 1 W, only 1 μW will be emitted for frequencies below 100 cm^{-1} . This energy deficiency was overcome by the development of Fourier transform spectroscopy.¹³⁸ The principle of operation can be understood in terms of the Michelson interferometer shown in Fig. 14.

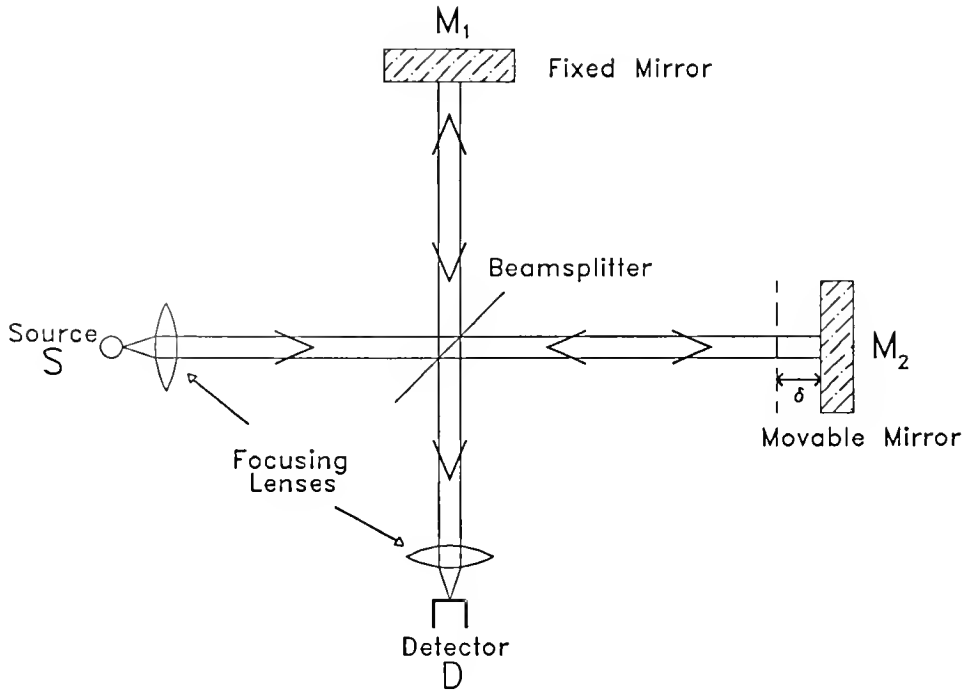


Fig. 14. Basic Michelson interferometer.

Light coming from a source falls onto a partially transmitting beamsplitter. In the ideal case, half of the radiation will be transmitted to the movable mirror M_2 . The other half is reflected onto the fixed mirror labeled M_1 . Both beams are reflected and they recombine again at the beamsplitter. When M_1 and M_2 are equidistant with respect to the beam-splitter position, the sum of the two beams will have maximum intensity. As M_2 moves away from this maximum position, the two beams will be out of phase by an amount $\theta = 2\pi\nu\delta$, where ν is the frequency of the incident light in units of cm^{-1} and δ is the distance as measured away from the position of maximum intensity or zero path difference. If the two beams have equal amplitudes $a(\nu)$, the sum of the amplitudes reaching the detector can be written as

$$A(\nu) = a(\nu)(1 + e^{i2\pi\nu\delta}). \quad (20)$$

The intensity of the radiation reaching the detector as a function of path difference can then be written as

$$I(\delta, \nu) = AA^* = 2a^2(1 + \cos 2\pi\nu\delta) = \frac{1}{2}S(\nu)(1 + \cos 2\pi\nu\delta), \quad (21)$$

where $S(\nu)$ is the spectral density of the source. For a source having frequencies from $\nu = 0$ to $\nu = \infty$, the total integrated intensity, or the interferogram $I(\delta)$, can be obtained by integration of Eq. 21. The result is

$$I(\delta) = \int_0^{+\infty} S(\nu)d\nu + \int_0^{+\infty} S(\nu) \cos 2\pi\nu\delta d\nu, \quad (22)$$

The first term in Eq. 22 is a constant equal to the total output intensity of the source S_0 . The spectrum itself can be found by computing the inverse Fourier transform of the interferogram,

$$S(\nu) = \int_{-\infty}^{+\infty} I(\delta)e^{2\pi\nu\delta}d\delta. \quad (23)$$

So if the moving mirror is scanned continuously over an infinite range of path differences and $I(\delta)$ is recorded at each δ , the spectrum can be obtained by performing

the integral in Eq. 23. The importance of this is that all the information about the spectrum is being observed continuously. This advantage was first recognized by Fellgett.¹³⁹

In practice, $I(\delta)$ is recorded over a finite range of path differences and with limited resolution. The discreet nature of $I(\delta)$ changes the Fourier integral into a Fourier series. In addition, the maximum finite path difference δ_m introduces side-lobes near sharp features of $S(\nu)$. This problem can be minimized by the method of apodization.^{140,141} The sampling interval of $I(\delta)$ determines the maximum cutoff frequency (ν_{max}) of $S(\nu)$. This will introduce aliasing for frequencies higher than (ν_{max}). This problem is solved by introducing proper optical filters that will attenuate those higher unwanted frequencies.

Optical Spectrometers

Bruker Fourier Transform Spectrometer

The instrument used to cover the far and midinfrared ($30-4000\text{ cm}^{-1}$) is a Bruker 113v fast-scan Fourier transform spectrometer. The principle of operation is very similar to the Michelson interferometer. A schematic diagram of the spectrometer is shown in Fig. 15. The instrument comes equipped with two sources; a Hg and globar lamps for the far infrared and midinfrared respectively. There are also detectors for each of those spectral regions. In the interferometer area, the emitted light from the source is focused to a beamsplitter that sends the transmitted beam to one mirror and the reflected light to other mirror facing the first one. Both beams are sent to a two-sided movable mirror which reflects both beams back to be recombined at the beam-splitter site. The two interfering beams are then directed to the sample compartment which contains two chambers; one for transmittance and the other for reflectance measurements. There is a reflectance stage, which is placed in

the reflectance chamber, that allows reflectivity measurements with near-normal incidence. The final destination of the light is the detector chamber. The whole area of the spectrometer is evacuated to avoid absorptions by water and CO_2 present in the air. Because the two-side mirror moves with constant speed v , the path difference δ between the transmitted and reflected beams at the beamsplitter, is changed according to the relation $\delta = 4vt$, where t is the time as measured from the moment $\delta = 0$. Hence, this moving mirror produces a modulation of the infrared signal, in the form

$$D(t) = D_0 \cos(2\pi f_a t), \quad (24)$$

where $D(t)$ is the signal as received by the detector and the infrared frequency ν_0 is turned into an audio frequency in the formula $f_a = 4\nu\nu_0$. The next stage is amplification and digitizing of this signal before is sent to an Aspect computer for apodization, phase correction, and finally application of the Fourier transform to the obtained interferogram to finally get the spectrum. Table 1 shows the parameters used in the Bruker spectrometer.

Bolometer Detector

As was mentioned before, the intensity of the source blackbody spectrum becomes rather weak in the far infrared. This can be partially overcome by using detectors that are sensitive enough to give an acceptable signal to noise ratio. The limitation that most infrared detectors have is that the sensitivity is limited by the background noise. For example, if the detector is operated at room temperature, the peak of the blackbody spectrum of this background is centered at around 1000 cm^{-1} , right in the middle of the infrared. This can be overcome by operating the detector at temperatures much lower than room temperature, *i.e.*, at liquid helium temperature or even lower. A diagram of the helium cooled detector that was used in this study

Table 1. Bruker FTIR Operating Parameters

Range	Beam Split.	Opt. Filt.	Source	Pol.	Detect.
cm ⁻¹	Material	Material		Material	
35 - 90	Mylar	Black PE	Hg arc	1	bolometer
80 - 400	Mylar	Black PE	Hg arc	1	bolometer
100 - 600	Mylar	Black PE	Hg arc	1	bolometer
450 - 4000	Germanium on KBr	none	Globar	2	DTGS, photocell

PE = polyethylene. Polarizer 1 = wire grid on oriented polyethylene; polarizer 2 = wire grid on AgBr.

is shown in Fig. 16. The detector element is made out of Si. It detects the signal by bolometric means, *i.e.*, by changing its temperature as the infrared light strikes it. This change in temperature is amplified and recorded as a voltage signal, which is then digitized and sent to the Aspect computer.

The Perkin-Elmer Monochromator

At higher frequencies, the Fellgett advantage loses its importance due to the availability of brighter sources and more sensitive detectors. For these reasons, a grating spectrometer is an excellent choice to cover frequencies in the near infrared and up to the UV (1000–40,000 cm⁻¹). The instrument used is a modified Perkin-Elmer 16U monochromator. The diagram showing the details of the instrument is in Fig. 17. Depending on the frequency of interest, there are three sources to choose from: a globar for the midinfrared, a tungsten lamp for the near infrared, and a deuterium source for the UV. After the light goes through filters and an exit slit, it goes through a grating where the different wavelengths are diffracted according to the

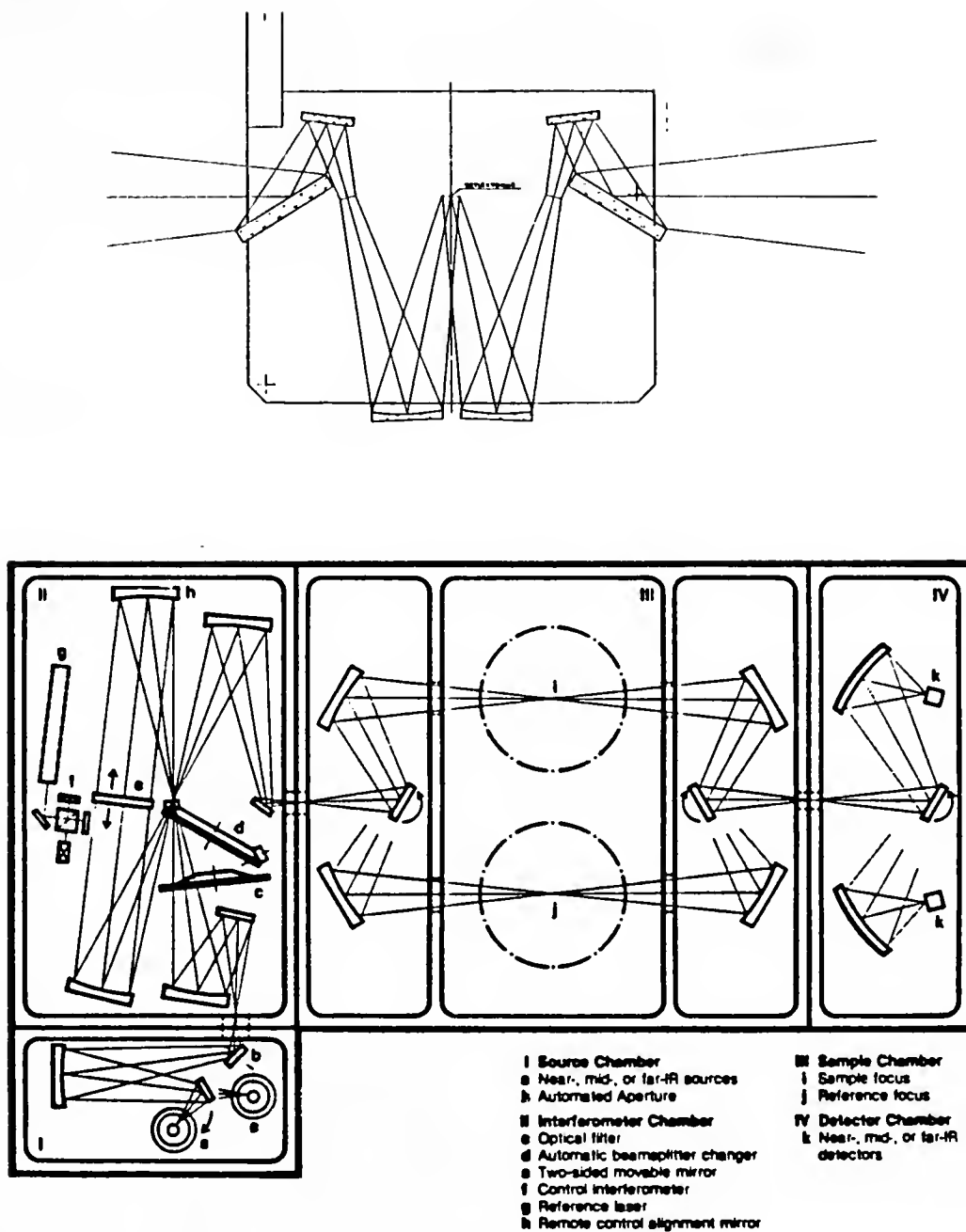


Fig. 15. Top: Reflectance stage that was used to perform near-normal incidence reflectance. Bottom: Schematic of the Bruker FTIR interferometer.

DEWAR, MODEL HD-3

OUTLINE SKETCH

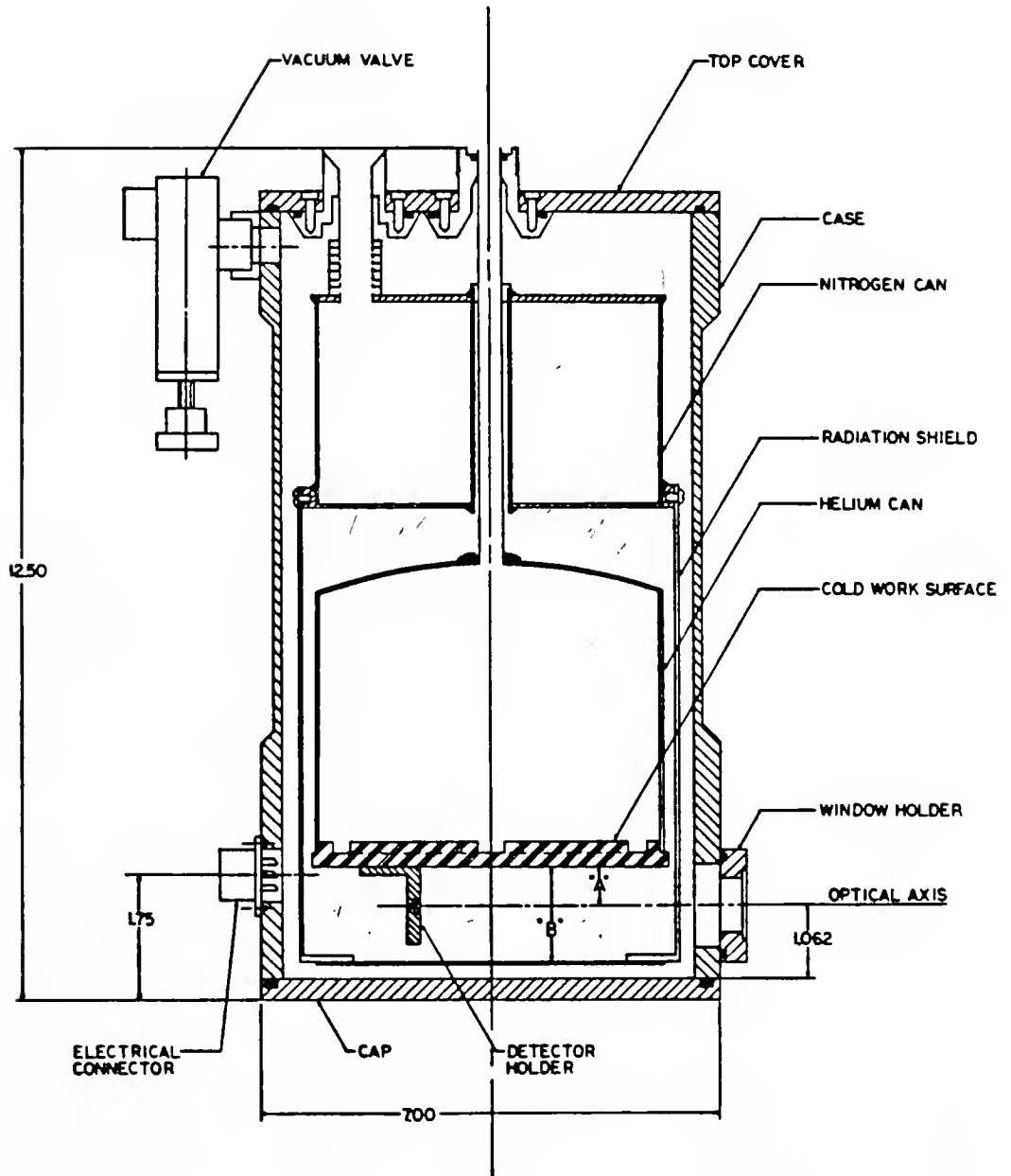


Fig. 16. Diagram of the liquid helium cooled detector.

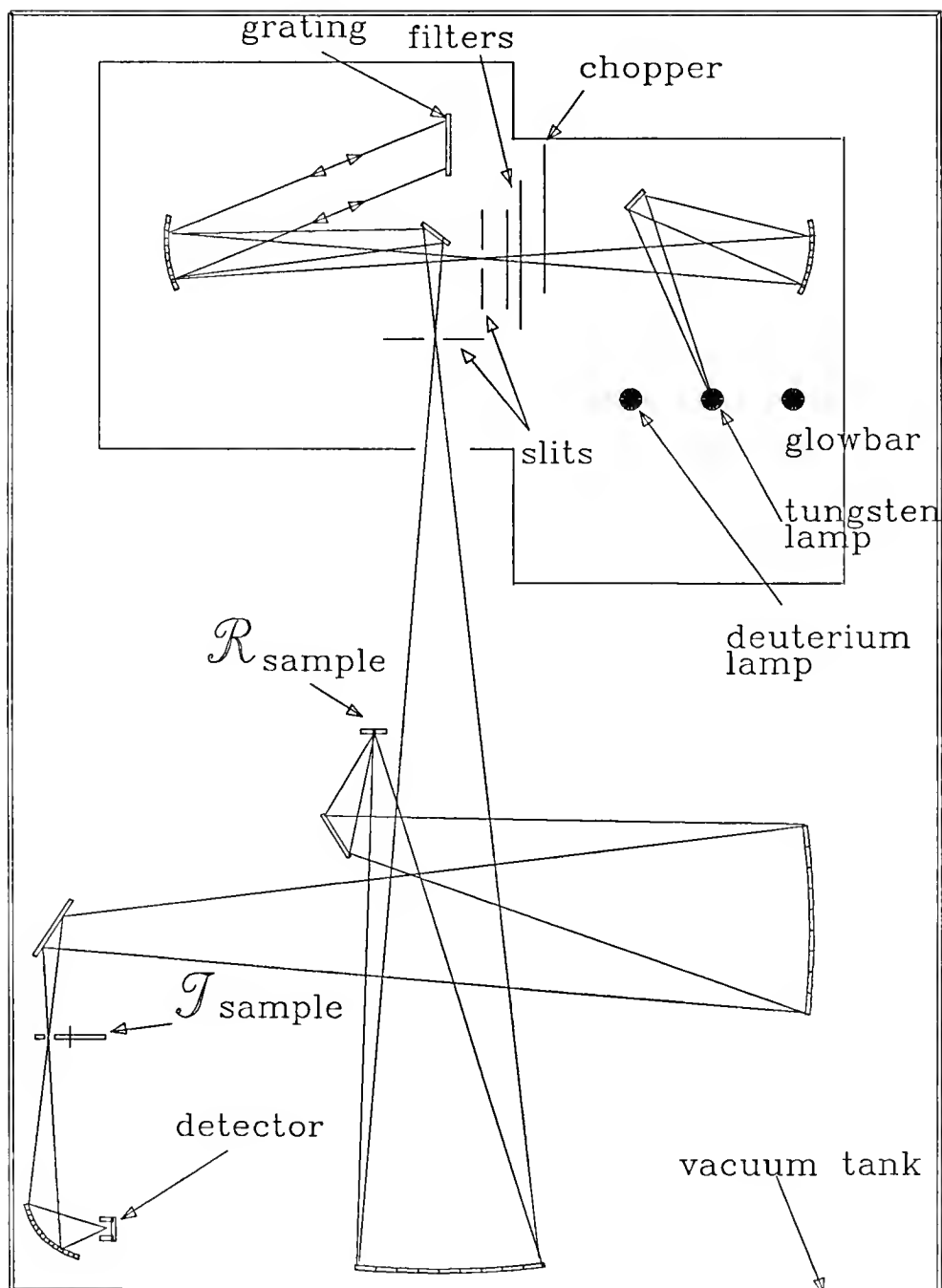


Fig. 17. Diagram of the Perkin-Elmer grating monochromator.

formula $2d \sin \theta = n\lambda$, where n is the n^{th} order of the diffracted light, λ is the wave length, θ is the angle of incidence, and d is the spacing between the grating lines. The angle of incidence is changed by rotating the grating with a step-motor controller. This allows access to different wavelengths sequentially. The now “filtered” light exits the monochromator and it is focused onto the position labeled R in Fig. 17. The sample and reference are placed there for reflectance measurements. In the case of transmittance, the sample and reference (in this case an empty, or “blank,” sample holder) are positioned at the point T . The reflected or transmitted light reaches a detector that is connected to a lock-in amplifier for amplification of the signal. The output of the lock-in is fed to a digital voltmeter that is remotely controlled by a PC computer that also controls the step-motor controllers of the grating and filters. The collection of the data is done through the computer by recording a single beam spectrum (signal *vs.* frequency) for the reference and the sample sequentially and taking the ratio of these two spectra (S_s/S_r) to obtain the true reflectance or transmission of the sample. During normal operation, the spectrometer chamber is evacuated down to 150 mTorr or so to prevent any absorption due to water or CO_2 present in the air. For more details about the operation of this machine the interested reader is referred to Reference 142. Table 2 lists the parameters used to cover each frequency range.

Polarizers

The need to resolve the dielectric tensor along the principal axes of the single crystals used in this work required us to polarize the electric field of the light. Since the radiation generated at the source is randomly polarized, the polarization of the light was accomplished by inserting a polarizer in the path of the beam. The characteristics of the polarizers vary depending on the frequency range of interest. In the infrared, the polarizers used are made of a gold wire grid, vapor deposited on a substrate. For

Table 2. Perkin-Elmer Grating Monochromator Parameters

Frequency (cm^{-1})	Grating ^a (line/mm)	Slit width (micron)	Source ^b	Detector ^c
801–965	101	2000	GB	TC
905–1458	101	1200	GB	TC
1403–1752	101	1200	GB	TC
1644–2612	240	1200	GB	TC
2467–4191	240	1200	GB	TC
4015–5105	590	1200	GB	TC
4793–7977	590	1200	W	TC
3829–5105	590	225	W	PbS
4793–7822	590	75	W	PbS
7511–10234	590	75	W	PbS
9191–13545	1200	225	W	PbS
12904–20144	1200	225	W	PbS
17033–24924	2400	225	W	576
22066–28059	2400	700	D ₂	576
25706–37964	2400	700	D ₂	576
36386–45333	2400	700	D ₂	576

^a Note the grating line number per cm should be the same order of the corresponding measured frequency range in cm^{-1} .

^b GB: Globar; W: Tungsten lamp; D₂: Deuterium lamp.

^c TC: Thermocouple; PbS: Lead sulfite; 576: Silicon photo-cell.

the midinfrared spectral range ($300\text{--}4000\text{ cm}^{-1}$) a silver bromide substrate is used, while in the far infrared ($30\text{--}600\text{ cm}^{-1}$), the substrate is polyethylene. Dichroic and plastic polarizers were used in the near infrared, visible and UV. In both the Bruker and Perkin-Elmer spectrometers, the desired polarization of the light was easily accomplished by mounting the polarizer in the path of the beam using a gear mechanism that also allowed rotation from the outside without breaking the vacuum in the spectrometers. This in-situ adjustment of the polarizers greatly reduces the uncertainty in the relative anisotropy of the reflectance (better than $\pm 0.25\%$). This is specially important when the relative anisotropy in the optical response of the crystal is not very large.

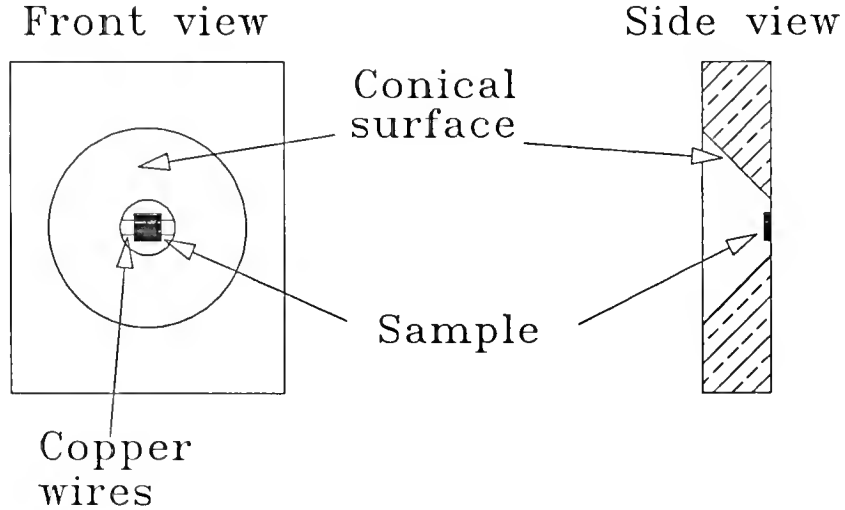


Fig. 18. Diagram of frame used to mount samples.

Sample Mounting and Low Temperature Measurements

Due to the small size of the samples used in this study, special care had to be taken to mount them for reflectance measurement. In the case of the single-domain $\text{YBa}_2\text{Cu}_3\text{O}_{7-\delta}$ sample, the size was around $1 \times 1\text{ mm}^2$ in the ab plane. In order to take

advantage of the whole area, the mounting of the sample was done in the following way. A copper frame was machined with a small hole at the center ($\simeq 2$ mm diameter). One side of the frame (the front side) had a conical surface as illustrated in Fig. 18. This conical surface was necessary to scatter away any light that may hit the copper frame when inserted in the beam path inside the spectrometer. The next step was to solder two very fine copper wires across the center of the hole on the back side of the frame. Then, the sample was carefully mounted on the two wires and glued there by a good thermal conductor (apiezon grease). A piece of Al-coated Si with approximately the same area as the sample was mounted on another frame in the same way as the sample in order to be used as a reference.

Mounting of the $\text{Bi}_2\text{Sr}_2\text{CaCu}_2\text{O}_8$ and $\text{La}_2\text{CuO}_{4+\delta}$ samples did not require the use of wires due to the larger size of these samples. Instead, each sample was mounted on the back side of a frame, as shown in Fig. 18, with a hole of slightly smaller diameter than the size of the sample. A frame with same hole-size as the frame of the sample was used to mount a Al-coated piece of glass to be used as a reference. Finally, frames containing the sample and the Al-coated reference were mounted facing out in opposite sides of a sample holder assembly that was later positioned inside the spectrometer for reflectance measurements. To facilitate the study of the polarization dependence in the reflectance, samples were mounted so that the principal axes of the measured face could be studied by setting the polarizer horizontal or vertical with respect to the spectrometer bench.

Low temperature measurements were possible by attaching the sample holder assembly to the tip of a Hansen and Associates High-Tran cryostat. A flexible transfer line was used to flow liquid helium from a storage tank to the cryostat. The temperature of the sample was stabilized by using a temperature controller (Hansen & Associates S000) connected to a previously calibrated SI diode sensor and a heating

element attached to the tip of the cryostat. In this set-up, the temperature of the sample could be lowered by increasing the flow of helium and increased by applying a current to the heater element. During measurements, the sample holder and cryostat units were placed inside a shroud equipped with optical windows in the spectrometer chamber. The pressure inside of this shroud was kept below 10^{-7} Torr to prevent the formation of ice on the cryostat or the surface of the sample. Since sample and mirror were on opposite sides of the sample holder, measurements of the sample and mirror spectra were possible by simply rotating the cryostat assembly by 180° . The final step was to take the ratio of these two spectra to obtain the reflectance of the sample.

Normalization Procedure of the Reflectance

After measuring the temperature dependence in the reflectance of the sample, the final normalizing of the reflectance was obtained by taking a final room temperature spectrum, coating the sample with a film 2000 Å thick of Al, and remeasuring this coated surface. A properly normalized room-temperature reflectance was then obtained after the reflectance of the uncoated sample was divided by the reflectance of the coated surface and the ratio multiplied by the known reflectance of Al. This result was then used to correct the reflectance data measured at other temperatures by comparing the two room-temperature spectra taken in the two separate runs. This procedure corrected for any misalignment between the sample and the mirror used as a temporary reference before the sample was coated and more importantly, it provided a reference surface of the same size as the actual sample area. In cases where the sample surface had some roughness, the procedure also corrected for losses due to a nonspecular sample reflectance.

Data Analysis of the Spectra: The Kramers-Kronig Transformations

The power reflectance measured in the experiment is related to the amplitude reflectivity which contains information about the optical absorption in the sample. For normal incidence, the amplitude reflectivity is given by

$$r(\omega) = \frac{(n - 1) + i\kappa}{(n + 1) + i\kappa}, \quad (25)$$

where n and κ are the real and imaginary parts in the complex refractive index of the sample under consideration. Information about these quantities can be obtained by noting that the power reflectance $R(\omega)$ is related to the amplitude reflectance $r(\omega)$ in the following way:

$$r(\omega) = \rho(\omega) \exp i\Theta(\omega), \quad (26)$$

where $\Theta(\omega)$ is the phase shift in the light upon being reflected from the sample and $\rho(\omega)$ is related to the power reflectance $R(\omega)$ by

$$R(\omega) = \rho^2(\omega). \quad (27)$$

Since the amplitude reflectance and the phase shift are the real and imaginary parts of a response function respectively, they can be related by means of the Kramers-Kronig transformations.^{143,144} Hence, the phase shift can be obtained from the Kramers-Kronig integral

$$\Theta(\omega) = \frac{\omega}{\pi} \int_0^\infty \frac{\ln R(\omega') - \ln R(\omega)}{\omega^2 - \omega'^2} d\omega'. \quad (28)$$

In principle, knowledge of the phase shift is only possible if the power reflectance is known over an infinite range of frequencies. In reality $R(\omega)$ is only measured over a finite frequency range, so there are certain approximations that must be taken before evaluating the integral in Eq. 28. In first place, it should be noticed that for $\omega' \ll \omega$,

$\omega' \gg \omega$, and for the regions where $R(\omega)$ is flat, there are negligible contributions to the integral in Eq. 28. This implies that for the frequencies where $R(\omega)$ is not available, it is possible to make extrapolations that would not affect very much the results for the range for which $R(\omega)$ is known. The kind of extrapolations that can be made depend on the type of material under consideration, as it will be discussed in the next section.

High-Frequency and Low-Frequency Extrapolations

For metals and insulators the high frequency reflectance is usually dominated by interband transitions of the inner core electrons to excited states. Only at very high frequencies (above $100,000 \text{ cm}^{-1}$) the free-electron behavior becomes important. In the absence of any published data that can be append to the existing data, the reflectance in the interband region is usually modeled using to the formula

$$R(\omega) = R_f \left(\frac{\omega_f}{\omega} \right)^s, \quad (29)$$

where R_f and ω_f are the reflectance and frequency of the last data point measured in the experiment. The exponent s is a number that can take up values between 0 and 4. At very high frequencies ($\omega_{f'}$), where the free-electron behavior sets in, the approximation used is

$$R(\omega) = R_{f'} \left(\frac{\omega_{f'}}{\omega} \right)^4. \quad (30)$$

It is still expected some dependence on the results for frequencies close to the last frequency measured on account of the choice of s and $\omega_{f'}$. (for metals this happen for frequencies above the plasma edge minimum.) At low frequencies, the scheme for extrapolation depends on the properties of the material under study. In the situations were the solid exhibits insulating-like behavior, the reflectance is assumed constant to dc. In the case of metals, the formula generally used is the so-called Hagen-Rubens

relation, $R(\omega) = 1 - A\sqrt{\omega}$, where A is a constant determined by the reflectance of the lowest frequency measured in the experiment. For high- T_c samples, it is found this procedure results inadequate and it can only be used as a first approximation. A more appropriate procedure is to fit the reflectance using a Lorentz-Drude model where the free-carrier response is assumed to have the typical Drude form. Other higher frequency excitations are modeled by Lorentz oscillators. The fitted reflectance is used as an extension below the lowest frequency that was measured in the experiment before the Kramers-Kronig analysis is finally performed on the data.

In the superconducting state, it is expected that the reflectance will approach unity for frequencies close to zero. An empirical formula that has been found to represent the way R approaches unity is $R = 1 - B\omega^4$, where B is a constant determined from the lowest frequency measured. It should be pointed out that typical uncertainties in $R(\omega)$ are in the order $\Delta R = \pm 0.5\%$. Hence, the propagated error in, for example, the optical conductivity $\sigma_1(\omega)$ obtained from the Kramers-Kronig analysis of the reflectance is roughly

$$\frac{\Delta\sigma_1}{\sigma_1} = \frac{1}{1-R} \frac{\Delta R}{R} \quad (31)$$

It is clear the RHS of Eq. 31 diverges, or the signal to noise ratio is very small as R approaches unity. Implications of this in the high- T_c materials will be discussed later.

Optical Constants

Once the proper extrapolations are made and the phase shift is obtained, the optical constants of the material are easily obtained by means of the formulae that follow. The frequency dependent refractive index n and extinction coefficient $\kappa(\omega)$ are given by

$$n(\omega) = \frac{1 - R(\omega)}{1 + R(\omega) - 2\sqrt{R(\omega)} \cos \Theta(\omega)}, \quad (32)$$

and

$$\kappa(\omega) = \frac{2\sqrt{R(\omega)} \sin \Theta(\omega)}{1 + R(\omega) - 2\sqrt{R(\omega)} \cos \Theta(\omega)} \quad (33)$$

respectively. These relationships can be re-written in terms of the dielectric function $\epsilon(\omega)$ as

$$\epsilon = N^2 = (n + i\kappa)^2. \quad (34)$$

where the real ($\epsilon_1(\omega)$) and imaginary ($\epsilon_2(\omega)$) parts are obtained from

$$\epsilon_1(\omega) = n^2 - \kappa^2 \quad (35)$$

and

$$\epsilon_2(\omega) = 2n\kappa. \quad (36)$$

Other important relations are the real and imaginary parts of the optical conductivity $\sigma(\omega)$, the skin depth $\delta(\omega)$, and the absorption coefficient $\alpha(\omega)$:

$$\begin{cases} \sigma_1 = \omega\epsilon_2/4\pi, \\ \sigma_2 = \omega(1 - \epsilon_1)/4\pi, \\ \delta = c/\omega\kappa, \\ \alpha = 2\omega\kappa/c. \end{cases} \quad (37)$$

All these equations reflect the fact that the absorptive (real) and inductive (imaginary) parts of a process are all related to each other due to the causality requirement in the Kramers-Kronig relations.

Sample Preparation Techniques

This section will provide a brief discussion of the sample-preparation techniques that were employed in making the samples used in this study.

YBa₂Cu₃O_{7- δ} Single-Domain Crystal

Untwinned crystals of YBa₂Cu₃O_{7- δ} that were used in this study were prepared at the University of Illinois in Urbana-Campaign by J.P. Rice and D.M. Ginsberg. The samples were grown using a standard Cu–O flux growth procedure.¹⁴⁵ One disadvantage of this method is that micro twinning develops in the crystals together with the transition from the tetragonal phase at high temperatures to the orthorhombic phase at room temperatures. This twinning happens because of randomly oriented mechanical stress present during the slow-cooling segment from temperatures around 850 °C.¹⁴⁶ In order to avoid development of twinning the slow-cooling process was interrupted by pulling the sample out of the furnace. Evidence for the quenching in the tetragonal phase was obtained by looking isotropic extinctions on the *ab* plane of the samples under a microscope with crossed polarizers in reflectance mode.¹⁴⁷ The tetragonal crystals were then oxygenated during a post-growth procedure that converted them to the orthorhombic phase having sharp superconducting transitions near 90 K.⁴⁰ Since the crystals were not subjected to any mechanical stress in the process of converting them from tetragonal to orthorhombic, there was a reduced possibility of creating dislocations or defects that otherwise may affect the intrinsic properties in the material. Typical crystals with single-domain regions of 1 × 1 mm² were obtained every third or fourth successful attempt. The dimension along the *c* axis was approximately 25 μ m. Determination of the *a* and *b* axes in all the crystals was done by the sample grower before the samples were sent to this author. The superconducting transition temperature, as determined by cooling the sample in a field of 10 G, was around 90 K. Fig. 19 shows the Meissner fraction measured for a crystal grown with this technique for the applied field parallel to the *a* and *b* axes. Clearly, the anisotropy of the Meissner fraction in the *ab* plane is much larger than the scatter in the data.¹⁷ The data show that the field-cooled diamagnetic response

(Meissner effect) is larger when the field is applied along b axis than when it is applied along the a axis. This indicates that flux pinning is larger when the field is along the chain direction.

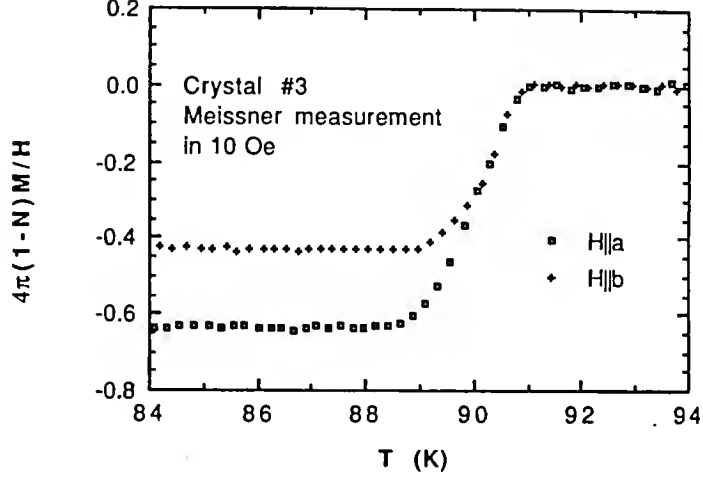


Fig. 19. Meissner effect measurements on single-domain crystals of $\text{YBa}_2\text{Cu}_3\text{O}_{7-\delta}$ (After Ref. 17).

A qualitative analysis of the data suggests that the critical current density (J_c) is larger perpendicular to the chain direction than parallel to it ($J_{ca} > J_{cb}$). Studies of the ab -plane anisotropy in the dc resistivity,¹⁶ performed on crystals from the same batch have given some interesting results regarding the effect of the chains in the dc transport properties. These results, which are shown in Fig. 20, indicate the ab -plane anisotropy ratio in the dc resistivity is around 2.2 with the lower resistivity being parallel to the b axis. This may suggest, to a first approximation, that the CuO chains provide an additional electronic channel for conductivity along this direction, assuming that the chain conductivity can be additive to conductivity of the CuO_2 planes. Raman scattering data¹⁵¹ have also given indication of a stronger electronic background for polarization of the light parallel to the chain direction in this material.

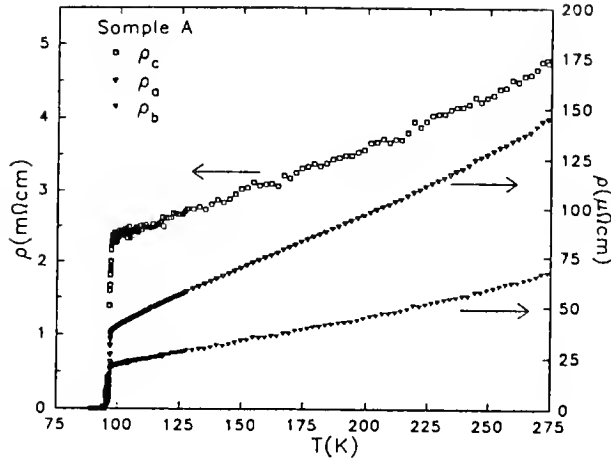


Fig. 20. Resistivity anisotropy in single-domain crystals of $\text{YBa}_2\text{Cu}_3\text{O}_{7-\delta}$ (After Ref. 16).

In addition, there is indication of anisotropy in the Raman-active phonon lines for the two polarizations in the ab plane.

$\text{Bi}_2\text{Sr}_2\text{CaCu}_2\text{O}_8$ Single-Domain Crystals

The $\text{Bi}_2\text{Sr}_2\text{CaCu}_2\text{O}_8$ crystals used in the study were grown by R. Kelley and M. Onellion at the University of Wisconsin in Madison, Wisconsin. The technique used is a flux method with slow cooling in a temperature gradient.¹⁵² In a typical experiment, the starting materials, Bi_2O_3 , SrCO_3 , CaCO_3 , and CuO are ground and placed in an alumina crucible. The mixture is then heated to a temperature of $50\text{--}70^\circ\text{C}$ above the liquidus temperature and equilibrated for 6 hrs. The temperature is subsequently lowered to $875\text{--}880^\circ\text{C}$, and after reaching equilibrium for 6 hrs, the temperature is slowly cooled at $0.5\text{--}2^\circ\text{C/h}$ to 820°C where the experiment is terminated. Samples are subsequently annealed in dry oxygen at 600°C for 8 h and later reannealed in Argon at 750°C for a period of 12 hrs.

Typical crystals are thin platelet with dimensions of a few millimeters in the ab plane. Identification of the a and b axes was done by the sample grower using

low electron energy diffraction (LEED) techniques. The incommensurate superlattice modulation pattern was seen along the b axis and not in the perpendicular direction (a axis), suggesting the samples were single-domain crystals. The alignment of the principal axes in the crystal was confirmed by observing the extinction points when the sample was rotated under a microscope (Olympus, model BHM) with crossed polarizers. Meissner effect measurements were performed on one of the samples to determine the superconducting state transition temperature. The results, which are shown in Fig. 21, reveal the onset of superconductivity is around 86 K. Moreover, the onset to the superconducting state, as determined by using four-probe resistance measurements, is around 91 K, with a transition width of 5–6 K. Results of the resistivity tensor along the a , b , and c axes on these crystals are reported in Chapter IX.

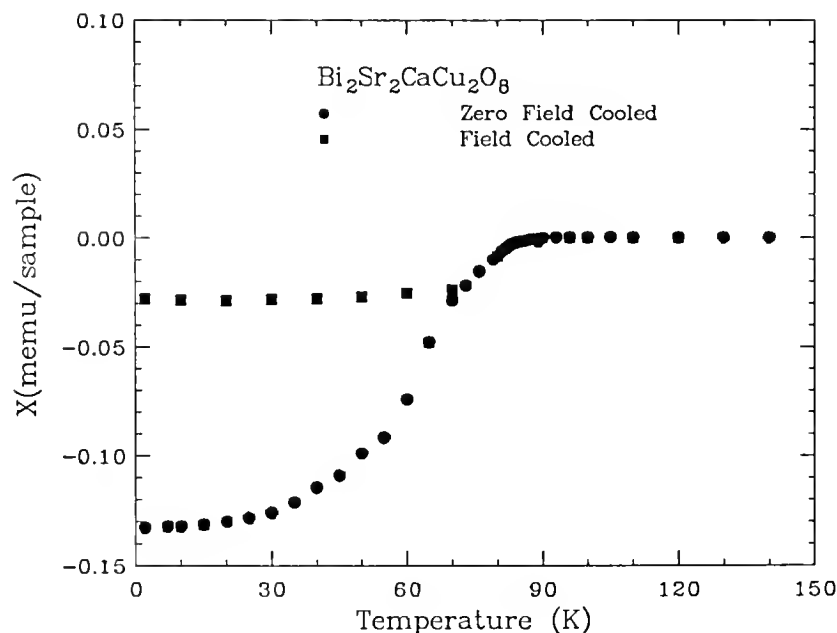


Fig. 21. Meissner effect measurements on a $\text{Bi}_2\text{Sr}_2\text{CaCu}_2\text{O}_8$ single crystal. The orientation of the magnetic field is $H \perp c$ axis.

La₂CuO_{4+δ} Single Crystal

This dissertation contains an optical study performed on an oxygen-doped La₂CuO_{4+δ} single crystal prepared at the University of Iowa by F.C. Chou and D.C. Johnston. A stoichiometric single crystal of La₂CuO₄ was prepared using a self-flux method.¹⁵⁰ The as-grown crystal was insulating. The oxidation procedure was carried out using an electrochemical cell¹⁵¹ with the La₂CuO₄ sample as one of the working electrodes. A platinum wire working as the negative electrode was attached to one side of the crystal using silver paint and the contact was fully covered with silicone rubber. The set-up of the electrochemical cell was La₂CuO₄/ 1N NaOH / Pt. Charging up of the cell was done by applying an anodic current of 10 μ A to the La₂CuO₄ crystal for a period of two months. In order to optimize the oxidation current, a constant electrical potential of 0.6 V (versus a Ag—AgCl reference electrode) was maintained during the charging process using a potentiostat. The exact oxygen content of this particular sample after the oxidation was completed is not known. Calculations based on the gained weight could not be used because small pieces of the crystal were lost during handling. Meissner effect data, which are shown in Fig. 22, indicate the onset of superconductivity is at around 40 K. A comparison of this with the onset of other samples of known oxygen concentration suggests the excess oxygen should be around $\delta \sim 0.12$. The sample that was provided to us contained two optically-smooth faces. One face contained the *ab* plane and the *c* axis, so with the help of a polarizer, it was possible to study the anisotropy between these two directions. The other face that was studied only contained the twinned *ab*-plane direction.

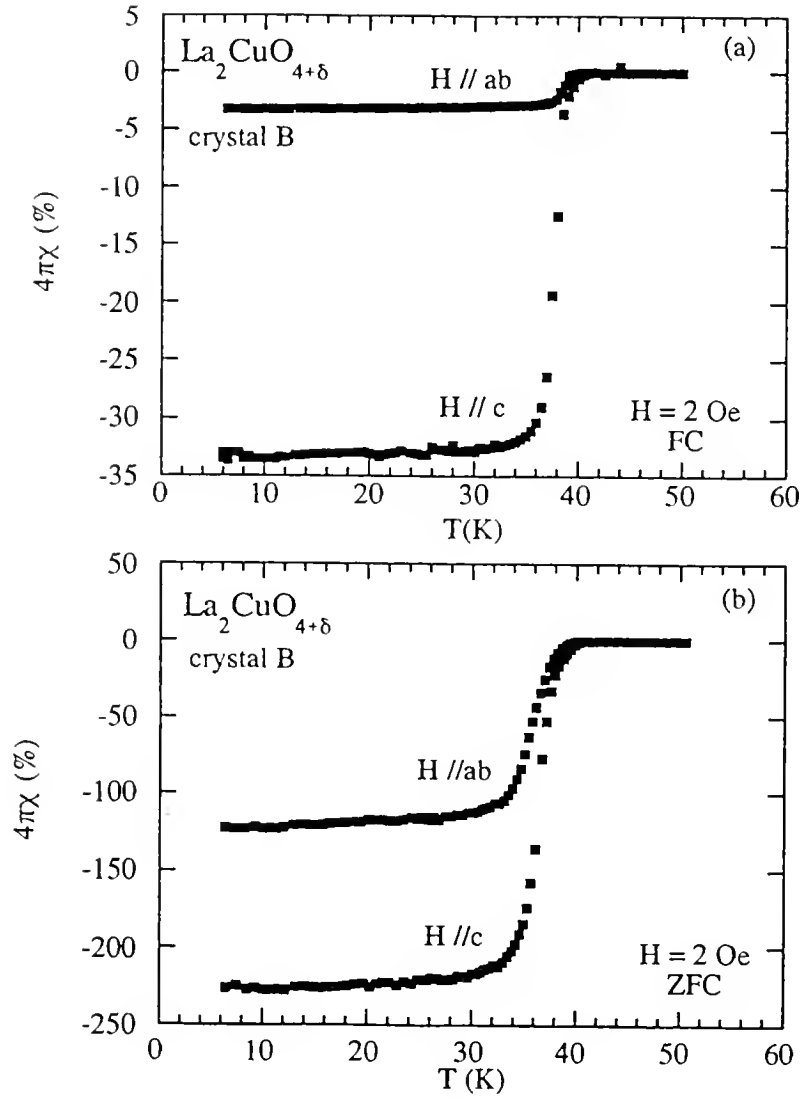


Fig. 22. Meissner effect measurements on $\text{La}_2\text{CuO}_{4+\delta}$ single crystal (After Ref. 155).

CHAPTER V

OPTICAL STUDY OF $\text{La}_2\text{CuO}_{4+\delta}$ SINGLE CRYSTAL

In this chapter, the optical properties of the ab plane and the c axis of superconducting $\text{La}_2\text{CuO}_{4+\delta}$ are described. The material is transformed from its insulating state by electrochemical insertion of oxygen. The sample was prepared at Iowa State University by F.C. Chou and D. Johnston in collaboration with S-W. Cheong from AT&T Bell Laboratories. Although the exact oxygen content is not known in this sample, it is estimated to be $\delta \sim 0.11$ from comparison of the observed T_c of 40 K with other samples of known concentration.¹⁵²

Optical absorption studies of the stoichiometric parent compound La_2CuO_4 have revealed this is a charge transfer insulator having marked anisotropy in both phonons and electronic features for polarization of the light parallel and perpendicular to the CuO_2 planes in the system.^{52,53,69,153-155} Most of the optical investigations of superconducting materials derived from this parent compound have been on the Sr-doped $\text{La}_{2-x}\text{Sr}_x\text{CuO}_4$.^{28,58,69,72,156} A review of some of these studies was done in Chapter III. In this system, a maximum T_c in the order of 35 K is obtained by substituting 15% of the La atoms by Sr. In addition, superconductivity is also obtained when additional oxygen is intercalated in the crystal structure of La_2CuO_4 . Normally, oxygen intercalation is obtained by annealing the sample at high temperatures ($\sim 500^\circ\text{C}$) in an oxygen-rich environment.^{33,34} In spite of its success, there are two major drawbacks in producing superconducting samples using this technique. In first place, there is the requirement of extremely high oxygen partial pressures (~ 25 kbar) in order to produce single-phase superconducting samples. Secondly, the maximum amount of oxygen that can be intercalated is not too high ($\sim 8\%$). Difficulties in producing

uniformly oxidized samples could be one of the reasons why reports on the optical investigation of oxygen-doped samples of this material have been limited to lightly doped nonsuperconducting samples.^{64,69,154} Recent developments in electrochemical techniques have made possible the synthesis of uniformly oxidized samples with relatively high oxygen content ($\delta \sim 0.12$) and transition temperatures near 40 K.^{152,158} Details of this technique were given in Chapter IV (p. 67).

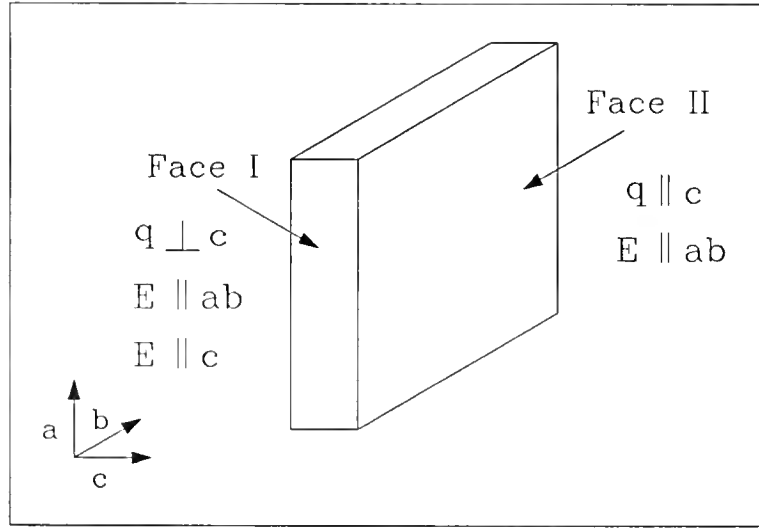


Fig. 23. Sketch of the sample with the two faces that were used to measure the reflectance on the $\text{La}_2\text{CuO}_{4+\delta}$ single crystal.

Results of reflectance studies of this oxygen-doped sample were obtained from two faces of the crystal. One of the faces (the face labeled I in Fig. 23) contains both the c -axis and either the a - or b -axis direction (on account of twinning, we were unable to distinguish). Face I allowed us, with the use of linearly polarized light, to probe the optical response of the c axis [001] as well as the ab -plane response. The frequency range covered was 50–32,000 cm^{-1} . The far-infrared and midinfrared spectral regions (50–3000 cm^{-1}) were measured at several temperatures above and

below the superconducting transition temperature. As in the undoped material, the spectrum along the c direction is mainly dominated by optical phonons and no evidence of metallic component is found in the optical conductivity. At the same time, the ab -plane response shows metallic reflectance in the far infrared and a plasma edge around $\omega \sim 7500 \text{ cm}^{-1}$.

The second face that was measured, the face II in Fig. 23, provided an average of the ab -plane response. Optical reflectance was measured in a frequency range that extended from the far-infrared and near-ultraviolet spectral regions ($80\text{--}38,000 \text{ cm}^{-1}$). Temperature dependence measurements, above and below T_c , were also carried out in the same range of frequencies. A Kramers-Kronig analysis of the ab -plane reflectance reveals the unusual non-Drude behavior in the midinfrared conductivity $\sigma_1(\omega)$ that is typical of the copper-oxide superconductors. For frequencies in the near infrared and above, a rather unusual temperature dependence was observed in the optical reflectance of the sample. In addition to the expected sharpening of the plasma edge at 7500 cm^{-1} , the reflectance became gradually lower as the temperature of the sample was lowered. This result may suggest a temperature dependence in some high-frequency interband transitions.

Moreover, the reflectance displays some structures in the far-infrared region that are not present when the ab -plane reflectance is measured on face I of the crystal. A comparison of the sum rule in both cases reveals that the differences in both spectra are not likely due to different oxygen compositions in both surfaces of the sample. Instead, the differences are most likely due to electron-phonon interactions that are enhanced when the wavevector of the incident light is parallel to the c axis in the sample.

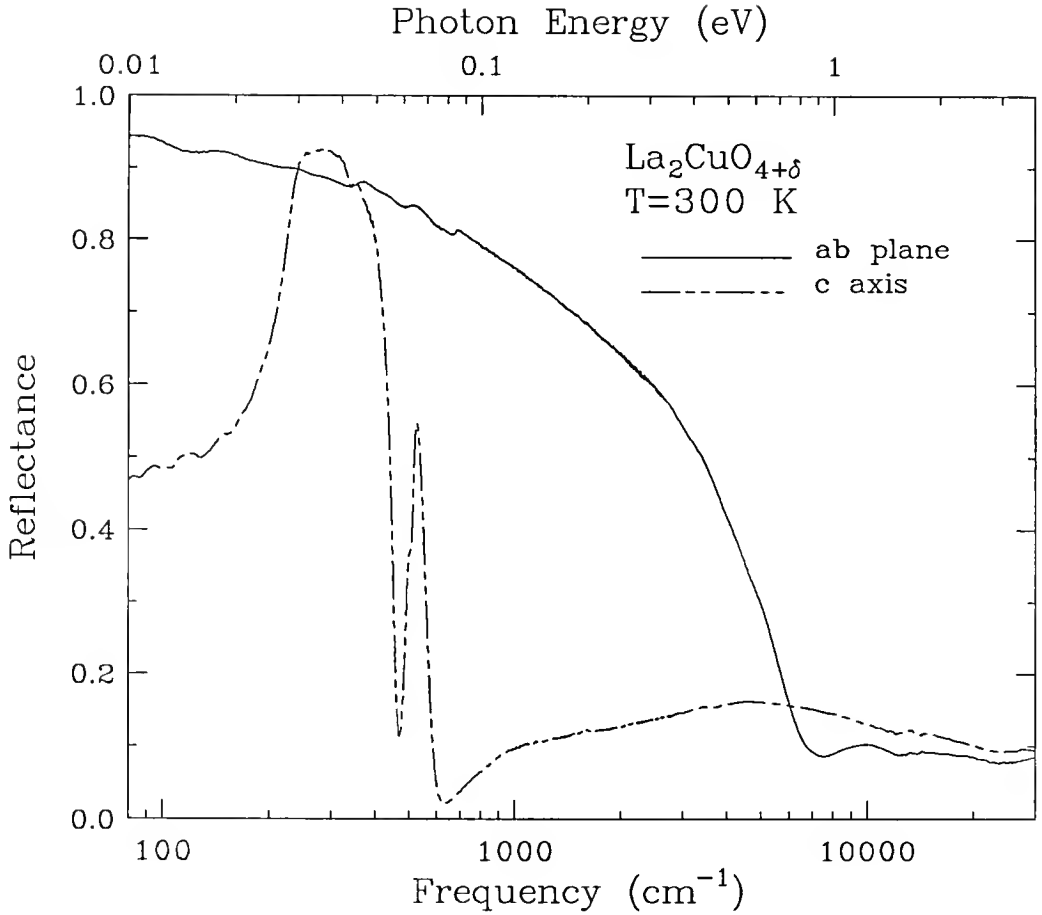


Fig. 24. Reflectance of $\text{La}_2\text{CuO}_{4+\delta}$ single crystal for light polarized along the ab plane and the c axis ($T = 300 \text{ K}$).

c -Axis Reflectance of $\text{La}_2\text{CuO}_{4+\delta}$

Room Temperature Spectra

Figure 24 shows the room temperature reflectance for light linearly polarized parallel and perpendicular to the c axis of the sample. The results show a dramatic anisotropy for the in-plane and out-of-plane optical properties, just as it has been reported in Sr-doped superconducting samples derived from the stoichiometric parent compound.^{28,69,156,158}

The c -axis reflectance has the character of an insulator at low frequencies. This reflectance is mainly dominated by four optical phonons in the far infrared. For higher

frequencies, the spectrum is almost featureless, showing only a broad electronic-like feature whose maximum is around $\omega \sim 5500 \text{ cm}^{-1}$. The spectrum is almost unchanged with respect to the c -axis spectrum of the undoped material. However, there is a weak structure that appears just below the peak of the phonon mode at 512 cm^{-1} . This structure, which is not present in the stoichiometric material,^{52,54} is resolved as a second phonon mode as the temperature of the sample is lowered. More discussion about this will be given later.

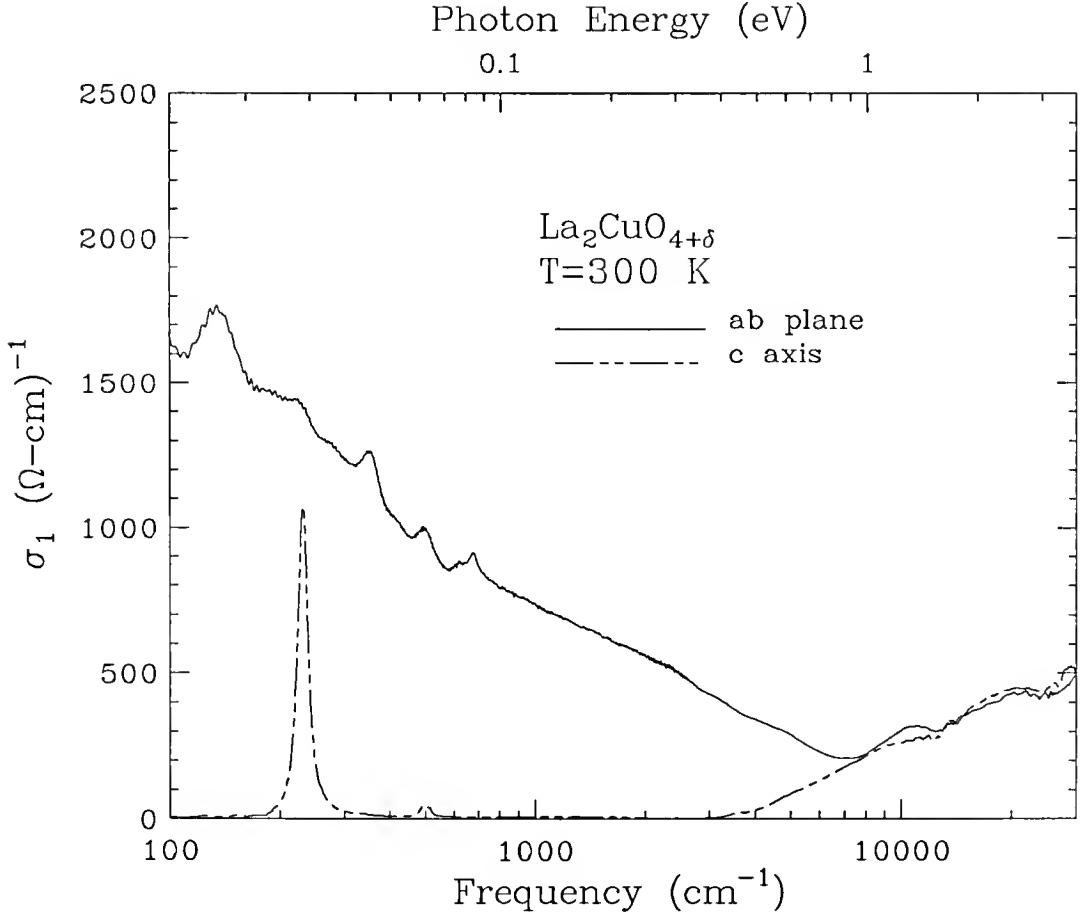


Fig. 25. Room temperature optical conductivity $\sigma_1(\omega)$ obtained from a Kramers-Kronig analysis of the reflectance shown in Fig. 24.

The reflectance spectrum perpendicular to the c axis (in-plane electric field) exhibits a metallic-like behavior at low frequencies. Weak phonon features, that are not

completely screened out by the free carriers in the CuO_2 planes are also visible in the far infrared. The real part of the conductivity $\sigma_1(\omega)$, obtained from a Kramers-Kronig analysis of the reflectance, is shown in Fig. 25. Here, the phonon modes and the electronic-like features are more easily seen. The results presented here indicate that oxygen doping in the lanthanum cuprate only affects the electronic excitations related to the copper-oxide planes in the system. Similar conclusions regarding the two dimensionality of the electronic properties in the copper-oxide superconductors have also been drawn from measurements on $\text{YBa}_2\text{Cu}_3\text{O}_{7-\delta}$ and $\text{Bi}_2\text{Sr}_2\text{CaCu}_2\text{O}_8$ materials.^{25,27,29,57}

Low Temperature c -Axis Reflectance

Figure 26 displays the reflectance in the infrared region along the c -axis direction as a function of temperature. As the sample is cooled down, the phonon lines become sharper, as expected. The structure that appears in the room temperature spectrum just below 512 cm^{-1} is more clearly resolved as a phonon mode at 492 cm^{-1} . This is not present in the c -axis spectrum of either undoped or Sr-doped samples.^{52,54}

At the low-frequency end, we notice all spectra above T_c approach a constant value for the reflectance. This is indicative of semiconducting behavior. On the other hand, the inset in Fig. 26 shows the data at the lowest temperature show a downward trend towards low frequencies that is not present in the data above T_c . This trend is most likely correlated with the appearance of a plasmon minimum in the superconducting-state reflectance as was first observed in the c -axis spectrum of $\text{La}_{2-x}\text{Sr}_x\text{CuO}_4$ by Tamasaku *et al.*⁵⁸ In this study, it was found the minimum forms part of a reflectance edge that is related to the formation of a superfluid condensate that provides coherent charge transport across the CuO_2 planes in the superconducting state of Sr-doped samples. A formula that has been proposed^{58,159} would account for the contribution

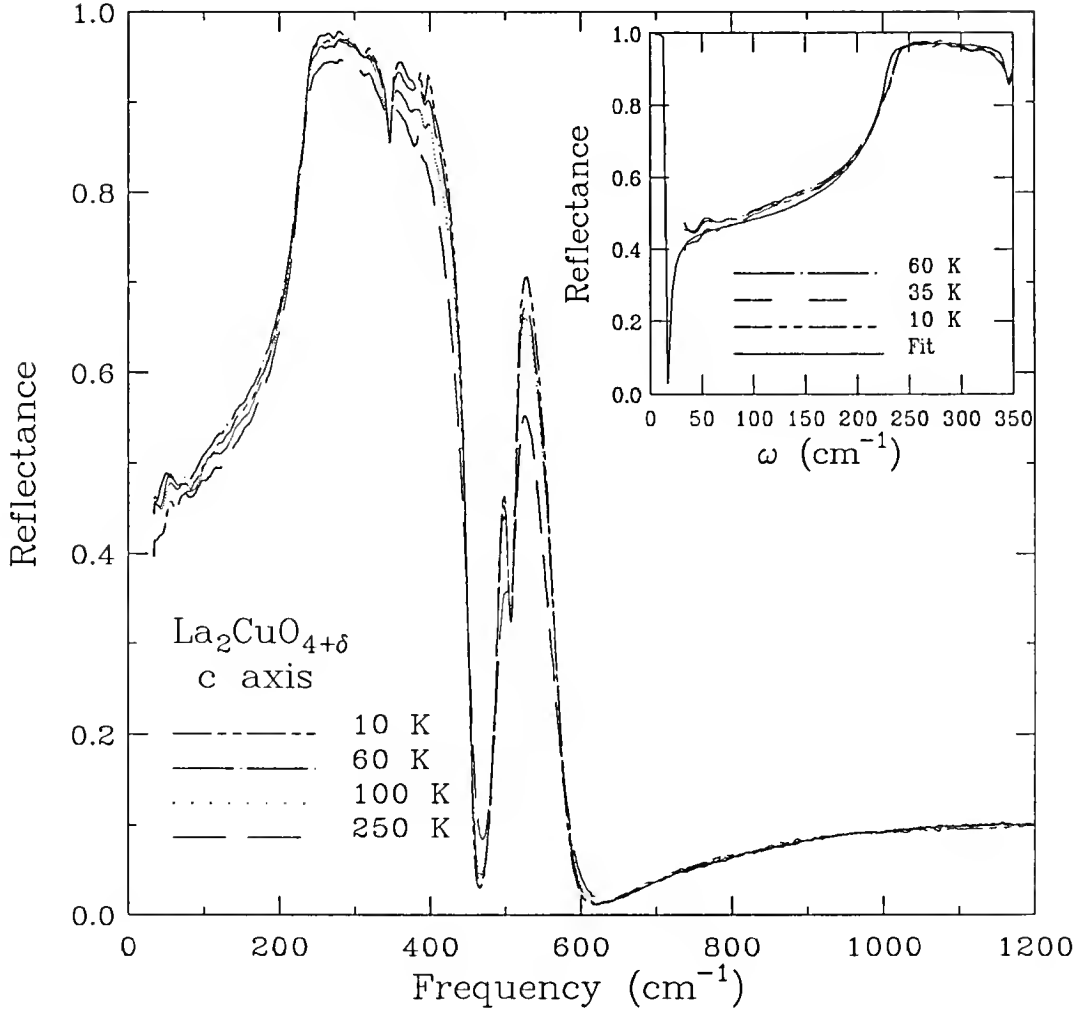


Fig. 26. Temperature dependence in the c -axis reflectance of $\text{La}_2\text{CuO}_{4+\delta}$ single crystal.

of this condensate to the dielectric function can be written as:

$$\epsilon(\omega) = \frac{-\omega_{ps}^2}{\omega(\omega + i0^+)}, \quad (38)$$

where ω_{ps} represents the oscillator strength of the superconducting condensate and $i0^+$ is the scattering rate that tends to zero as the mean free path becomes infinite in the superconducting state. Equation 38 resembles the contribution a condensate that gives rise to a δ -function peak at $\omega = 0$. Doping dependence studies⁵⁸ suggest

the reflectance edge associated with this condensate moves toward lower frequencies as the doping level in the sample is decreased. In order to fit this edge in our data, we used a condensate oscillator strength with $\omega_{ps} \sim 85 \text{ cm}^{-1}$. A comparison of this value with the results presented by Tamasaku *et al.*⁵⁸ for one of their Sr-doped samples indicates that the effective oxygen doping is ($\delta \sim 0.11$), and that the reflectance edge should appear around $\omega \sim 20 \text{ cm}^{-1}$ in the present sample. Due to the small sample size, the lowest frequency measured in the present experiment was around 33 cm^{-1} . This would explain why the edge was not observed in the present experiment.

Assignment *c*-Axis Phonons

Let us turn our attention to a quantitative analysis of the phonon modes shown in Fig. 26. In order to perform a Kramers-Kronig analysis, the reflectance at the low-frequency end was kept constant, as is customary for insulators. On the other hand, the positive slope of $R(\omega)$ below T_c at low frequencies, required us to use Eq. 38 as a low-frequency extension. The procedure followed for high-frequency extrapolation is as described in Chapter IV. The results of the Kramers-Kronig analysis performed on the data are shown in Fig. 27. The top panel of this figure shows the optical conductivity, while the bottom panel shows $\text{Im}(-1/\epsilon)$ both at several temperatures. This analysis reveals that the *c*-axis conductivity is dominated by a total of four infrared-active modes centered at 230, 340, 492, and 512 cm^{-1} . A comparison of these frequencies with other optical studies^{52,54,69} of the *c*-axis spectrum in undoped and Sr-doped samples of La_2CuO_4 indicates good agreement with the first two phonon modes. However, in those studies only one mode is observed at $\sim 501 \text{ cm}^{-1}$. Group theoretical analyses^{161,162} indicate that modes of ionic displacements ($\mathbf{q} = 0$) along the *c* axis in the nearly tetragonal structure of $\text{La}_2\text{CuO}_{4+\delta}$ will have the A_{2u} symmetry. In particular, calculations of the eigenfrequencies by Mostoller *et al.*,¹⁶¹ using a shell model in the undoped unit cell, give modes with A_{2u} symmetry at 242, 361, and 491

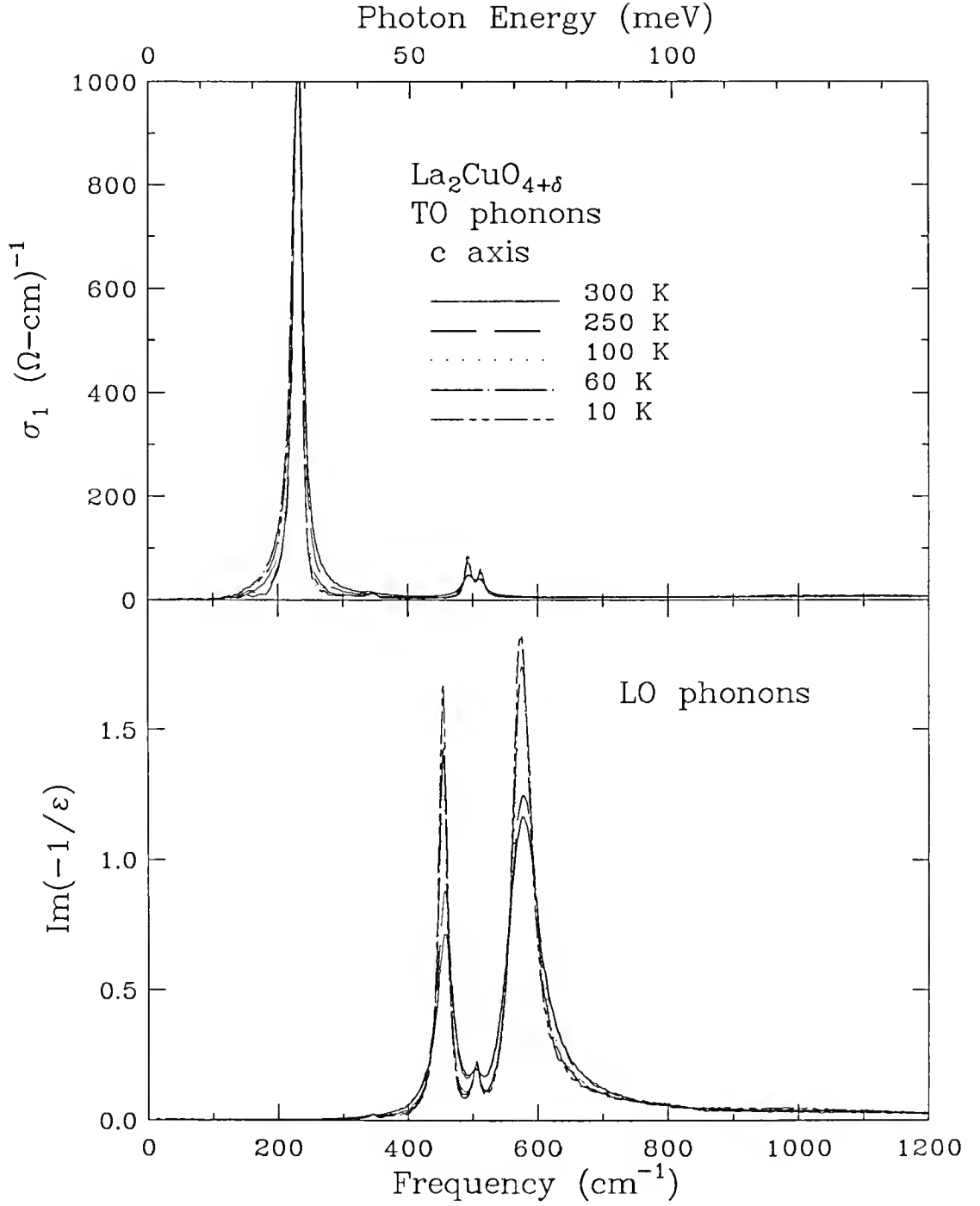


Fig. 27. Optical conductivity (upper panel) and loss function (bottom panel) along the c axis of $\text{La}_2\text{CuO}_{4+\delta}$ at several temperatures. The peaks in these quantities determine the TO and LO phonon frequencies respectively.

cm^{-1} . The eigenvector for the latter mode at 491 cm^{-1} involves in-phase vibrations of the apical oxygens above and below with respect to the four oxygen atoms in the plane. Based on this, the present data suggest that the presence of two modes at 492 cm^{-1} and 512 cm^{-1} is most likely associated with the incorporation of additional oxygen atoms in the structure. These additional oxygens, which are located in or between the LaO layers, may provide two slightly different force constants between the apical oxygens and the CuO_2 layers.

A quantitative analysis of the intensity and linewidth for each phonon mode as a function of temperature can be done by modeling the reflectance using a dielectric function model consisting of four Lorentz oscillators plus a core dielectric constant ϵ_∞ to account for contributions at higher frequency. The formula is

$$\epsilon(\omega) = \sum_{j=1}^4 \frac{\omega_{pj}^2}{\omega_j^2 - \omega^2 - i\omega\gamma_j} + \epsilon_\infty, \quad (39)$$

where each term in the sum corresponds to an optical phonon with ω_{pj} , ω_j , and γ_j being the intensity, center frequency and damping of each mode respectively. The top panel of Fig. 28 shows the temperature dependence of γ_j obtained from a fit to the reflectance at each temperature using Eq. 39. The bottom panel shows the corresponding oscillator strength (ω_{pj}) for the j^{th} phonon mode. The results shown in Fig. 28 indicate that most of the temperature dependence in the reflectance is the result of a reduction in γ_j (increase in the lifetime) as the temperature of the sample is decreased. This is what should be expected, since at low temperatures, the thermal motion of the atoms in the structure will be frozen out. This diminishes the chances of scattering among the atomic vibrations in the crystal. The results show some saturation in γ_j below 60 K and no anomaly is observed in the superconducting state data. On the other hand, both the phonon intensities and center frequencies do

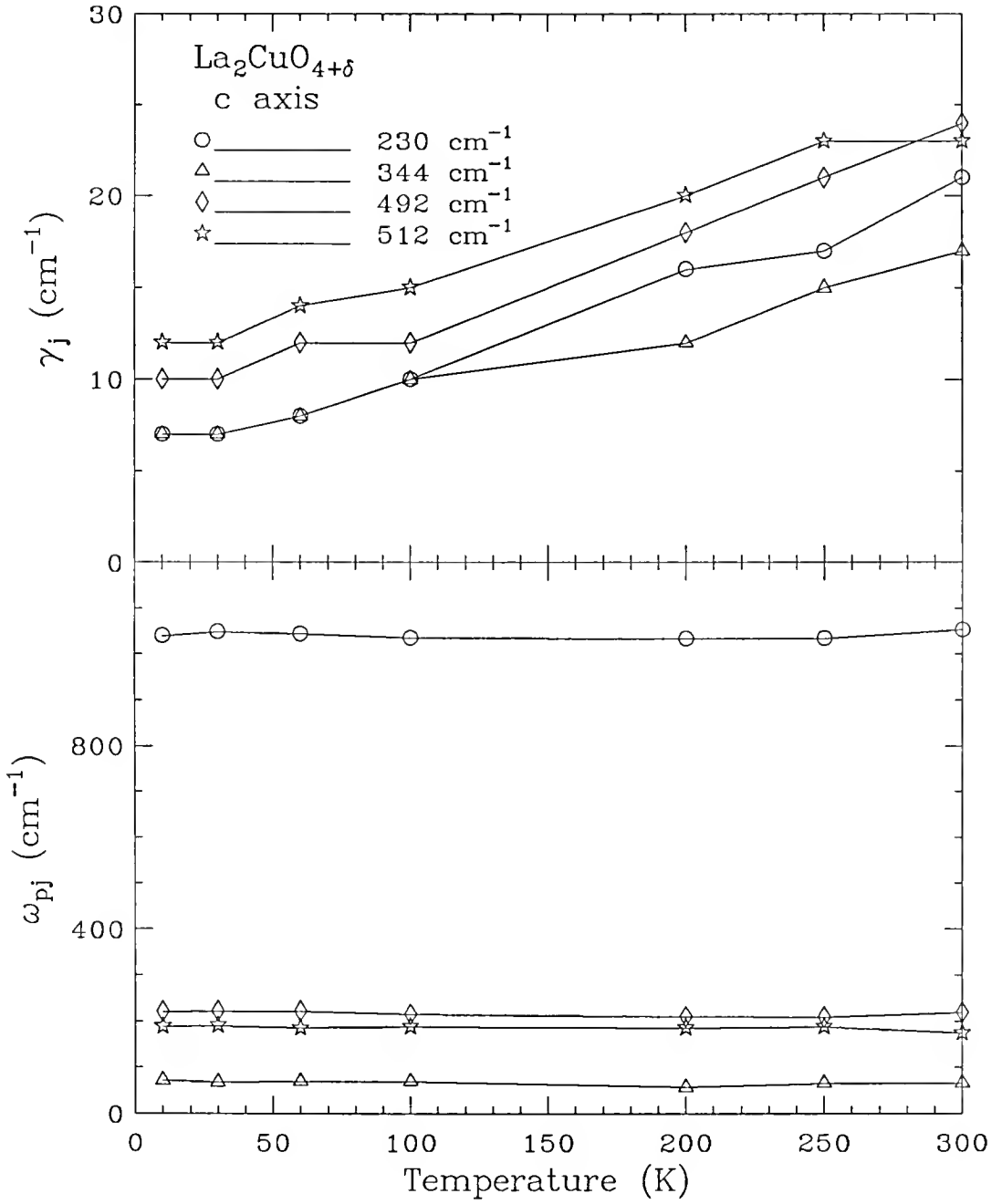


Fig. 28. Temperature dependence of the phonon parameters showing the linewidth γ_j (upper panel) and the oscillator strength ω_{pj} (bottom panel) obtained from Lorentz-model fit to the reflectance.

not show any significant temperature variation in the measured range; only the mode at 340 cm^{-1} exhibits some systematic hardening as the temperature is lowered. The center frequency for this mode goes from 340 cm^{-1} at room temperature to 347 cm^{-1} at $T = 10\text{ K}$.

Effective Charge

The intensities (ω_{pj}) in each phonon line are related to the effective charge that is carried by each ion. To establish this relationship, the first thing that should be considered is that each phonon mode splits into transverse (TO) and longitudinal (LO) ionic vibrations in the crystal. Since the TO frequencies involve transverse vibrations of the atoms, they are obtained directly from the peak position in the absorption, *i.e.*, the real part of the optical conductivity $\sigma_1(\omega)$. On the other hand, the LO frequencies involve long range changes in the dipole moment along the direction of propagation in the crystal. Information about the center frequencies of these LO oscillations can be obtained, in principle, from the peak positions in the loss function $\text{Im}(-1/\epsilon)$ as shown in the bottom panel of Fig. 27. A direct determination of the LO-TO splitting is also possible by noting that this splitting is related to the oscillator strength of the phonon mode in the context of the Lyddane-Sachs-Teller relation. The formula is written as

$$\omega_{pj}^2 = (\omega_{LOj}^2 - \omega_{TOj}^2)\epsilon_\infty. \quad (40)$$

Table 3 displays the parameters from a Lorentz fit to the room temperature reflectance along with the TO and the LO frequencies derived from Eq. 40. Once the TO-LO splitting is determined for each phonon, the effective charge of the ions can be estimated by using an expression based on a rigid-ion model of lattice dynamics that

Table 3. Parameters of a Lorentz fit for the measured c -axis room temperature reflectance of $\text{La}_2\text{CuO}_{4+\delta}$.

Oscillator#	ω_{TOj} (cm^{-1})	ω_{LOj} (cm^{-1})	ω_{pj} (cm^{-1})	γ_j (cm^{-1})
$\vec{E} \parallel c$				
1	230	498	1052	20
2	342	343	65	15
3	492	502	218	24
4	512	515	174	23
$\epsilon_\infty = 5.3$				

has been applied successfully to other systems with ionic character.¹⁶² The formula is

$$\sum_j [\omega_{LOj}^2 - \omega_{TOj}^2] = \frac{4\pi}{V} \sum_k \frac{(Ze)^2}{m_k}, \quad (41)$$

where j is the sum over all LO-TO splitting, V is the volume of the unit cell and k is the sum over all ions with mass m_k and effective charge Z_k . Since the crystal must obey charge neutrality: $\sum_k Z_k = 0$. In general, Eq. 41 can not be solved unless the number of unknown parameters Z_k is less than or equal to two. In the case of $\text{La}_2\text{CuO}_{4+\delta}$, since oxygen is much lighter compared to the other atoms, the right hand side of Eq. 41 will be dominated, in first approximation, by the term related to the oxygen atoms. Thus by neglecting all but the oxygen contributions, the result of solving Eq. 41 will yield the effective charge of oxygen averaged over all sites. Such procedure gives an effective charge for oxygen in the order of $Z_o \sim 1.28$. Similar analyses^{52,154} carried out on insulating La_2CuO_4 samples yield an effective charge for

oxygen in the order of ~ 1.1 . The slightly higher value obtained here (14%) is most likely due to the insertion of additional oxygen in the structure. These results differ from the nominal effective charge of two expected for the oxygen in the structure and they indicate the high degree of covalency of the bonds in the structure.

ab-Plane Reflectance

Result of the reflectance for polarization of the electric field parallel to the CuO_2 is shown in Fig. 24. As mentioned above, there is a marked contrast for polarization of the light parallel and perpendicular to CuO_2 planes. The *ab*-plane spectrum exhibits metallic behavior with optical phonon modes at low frequencies that are not completely screened out by the free carriers. At higher frequencies, we observe the plasma edge minimum at $\omega \sim 7500 \text{ cm}^{-1}$. This energy is not much different than the one observed in Sr-doped superconducting samples.^{28,69} For frequencies above the plasmon minimum, we see the usual charge transfer (CT) peak at $\omega \sim 11,500 \text{ cm}^{-1}$, followed by higher energy interband transitions.

Assignment *ab*-Plane Phonons

In view of the fact that the crystal structure in La_2CuO_4 is almost tetragonal, with only a weak orthorhombic distortion that occurs at low temperatures, all phonon lines can be classified under the D_{4h}^{17} point group symmetry. Therefore, the irreducible representation of the vibrations that involve in-plane atomic displacements will correspond to the E_u symmetry. Hence, we should expect four infrared-active modes in the in-plane spectrum. In our oxygen-doped sample, we observe a total of six major phonon-like features at 80, 140, 230, 355, 484, and 680 cm^{-1} . Previous measurements and assignment of the *ab*-plane phonon modes of La_2CuO_4 indicate that only infrared-active modes at ~ 140 , ~ 360 , and $\sim 690 \text{ cm}^{-1}$ have been seen in the spectrum of this material with the E_u symmetry.^{52-54,69,153,154,160} The greater number of phonon lines

in the present sample suggests that the assumption of a tetragonal symmetry is only good as a first approximation. Nonetheless, the close correspondence of three measured frequencies in our sample with the assigned modes in La_2CuO_4 allows us to conclude they indeed correspond to the E_u symmetry. The low-frequency mode at 140 cm^{-1} corresponds to bending vibrations of the out-of-plane atoms (apex oxygens) against the CuO_2 planes.¹⁵⁴ The remaining two modes at 355 cm^{-1} and 680 cm^{-1} are related to bending and stretching vibrations of the Cu–O bonds respectively.

This leaves us with the question for the assignment of the three remaining modes. Various Raman measurements consistently show Raman-active modes at $\sim 230\text{ cm}^{-1}$ and $\sim 445\text{ cm}^{-1}$ in the undoped material.^{160,163–165} Moreover, a mode at $\sim 90\text{ cm}^{-1}$ has also been seen in Sr-doped samples using inelastic neutron scattering¹⁶⁶ and Raman¹⁶⁵ measurements. Based on a tetragonal structure for the unit cell, group theoretical calculations^{160,161} indicate that the mode at 230 cm^{-1} is double degenerate with even vibrations that correspond to the E_g and A_{1g} symmetries. On the other hand, the frequency at ~ 445 is related to the A_{1g} irreducible representation. The assignment of the mode at $\sim 90\text{ cm}^{-1}$ is regarded as belonging to the E_g symmetry.^{53,160} Hence, if a correlation is made between the additional infrared modes in this oxygen-doped sample and the Raman-active modes in undoped samples, it can be argued that doping in the material lowers the crystal symmetry making even (gerade) vibrations in the unit cell become infrared actives. One explanation for this could be that the A_{1g} mode may couple to electronic excited states of E_u symmetry making the former infrared allowed modes. Similar observations have been made by Shimada *et al.*⁶⁹ where modes at ~ 87 , ~ 230 , and $\sim 460\text{ cm}^{-1}$ have been observed to grow with Sr doping in $\text{La}_{2-x}\text{Sr}_x\text{CuO}_4$ samples. A second explanation for the mode at 483 cm^{-1} might be related to an antiresonance peak that should be present at this frequency due to the proximity of the modes at 355 cm^{-1} and 680 cm^{-1} . This structure, as we

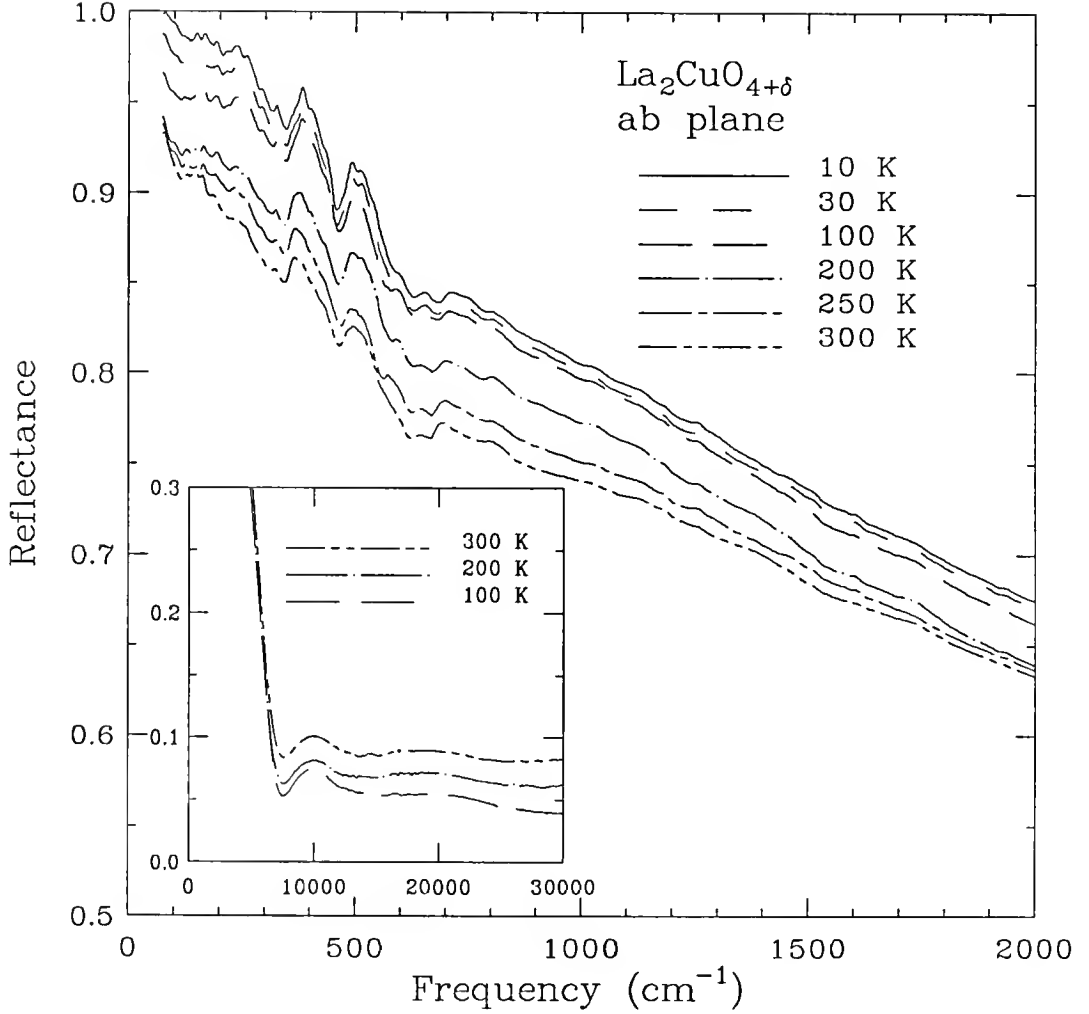


Fig. 29. Measured temperature dependence in the ab -plane reflectance (face II) of $\text{La}_2\text{CuO}_{4+\delta}$ sample. Inset: The reflectance at three selected temperatures in the near infrared and the visible.

will see later, is enhanced by interactions of the electronic background with the c -axis LO phonon modes in the sample.

Low Temperature ab -Plane Reflectance

Figure 29 shows the temperature dependence in the ab -plane infrared reflectance measured on face II of the sample. In the far infrared, we observe an increase in the reflectance that is in accord with the increase in the ab -plane dc conductivity that is observed in the sample.¹⁵² Evidence of the orthorhombic distortion in the

crystal lattice is also more clear at low temperatures where weak splitting of the phonon modes at 140 cm^{-1} and 680 cm^{-1} are observed.⁷² In addition, the weak modes at $\sim 182\text{ cm}^{-1}$ and $\sim 296\text{ cm}^{-1}$ are more easily resolved at low temperatures. These infrared-active modes are visible in the spectrum since they are not completely screened by the electronic background.

The inset in Fig. 29 shows the reflectance at three selected temperatures in the near-infrared and visible. We observe a marked temperature dependence of the reflectance in this range. As expected, there is a sharpening and steepening of the plasma edge minimum at 7500 cm^{-1} as the temperature of the sample is reduced. At the same time, the reflectance is reduced (sample becomes more transparent) for frequencies in the visible and above. A similar temperature dependence has been observed in the *ab*-plane reflectance of $\text{La}_{2-x}\text{Sr}_x\text{CuO}_4$ thin film⁷² and lightly oxygen-doped $\text{La}_2\text{CuO}_{4+\delta}$ single crystals.⁶⁴ In contrast to the result of the Sr-doped thin film, where a rather abrupt change is observed in the reflectance at 250 K and no change below this temperature,⁷² the temperature dependence here is more gradual. There are two things that could be said about this temperature dependence. In the first place, the fact that the reflectance is decreasing at lower temperatures implies there should be a strong temperature dependence in the opposite direction in some interband transition at a higher frequency.

This must be the case in order to satisfy the sum rule. Secondly, this temperature dependence could be related to the structural phase transition (tetragonal to orthorhombic) that occurs at low temperatures in the lanthanum-based superconductors. Such transition is known to be produced by a small staggered tilt of the apical oxygens in the CuO_6 octahedron. There are two effects associated with this. One of them is a doubling of the unit cell in the orthorhombic phase. The second is a redistribution of the electronic density of states near the Fermi surface.¹⁶⁷

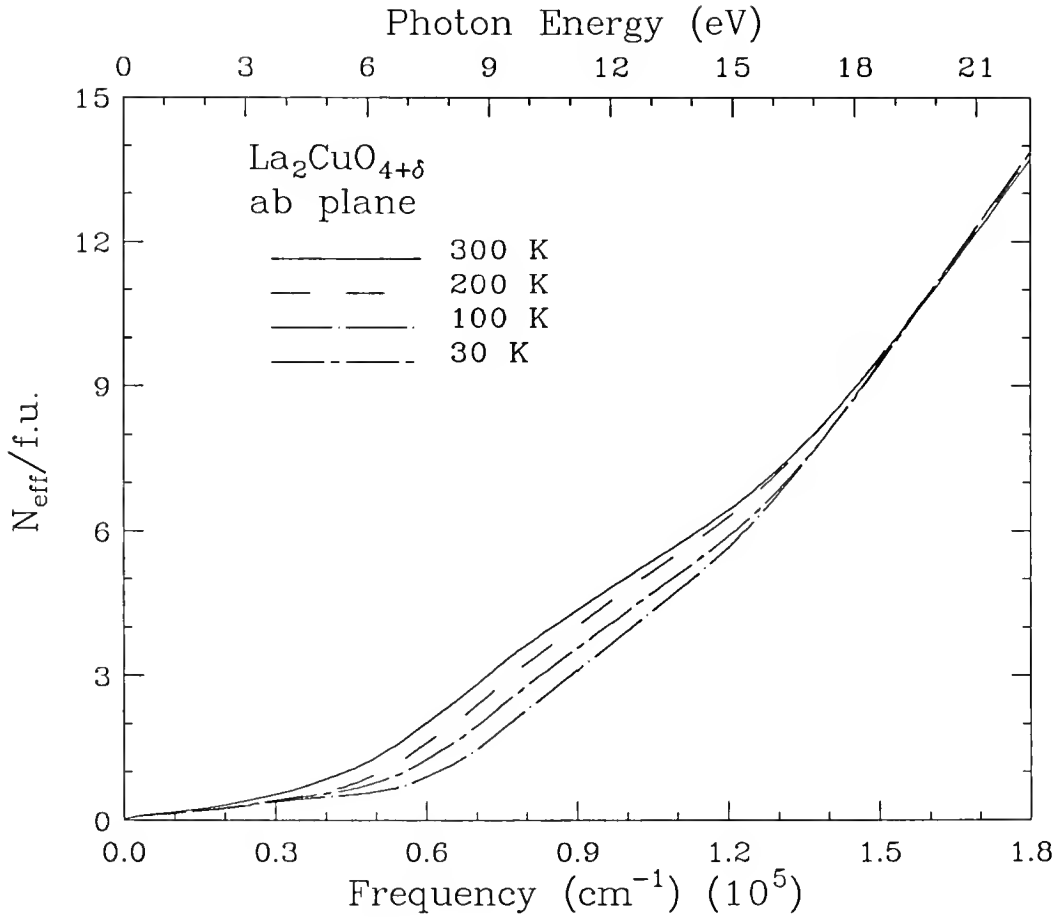


Fig. 30. Temperature dependence of sum rule on a wide frequency range to show transfer of oscillator strength from low to high frequencies.

Results of *ab*-Plane Optical Constants

This section is devoted to present results of the temperature dependence in the *ab*-plane optical properties of La₂CuO_{4+δ} obtained from a Kramers-Kronig analysis of the reflectance. The usual requirement of the Kramers-Kronig integrals to extend the reflectance at the low- and high-frequency ends was done in the following way. The low-frequency extension was done by modeling the reflectance using a Lorentz-

Drude model and using the fitted results to extend the reflectance below the lowest frequency measured in the experiment as explained in Chapter III (p. 60). The high-frequency extrapolation of the room temperature results was done by merging the data, which only extend up to $38,000\text{ cm}^{-1}$ (4.7 eV), with published results on Sr-doped samples by Tajima *et al.*,¹⁶⁸ which extend up to 40 eV. The range beyond 40 eV was extended with a power law $R \sim \omega^{-4}$, which is the free-electron behavior limit. Since there is a temperature dependence in the reflectance all the way up to $38,000\text{ cm}^{-1}$, as the temperature of the sample is reduced, the scaling factor used in appending the data from Tajimas *et al.* to our low-temperature results was rescaled upward in the range 10–15 eV and this was joined with the unchanged data above 15 eV in order to make the sum rule results equal in the range of frequencies above 15 eV. The results of the sum rule, shown in Fig. 30, suggest that what this procedure does is to transfer some of the spectral weight that is missing in the range where we measured a lower reflectance to higher frequencies. This might suggest some strong temperature dependence that is occurring in some interband electronic transition at frequencies much higher than $38,000\text{ cm}^{-1}$. It should be pointed out that doing this extrapolation procedure did not make a significant effect on the results of the Kramers-Kronig analysis below $10,000\text{ cm}^{-1}$ (1.2 eV).

Loss Function

An second illustration of the observed temperature dependence is shown in Fig. 31. Here the imaginary part of $-1/\epsilon$ is plotted *vs.* frequency at several temperatures. In ordinary metals, the peak position of this function gives the longitudinal (LO) mode frequency for plasma excitations of the charge carriers. The width of this peak is related to the lifetime of these excitations. As will be discussed later, the anomalous behavior of the optical conductivity in the high- T_c materials does not allow us to make such an assignment here. A direct consequence of the anomalous

absorption in the midinfrared electronic background is the broad width (~ 0.4 eV) that is observed in the present results and in nearly all copper-oxide superconductors.^{28,72,81} Estimates for the screened plasma $\widetilde{\omega}_p \approx \omega_p/\sqrt{\epsilon_\infty}$, can also be deduced from the position of this peak.

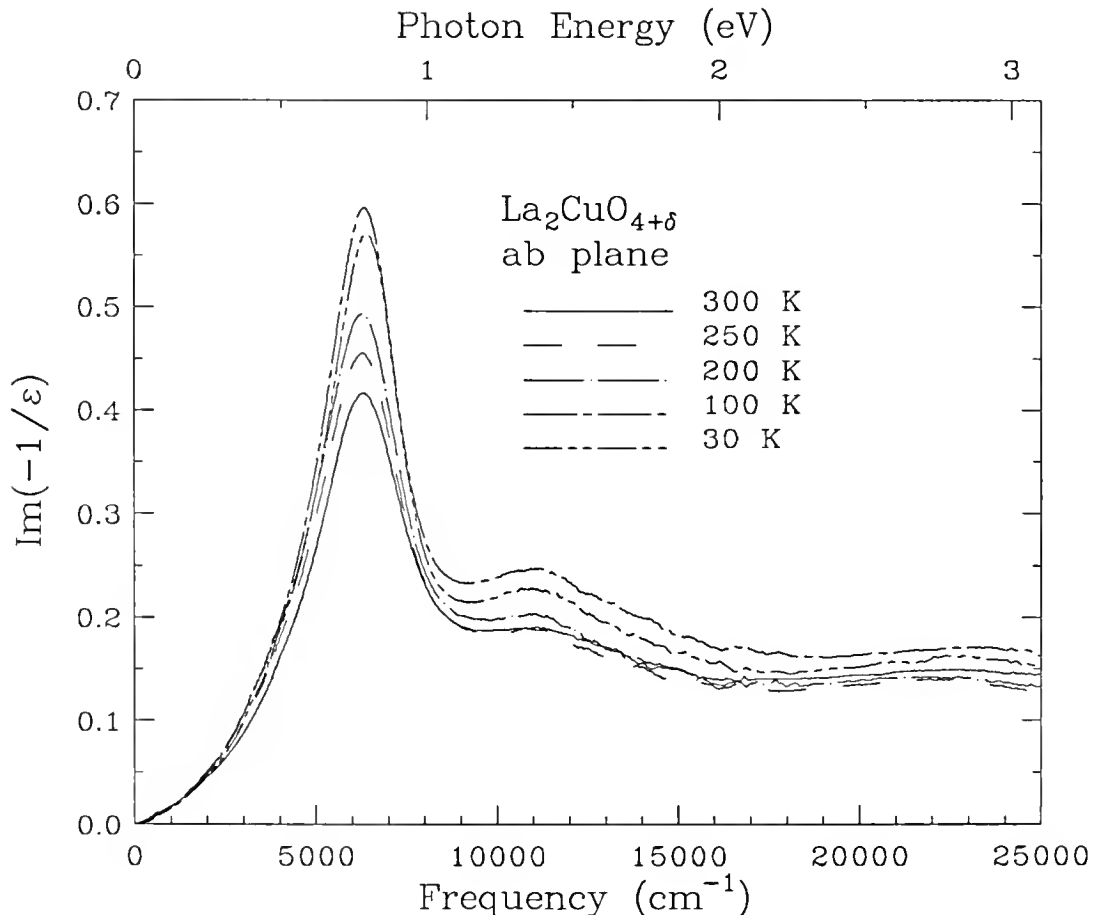


Fig. 31. Temperature dependence in the loss function.

In the present sample $\widetilde{\omega}_p \simeq 6300\text{cm}^{-1}$. This frequency is nearly the same as in other Sr-doped samples with similar doping level.^{28,72} The intensity of this peak is greatly enhanced at low temperatures, while the position does not show much shifting as the temperature of the sample is reduced. We also observed the bump at $11,500\text{ cm}^{-1}$ (1.43 eV), which is associated the with charge transfer band in the

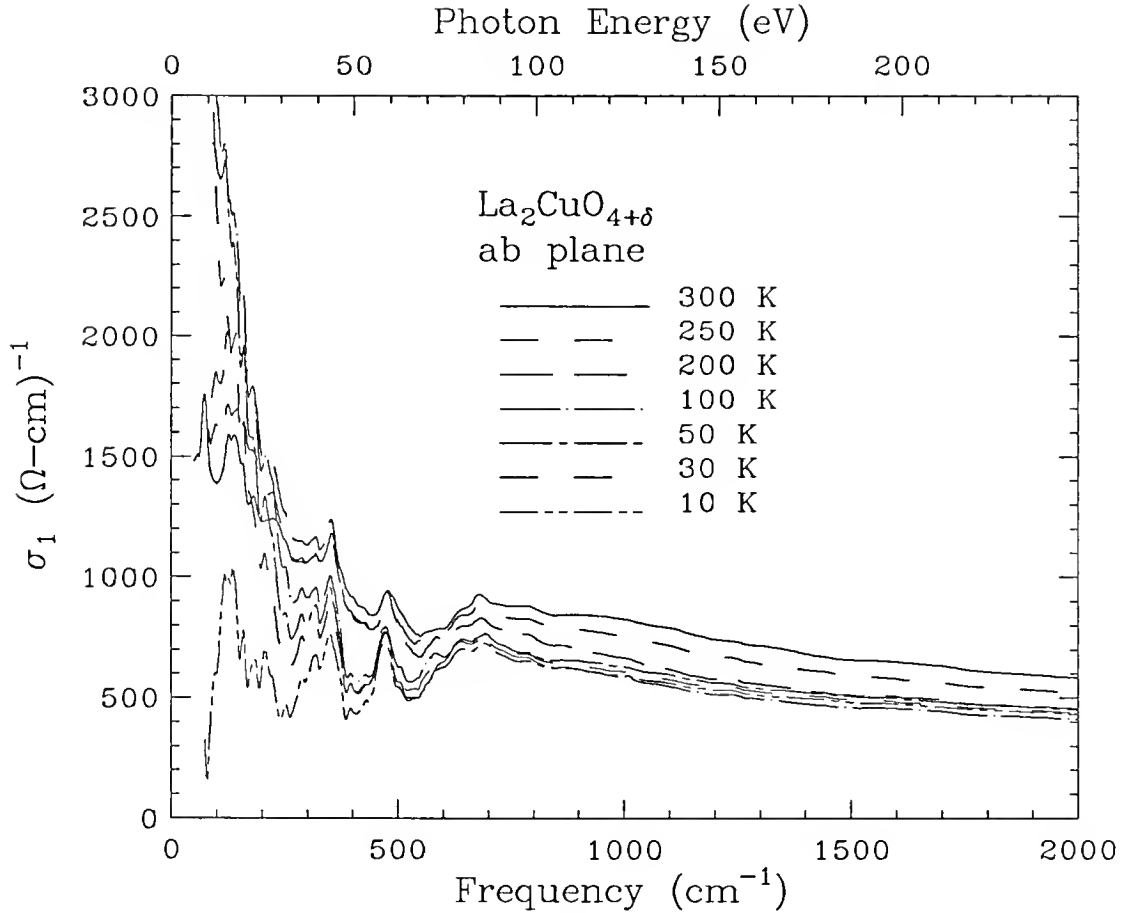


Fig. 32. Real part of the optical conductivity $\sigma_1(\omega)$ at several temperatures in the far and midinfrared.

doped samples, becomes more resolved and the center position shifts slightly towards lower energies at lower temperatures.

ab-Plane Optical Conductivity

The results of the temperature dependence in the infrared optical conductivity $\sigma_1(\omega)$ are shown in Fig. 32. These results were obtained from face II of the sample. As mentioned before, any structure that may be present in the reflectance is more easily resolved in the spectrum of $\sigma_1(\omega)$. We observe that, as the temperature of the sample is lowered, the phonon modes become sharper. There is also a minimum or “notch-like” structure in the frequency range 450–500 whose origin will be discussed

later. Moreover, the electronic far-infrared background has a strong temperature dependence with a steep enhancement as the sample is cooled down. This is followed by a more weaker temperature dependence at frequencies in the midinfrared. There is a reduction in the midinfrared conductivity when cooling the sample from room temperature down to 200 K with not further appreciable change below this temperature. This is connected with the temperature dependence of the reflectance in the near infrared and visible that is observed in the inset of Fig. 29. As mentioned earlier, this could be due to the phase transition from tetragonal to orthorhombic that occurs in the material at lower temperatures. Similar results were reported on a Sr-doped film by Gao *et al.*. Gao *et al.* found no further temperature dependence was present above 300 K. Similar check was not done in the present sample since oxygen could be driven out of the structure at temperatures above 300 K.

As discussed in Chapter IV, there are two ways to analyze the optical conductivity $\sigma_1(\omega)$ in the high- T_c superconductors. The two approaches are the one- and two-component models. Since the present data strongly suggest the presence of two or more components to $\sigma_1(\omega)$, we performed an analysis based on a decomposition of the conductivity in two parts, a Drude or free-carrier part and a midinfrared contribution. Discussion of the results in this analysis is done in next section.

Midinfrared Component

The results of the midinfrared component, after subtracting the phonons and free-carrier contribution at zero frequency, are shown in Fig. 33 at several temperatures. The scattering rate of the free-carrier or Drude contribution shows a linear temperature dependence as shown in Fig. 34, while the oscillator strength is temperature independent with a magnitude of $\omega_{pD} \sim 5800 \pm 100 \text{ cm}^{-1}$. A fit of the form $\hbar/\tau = 2\pi\lambda/\tau + 1/\tau_0$ yields a value for the coupling constant $\lambda \simeq 0.25$. The midinfrared part shows some interesting features which are summarized next. The

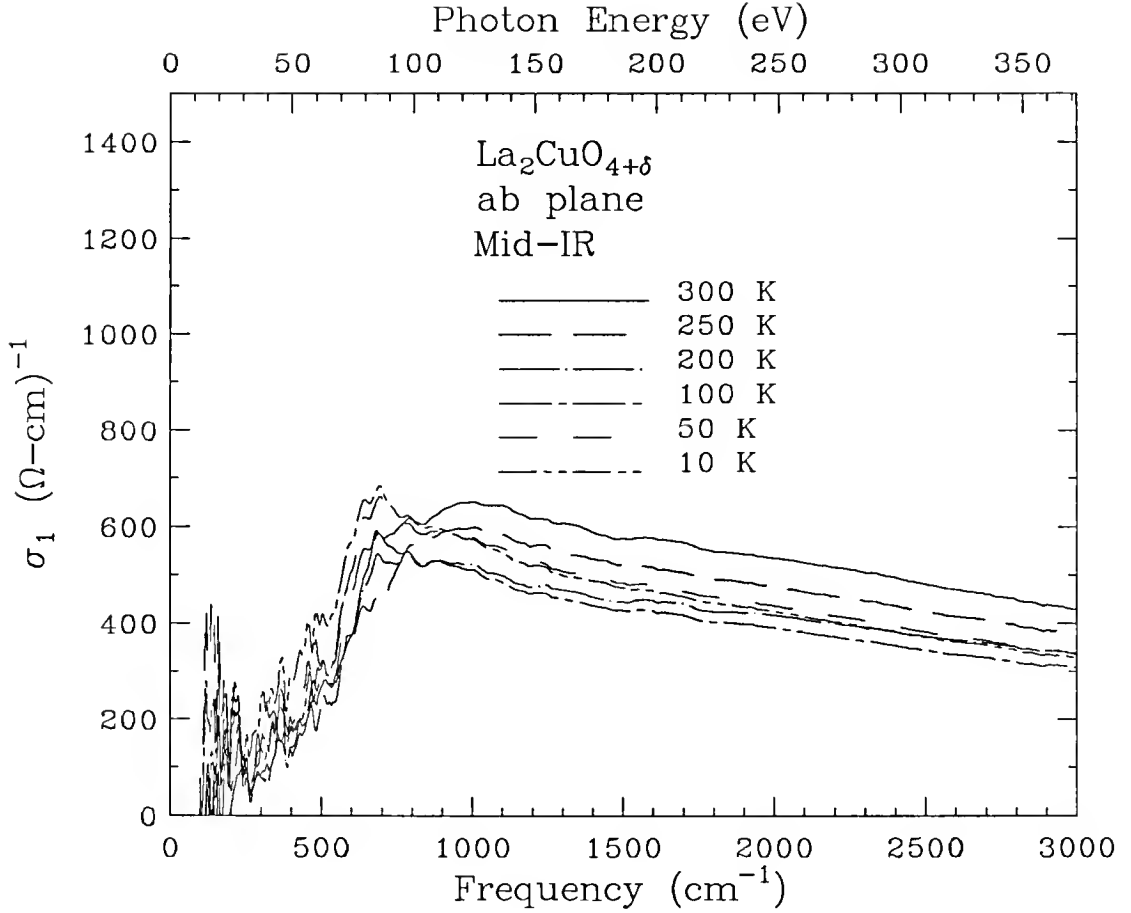


Fig. 33. Midinfrared conductivity of $\text{La}_2\text{CuO}_{4+\delta}$ at several temperatures obtained after subtracting the Drude-like contribution from the data shown in Fig. 32.

overall oscillator strength of the midinfrared conductivity appears to decrease as the temperature of the sample is decreased from room temperature down to 200 K. A less noticeable change is seen below this temperature. This temperature dependence is connected with the decrease that is seen in the near-infrared reflectance shown in the inset of Fig. 29. Hence, it appears that some spectral weight is being transferred to higher frequencies, which is also affecting $\sigma_1(\omega)$ in the midinfrared. It is interesting to note that the oscillator strength of the Drude part, the one that is responsible for the conduction of current in the two-component model, remains nearly

constant. We also observe that a bump-like structure, which at 300 K appears at around 1000 cm^{-1} , diminishes in intensity with a reduction in temperature. Then, at about 200 K, a second and sharper feature reappears at a lower energy, $\sim 750\text{ cm}^{-1}$, growing again in intensity as the temperature of the sample is further reduced. Similar midinfrared-like modes in the optical conductivity of both lightly doped^{64,169} and superconducting samples have also been reported in the literature.^{68,72,87,135} The present results underscore the generality of these features in the optical properties of the copper-oxide-based materials.

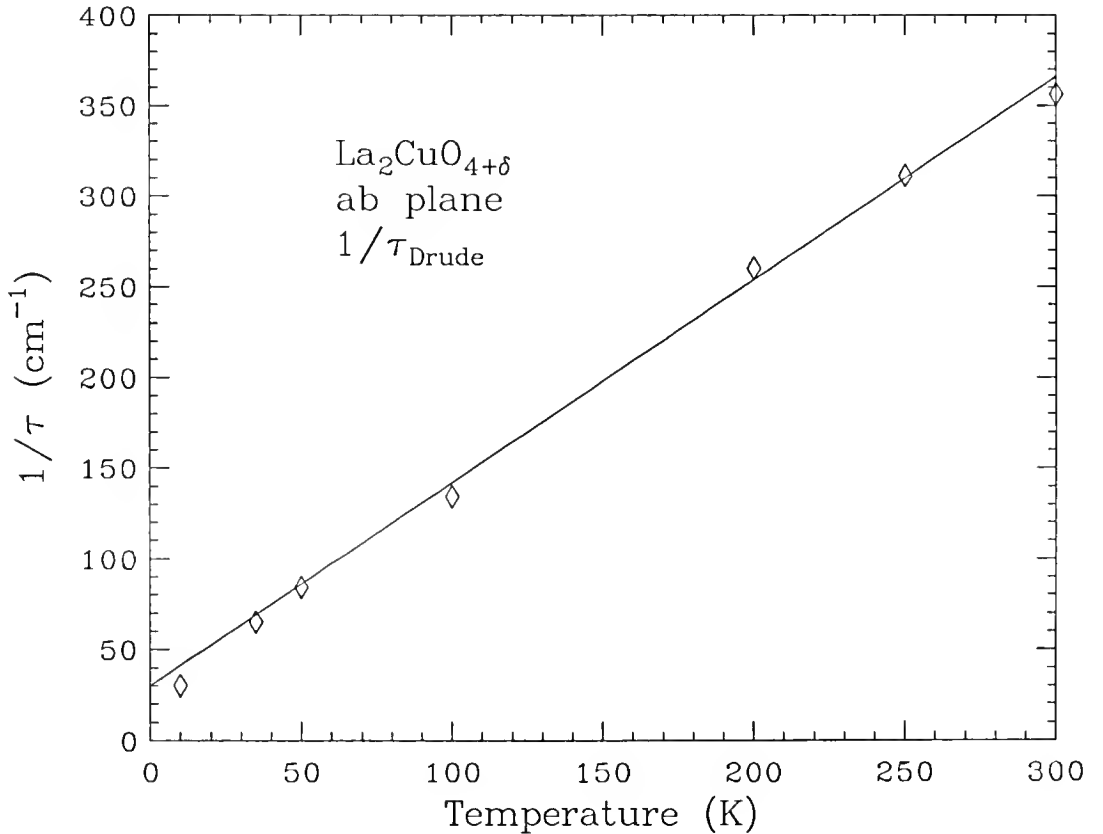


Fig. 34. The scattering rate of the Drude-like part from a two-component fit to the optical conductivity shown in Fig. 35 (Notice the linear temperature dependence).

Comparison of ab -Plane Reflectance: $\mathbf{q} \parallel c$ and $\mathbf{q} \perp c$

One aspect that has become relevant in the study of the infrared properties of the copper-oxide superconductors is the effect of the electron-phonon interactions. Early on, evidence for the importance of these interactions had been gathered mainly from neutron time-of-flight spectroscopy, where a softening of the phonon density of states was observed when doping in the parent compound $\text{YBa}_2\text{Cu}_3\text{O}_{6+x}$ was changed from insulating to metallic.¹⁷⁰ There was also evidence of some anomalies with certain phonon branches associated with stretching modes of Cu–O bonds near the zone boundaries.¹⁷¹ Such interactions could give a natural explanation to the observed normal-state linear resistivity as a function of temperature that is seen in nearly all copper-oxide superconductors. This might imply that the charge carriers are scattered by some sort of thermal excitations such as phonons. However, this interpretation should be taken with some caution, because in ordinary metals the T -linear resistivity is a high-temperature phenomenon whereas in the high- T_c materials this T -linear behavior is observed even below the Debye temperature, where a T^5 or T^3 behavior should be expected.

The type of interactions that are considered to be relevant are the ones that have been observed in organic conductors.¹⁷² As first pointed out by Rice,¹⁷³ linear coupling of charge carriers to totally symmetric A_g modes in the organics can lead to structure in the conductivity spectrum at infrared frequencies. The overlapping of these phonon frequencies with the continuum of excitations give rise to minima or characteristic Fano lineshape antiresonances in the conductivity spectrum. It has been proposed^{103,174} that similar effects in the copper-oxide superconductors could give rise to the “knee-like” structures that are seen at 140 cm^{-1} and 440 cm^{-1} in the ab -plane reflectance spectrum of $\text{YBa}_2\text{Cu}_3\text{O}_{7-\delta}$.^{65,68} These structures show up as an onset at lower energy and a “notch” at higher energy in the spectrum of $\sigma_1(\omega)$. Similar

features have also been seen in the conductivity spectra of $\text{Bi}_2\text{Sr}_2\text{CaCu}_2\text{O}_8$,^{84,87} $\text{La}_{2-x}\text{Sr}_x\text{CuO}_4$,^{69,72} and $\text{Pb}_2\text{Sr}_2(\text{Y/Ca})\text{Cu}_3\text{O}_8$.¹³⁵

In explaining the physical origin of these structures it has been proposed by Reedyk *et al.*¹³⁶ that the coupling in the high- T_c and isostructural materials is between the longitudinal c -axis phonons and the ab -plane bound carriers in the midinfrared. This idea is based on the fact that the coupling and, hence, the presence of structure in $\sigma_1(\omega)$ is enhanced in the so-called parallel geometry, *i.e.*, when measurements of the ab -plane optical reflectance are performed when the wavevector of the incident light \mathbf{q} is parallel to the c axis of the sample and the electric field \mathbf{E} is polarized within the ab plane. Such structures have been found to be absent when the ab -plane optical properties are measured on the ac (or bc) face of the crystal.¹³⁵ In this geometry, the wavevector of the light, which lies either along the a - or b -axis, is perpendicular to the c axis and therefore no coupling should occur.

In order to illustrate this kind of electron-phonon coupling in the present oxygen-doped $\text{La}_2\text{CuO}_{4+\delta}$ sample, we display in Fig. 36 the ab -plane reflectance when the wavevector of the light \mathbf{q} is parallel and perpendicular to the c axis in the sample. A comparison of the two room-temperature spectra indeed shows some differences. The results indicate that when $\mathbf{q} \parallel c$, the far-infrared reflectance displays two shoulders each one followed by minima at 450 cm^{-1} and 560 cm^{-1} . Such structures appear to be absent in the case when $\mathbf{q} \perp c$. A second observation is that at higher frequencies both reflectance spectra are nearly of the same level with a slight shift of the plasma edge minima in the two polarizations. Also the charge transfer band, located around $12,000 \text{ cm}^{-1}$, appears to have equal strength in both polarizations. Since the strength of this band gives an indication of the doping in the sample, this means that both surfaces of the crystal have nearly equal doping.

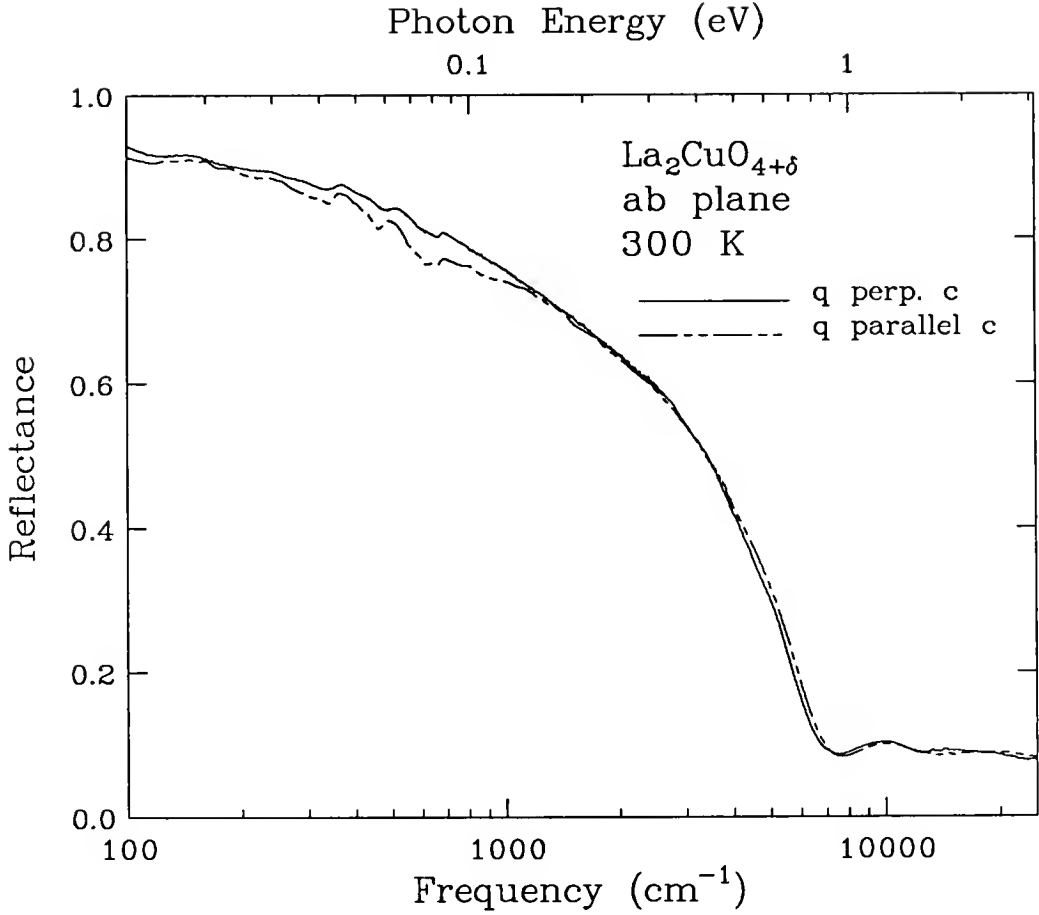


Fig. 36. A comparison of the *ab*-plane reflectance measured from face I ($\mathbf{q} \perp c$) and face II ($\mathbf{q} \parallel c$) of $\text{La}_2\text{CuO}_{4+\delta}$ at $T = 300$ K.

To further illustrate the differences at low frequencies, we show in the top part of Fig. 37 the optical conductivity $\sigma_1(\omega)$ obtained from a Kramers-Kronig analysis of the reflectance in the two geometries indicated above. For more clarity, we have subtracted the phonons that are present in both spectra. This figure clearly shows that $\sigma_1(\omega)$ displays two minima-like structures at 450 cm^{-1} and 560 cm^{-1} . A remarkable coincidence exists between these frequencies and the peak positions of the *c*-axis LO frequencies, as determined from the peak maxima of the *c*-axis loss function $\text{Im}(-1/\epsilon)$. This function is also shown in the figure. Another observation is that there is a redistribution of spectral weight from low to high frequencies in the spectrum when $\mathbf{q} \parallel c$.

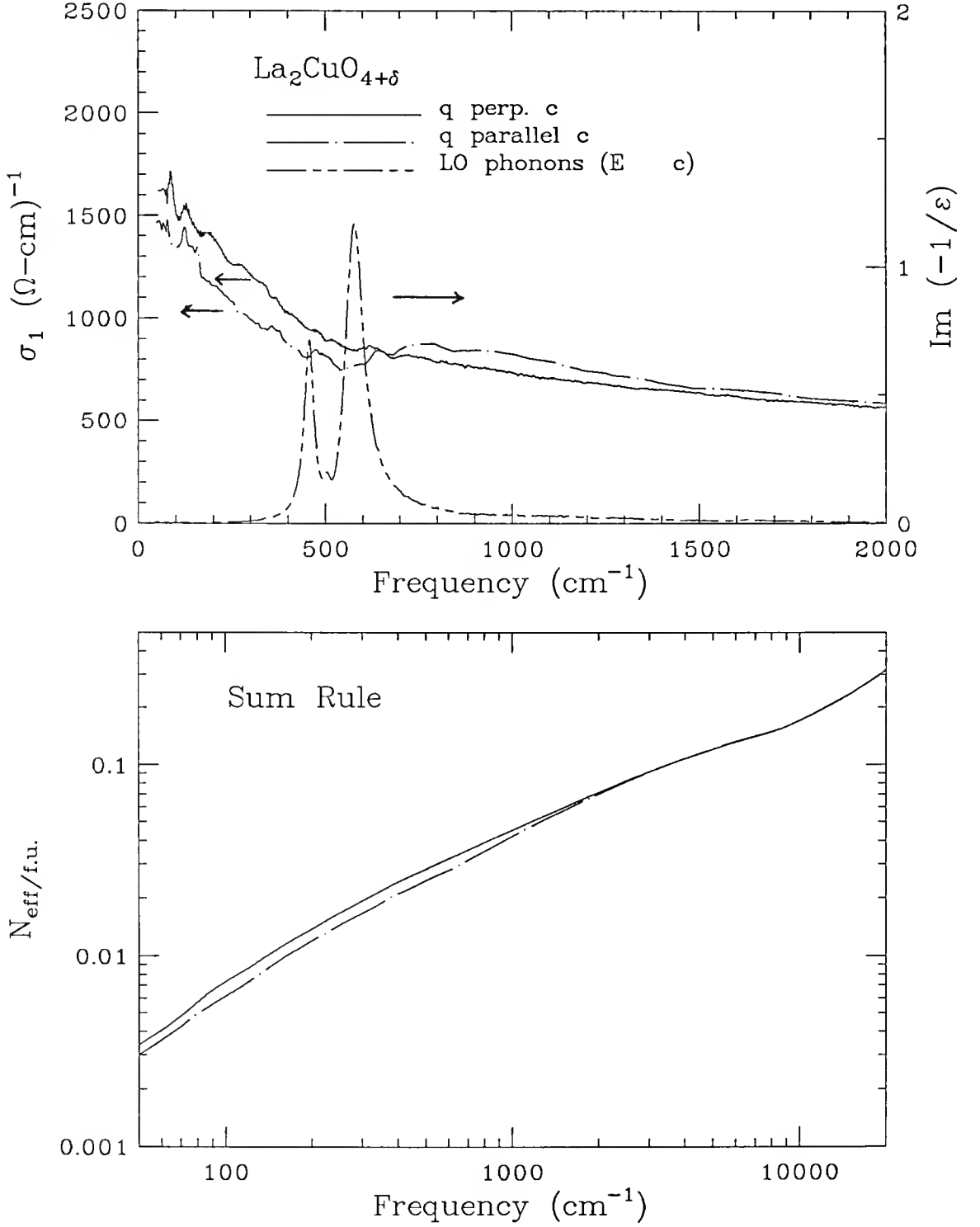


Fig. 37. Top: A comparison of the ab -plane conductivity measured on the sample for $\mathbf{q} \perp c$ (face I) and $\mathbf{q} \parallel c$ (face II) at $T = 300$ K. Bottom: Sum rule of the reflectance at room temperature for $\mathbf{q} \parallel c$ and $\mathbf{q} \perp c$.

The midpoint of such redistribution appears to coincide with the peak position of the strongest c -axis LO phonon at 560 cm^{-1} . This redistribution also appears to conserve the sum rule in the two polarizations as shown in the bottom part of Fig. 37. These results clearly underscore the importance of electron-phonon coupling in the optical properties of the high- T_c materials.

Concluding Remarks

In sum, results of polarized reflectance performed on superconducting $\text{La}_2\text{CuO}_{4+\delta}$ ($T_c \simeq 40\text{ K}$) reveal an insulator for polarization of the light along the c axis, while the ab -plane response has a metallic-like properties. A total of four optic phonons, one more than in insulating La_2CuO_4 , are resolved in the c -axis polarization with A_{2u} symmetry. Using a rigid-ion model, we find an estimate of the average oxygen effective charge in the structure to be 14% higher than in insulating La_2CuO_4 ,¹⁵⁴ This is close to the estimated 12% oxygen doping in the sample. We also find an anomalous temperature dependence in the ab -plane reflectance for frequencies in the visible and above. This result may indicate some restructuring of the electronic interband transitions possibly due to the phase transition from tetragonal to orthorhombic that is known to occur in the material at lower temperatures. Such transition appears to affect the oscillator strength in the midinfrared conductivity. At the same time, it does not appear to affect the oscillator strength of the free-carrier contribution in a two-component analysis of $\sigma_1(\omega)$. In this analysis, we find $\omega_{pD} \sim 5800 \pm 100\text{ cm}^{-1}$ with a scattering rate that is linear in temperature. A comparison of the ab -plane optical conductivity obtained from two different faces reveals some qualitative differences. In the case when the wavevector of the light is parallel to the c axis, face II on Fig. 23, the midinfrared conductivity shows two minima-like structures whose positions are correlated with the peaks in the LO frequencies of the c -axis phonons. Such features are absent in the spectrum of $\sigma_1(\omega)$ measured when $\mathbf{q} \perp c$ (face I). This, combined

with the fact that the coupling constant obtained from the slope of the linear temperature dependence of $1/\tau$ of the Drude-like carriers in a two-component analysis of $\sigma_1(\omega)$ is rather small ($\lambda \simeq 0.25$), suggests that the coupling of the c -axis LO phonons is stronger with the midinfrared carriers.

CHAPTER VI
ANISOTROPY IN THE AB-PLANE
OPTICAL PROPERTIES OF $\text{YBa}_2\text{Cu}_3\text{O}_{7-\delta}$

This chapter is devoted to results of the *ab*-plane anisotropy in the optical properties of single-domain crystals of $\text{YBa}_2\text{Cu}_3\text{O}_{7-\delta}$. The room temperature reflectance was measured along the two principal axes in the *ab* plane in the frequency range 100–32,000 cm^{-1} . In addition, the reflectance in the far-infrared and midinfrared regions was measured at three temperatures: 300 K, 100 K, and 30 K. From the results at each temperature, a Kramers-Kronig analysis was performed to obtain the temperature dependence in the optical conductivity and related optical constants. From this analysis, a discussion is made related to the different interpretations that have been proposed to explain the optical properties in the copper-oxide materials.

Room Temperature Spectra

Figure 38 shows the room temperature reflectance of $\text{YBa}_2\text{Cu}_3\text{O}_{7-\delta}$ over the measured frequency range for polarizations parallel to the *a* and *b* axes. The results show a strong anisotropy between these two directions. As was mentioned before, there is a network of one dimensional CuO chains along the *b* axis in this material. Hence, it is not surprising that such anisotropy exists, since it should be expected that additional dipole allowed transitions will be present in the *b* direction. The low-frequency results are characterized by a reflectance that is higher along the *b* direction by 2–3%. As the frequency increases, the reflectance along the *a* axis falls faster than the *b* axis. In the *a* axis, the plasma edge minimum occurs at around 8500 cm^{-1} . The reflectance along the chain direction shows a bump-like structure at around 3500 cm^{-1} , followed by a plasma edge minimum at 14,000 cm^{-1} . In

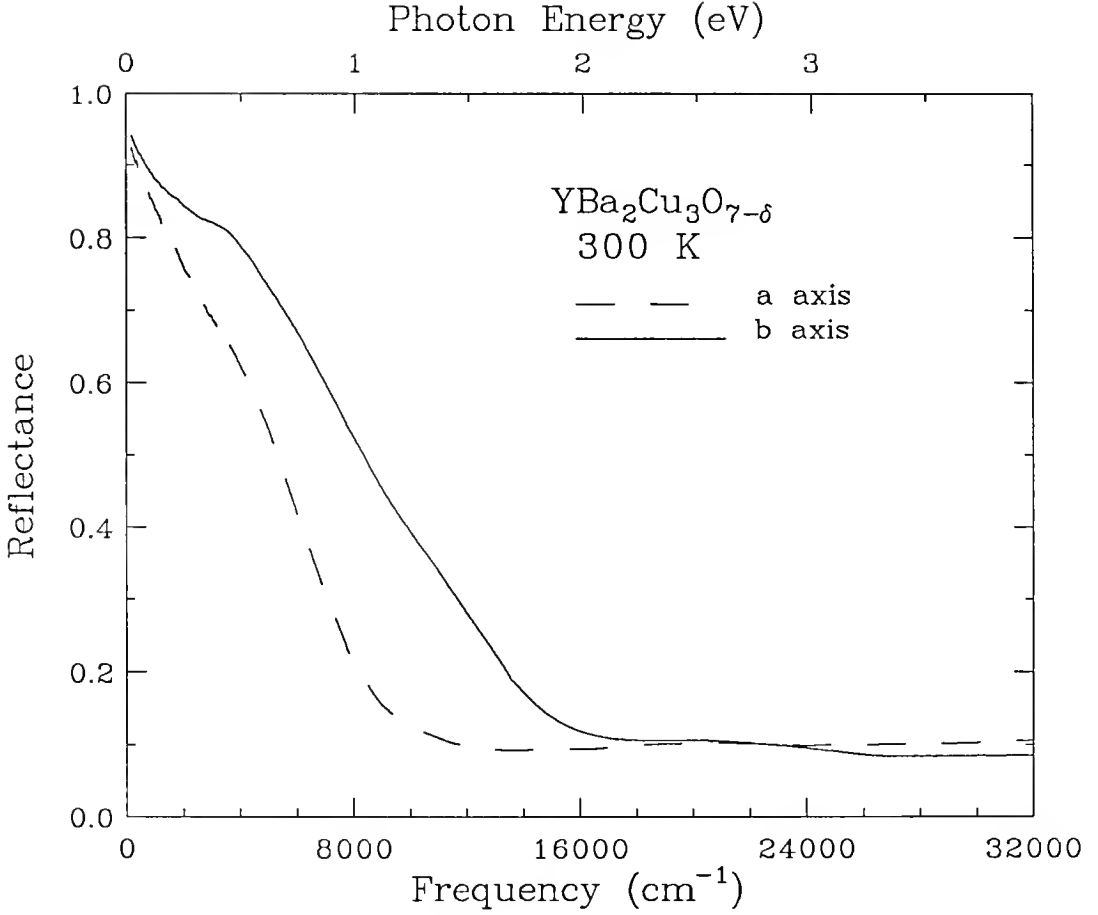


Fig. 38. Room temperature reflectance of YBa₂Cu₃O_{7-δ} single-domain crystal along the *a* and *b* axes.

the interband-transition region, the condition $R_a = R_b$ is reached at approximately 22,000 cm⁻¹, and for higher frequencies $R_a > R_b$. Similar results have been reported in the literature previously.^{4,26,31,75,175} A Kramers-Kronig analysis of this reflectance was performed by following high- and low-frequency extrapolations as mentioned in Chapter IV. The results of the loss function are displayed in Fig. 39. There is a splitting in the peak position of the *a*- and *b*-axis maxima of this function that is consistent with the splitting in the plasma edge minima observed in the reflectance along the two directions.

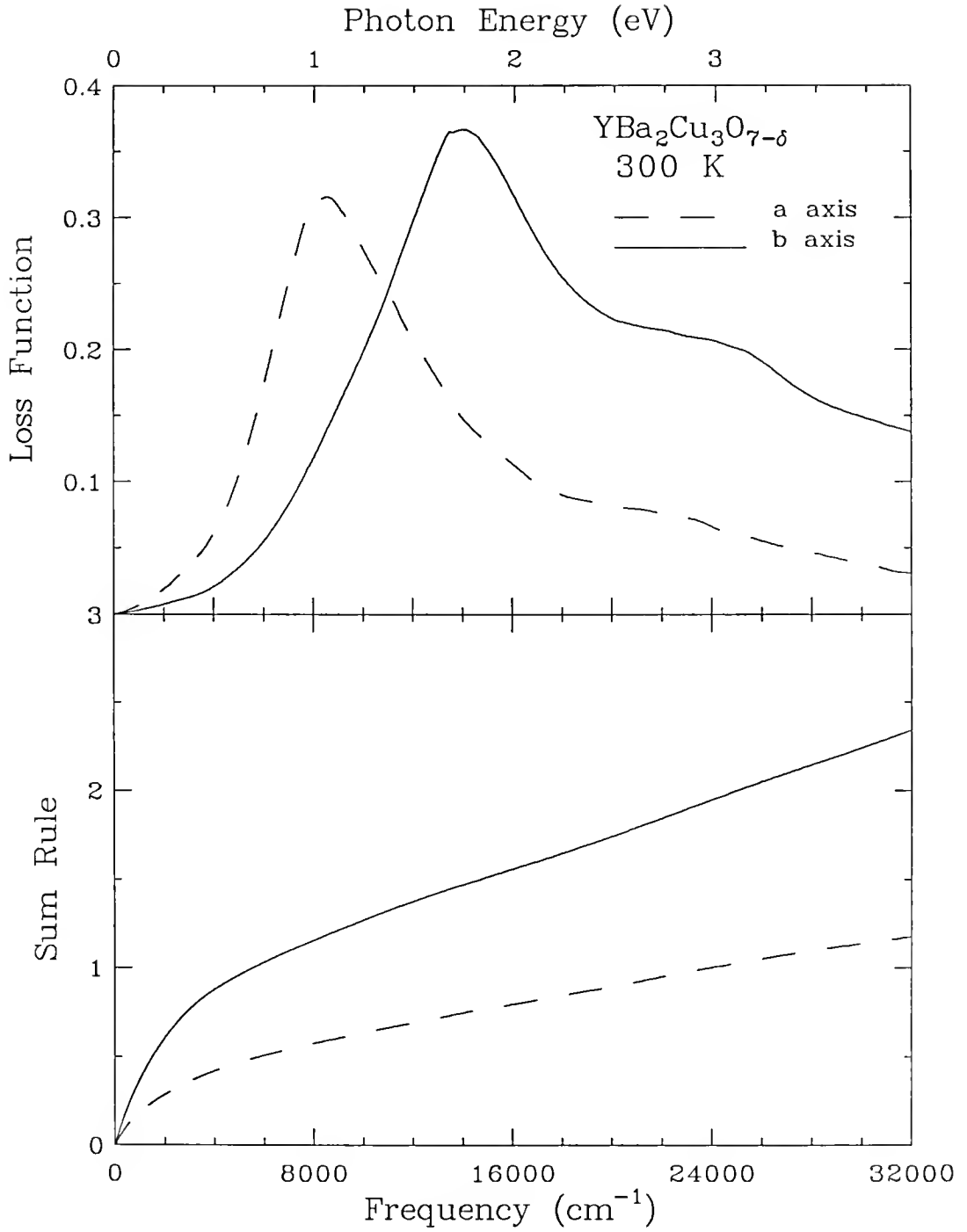


Fig. 39. Loss function (upper panel) and sum rule (lower panel) of YBa₂Cu₃O_{7-δ} for light polarized parallel and perpendicular to the chain axis in single-domain YBa₂Cu₃O_{7-δ} at 300 K.

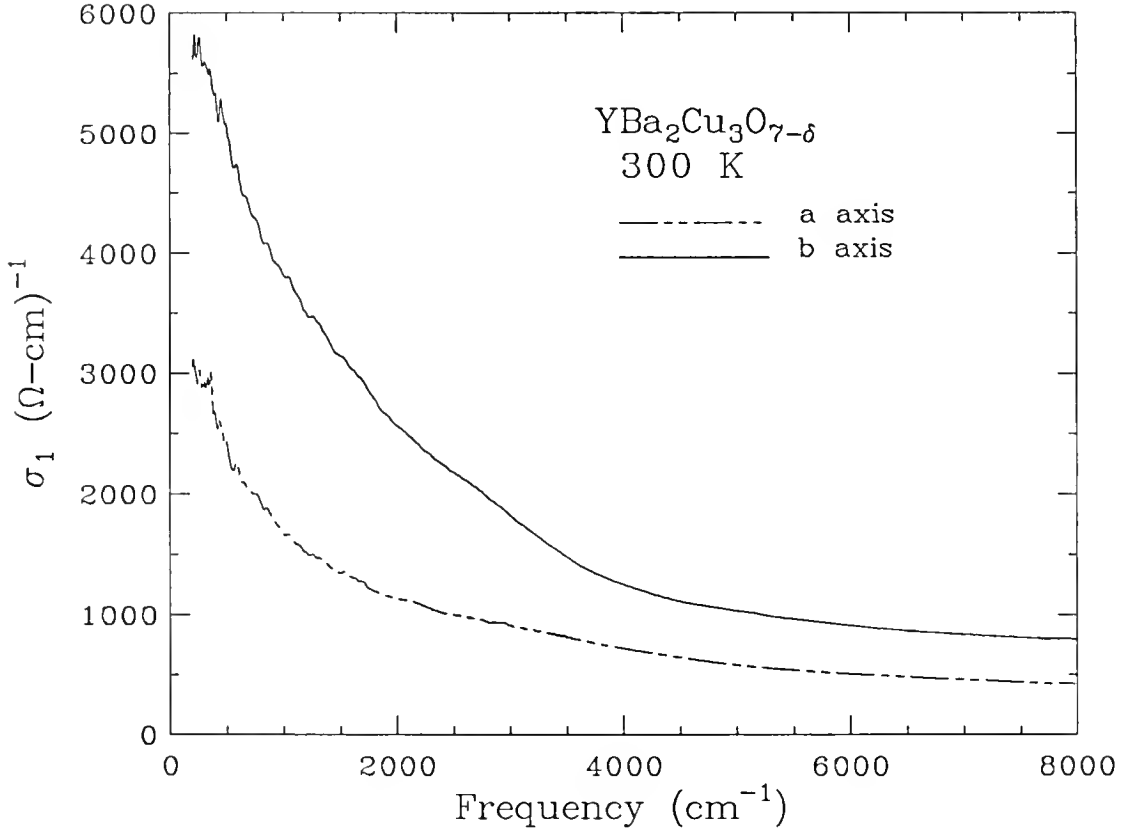


Fig. 40. Optical conductivity, σ_a and σ_b , along principal axes of single-domain YBa₂Cu₃O_{7-δ}.

We now turn our attention to the optical conductivity shown in Fig. 40. The results indicate a ratio in the far-infrared conductivity of roughly of 2:1, with the higher value corresponding to the b axis. This is in good agreement with the reported anisotropy in the dc conductivity obtained in similarly prepared samples.¹⁶ It is also observed that there is a bump-like structure in the b -axis conductivity at $\sim 3200 \text{ cm}^{-1}$ that is most likely associated with localized transitions occurring in the CuO chains. This is concluded from the absence of such structure along the a -axis polarization. Aside from this structure, a closer look to these data reveals, as observed previously,^{4,31,75} it is not possible to fit either of those curves over the whole infrared region using a single Drude term with a fixed scattering rate. The

conductivity in the far infrared falls off much more slowly than the typical ω^{-2} dependence expected from a metallic Drude term. The actual slope is $\omega^{-.53 \pm 0.02}$. As it will be shown in Chapter VII, this exponent is the same in results obtained from $\text{Bi}_2\text{Sr}_2\text{CaCu}_2\text{O}_8$ samples. This suggests the presence of an additional mechanism for absorption in the midinfrared. As already discussed in Chapter III, of the two models that have proposed to explain this anomalous behavior the one-component or marginal Fermi liquid model predicts a frequency dependence of $\sigma_1(\omega)$ in the order $\sigma_1(\omega) \propto \omega^{-1}$.^{106,107} In the two-component model, on the other hand, the conductivity in these materials viewed as composed of a two-component absorption involving a Drude or free-carrier part combined with other midinfrared modes in addition to higher-frequency interband transitions.^{24,28,68,103}

Temperature Dependent Reflectance

Figure 42 displays the reflectance at 100 K (upper panel) and 30 K (lower panel). At 100 K, we find an increased reflectivity for both polarizations in the far infrared with respect to the room temperature. This correlates with a higher conductivity with respect to the room temperature data. At this temperature, the anisotropy in the far-infrared absorptivity ($1 - R$) is again in the order of 2:1 with the higher value corresponding to the b axis. In the superconducting state, which is shown in the lower panel of Fig. 42, we observe a dramatic change in the reflectance. At lower frequencies, the reflectance is now higher along the a axis, reaching a value close to 100% below 450 cm^{-1} . By contrast, the b -axis reflectance is lower with respect to the a axis by about 1–2%. Since both spectra were recorded in a single cool down, by just rotating the polarizer between the two polarizations, there is a high accuracy (typically better than $\pm 0.25\%$) in determining the anisotropy in the reflectance. On the other hand, uncertainties in the absolute reflectance in the order of 1–2% makes it hard to determine with high accuracy how close to 100% the a -axis reflectance

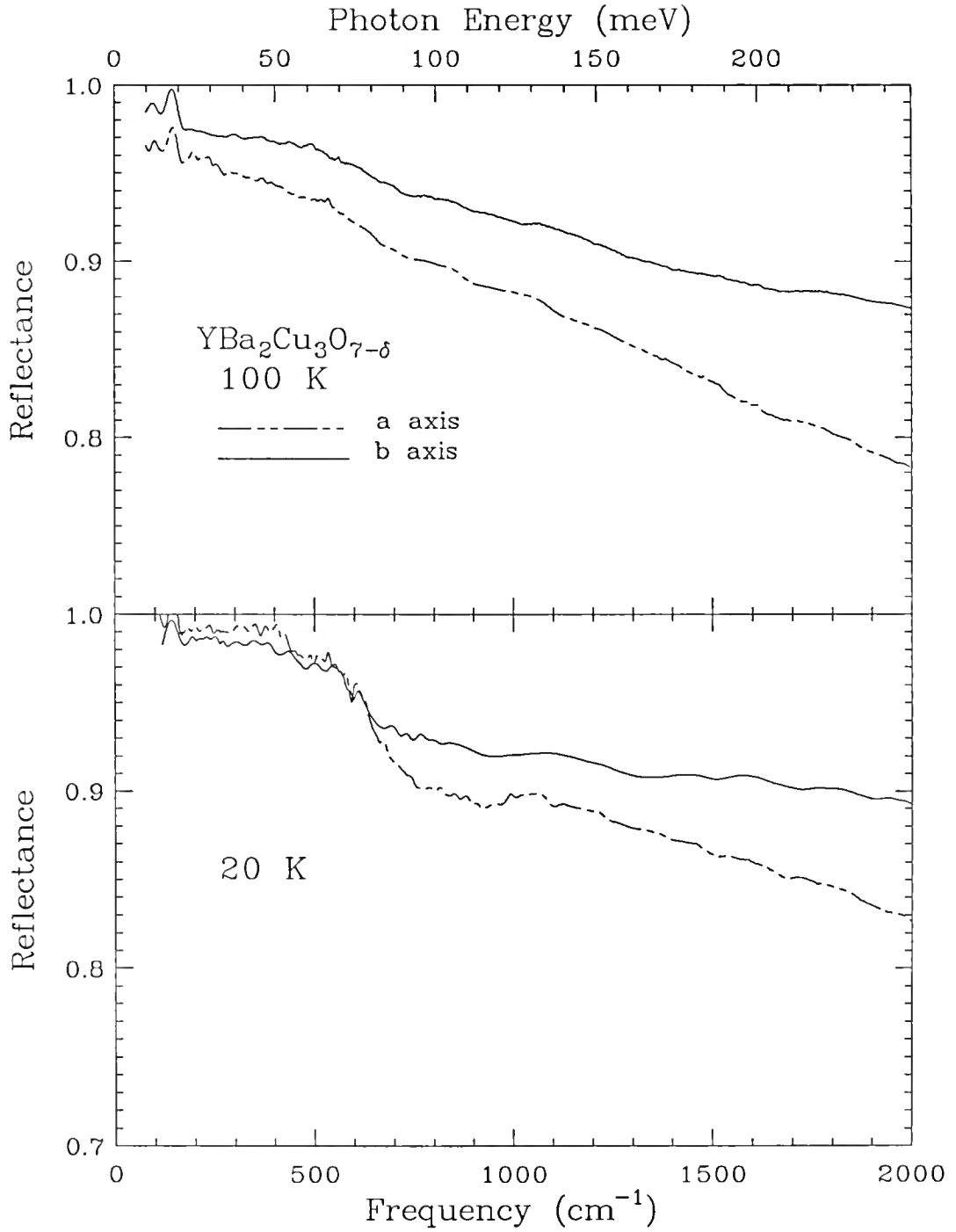


Fig. 41. Temperature dependence in the reflectance 100 K (upper panel) and 30 K (lower panel) along the a and b axes.

really is. Experiments that can achieve a higher accuracy, such as direct absorption measurements, have been performed by Pham *et al.*³⁰ on single-domain crystals of this material. In this study, it is found the a -axis absorptivity is around 0.5% in the region below 400 cm^{-1} . The optical conductivity, obtained from a Kramers-Kronig analysis of the reflectance at the three measured temperatures, is shown in Fig. 43 and Fig. 44 for the a and b axes respectively.

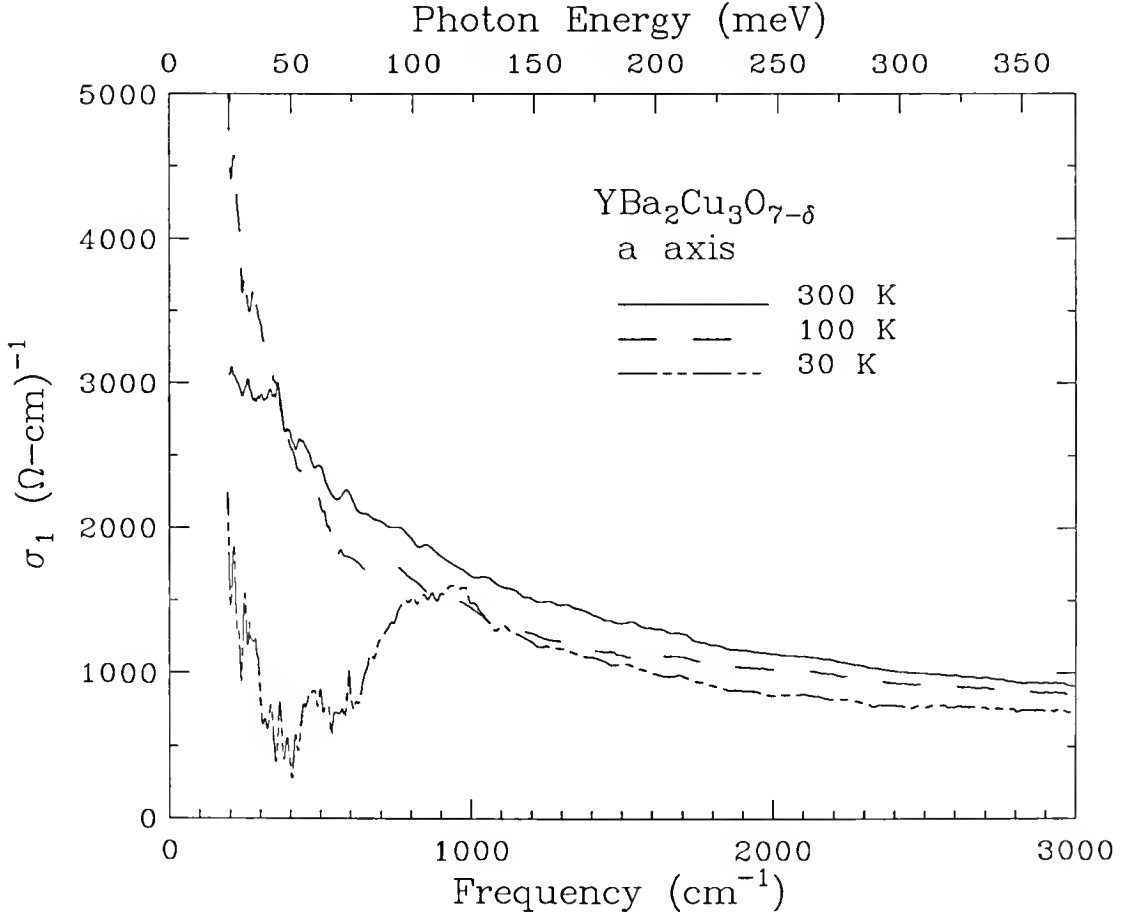


Fig. 43. Temperature dependence in the a -axis optical conductivity of single-domain $\text{YBa}_2\text{Cu}_3\text{O}_{7-\delta}$.

Qualitatively, both set of data look quite similar. In the normal state, it is evident the higher conductivity at lower temperatures accompanied by a sharper far-infrared

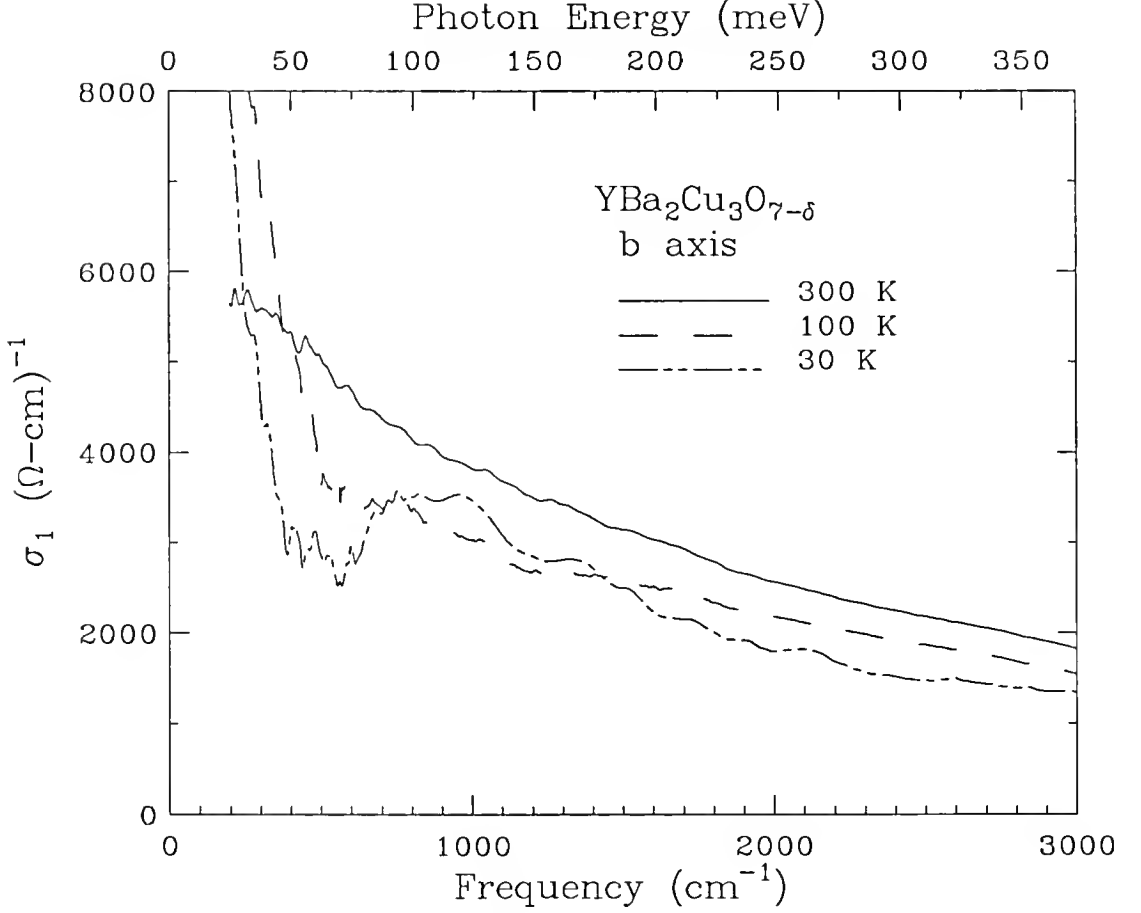


Fig. 44. Temperature dependence in the b -axis optical conductivity of single-domain YBa₂Cu₃O_{7- δ} .

peak in both crystallographic directions. At the same time, the conductivity in the midinfrared exhibits a weaker temperature dependence. This behavior in the optical conductivity of fully-doped sample is one of the key features that suggest a description of $\sigma_1(\omega)$ in terms of two components.

Below the transition temperature, there is a minimum-like structure present in both $\sigma_1(\omega)_a$ and $\sigma_1(\omega)_b$ that starts at around 500 cm⁻¹. At lower frequencies, this minimum is then followed by an upturn that signals the presence of low-lying excitations. This upturn in $\sigma_1(\omega)$ is consistent with results of direct-absorption measurements performed by Pham *et al.*³⁰

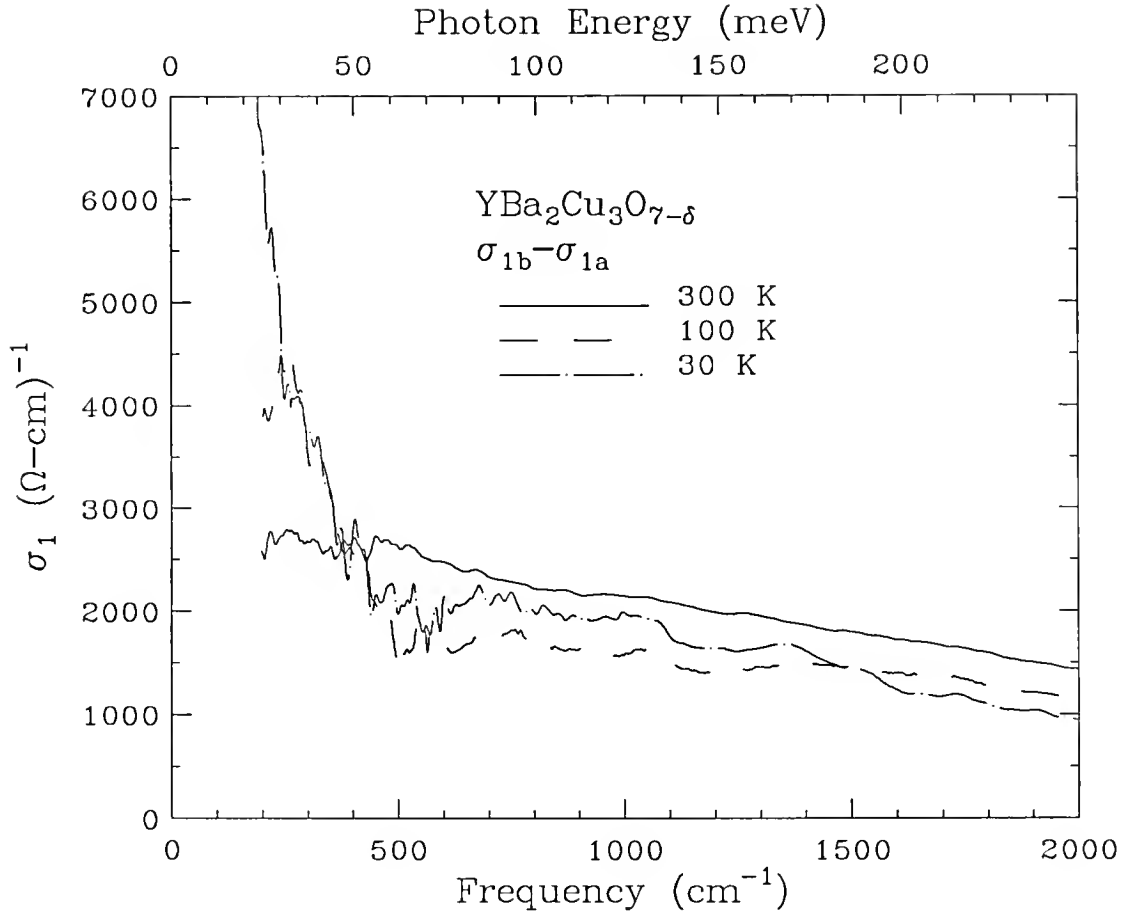


Fig. 45. Temperature dependence in the “chain” conductivity obtained from the formula $\sigma_1(\omega)_{chain} = \sigma_1(\omega)_b - \sigma_1(\omega)_a$.

Effect of the Chains

As mentioned earlier, there have been several studies of the *ab*-plane anisotropy of single-domain crystals of $\text{YBa}_2\text{Cu}_3\text{O}_{7-\delta}$.^{4,26,31,75,175} The conventional approach in this system has been to assume that the the *b*-axis conductivity involves two channels. One channel, which is assumed to be isotropic, involves the conduction of charge carriers in the CuO_2 planes. The second channel is the contribution of dipole allowed transitions in the CuO chains. Based on these assumptions, the chain conductivity is considered to be additive to the conductivity of the CuO_2 planes. The formula used to separate the two channels involves the subtraction of $\sigma_1(\omega)$ along the *a* axis from

the b -axis conductivity

$$\sigma_1(\omega)_{chain} = \sigma_1(\omega)_b - \sigma_1(\omega)_a. \quad (42)$$

Notice that the orthorhombic distortion that exists in the CuO_2 plane of these materials is considered unimportant. This, as we will see from measurements on single-domain crystals of $\text{Bi}_2\text{Sr}_2\text{CaCu}_2\text{O}_8$ in Chapter VII, might not be completely accurate. Measurements of the chain conductivity using Eq. 42 have resulted in that, depending on the level of ordering in the chains, the chain contribution to the b -axis conductivity may vary. This happens at the same time the a axis or plane conductivity does not show much variation. For disordered crystals, there is evidence the transitions on the chains are localized. The frequency-dependent conductivity along the chains in materials with highly disordered chains has been interpreted as a hopping conductivity. In this interpretation, the hopping of carriers along the 1-dimensional chains is interrupted by oxygen vacancies.¹⁷⁵

To illustrate the degree of ordering in the single-domain of $\text{YBa}_2\text{Cu}_3\text{O}_{7-\delta}$ that we studied, we show in Fig. 45 the results of calculating the chain conductivity by using Eq. 42 at three temperatures. Contrary to what has been observed in disordered crystals, the results here suggest the chain conductivity in our samples appears to have both a Drude and midinfrared components. This is more evident at lower temperatures, where the conductivity in the far infrared appears to have a narrow Drude contribution in addition to a much broader contribution at higher frequencies. At room temperature, $\sigma_1(\omega)_{chain}$ resembles the response of a strongly overdamped Drude conductivity. At lower temperatures, the far-infrared peak can be fitted with a Drude oscillator with $\omega_{pD} \sim 12,000 \text{ cm}^{-1}$ and $\Gamma \sim 250 \text{ cm}^{-1}$. This is contrast to what should be expected in a hopping conductivity model, where a maximum in $\sigma_1(\omega)$ should only appear at a finite frequency.¹⁷⁵

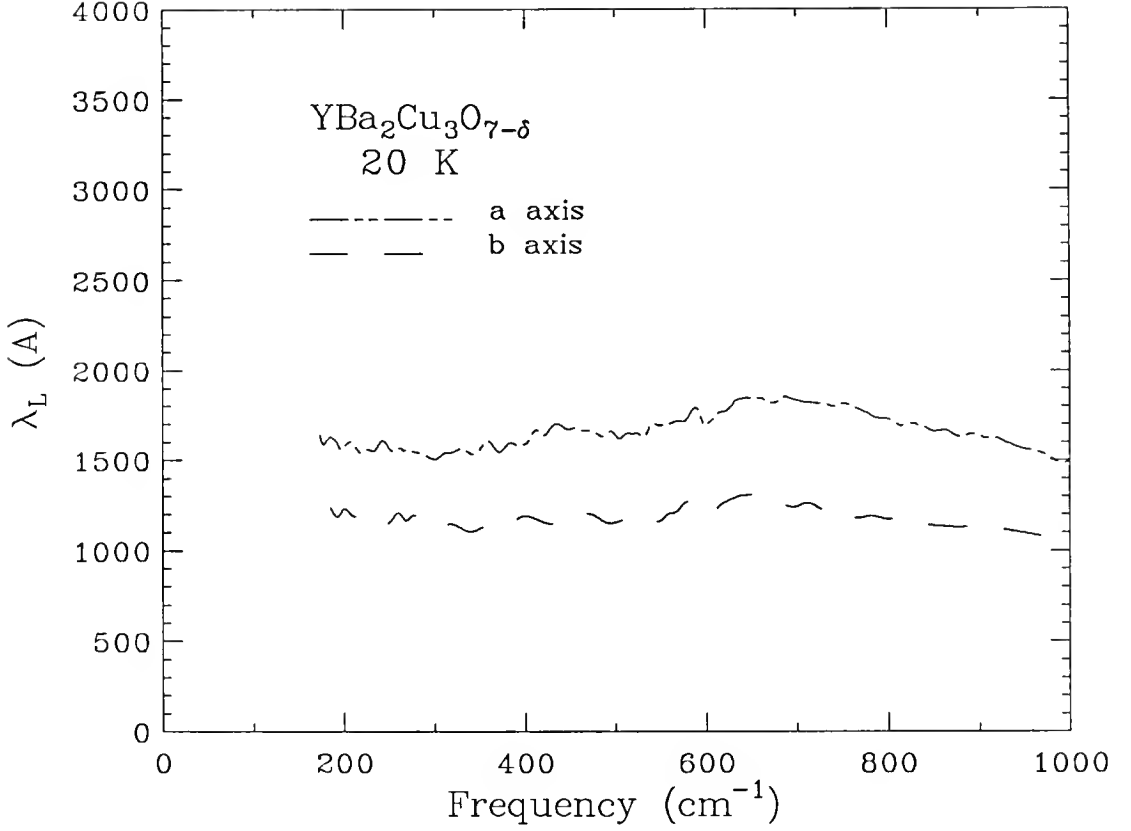


Fig. 46. Plot of the London penetration length as a function of frequency along the a and b axes of YBa₂Cu₃O_{7-δ}.

ab -Plane Anisotropy in the London Penetration Depth

The temperature dependence in the a - and b -axis conductivities shown in Fig. 43 and Fig. 44 shows that some spectral weight in $\sigma_1(\omega)$ is missing in the superconducting state. This is the spectral weight that, in the clean limit picture, goes to a δ -function at zero frequency. The response of this “missing” area under $\sigma_1(\omega)$ is what determines the London penetration length λ_L , which is the distance over which an electromagnetic wave is attenuated inside a superconductor. Since this length is a measure of the superfluid response in a superconductor, it is related to the superfluid oscillator strength ω_{ps} by the formula $\lambda_L = 1/2\pi\omega_{ps}$. Polarized spectroscopy techniques allows the determination of the different components of λ_L , since in anisotropic

materials, λ_L is a tensor quantity. Since the response of a superconductor to an electromagnetic field in a reflectance experiment is governed by the imaginary part of the optical conductivity (σ_2), λ_L can be determined using the formula

$$\left(\frac{1}{\lambda_L}\right)^2 = \frac{4\pi}{c^2}\omega\sigma_2(\omega). \quad (43)$$

An alternative method to determine λ_L is by way of integrating the missing area under the real part of the optical conductivity, which is just the difference in $\sigma_1(\omega)$ just above and below the superconducting state. This integrated area is then proportional to the superfluid-carrier response or ω_{ps} . Figure 46 displays λ_L along the a and b axes obtained from Eq. 43. The results suggest λ_L approaches a constant value in the far infrared, where the zero-frequency extrapolated values along the a and b axes are $\gamma_a = 1600 \text{ \AA}$ and $\gamma_b = 1200 \text{ \AA}$. These results suggest a much reduced value for λ_L along the chain direction. This implies there is a superconducting response associated with the CuO chains. These results are in sharp contrast to earlier reporters, where the chains have been found to have a contribution to the Drude conductivity of the planes, while remaining normal in the superconducting state.³¹ A qualitative explanation for this can be given by noticing that the anisotropy between the a and b axes conductivity in the samples of those earlier reports is not as high as in the present sample. In this argument, the degree of order in the chains determines if they also have a superconducting response.

CHAPTER VII

ANISOTROPY IN THE AB-PLANE

OPTICAL PROPERTIES OF $\text{Bi}_2\text{Sr}_2\text{CaCu}_2\text{O}_8$

Results regarding *ab*-plane anisotropy in the optical properties of $\text{YBa}_2\text{Cu}_3\text{O}_{7-\delta}$ were presented in Chapter VI. As it was mentioned there, the conventional approach in this system has been to divide the response into chain and plane components and to assume that the plane response is identical along the *a* and *b* axes. This chapter is devoted to results of the *ab*-plane anisotropy in the optical properties of single-domain crystals of $\text{Bi}_2\text{Sr}_2\text{CaCu}_2\text{O}_8$. Unlike $\text{YBa}_2\text{Cu}_3\text{O}_{7-\delta}$, this system does not have the complication of the CuO chains in the *b* direction, making it easier to address issues of the anisotropy in the quasi-two dimensional CuO_2 planes. One of such issues is the anisotropy of the 2-dimensional electronic structure in the normal state. A second issue is the possible anisotropy of the order parameter in the superconducting state.

The CuO_2 planes in $\text{Bi}_2\text{Sr}_2\text{CaCu}_2\text{O}_8$ are separated by Bi_2O_2 double layers, which are believed to act as a charge reservoir. As in most high- T_c superconductors, there is an orthorhombic distortion in the *ab* plane on account of a weak superlattice modulation along the *b* axis, which is attributed to an incommensurate defect structure in the Bi_2O_2 layers.^{13,45,48} Moreover, the *a* and *b* axes in this material are along the Bi–O bonds and nearly 45° from the Cu–O bonds. Based on the very small difference in the *a* and *b* bond lengths (≈ 0.04 Å), one would expect an almost isotropic optical conductivity in the *ab* plane of this compound.

In this system, like in $\text{YBa}_2\text{Cu}_3\text{O}_{7-\delta}$, the reflectance was measured for light polarized along the two principal axes in the *ab* plane in a frequency range of 100–32,000 cm^{-1} . The reflectance in the far-infrared and midinfrared regions was measured for

temperatures above and below the superconducting transition temperature. The optical conductivity and related optical constants were obtained from a Kramers-Kronig analysis of the measured reflectance at each temperature. Analysis of the optical conductivity was carried out using the one- and two-component models. A discussion of the anisotropy in the superconducting state will be given in the context of these two models. A study of dc transport measurements performed on similar single-domain crystals is reported in Chapter VIII.

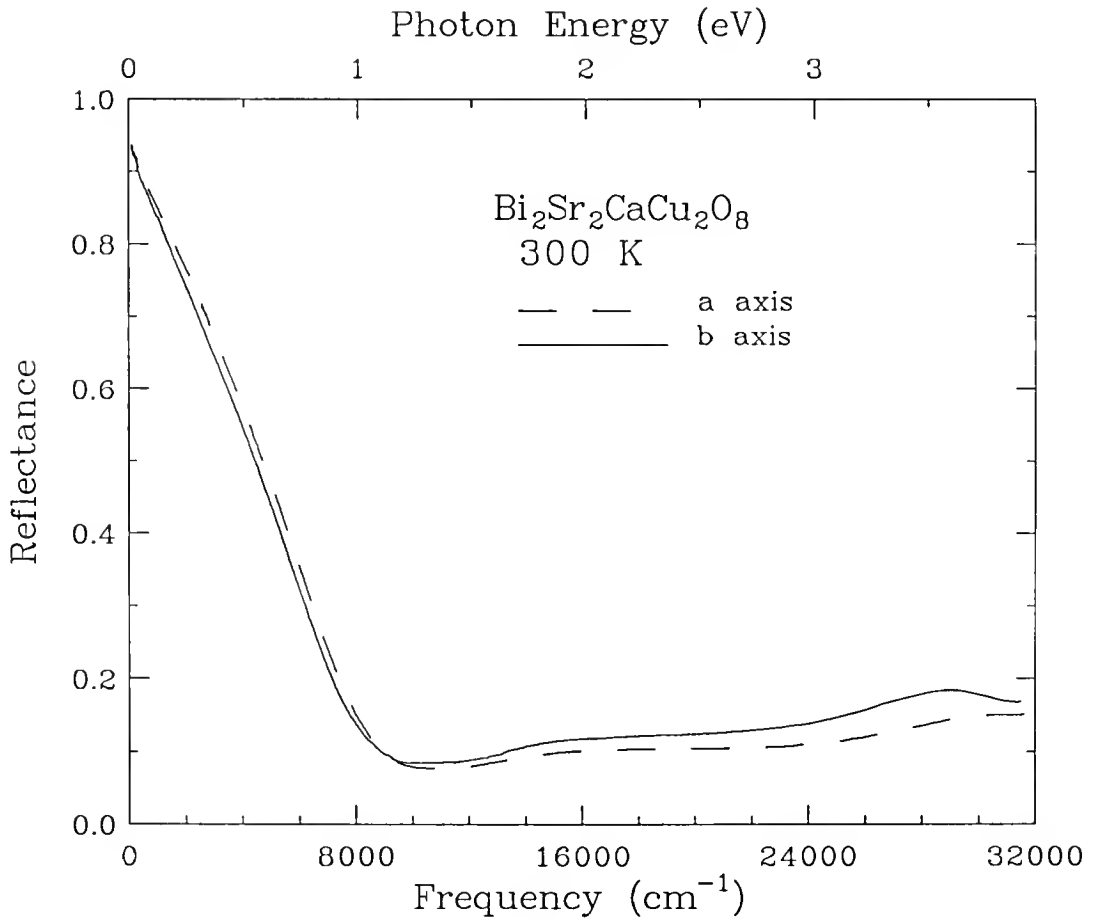


Fig. 47. The 300 K reflectance of $\text{Bi}_2\text{Sr}_2\text{CaCu}_2\text{O}_8$ for light polarized along the a and b axes.

Results of the Optical Reflectance

Room Temperature Spectra

Figure 47 displays the room temperature reflectance of $\text{Bi}_2\text{Sr}_2\text{CaCu}_2\text{O}_8$ on a wide frequency scale for polarization of the light along the a and b axes. First, we notice that at low frequencies the reflectance along the a axis is higher than the reflectance along the b axis by 1–2%. As the frequency increases, the reflectance falls off in a quasilinear fashion with increasing frequency in both polarizations. Near the plasmon minimum, we observe that the plasma edge for the polarization parallel to the b axis occurs at a slightly lower frequency compared to the a axis. The splitting is estimated to be around 500 cm^{-1} . These results indicate the in-plane anisotropy of $\text{Bi}_2\text{Sr}_2\text{CaCu}_2\text{O}_8$ is less pronounced when compared to similar measurements on $\text{YBa}_2\text{Cu}_3\text{O}_{7-\delta}$. In $\text{YBa}_2\text{Cu}_3\text{O}_{7-\delta}$, the splitting in the a - and b -axis plasma edge minima has been estimated to be 5500 cm^{-1} . The larger plasma edge along the b direction in this system has been explained^{31,74,75,176} as due to the presence of CuO chains along the b axis, while the orthorhombic distortion of the CuO_2 planes in this compound has been assumed to be unimportant. The fact that we are able to observe anisotropy in $\text{Bi}_2\text{Sr}_2\text{CaCu}_2\text{O}_8$, which does not have chains, indicates the electronic excitations within the CuO_2 planes are themselves anisotropic. One possible explanation could be the different bond lengths in the two directions. This consideration will make it impossible to separate accurately the effect of the chains from the planes in $\text{YBa}_2\text{Cu}_3\text{O}_{7-\delta}$. Therefore the optical investigation of $\text{Bi}_2\text{Sr}_2\text{CaCu}_2\text{O}_8$ is of particular interest since in this compound the orthorhombic distortion of the metal-oxygen layers appears to be the only reason for the in-plane anisotropy in the optical properties.

We find the reflectance is substantially higher for $\mathbf{E} \parallel b$ and for frequencies above the plasmon minimum. In addition, two interband transitions are evident in this

region. The first interband peak is present in both directions, while the second one, centered around 3.8 eV, is more pronounced for the polarization along b and is almost absent along the a direction. The first peak centered at 2.3 eV is interpreted as the charge transfer CT band in the CuO_2 planes of this material, while the second one is most likely associated with interband transitions occurring in the Bi_2O_2 layers and not in the CuO_2 planes as previously reported.⁸² This result is in agreement with ellipsometric measurements done by Kelly *et al.*⁸⁵

Temperature Dependent Spectra

The temperature dependence in the reflectance in the far-infrared and midinfrared regions is shown in Fig. 48 for the a and b axes. There are two things that should be noticed in these results. First of all, there is an increase in the far-infrared reflectance as the temperature of the sample is lowered, developing a shoulder-like feature in both directions as the sample enters in the superconducting state. Secondly, the reflectance is higher for $\mathbf{E} \parallel a$ at all frequencies and temperatures. Even when the sample is superconducting, there remains a difference in the reflectance ($R_a > R_b$) in the order of 1–2% (see Fig. 49).

Earlier, it was found that the transmittance of free-standing single crystals of $\text{Bi}_2\text{Sr}_2\text{CaCu}_2\text{O}_8$ is higher for light polarized along the a axis, implying more absorption for the b -axis polarization.⁸⁶ The reflectance data in Fig. 48 agree with these published results. Although the accuracy in absolute reflectance is only $\pm 1\%$, so that we cannot determine whether the a -axis reflectance is indeed unity below 200 cm^{-1} , our accuracy in anisotropy determination is $\pm 0.25\%$. Therefore, we can say with certainty that the b -axis reflectance is *less* than 100% down to $\sim 150 \text{ cm}^{-1}$ ($\sim 20 \text{ meV}$). We also observe two edges in the far infrared reflectance in both polarizations in the superconducting state. The first edge, at a frequency between 100 and 200 cm^{-1} , is followed by a stronger threshold at $\omega = 400 - 450 \text{ cm}^{-1}$. More discussion

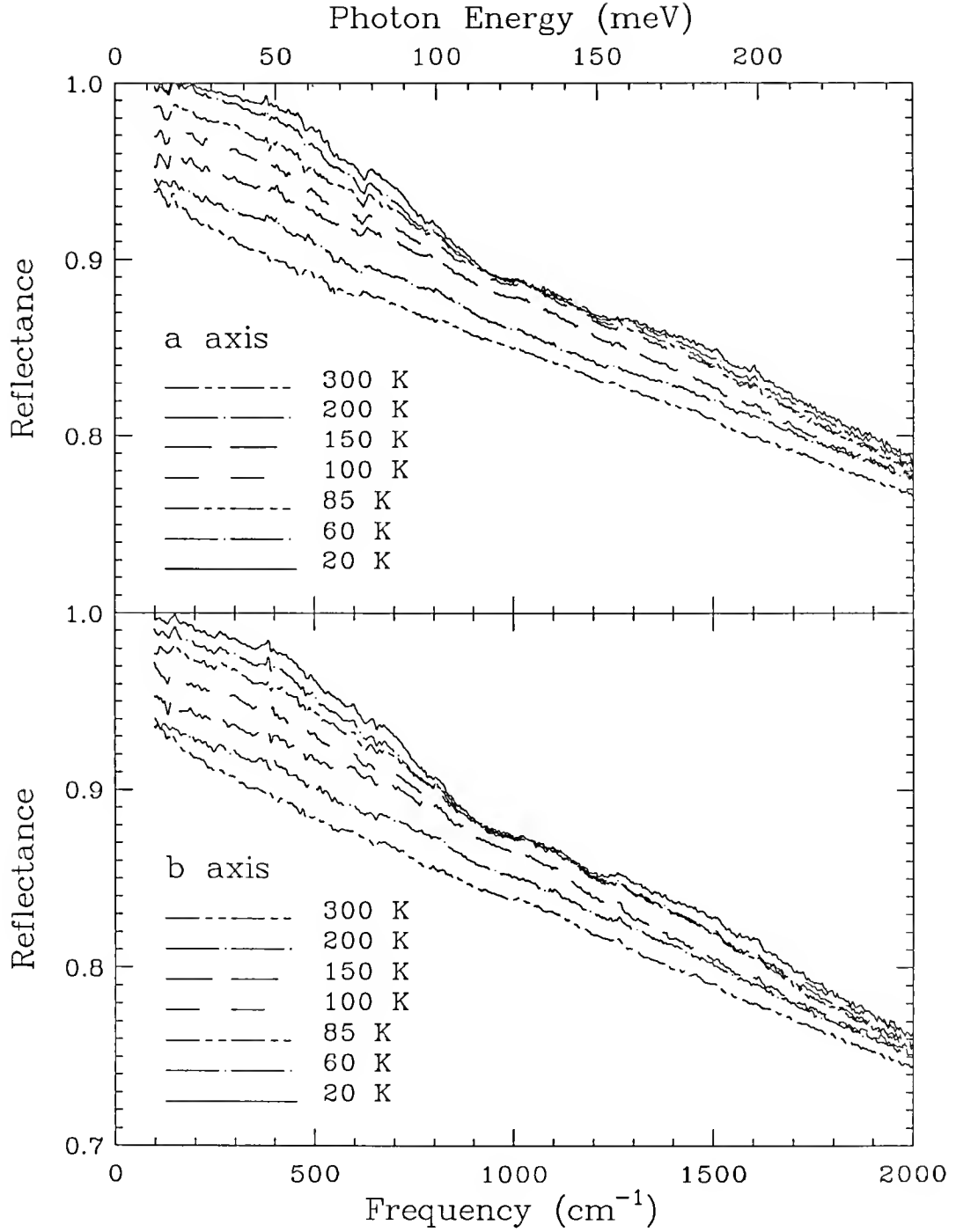


Fig. 48. Temperature dependence of the a - and b -axis reflectance of $\text{Bi}_2\text{Sr}_2\text{CaCu}_2\text{O}_8$.

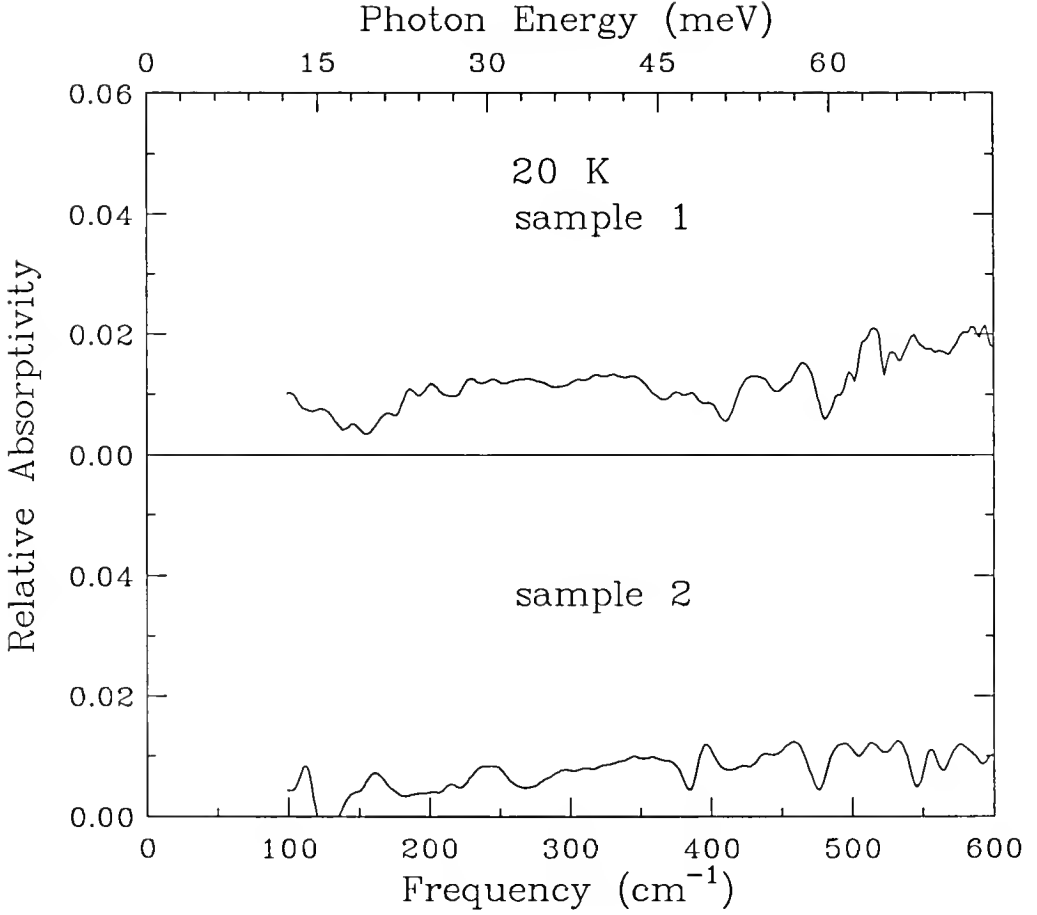


Fig. 49. Relative absorptivity ($R_a - R_b = A_b - A_a$) for two different samples in the superconducting state.

related to the interpretation of these structures will be given when discussing the optical conductivity obtained from the Kramers-Kronig analysis.

Discussion of Optical Constants

For a quantitative discussion let us now turn our attention to the optical constants derived from the Kramers Kronig transformations of the reflectance data. Extrapolation procedures were done as discussed in Chapter IV. The results for the 300 K optical conductivity $\sigma_1(\omega)$ are shown in Fig. 50. All the electronic bands that were seen in the reflectance are more evident here. First, there is a weak anisotropy in the

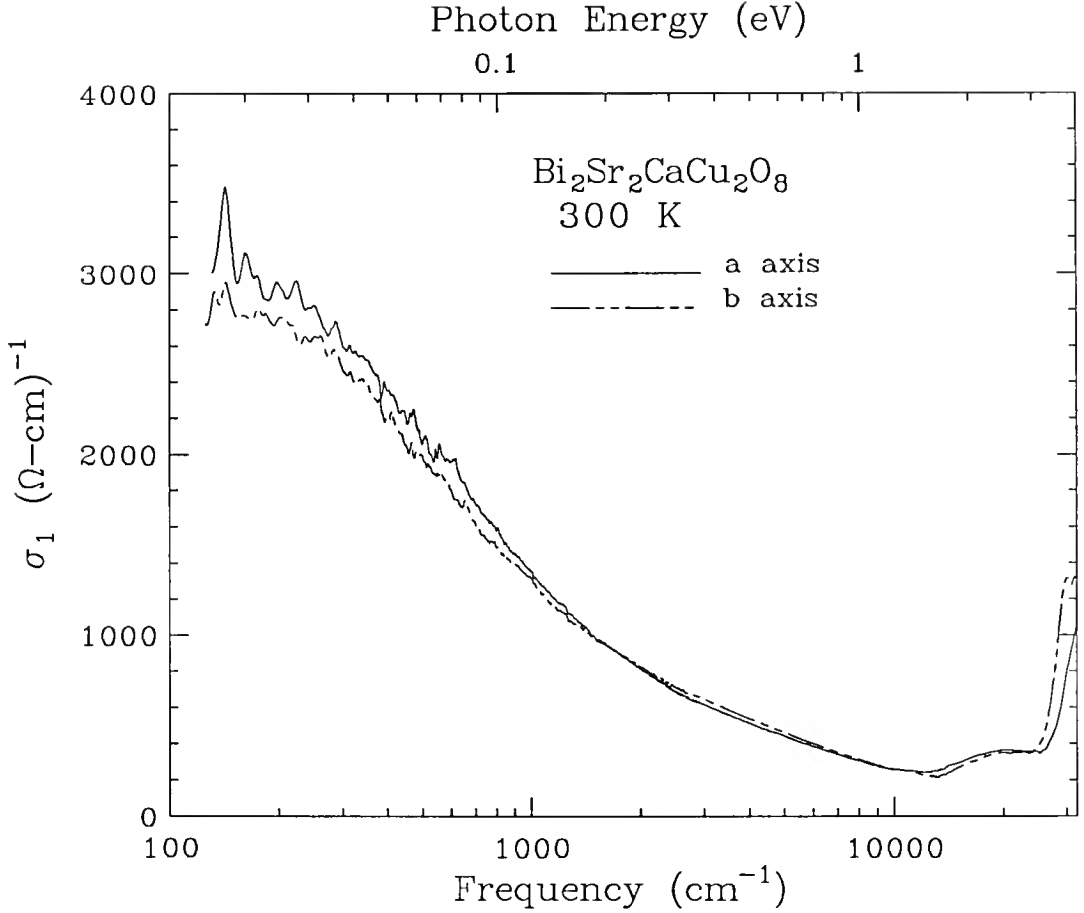


Fig. 50. Room temperature conductivity on a wide frequency scale along the principal axes in the ab plane of $\text{Bi}_2\text{Sr}_2\text{CaCu}_2\text{O}_8$.

far-infrared conductivity ($\sigma_a > \sigma_b$) that is in agreement with the dc value reported in Chapter VIII. Second, the low-frequency $\sigma_1(\omega)$ falls off much more slowly than the ω^{-2} dependence of a simple Drude spectrum.²³ For these samples the slope of $\sigma_1(\omega)$ between 400–8000 cm^{-1} region is $\omega^{-0.56 \pm 0.02}$. This is nearly the same slope that was estimated from the a -axis room temperature conductivity of $\text{YBa}_2\text{Cu}_3\text{O}_{7-\delta}$ ($\omega^{-0.53 \pm 0.02}$). Interpretation of this non-Drude behavior in the optical conductivity of the copper-oxide superconductors has been one of the most debated issues related to the optical properties of these materials.

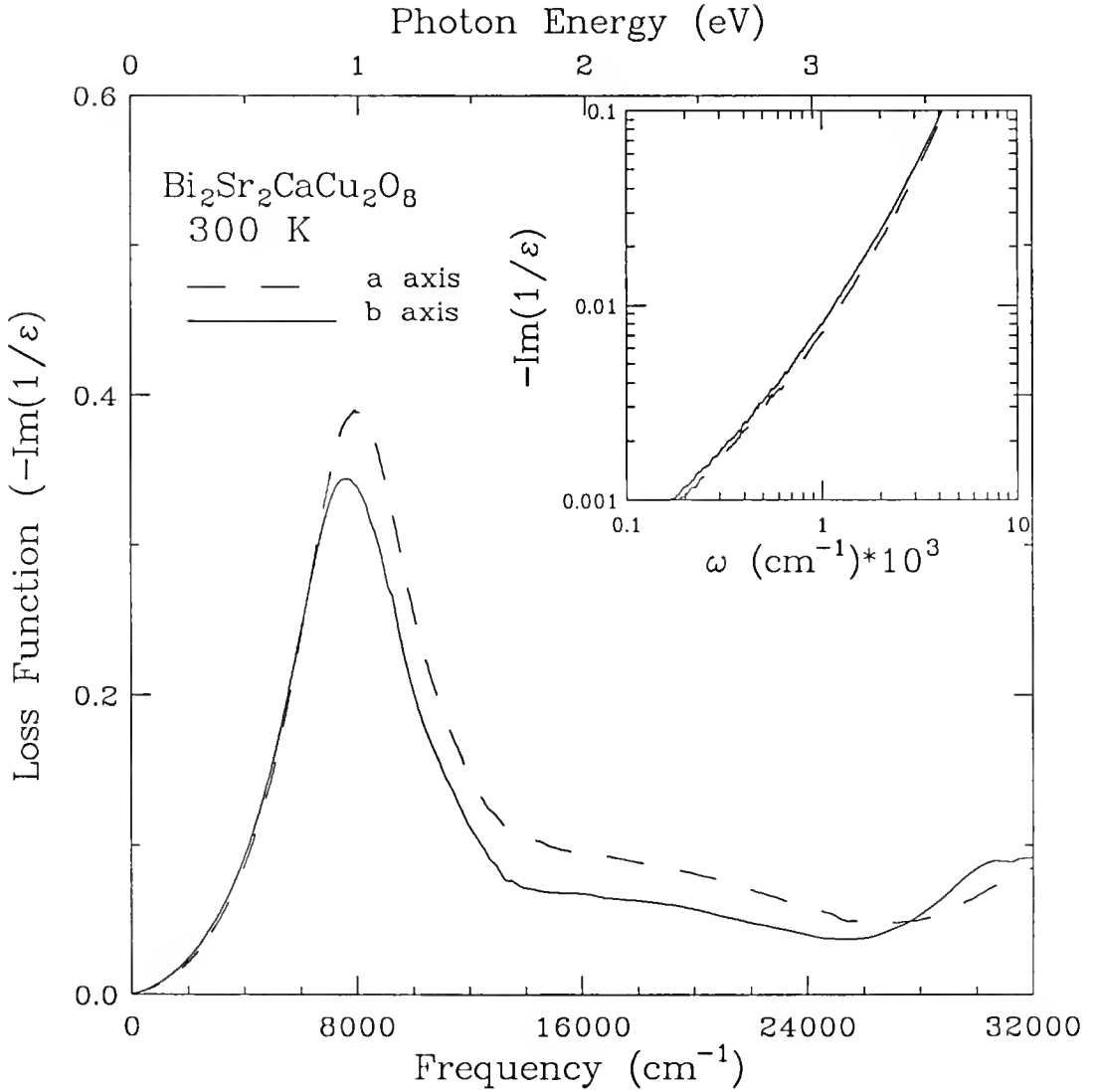


Fig. 51. Room temperature loss function ($-\text{Im}(1/\epsilon)$) on a wide frequency scale along the principal axes in the ab plane of $\text{Bi}_2\text{Sr}_2\text{CaCu}_2\text{O}_8$. Inset: Logarithmic scale to show power law dependence at low frequencies.

Next, Fig. 51 displays the energy loss function or $\text{Im}(-1/\epsilon)$. There is a slight splitting in the position of the loss function maxima for the two polarizations. In simple metals, the position of this peak together with its width give information about the “screened” plasma frequency as well as the scattering rate of the free carriers respectively. But, because of the unusual behavior of the conductivity in the

midinfrared, it is difficult to make the same assignment here unless some assumptions are made about this extra absorption. If a frequency dependent $1/\tau^*$ is introduced in a generalized Drude model,¹⁰⁵ the broad $1/\tau^*$ is the result of an increase in the relaxation rate of the carriers as the frequency of the light is increased. On the other hand, if two or more type of carriers contribute to $\sigma_1(\omega)$ the broadening in the scattering rate would be the combination of the free carriers with other type of bound-carrier excitations in the midinfrared.

It has been suggested by Bozovic⁸¹ that there is an universal frequency dependence in the loss function of all the copper-oxide superconductors, where $-\text{Im}1/\epsilon \propto \omega^2$ for small ω . The results shown in the inset of Fig. 51 actually show there are two regimes to consider in the $\text{Bi}_2\text{Sr}_2\text{CaCu}_2\text{O}_8$ samples we measured. In one, for frequencies below 1000 cm^{-1} , the power law dependence in $-\text{Im}1/\epsilon$ is more like $\omega^{0.99 \pm 0.02}$. Only for $\omega > 1000 \text{ cm}^{-1}$, the exponent in ω becomes in the order of 2. Similar observations were made by Gao *et al.*⁷² from measurements on a $\text{La}_{2-x}\text{Sr}_x\text{CuO}_4$ film.

In the upper panel of Fig. 52, we show the sum rule that is given by the formula

$$N_{eff}(\omega)m/m_b = \frac{2mV_{cell}}{\pi e^2} \int_0^\omega \sigma(\omega') d\omega' \quad (44)$$

where e and m are the free-electron charge and mass respectively. The band mass is given by m_b and V_{cell} is the volume of one unit cell. This formula gives the effective number of carriers per formula unit participating in the optical transitions below frequency ω . The results indicate that while N_{eff} is roughly isotropic at low frequencies, some differences start to show up at higher energies, particularly in the interband region where transitions in the Bi_2O_2 layers are occurring. At a frequency of 8000 cm^{-1} , we find N_{eff} to be ≈ 0.5 . This result agrees with having approximately 0.25 carriers per CuO_2 plane if we assume $m_b = m$.

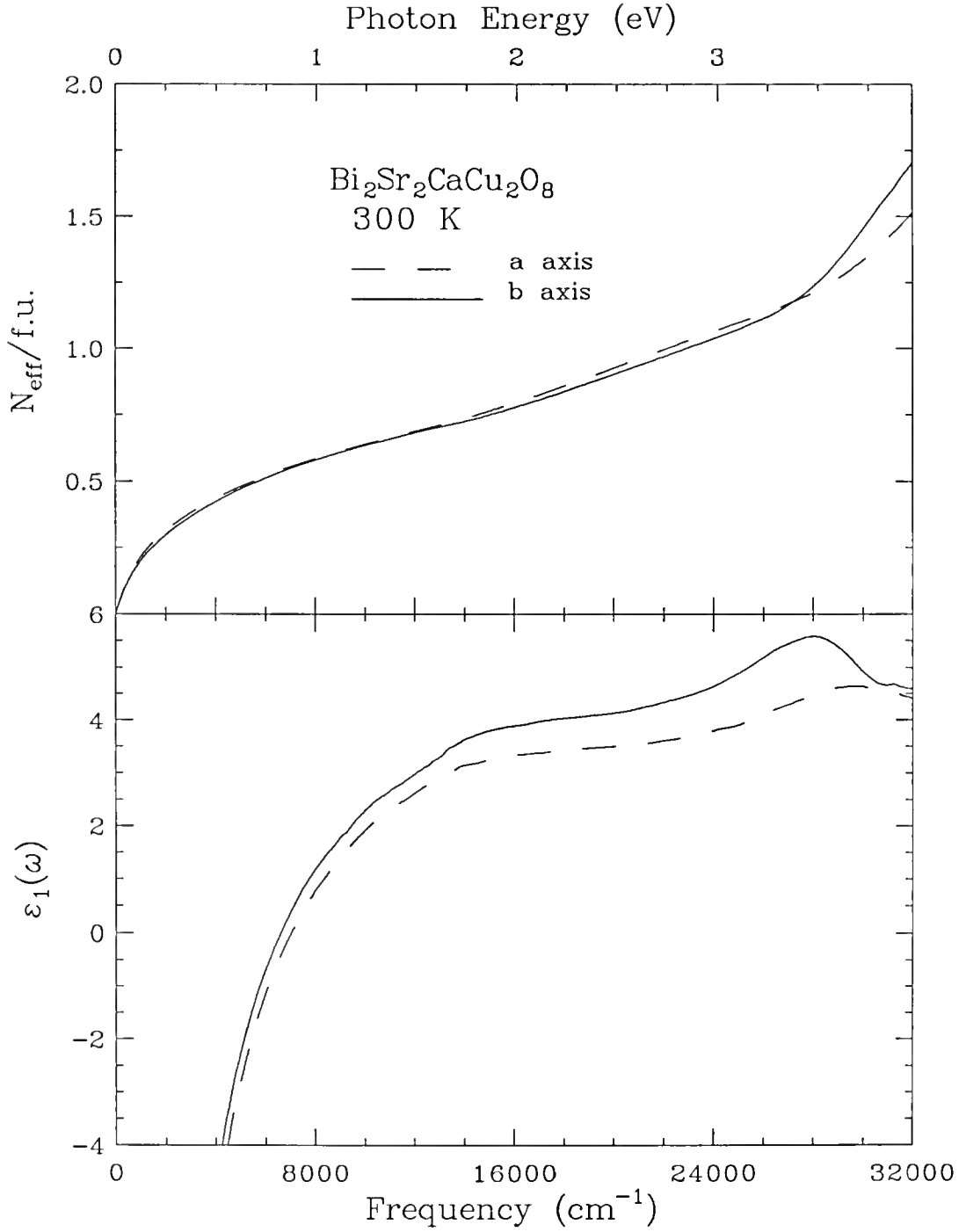


Fig. 52. Sum rule (upper panel) and real part of dielectric function (lower panel) showing anisotropy in these quantities in the ab plane of $\text{Bi}_2\text{Sr}_2\text{CaCu}_2\text{O}_8$.

The real part of the dielectric function $\epsilon_1(\omega)$ is shown in the lower panel of Fig. 52. The zero crossing of $\epsilon_1(\omega)$, which also is related to the screened plasma frequency $\widetilde{\omega}_p = \omega_p/\sqrt{\epsilon_\infty}$, evidently occurs at a lower energy for $\mathbf{E} \parallel b$ when compared to $\mathbf{E} \parallel a$. This difference could be due to either having more oscillator strength for the bare plasma frequency ω_p for the free carriers along the a direction or the background dielectric constant ϵ_∞ being larger for $\mathbf{E} \parallel b$. The more pronounced peak in the interband transition centered at $\omega = 3.8$ eV for $\mathbf{E} \parallel b$ suggests a larger ϵ_∞ for this direction, making the latter as the most likely possibility.

Temperature Dependent Optical Conductivity

The temperature evolution in the optical conductivity is shown in Fig. 53, and Fig. 54 for $\mathbf{E} \parallel a$ and $\mathbf{E} \parallel b$ respectively. In the normal state, we observe a narrowing in the far-infrared conductivity at low temperatures, whereas at higher frequency, $\sigma_1(\omega)$ does not show much variation. At the same time, we observe a minimum that develops in the superconducting state at around $\omega \approx 400 \text{ cm}^{-1}$. In some studies, this structure in the conductivity has been interpreted as evidence of the superconducting energy gap.³¹ The fact that we observe the feature for the polarization along b , which has lower reflectance puts this interpretation in contradiction with the conventional notion of a gap in which for frequencies below 2Δ no excitations are allowed. The lower reflectance in the b direction is also responsible for the upturn observed in $\sigma_1(\omega)$ at the lowest temperature. This result may have interesting consequences for the understanding of dynamic properties in these materials. For instance, it indicates the presence of low-lying excitations for carriers moving along the b axis. It is not clear what is the origin of these excitations. Perhaps, the presence of the superlattice structure in the b axis introduces a source for scattering along this crystallographic direction. If this is correct, it seems reasonable to expect evidence of this in other dynamic properties of the material.

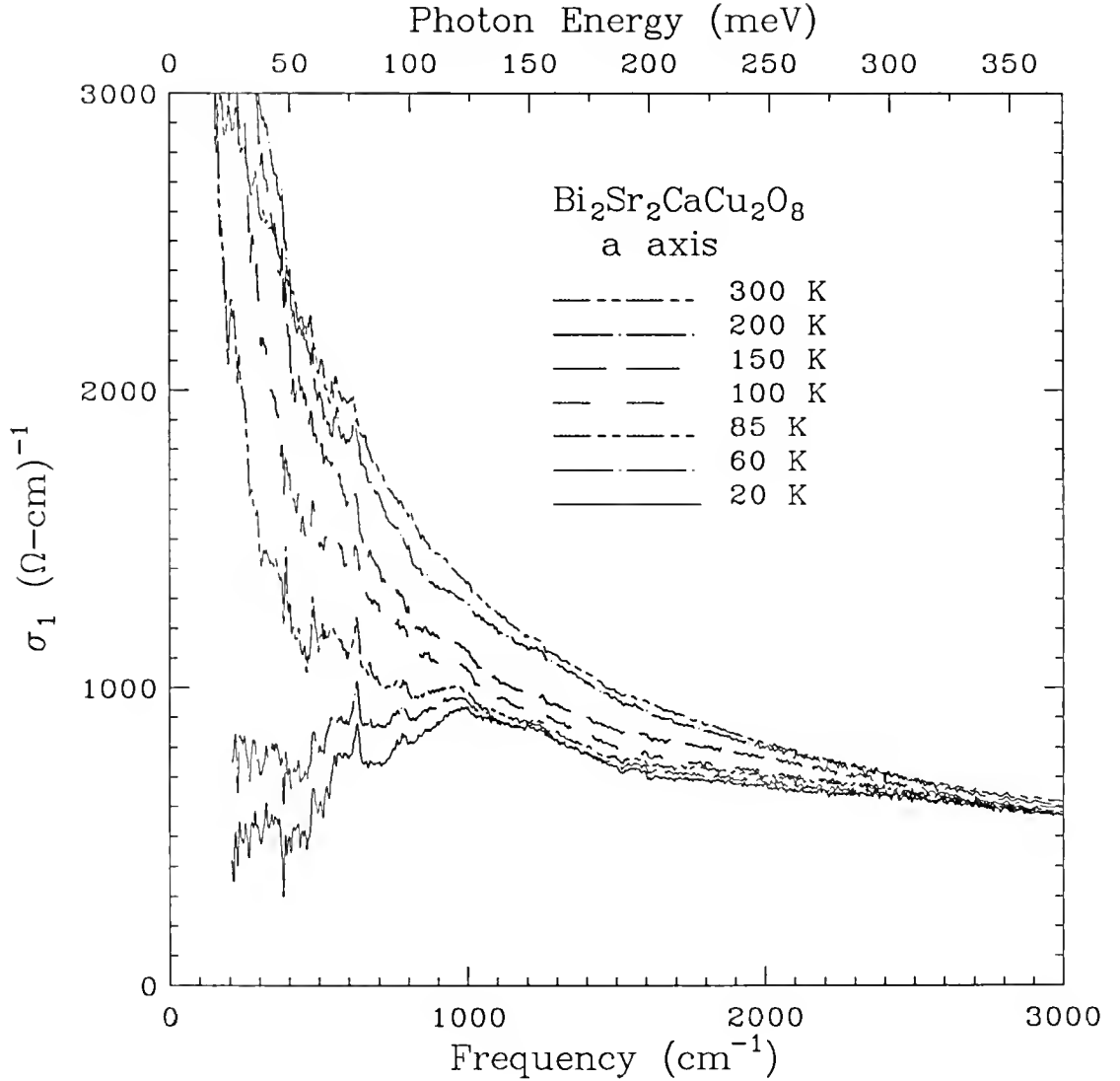


Fig. 53. Temperature dependence in the a -axis optical conductivity obtained from a Kramers-Kronig analysis of the reflectance.

We should point out that photoemission experiments done on samples from the same batch as the one used in this study have shown convincing evidence for the opening of a gap in the energy spectrum around the Fermi level.^{6,7} The maximum gap parameter obtained from the analysis of the photoemission data has given a value of Δ close to 25 meV. Although twice this energy is close to the minimum position observed in the conductivity data, it can not be assigned unambiguously as

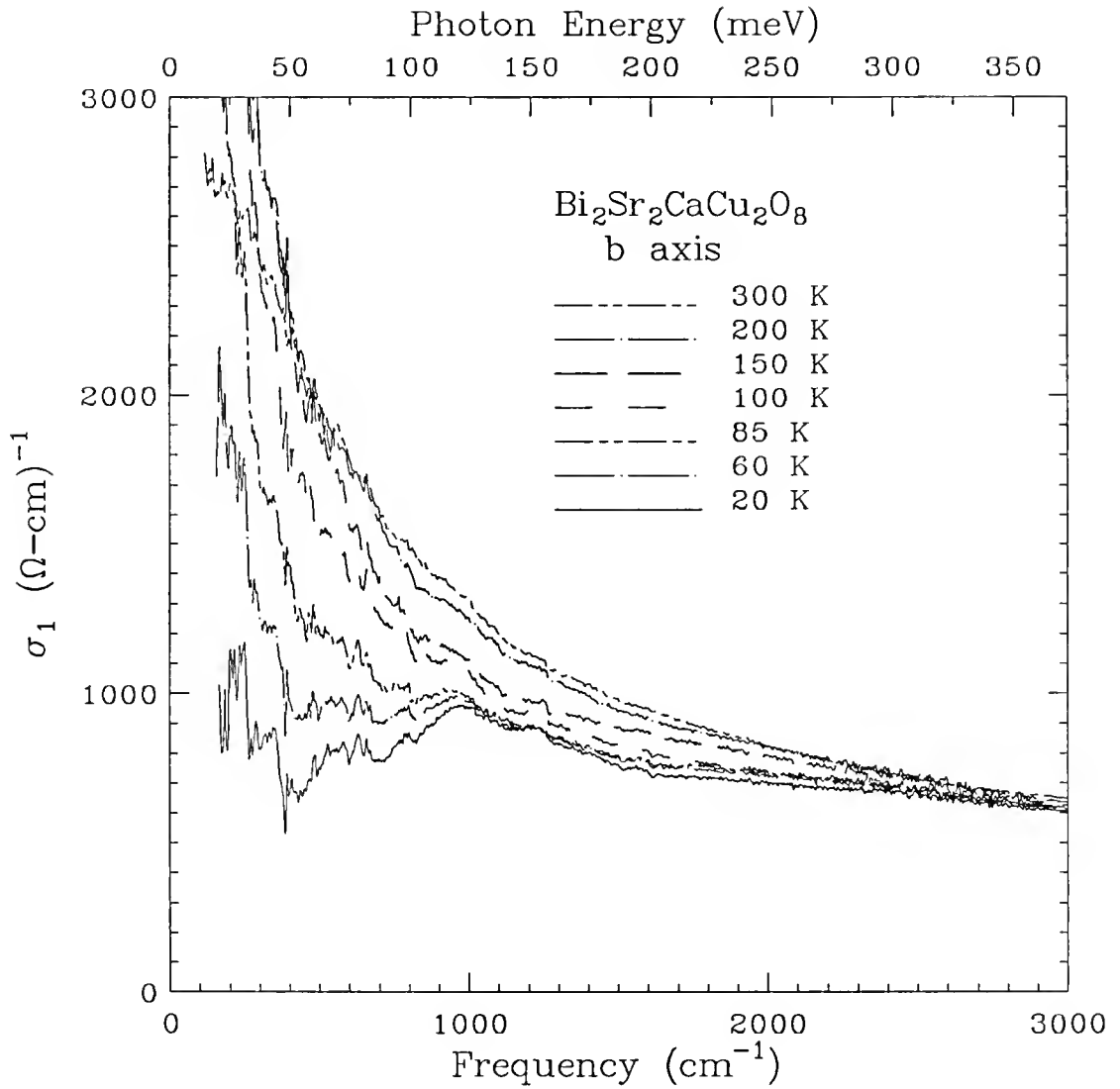


Fig. 54. Temperature dependence in the b -axis optical conductivity obtained from a Kramers-Kronig analysis of the reflectance.

evidence of the superconducting energy gap. Moreover, since similar structures have been observed in all copper-oxide superconductors, they have also been explained as due to strong bound-carrier interactions with phonon excitations.^{103,135,136,174} More discussion about this will be given later. Next section will address the analysis of the optical conductivity in terms of the one- and two-component models.

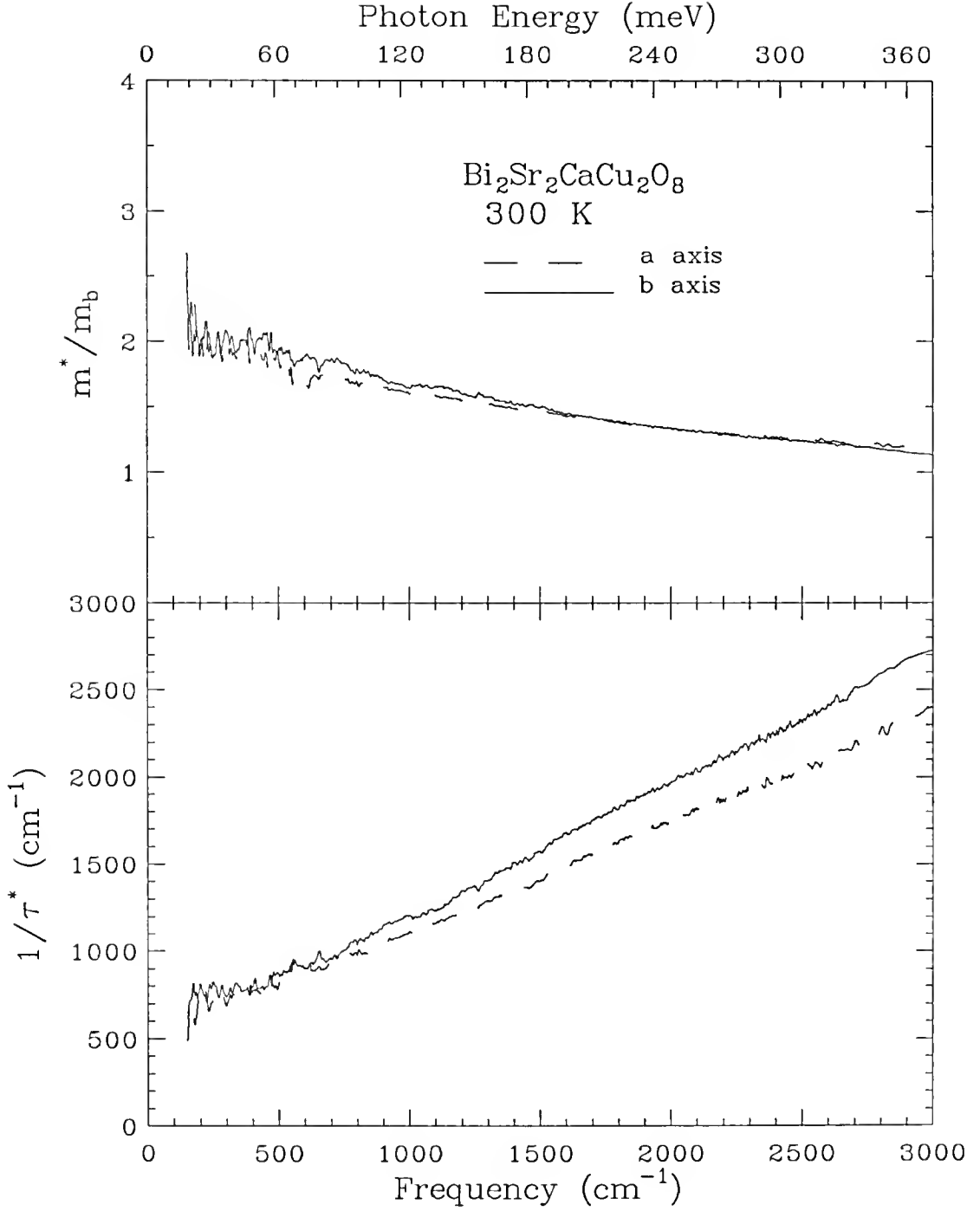


Fig. 55. One-component analysis showing the renormalized scattering rate (upper panel) and effective mass enhancement (lower panel) along the a and b axes.

One-Component Analysis

As mentioned already, one of the approaches that has been proposed to explain the anomalous non-Drude behavior in the infrared conductivity of the copper-oxide materials is to model $\sigma_1(\omega)$ using a generalized Drude model,¹⁰⁵ with a frequency dependent scattering rate $\tau(\omega)$. Details of this model were discussed in Chapter III.

The self-energy function $\Sigma(\omega)$ may be calculated from Eq. 12 once good estimates for ω_p and ϵ_∞ are obtained. Figure 55 shows the result of m^*/m_b and $1/\tau^*(\omega)$ at room temperature for $\text{Bi}_2\text{Sr}_2\text{CaCu}_2\text{O}_8$ along the a and b axes. The values of ω_p and ϵ_∞ for the a axis are 16200 cm^{-1} and 4.6 respectively, while for the b axis we used $\omega_{pb} = 16240 \text{ cm}^{-1}$ and $\epsilon_{\infty b} = 4.8$. In Fig. 55 it is interesting to notice that while there is a mass enhancement at low frequencies, it is isotropic in the ab plane, on account of the nearly isotropic values of ω_p . On the other hand, Fig. 55 shows an anisotropic renormalized scattering rate that increases linearly with frequency up to a frequency of 1500 cm^{-1} . This seems to be in agreement with the predicted behavior in the MFL model, although the cutoff frequency as suggested by the saturation of $1/\tau^*(\omega)$ seems to be rather low. Experiments that have provided support to this model, such as Raman^{60,109} scattering measurements, have given evidence of a broad continuum of electronic background in the spectrum. The cutoff frequency obtained from Raman experiments is around $\omega_c \sim 8000 \text{ cm}^{-1}$. Hence, the MFL model appears to give an adequate fit to the data provided a much lower value for ω_c is taken in comparison to the one suggested from Raman measurements.

The temperature dependence of the one-component fit to the data is shown Fig. 56. Here we show the imaginary part of the self-energy $\Sigma_2(\omega)$ at three temperatures for the a and b directions. As shown in Eq. 13, there are two regimes to consider for this function, *i.e.*, $\omega < T$ and $\omega > T$. Evaluations of the slope in the regime $\omega < T$ give a coupling constant $\lambda_T = 0.5 \pm 0.1$ in both polarizations.

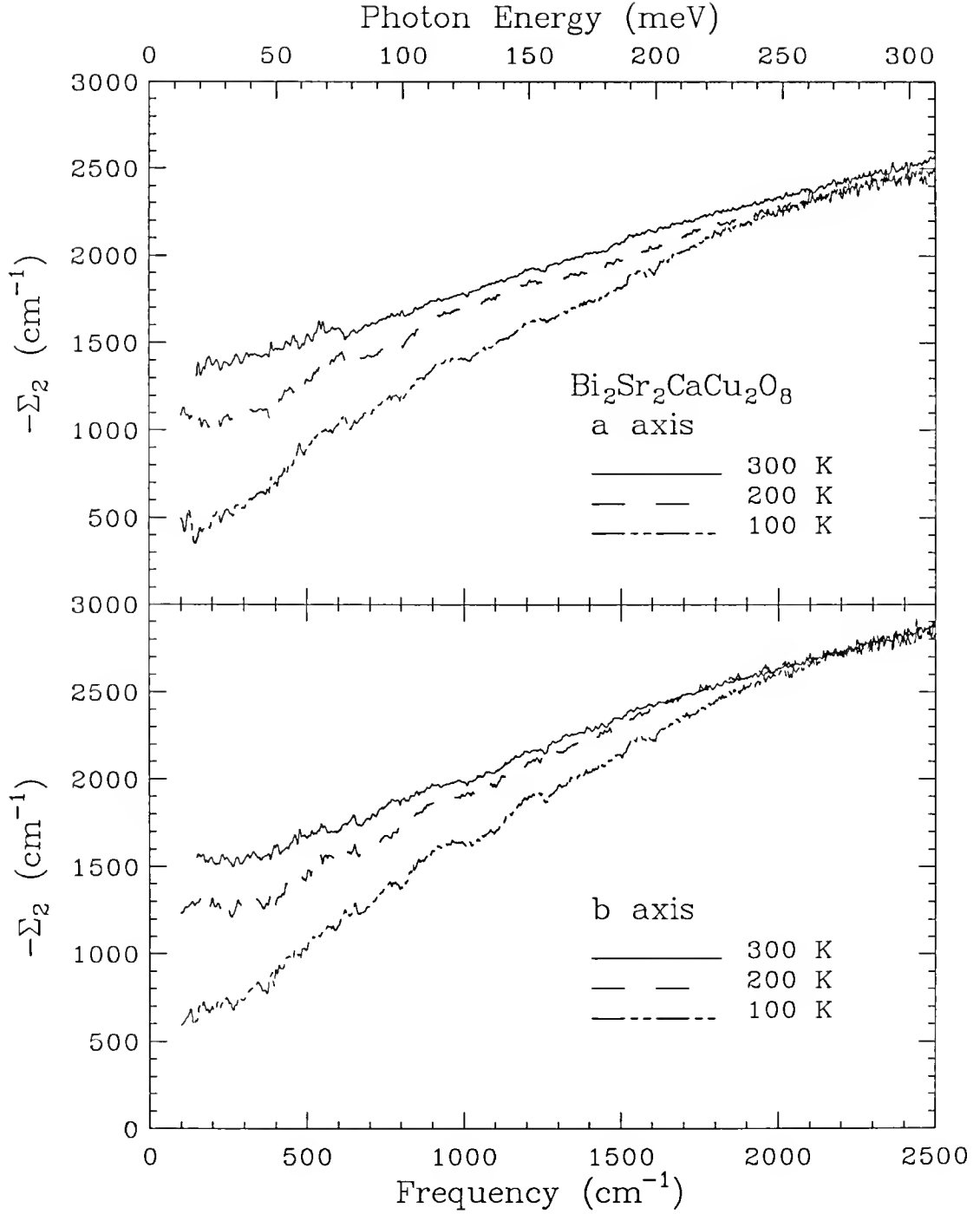


Fig. 56. Temperature dependence in the imaginary part of the self-energy $\Sigma_2(\omega)$ for *a* (upper panel) and *b* (lower panel) axes.

Furthermore, from evaluation of the slopes in the region where $\Sigma_2(\omega)$ is linear in ω , it is found that at room temperature $\lambda_{wa} \approx \lambda_{wb} = \lambda_\omega \sim 0.20 \pm 0.01$, while at 100 K this number is a factor of 2 larger. The temperature dependence in λ_ω clearly shows that the coupling mechanism that is causing the linear scattering rate in the charge carriers becomes stronger as the temperature of the sample is decreased. Similar behavior has also been reported in same analyses of unpolarized measurements of $\text{Bi}_2\text{Sr}_2\text{CaCu}_2\text{O}_8$ by Romero *et al.*⁸⁶ As mentioned earlier, doping dependence studies also suggest a coupling constant that increases as the doping in the sample is reduced.⁷⁵ In this respect, it appears that lowering the temperature of the sample would be equivalent to reducing the doping and, hence, to an increase in the interactions that are causing the scattering of the carriers. Interpretation for this based on models of strongly correlated systems is unclear.

Two-Component Analysis

An alternative approach that has been proposed to explain the optical properties of these materials is to assume the infrared conductivity is composed of two or more components. As discussed previously, the underlying reason for this analysis is based on two key observations. First, the optical conductivity $\sigma_1(\omega)$ obtained from doping dependent studies clearly shows the appearance of free-like as well as bound excitations in the midinfrared as doping in the the CuO_2 planes of the samples is increased.^{24,28,70,77,177} Second, the $\sigma_1(\omega)$ in optimally doped samples exhibits an unusual temperature dependence in the infrared. There is a narrow range of frequencies in the far infrared where $\sigma_1(\omega)$ shows a variation in T that is consistent with the linear change in resistivity that is observed the sample. At higher frequencies, $\sigma_1(\omega)$ shows a weaker temperature dependence.^{65,68,71,72,178} The data shown in Fig. 53 and Fig. 54 exhibit a behavior that is consistent with this observation.

In this model, the total conductivity in doped materials is assumed to be made up of at least three parts:

$$\sigma_1(\omega) = \sigma_{1D} + \sigma_{1MIR} + \sigma_{interband}, \quad (45)$$

where σ_{1D} is associated with a free or Drude-like part, σ_{1MIR} corresponds to the bound transitions in the infrared, and $\sigma_{interband}$ includes higher interband absorptions. One way of separating individual contributions is obtained by using the Lorentz-Drude model discussed in Chapter IV. Each term would consist of three parameters: line width γ , plasma frequency ω_p , and center frequency ω_0 . A self-consistent approach to separate the Drude-like from the bound-like excitations has been suggested by Romero *et al.*⁷¹ What follows is a brief description of this method applied to the conductivity curves shown in Fig. 53 and Fig. 54. In the superconducting state and for $T \ll T_c$, all the free-carrier part is presumed to have collapsed into a delta function at $\omega = 0$. Therefore, in first approximation the total conductivity at the lowest temperature ($T = 20$ K) would only have a negligible “free” carrier contribution, and it will correspond to the σ_{1MIR} term in Eq. 45. Hence, the free-carrier part in the normal state can be obtained by subtracting σ_{1MIR} from the experimental $\sigma_1(\omega)$ at $T > T_c$. This first iteration produces free-carrier conductivity ($\sigma_{1D}^{(1)}$) at individual temperatures above T_c . If this conductivity has a Drude line shape, a linear fit to the curve obtained by plotting $1/\sigma_{1D}^{(1)}$ vs. ω^{-2} will yield a slope and intercept that can be used to get initial guess values for ω_{pD} and $1/\tau$. Once values for ω_{pD} and $1/\tau$ are obtained, they can be used to calculate a Drude conductivity with the formula

$$\sigma_{1D}^{fit} = \frac{1}{4\pi} \frac{\omega_{pD}^2 \tau}{1 + \omega^2 \tau^2}, \quad (46)$$

Then, a new midinfrared conductivity σ_{1MIR} is generated at each temperature by subtracting σ_{1D}^{fit} from the total $\sigma_1(\omega)$ at each temperature above T_c . A self-consistent

check of the ω_{pD} and $1/\tau$ obtained at each temperature is done by first computing an average midinfrared conductivity $\langle\sigma_{1MIR}\rangle$ from the σ_{1MIR} obtained as explained above, and using this average as the starting midinfrared term in a second iteration. We found the results are self-consistent after performing a few (3 or 4) iterations.

In order to further test the convergence of the method, the starting guess for the midinfrared component, *i.e.*, $\sigma_{1MIR}(\omega, 20K)$ was cut below $\omega \sim 380\text{cm}^{-1}$ and the procedure was carried out and compared when the calculation is done without cutting the data. The results indicate this did not affect the fits obtained for the *a*-axis data. However, the convergence of the results was poor when the starting midinfrared conductivity included part of the upturn that is shown in Fig. 54 for $\sigma_1(\omega)$ in the *b* direction at the lowest temperature. Consequently, the analysis in the *b* axis was carried out by first removing this upturn in σ_{1MIR} and using this as the first iteration in decomposing the conductivities. After this was done, better convergence for the *b*-axis results was obtained as well.

Drude Component

The Drude conductivities ($\sigma_1(\omega) - \langle\sigma_{1MIR}\rangle$) obtained from this analysis are shown in Fig. 57 and Fig. 58 along with fits obtained from the estimated values of ω_{pD} and $1/\tau$ at each temperature. The results indicate that the oscillator strength for the Drude term is nearly temperature independent. In the analysis, we find $\omega_{pD}^a = 9300 \pm 200 \text{ cm}^{-1}$, while $\omega_{pD}^b = 8900 \pm 200 \text{ cm}^{-1}$. There is indication of slightly smaller values of ω_{pD} at 100 K, suggesting possible fluctuation effects at this temperature. The results of the extrapolated dc resistivities using this procedure as function of temperature are shown in Fig. 59 along with the measured ρ along the *a* and *b* axes for similar samples. The measured ρ_{dc} in both polarizations were multiplied by a constant factor (1.4) due to a systematic error in estimating the dimensions of the sample (more details are given in Chapter VIII). Two things should be noticed about

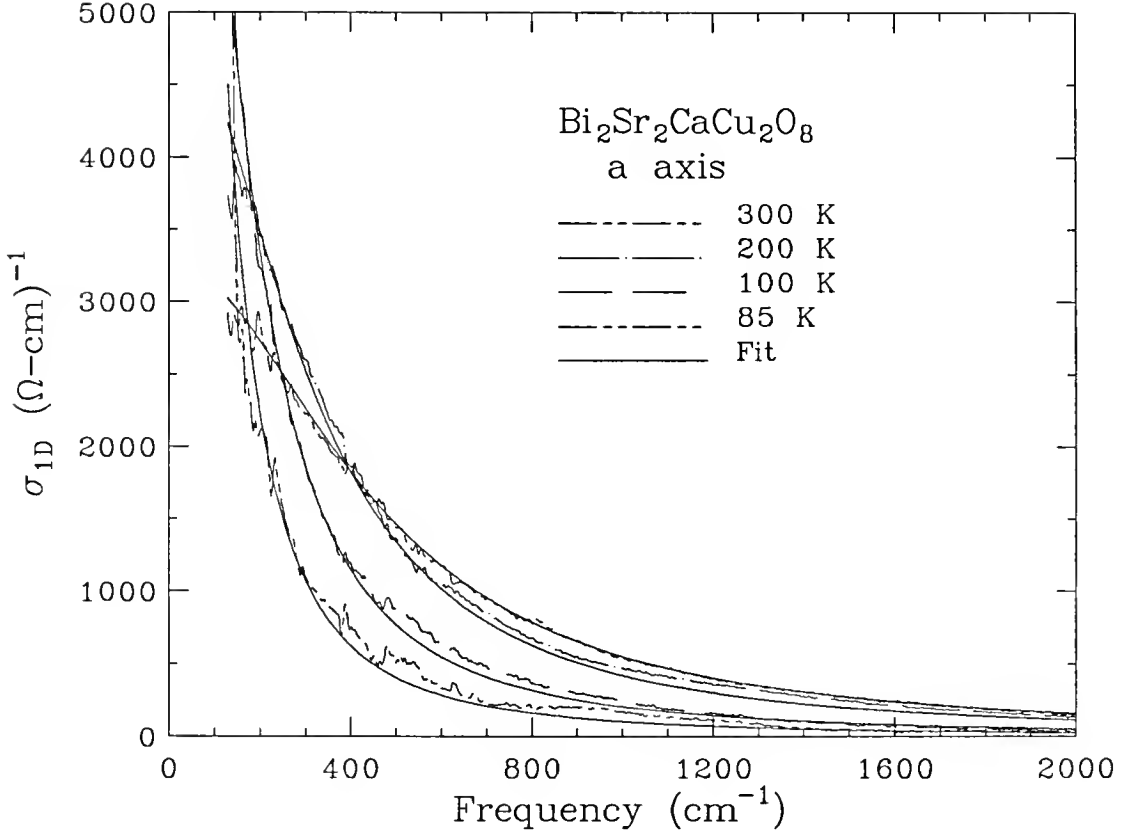


Fig. 57. Drude part from two-component analysis of $\sigma_1(\omega)$ and fits obtained from the ω_{pD} and $1/\tau$ at each temperature.

this figure. The first is that ρ_{dc} and ρ_{optic} derived from the two-component analysis of $\sigma_1(\omega)$ follow a temperature dependence that is linear in both cases. Secondly, we find a good agreement between the anisotropy determined from optical as well as dc transport measurements. A comparison of $1/\tau_{optic}$ obtained from the fits with $1/\tau_{dc}$ obtained from formula

$$1/\tau_{dc} = \frac{\omega_{pD}^2}{60} \rho_{dc}, \quad (47)$$

where ω_{pD} is the average Drude oscillator strength given above, is shown in Fig. 60. This figure shows that the temperature variation of $1/\tau_{dc}$ and $1/\tau_{optic}$ is indeed linear in the normal state as expected. This linear temperature dependence of $1/\tau$ in the

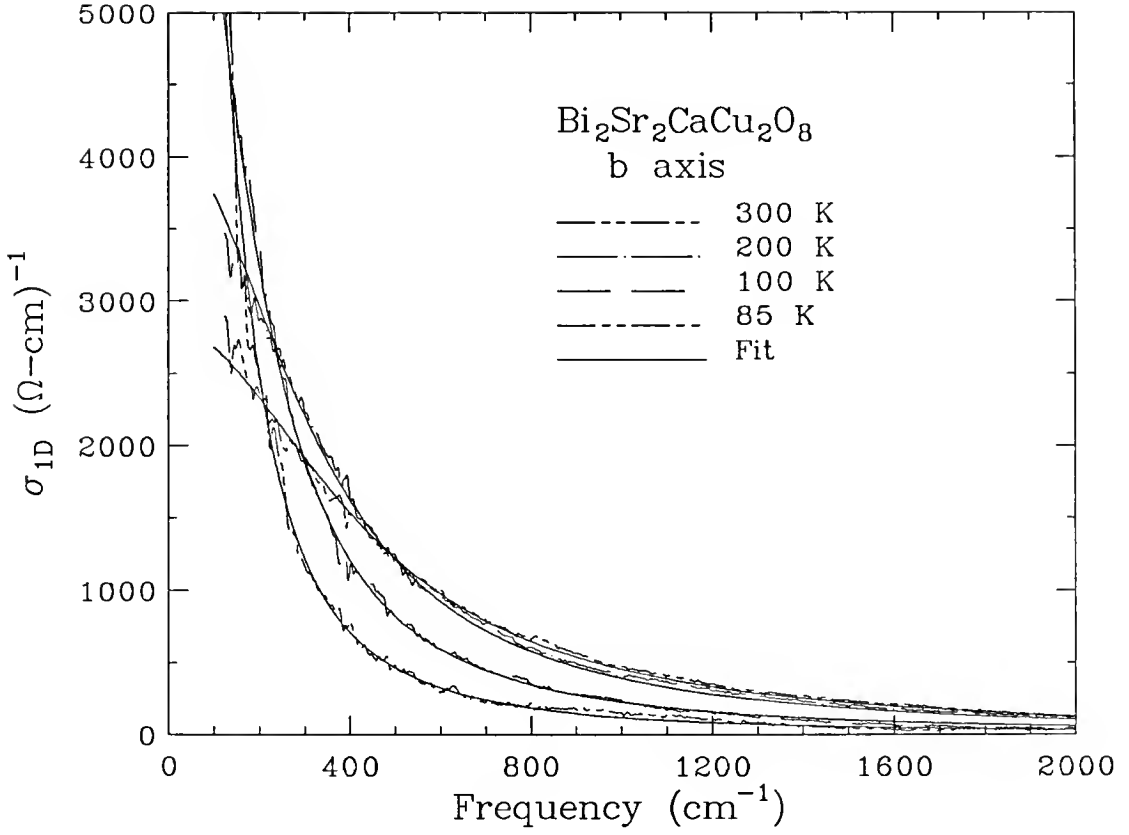


Fig. 58. Drude part from two-component analysis of $\sigma_1(\omega)$ and fits obtained from the ω_{pD} and $1/\tau$ at each temperature.

high- T_c has been expressed as^{23,179}

$$\hbar/\tau = 2\pi\lambda k_B T + \hbar/\tau_0$$

where λ is a dimensionless constant that couples the free carriers to whatever excitations are causing the scattering. From a numerical evaluation of the two slopes we find $\lambda_a \sim 0.35$, while $\lambda_b \sim 0.31$. These results are in good agreement with previously estimated values for λ using a two-component analysis in other samples.²³ Furthermore, these results suggest the transport properties of the copper-oxide superconductors are in the weak coupling regime. This is in contrast with the coupling constant obtained in the one-component analysis, where the λ obtained suggests the

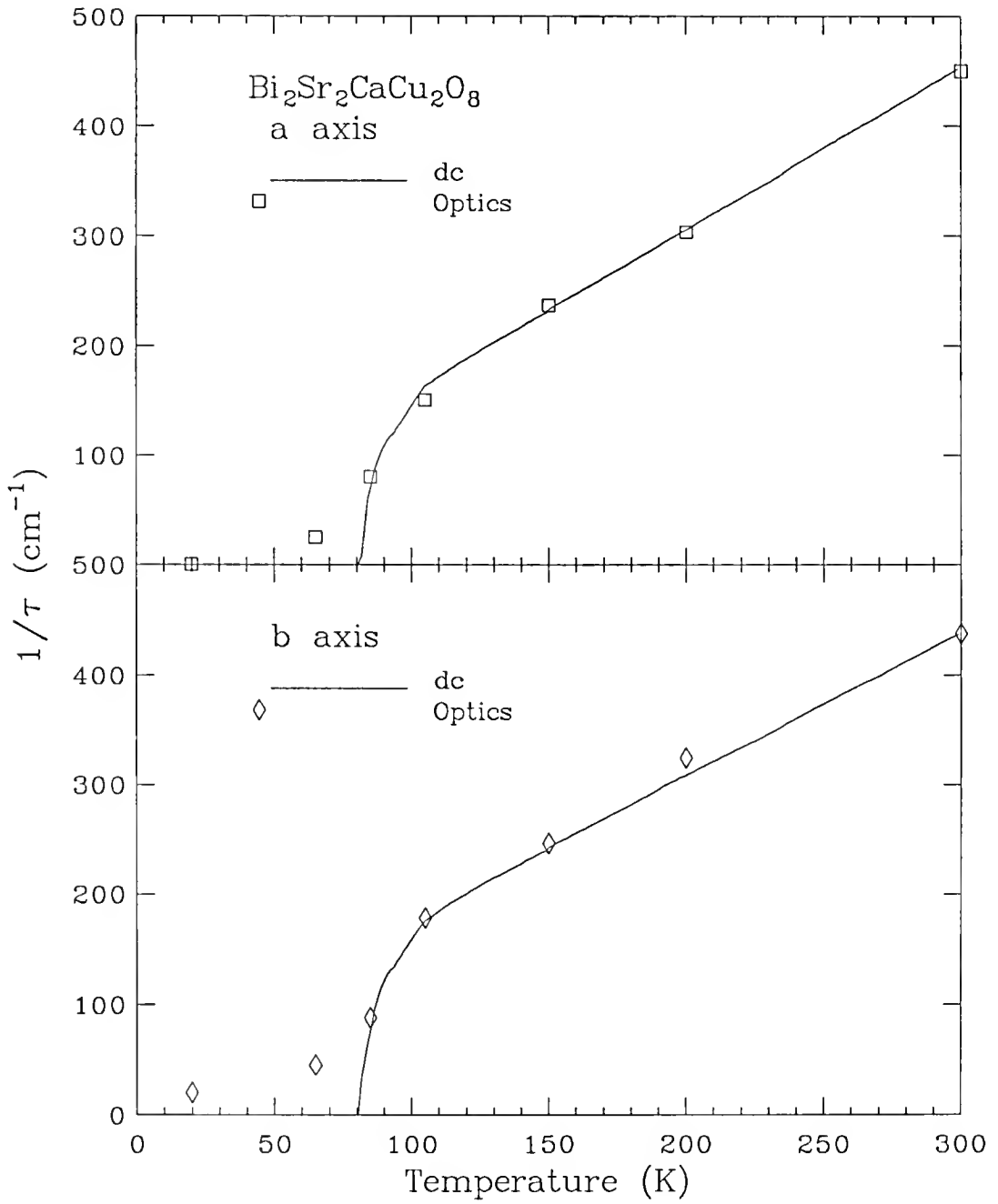


Fig. 60. Scattering rate ($1/\tau$) obtained from dc transport and zero-frequency extrapolation of the optical conductivity.

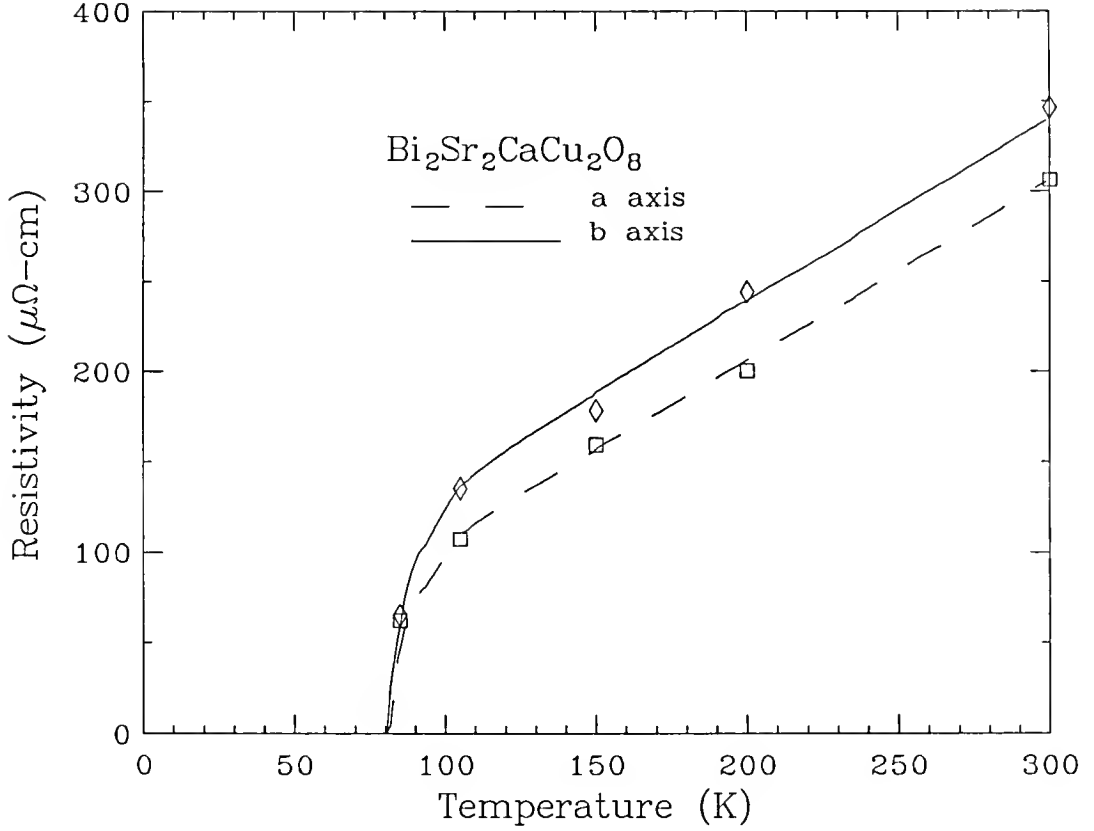


Fig. 59. Temperature dependence in the a - and b -axis resistivities obtained from dc transport measurements and extrapolations of the optical conductivity.

material goes from the weak coupling limit at room temperature to an intermediate limit at lower temperatures.

In the superconducting state, $1/\tau_{dc}$ drops to zero on account of ρ_{dc} also going to zero. At the same time $1/\tau_{optic}$ exhibits a sudden drop in the superconducting state. This suggests that whatever excitations are causing the scattering of the carriers in the normal state are suppressed below T_c . The limited number of points and possible uncertainties specially below 100 cm^{-1} prevent us from making a reasonable guess of what is the temperature dependence of this $1/\tau$ in the superconducting state. Nonetheless, the result suggests the $1/\tau_{optic}$ obtained for the b axis is larger than the one obtained for the a axis in the superconducting state. Evidence for an additional

channel for elastic scattering in the crystallographic b direction is also consistent with the final intercept observed in ρ_{dc}^b from extrapolations to the zero temperature value ρ_{dc} .

Sudden drops below T_c in the quasiparticle scattering rate determined from infrared measurements have also been observed in unpolarized measurements of $\text{Bi}_2\text{Sr}_2\text{CaCu}_2\text{O}_8$,⁷¹ and $\text{La}_{2-x}\text{Sr}_x\text{CuO}_4$,⁷² and in experiments of femtosecond optical transient and microwave absorption measurements on $\text{YBa}_2\text{Cu}_3\text{O}_{7-\delta}$ ¹¹⁶ and on $(\text{BiO})_2\text{Sr}_2\text{Ca}_2\text{Cu}_3\text{O}_{10}$. The temperature dependence of the $1/\tau$ obtained in these measurements has a power law in the form of T^n where n is a number that has ranged between 1 and 2. Similarly, there have been predictions of drop of the quasiparticle scattering rate in the superconducting state within the phenomenology of the Marginal Fermi Liquid approach.¹⁸⁰ This sudden drop in $1/\tau$ has been proposed is the reason for the appearance of a “coherent” peak in $\sigma_1(\omega)$ in studies of $\text{YBa}_2\text{Cu}_3\text{O}_{7-\delta}$ thin films^{181,182} and in single crystals of $\text{Bi}_2\text{Sr}_2\text{CaCu}_2\text{O}_8$ ^{71,183} for temperatures just below T_c and for frequencies in the microwave region.

Midinfrared Absorption

The midinfrared conductivity that remains after subtracting the Drude term or low-frequency part is shown in the top and bottom panels of Fig. 61 for the a and b axes respectively. This is the so-called midinfrared absorption that occurs in nearly all copper-oxide superconductors. The results indicate that σ_{1MIR} does not have much temperature dependence. This is self-consistent with the fact that most of the temperature dependence in the total $\sigma_1(\omega)$ comes from the relaxation rate of the free-carrier contribution in the samples. For a comparison, Fig. 62 shows σ_{1MIR} for the a and b directions at 100 and 200 K. The onset of absorption appears to be at around 250 cm^{-1} in the a axis, while the b -axis absorption extends to a slightly lower frequency ($150\text{--}200 \text{ cm}^{-1}$) and is higher in the frequency range $150\text{--}700 \text{ cm}^{-1}$. In

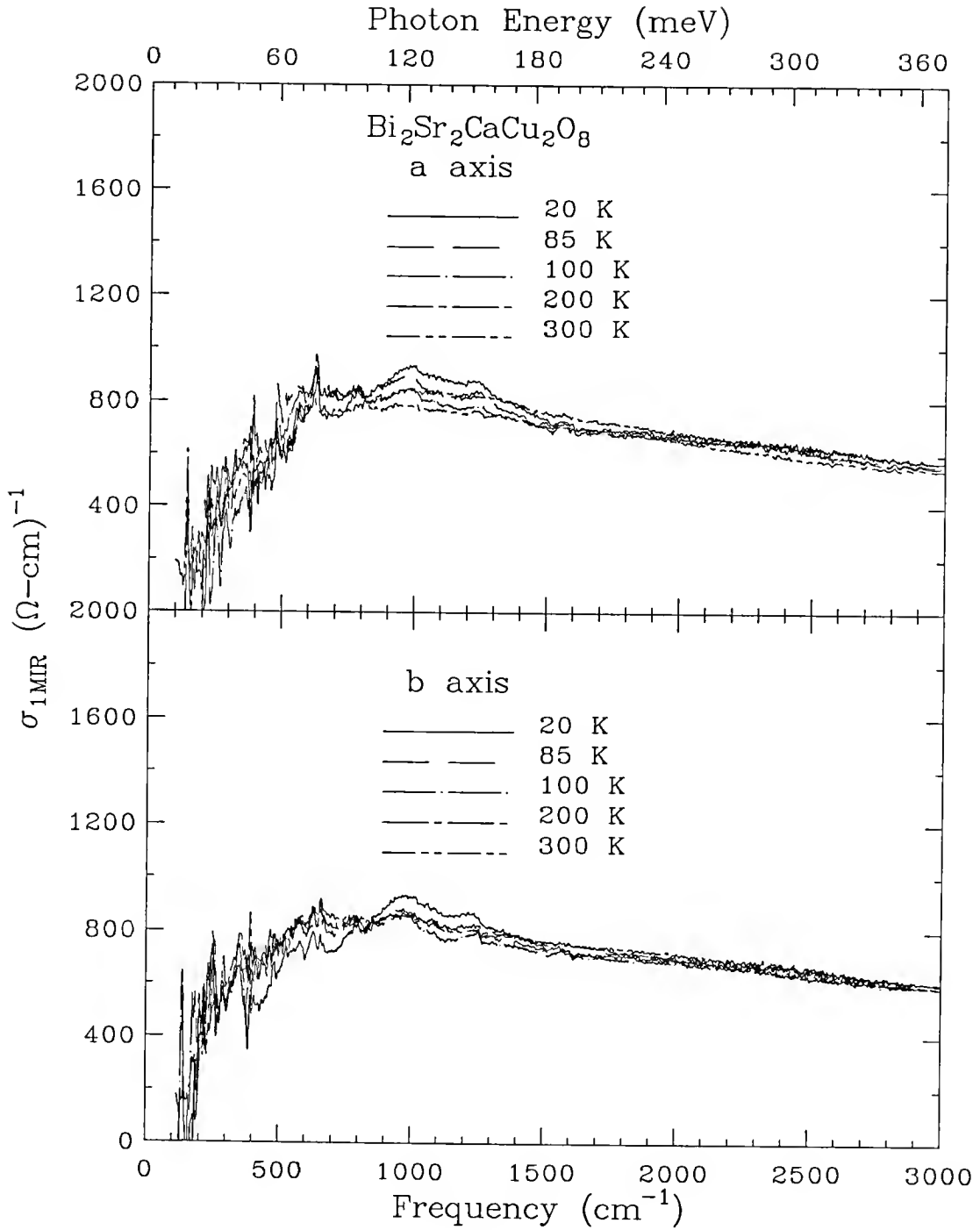


Fig. 61. Midinfrared part to the total conductivity.

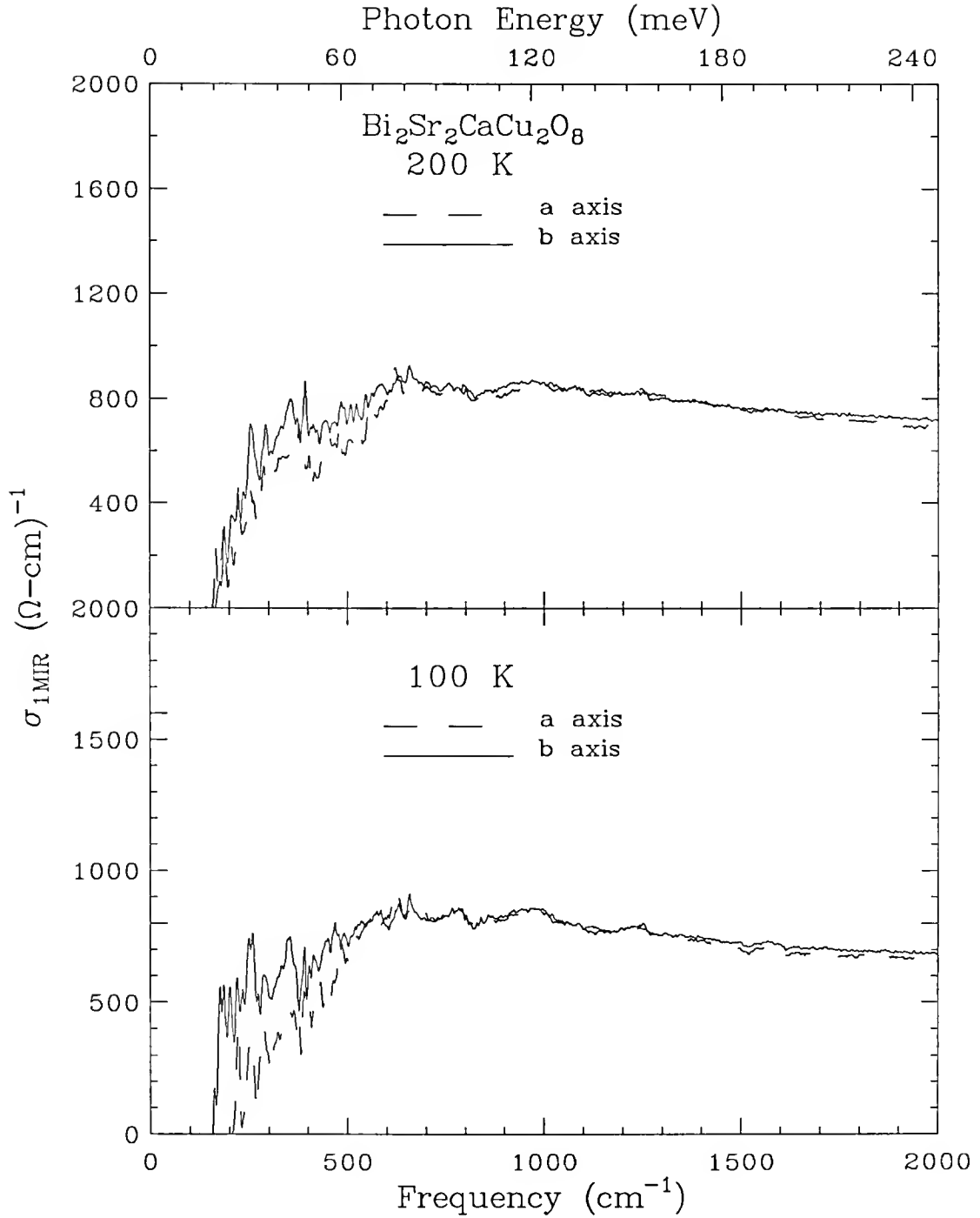


Fig. 62. Midinfrared part to the total conductivity showing the relative difference along a and b axes at two temperatures in the normal state.

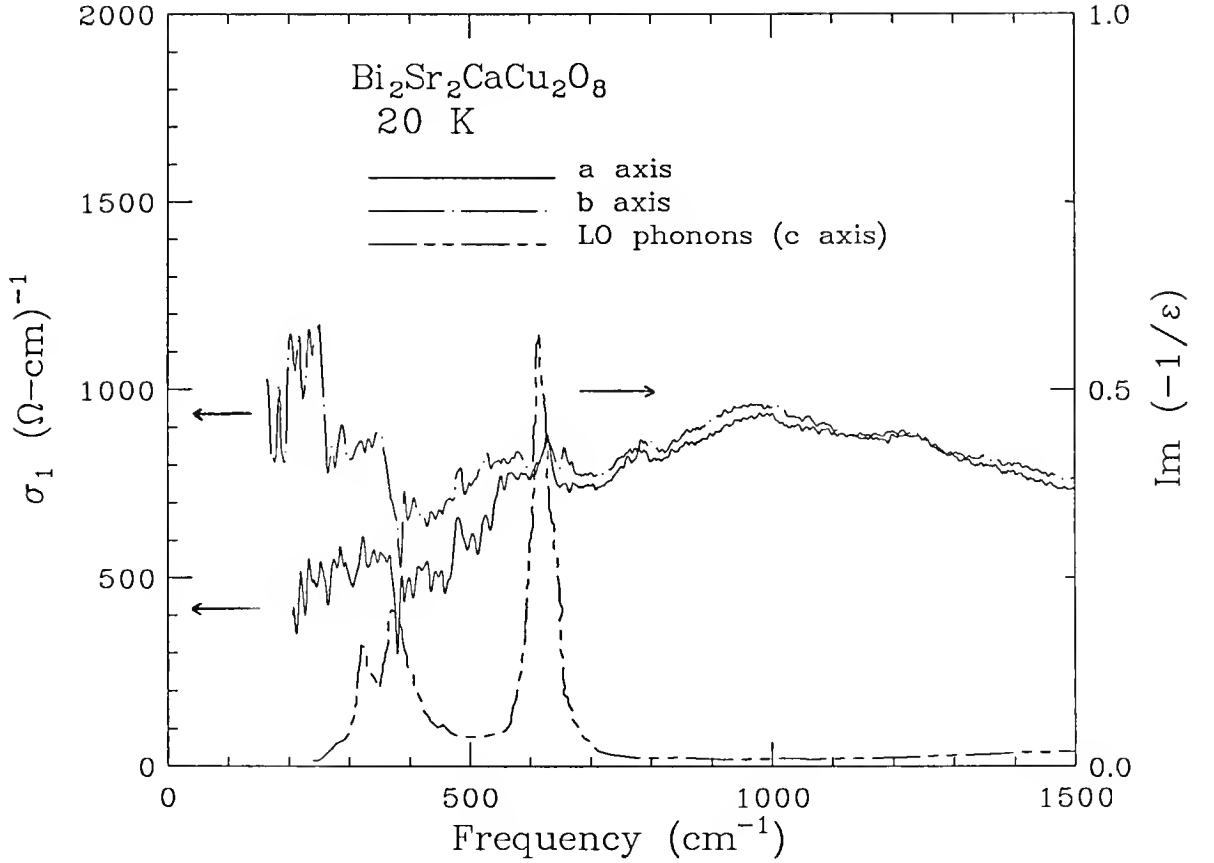


Fig. 63. Plot of $\sigma_1(\omega)$ at $T = 20$ K in the a - and b -axis polarizations along with the c -axis LO phonons taken from Reference 57.

both cases, there are some weak structures due to phonons and a notch-like structure at $\omega \sim 400 \text{ cm}^{-1}$ that appears in both the normal and superconducting state. Earlier optical studies^{31,78} interpreted this notch, which in samples of $\text{YBa}_2\text{Cu}_3\text{O}_{7-\delta}$ occurs at $\omega \sim 430 \text{ cm}^{-1}$, as the superconducting energy gap. One problem that exists with this interpretation is that this minimum in $\sigma_1(\omega)$ is also observed above T_c in nearly all samples, making its association with an energy gap very unlikely.^{68,72,86}

An alternative explanation that has been proposed is that all of the structures that appear in the midinfrared absorption is the result of electron-phonon interactions.^{103,135,136,174} As discussed in Chapter V, these interactions are between the c -axis LO phonons and the ab -plane bound carriers. A supporting evidence for this is

shown in Fig. 63, where the c -axis LO phonon frequencies for $\text{Bi}_2\text{Sr}_2\text{CaCu}_2\text{O}_8$ (Taken from Reference 57) are plotted along with a - and b -axis conductivities at 20 K. The coincidence between the peak maxima in the LO phonons and the minima in $\sigma_1(\omega)$ is quite remarkable. Further evidence for this was found in the results of $\sigma_1(\omega)$ obtained from measurements on $\text{La}_2\text{CuO}_{4+\delta}$ single crystal discussed in Chapter V.

We now turn our attention to broad maximum that is seen in the results of σ_{1MIR} shown in Fig. 61 at around 1000 cm^{-1} . This maximum appears to get enhanced in the superconducting state and it is due to a minimum-like structure that is seen the reflectance shown in Fig. 48 in both a - and b -axis polarizations around the same frequency. Similar enhancements have also been observed in the optical conductivity of other high- T_c superconductors. The possible connection of this feature with superconductivity has also been suggested. For example, Romero *et al.*⁸⁶ found the transmittance of $\text{Bi}_2\text{Sr}_2\text{CaCu}_2\text{O}_8$ free-standing single crystals is maximum at this energy in the superconducting state and suggested it could be interpreted as the 4Δ peak of the marginal Fermi liquid theory.^{107,180}

Furthermore, due to the fact that this energy is close to the antiferromagnetic spin interaction energy J , it has also been attributed to a magnetic origin.²⁴ Thomas *et al.*¹⁶⁹ found the linewidth of this midinfrared excitation has a linear temperature dependence in lightly-doped crystals of $\text{Nd}_2\text{CuO}_{4-y}$. One argument for its origin is that this electronic band involves the transition of a bound charge coupled to both the lattice and spin excitations. The fact that the broadening of this transition is linear in temperature is found as evidence that the same or similar mechanism might responsible for the linear temperature dependence observed in the scattering rate of the mobile carriers in metallic samples. To further illustrate the similarities, Thomas *et al.* found a coupling constant in the order of $\lambda \simeq 0.5$, which is close to the coupling constant obtained from the linear temperature dependence in the relaxation rate of

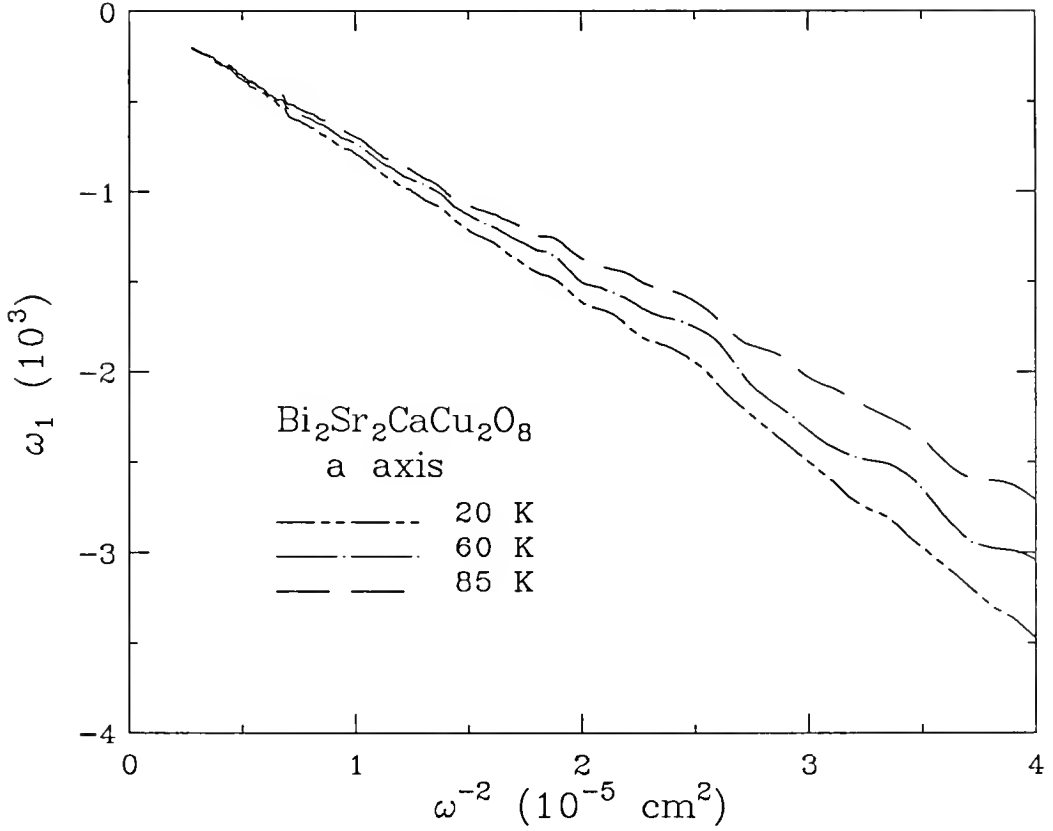


Fig. 64. Plot of ϵ_1 vs. ω^{-2} in the superconducting state along the a direction.

the free-carrier conductivity in the two-component analysis of our results and in other samples.²³

Superconducting Condensate

We saw from the two-component analysis the a -axis scattering rate for the Drude carriers is close to 150 cm^{-1} at 100 K, and it is suddenly suppressed in the superconducting state. If $1/\tau$ at 100 K is used together with published estimates^{14,184} for the Fermi velocity in the CuO_2 planes to compute the mean free path for quasiparticles propagating along this direction we obtain $l = v_f \tau \sim 100 \text{ \AA}$. When this number is compared with the typical coherence length reported^{14,15} for this and other high- T_c compounds, ($\xi \sim 15$) we find the condition that places this and other type II high- T_c

materials in the clean limit, *i.e.*, $l > \xi$, as was first pointed by Kamaras *et al.*⁶⁸ In this limit, a gap feature is not observable because in the superconducting state most of the spectral weight, which is associated with the area under $\sigma_1(\omega)$, moves to a delta function at zero frequency. However, there is a way to determine the presence of a condensate at zero frequency. The method involves the real part of the dielectric function, $\epsilon_1(\omega)$, since this quantity measures the inductive response that is responsible for the expulsion of electromagnetic radiation inside a superconductor. It can be shown that, in the superconducting state, the zero frequency $\epsilon_1(\omega)$ is given by the expression²²

$$\epsilon_1(\omega) = \epsilon_{1b} - \frac{\omega_{ps}^2}{\omega^2}, \quad (48)$$

where ω_{ps} is the oscillator strength of the superconducting condensate defined as $\omega_{ps} = 4\pi n_s e^2 / m$ and n_s is the density of superfluid carriers. Term ϵ_{1b} is the bound carrier contribution to $\epsilon_1(\omega)$. Hence, a determination of the condensate contribution ω_{ps} to $\epsilon_1(\omega)$ can be done by first plotting $\epsilon_1(\omega)$ as a function of ω^{-2} . As shown in Fig. 64, the result of doing this for the *a*-axis results gives a straight line whose slope is ω_{ps}^2 . From Numerical evaluation of this slope at $T = 20$ K, we find $\omega_{ps}^a = 9000 \pm 200$ cm⁻¹. At this temperature, we also find that $\omega_{ps}^b = 8200 \pm 200$ cm⁻¹ in the *b*-axis direction. Hence, the results indicate a superconducting-carrier response that is larger along the *a*-axis direction of the sample.

An independent verification of these results is obtained by finding estimates of the missing area under $\sigma_1(\omega)$ in the superconducting state. This is done by subtracting the conductivity at the lowest temperature ($T = 20$ K in this case) from the conductivity just above T_c or $T = 100$ K. Then, the sum rule or density of superfluid carriers, $N_{eff}^s m / m_b$, is evaluated by performing the integral

$$N_{eff}^s(\omega) \frac{m}{m_b} \sim \int_0^\omega (\sigma(\omega, 100\text{K}) - \sigma(\omega, 20\text{K})). \quad (49)$$

Evaluation of the integral in Eq. 49 yields that $N_{eff}^s m/m_b \sim 0.20$ and ~ 0.16 along the a and b axes respectively. Hence, by noticing that $(N_{eff}^s m/m_b) = \omega_{ps}^2 m V_{cell} / 4\pi e^2$ and from the known unit cell volume of $\text{Bi}_2\text{Sr}_2\text{CaCu}_2\text{O}_8$, we find that

$$\omega_{ps} = 19,900 \sqrt{N_{eff}^s} \simeq 8900 \text{ cm}^{-1}$$

in the a -axis polarization, while $\omega_{ps} \simeq 8100$ along the b axis. Both quantities agree with the results obtained from the independent calculations shown above.

ab -Plane Anisotropy in the London Penetration Depth

The London penetration length λ_L measures the distance over which an electromagnetic wave is attenuated inside a superconductor. Since this length is a measure of the superfluid response in a superconductor, it is also related to the superfluid oscillator strength ω_{ps} by the formula $\lambda_L = 1/2\pi\omega_{ps}$. In anisotropic materials, λ_L is a tensor quantity. Hence, polarized infrared spectroscopy offers the unique opportunity to determine the different components of this tensor. Other techniques, such as magnetic inductance method or μSR ,^{11,185} only give values of λ_L which are averages of the different components of λ_L .

Thus by substituting the ω_{ps} along the a and b axes of $\text{Bi}_2\text{Sr}_2\text{CaCu}_2\text{O}_8$, we find that the London length along the a axis $\lambda_L^a \sim 1800 \text{ \AA}$, while $\lambda_L^b \sim 1960 \text{ \AA}$ in the b axis. The ratio in these two quantities is $\lambda_b/\lambda_a \sim 1.1$. Before discussing the possible reasons for this anisotropy, Fig. 65 displays λ_L along the a and b axes obtained from the formula

$$\left(\frac{1}{\lambda_L}\right)^2 = \frac{4\pi}{c^2} \omega \sigma_2(\omega), \quad (50)$$

where $\sigma_2(\omega)$ is the imaginary part of the optical conductivity. The fact that both curves in Fig. 65 are nearly flat in the far infrared, approaching the values given above

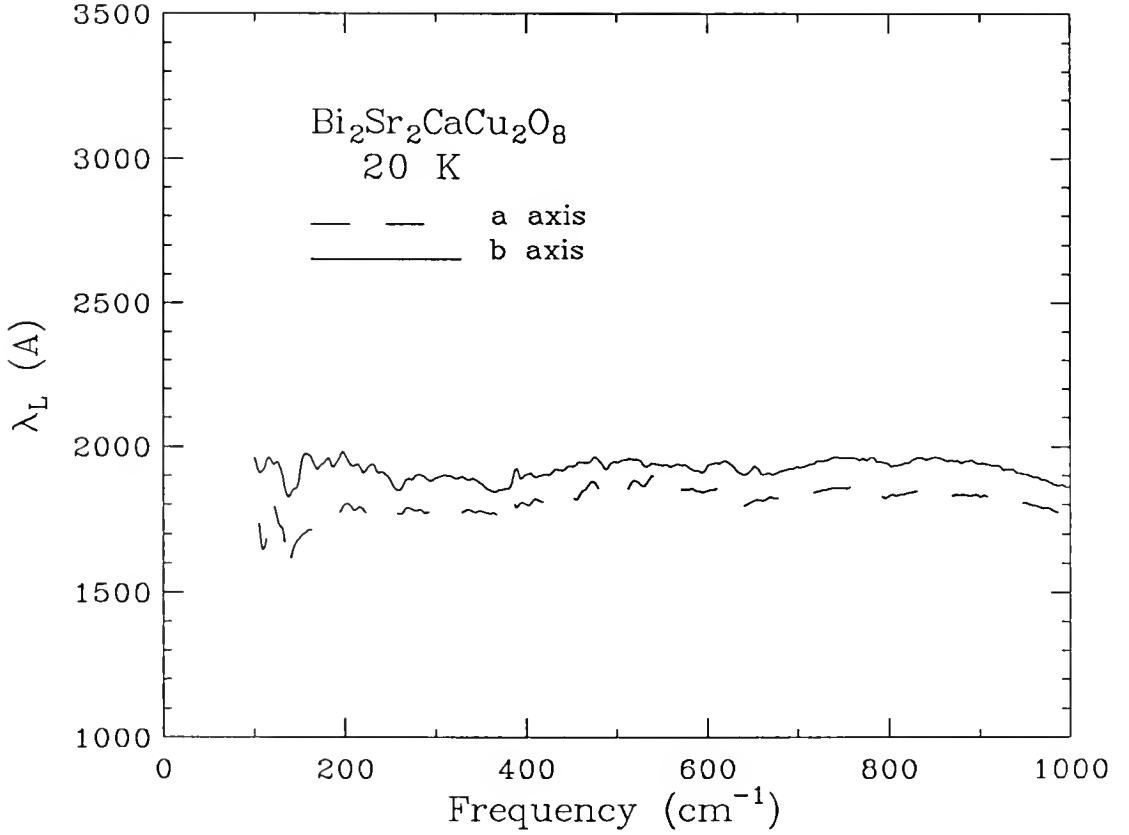


Fig. 65. Plot of the London penetration length as a function of frequency using Eq. 50.

at $\omega = 0$, suggests that the only contribution to $\sigma_2(\omega)$ is mainly from the superfluid carrier response which in this case is $\sigma_2(\omega) \propto 1/\omega$.

To explain the source of this anisotropy the first thing that should be considered is whether the anisotropy that is observed in λ_L is due to mass enhancement effects. In the normal state, the ab -plane anisotropy in the dc resistivity, from extrapolations of the optical data and direct dc transport, is $\rho_b/\rho_a \sim 1.25$. As discussed previously, the normal-state anisotropy in the Drude plasma frequency derived from a two-component analysis of the optical data is found to be smaller than this anisotropy, *i.e.*, $\omega_{pa}/\omega_{pb} = 1.04 \pm 0.04$. Hence, most of the anisotropy in ρ_{dc} is due to a free-carrier relaxation rate that, at $T = 100$ K, is 20% larger along the b -axis in the

sample. This suggests the interactions, which are responsible for the relaxation of the free carriers in the material, are not isotropic. Thus, we find that for the a axis, ω_{ps} is 97% of the normal state value of the ω_{pD} , while in the b direction $\omega_{ps} = 8100 \pm 200$ cm^{-1} and $\omega_{pD} = 8900 \pm 200$ cm^{-1} . This suggests that the relative difference between ω_{psa} and ω_{psb} in the superconducting state does not appear to be related to a mass enhancement effect. In explaining this, it is noticed that the zero-temperature extrapolation of ρ_{dc} (or $1/\tau$) along the b axis appears to be finite, whereas in the a axis the zero-temperature intercept is very close to zero. This suggests there is an additional scattering channel in the b or superlattice direction that is causing additional absorption at finite frequencies in the superconducting state. This could explain a larger value for λ_L when the electric field is polarized along this direction.

Optical Conductivity and Symmetry of the Order Parameter

One of the most fundamental aspects regarding the microscopic description of superconductivity is the symmetry of the order parameter. In Chapter IV, a discussion was given about pairing scenarios that have been proposed in the copper-oxide superconductors mainly from electromagnetic penetration depth and ARPES measurements. The interpretations of these results strongly suggest that the order parameter in the high- T_c materials is highly anisotropic,^{5,7,55,116,127-130,186} with some studies predicting an order parameter with $d_{x^2-y^2}$ symmetry.^{5,116,186}

An answer to the important question of the symmetry of the order parameter in a superconductor can be obtained, in principle, from anisotropy in the electromagnetic absorption $\sigma_1(\omega)$. By considering first a superconductor with isotropic s -wave order parameter Δ , Mattis and Bardeen derived¹⁸⁷ an expression for the ratios of the conductivity in the the superconducting and normal states. The formula adapted for

a type II superconductor in the dirty limit can be written as¹⁸⁸

$$\frac{\sigma_{1s}}{\sigma_n} = \frac{1}{\hbar\omega} \int_{-\infty}^{\infty} \frac{|(E(E + \hbar\omega) + \Delta^2)[f(E) - f(E + \hbar\omega)]|}{(E^2 - \Delta^2)^{1/2}[(E + \hbar\omega)^2 - \Delta^2]^{1/2}} dE \quad (51)$$

where E is the quasiparticle energy and $E' = E + \hbar\omega$. The Fermi distribution function is denoted by $f(E)$. A numerical evaluation of Eq. 51 at zero temperature indicates that σ_{1s} vanishes for $\omega < 2\Delta$. The missing spectral weight of σ_{1s} in the range $0 < \omega < 2\Delta$ is argued¹⁸⁸ appears as a δ -function at $\omega = 0$. A physical explanation for this is given in the context of the BCS theory where excitations of Cooper pairs at $T = 0$ can only occur for energies larger than 2Δ . In the case of finite temperatures, thermally excited quasiparticles can give rise to a Drude-like contribution to $\sigma_1(\omega)$ with a width in the order of $1/\tau$.

Similarly, a superconductor with a gap function that has nodes on the Fermi surface will also result in a finite contribution to $\sigma_1(\omega)$ for $\omega < 2\Delta$ even at zero temperature. The reason for this is that it only takes an arbitrarily small energy to excite Cooper pairs of electrons close to the location of the nodes on the Fermi surface. In general, it takes long and laborious analytical and numerical calculations to obtain a quantitative effect of a nonisotropic gap in the spectrum of $\sigma_1(\omega)$ in the superconducting state. Using a self-consistent T -matrix approximation, Hirschfeld *et al.*¹⁸⁹ carried out the calculation of σ_{1s}/σ_n for unconventional nons-wave superconductors. It is found the results reproduce the Mattis-Bardeen formula for conventional type II superconductors in the dirty. Furthermore, the Mattis-Bardeen formula is not recovered for a unconventional superconductor in the case of high impurity scattering. In the collisionless limit with a small scattering phase shift, which would be the appropriate limit for the high- T_c superconductors, an expansion of σ_{1s}/σ_n in ω indicates a square power law dependence for ω close to zero in the case of a gap function with polar symmetry, while it is found a ω^4 for gap with axial symmetry. Hence, these

results indicate that for a superconductor with anisotropic order parameter, electromagnetic radiation is always absorbed for frequencies down to $\omega = 0$ and that the low frequency $\sigma_1(\omega)$ will show substantial anisotropy when measured on a single crystal.

The results shown here unambiguously show that the ab -plane optical response of $\text{Bi}_2\text{Sr}_2\text{CaCu}_2\text{O}_8$ is anisotropic both above and below T_c . The a -axis reflectance in the superconducting state reaches almost 100% for frequencies in the far infrared, while there is a difference in the reflectance level ($R_a > R_b$) in the order 1–2%. To illustrate this, we show in Fig. 49 the relative absorptivity ($R_a - R_b = A_b - A_a$) at 20 K for two different samples. Then, a Kramers-Kronig analysis of the reflectance in the two polarizations gives anisotropy in $\sigma_1(\omega)$. In the normal state the anisotropy in the far-infrared conductivity is in the order of 20% larger along the a -axis. In the superconducting state, the anisotropy in $\sigma_1(\omega)$ is a factor of two larger along the b axis down to the lowest frequency measured in the experiment.

Of the two possibilities that have been proposed to explain the optical conductivity in the copper-oxide superconductors, there will be two interpretations that can be advanced for this low-frequency anisotropy below T_c . If a one-component analysis with a frequency dependent $1/\tau$ is used to explain these results, the superconducting-state conductivity should then be due to excitations across the superconducting gap. The observed anisotropy in $\sigma_1(\omega)$ below T_c will imply an order parameter consistent with a C_{2v} rather than a C_{4v} symmetry. If this interpretation is taken, these data are incompatible with s -wave pairing or pure $d_{x^2-y^2}$ gap symmetry. The results would be compatible with a p -wave gap, a combination of s and d pairing or with some d -wave order parameter like the d_{xz} that has been suggested in a recent photoemission experiments.⁷

In the second interpretation, if the conductivity is decomposed in two components, explanation for the observed anisotropy in σ_a and σ_b could then be due to two factors.

Above T_c the free-carrier damping rate is 20% stronger along b ($1/\tau(100K) = 180$ cm^{-1} for the b axis and 150 cm^{-1} for the a axis). Above and below T_c , the second midinfrared component has a larger contribution along b than along the a axis. This anisotropy is compatible with the observed orthorhombic unit cell in this material.

CHAPTER VIII

RESISTIVITY TENSOR OF $\text{Bi}_2\text{Sr}_2\text{CaCu}_2\text{O}_8$ SINGLE-DOMAIN CRYSTALS

The anisotropy that is observed in the transport properties of the copper-oxide superconductors is another indication of the anisotropy that is present in their crystal structure as was discussed in Chapter II. For example, the 2-dimensional stacking of the CuO_2 planes is considered the main reason why the conduction of electrical current is basically a 2-dimensional process in these materials. Hence, this anisotropy provides a natural explanation for the observed much lower conductivity along the c axis in comparison to the higher conductivity in the basal planes. Moreover, it has become evident that anisotropy in the electrical properties is not just limited for transport within and between the CuO_2 planes. It has become clear the transport properties within the orthorhombic planes of these materials exhibit anisotropic properties as well. In $\text{YBa}_2\text{Cu}_3\text{O}_{7-\delta}$, for example, anisotropy ratios, ρ_a/ρ_b , in the order of 2:1 have been reported in the literature.^{16,190} These results conclusively show the b or the CuO chain direction is more conductive in this material. This is also consistent with the anisotropy that has also been observed in the far-infrared conductivity of single-domain crystals of $\text{YBa}_2\text{Cu}_3\text{O}_{7-\delta}$ shown in Chapter VI and reported in previous measurements.

There have been two reports of the basal plane resistivity anisotropy in $\text{Bi}_2\text{Sr}_2\text{CaCu}_2\text{O}_8$ as well. In this case, the results appear to be somewhat conflicting about whether the a or b direction is more conductive. In one study, Martin *et al.*¹⁸ reported the conductivity parallel to the b axis, or superlattice direction, is a factor of two larger compared to the a axis, while Yamaya *et al.*¹⁹¹ reported the higher conductivity of $\text{Bi}_2\text{Sr}_2\text{CaCu}_2\text{O}_8$ is along the a axis.

This chapter is devoted to presenting dc resistivity measurements along the three principal axes of $\text{Bi}_2\text{Sr}_2\text{CaCu}_2\text{O}_8$ single-domain crystals. These measurements are unique, in comparison with previous measurements, in the sense they were performed on the same crystals that were studied using polarized optical reflectance along the principal axes in the ab plane. Hence, this enable a direct comparison of the results of the ab -plane anisotropy in the frequency-dependent conductivity with the anisotropy directly measured using dc resistivity methods.

Sample Preparation and Measurement Method

Sample preparation method is as described on p. 65. We cleaved and cut two pieces from a sample that was previously studied using polarized reflectance in the ab plane. The dimensions along the three principal axes for sample one were $L_a = 0.84$ mm, $L_b = 0.73$ mm, and $L_c = 5.4 \times 10^{-3}$ mm. Sample two had the dimensions $L_a = 0.59$ mm, $L_b = 0.73$ mm, and $L_c = 12.6 \times 10^{-3}$ mm. Gold contacts were evaporated near the corners on each sample. In the case of sample one, contacts were placed as shown schematically in Fig. 66 (Sample two only had contacts on the ab plane). The evaporation of gold pads was followed by an annealing procedure that was performed at a temperature of ~ 340 °C in flowing O_2 for a period of 6 hours. This heat treatment lowered the contact resistance and ensured a stable Ohmic behavior of the contacts with temperature cycling. As a first step, very fine gold wires (20 μm diameter) were first soldered to a connector with up to six gold coated pins. The other end of these wires were then affixed to each of the contact pads on the sample under a microscope using fast-drying Ag paint. The measured contact resistance of the completed electrode was 2 Ω or less. The connector (with the sample attached) was then mounted on a lead probe that was thermally anchored to the cold head of a closed-cycle refrigerator (CTI Cryogenics). A couple of radiation shields were placed on top of the cold head to ensure uniform temperature across the probe leads and the

sample. The sample temperature was monitored with a temperature controller (Lake Shore DRC 80C) that was connected to a silicon diode sensor and a heater element both attached to the cold head of the cryostat unit. A typical run was done by first cooling down the sample to the desired temperature, and taking the data in the warm up cycle. Temperature reproducibility obtained in this set up has been determined to be ± 0.2 K or better over the temperature range measured (70–300 K).

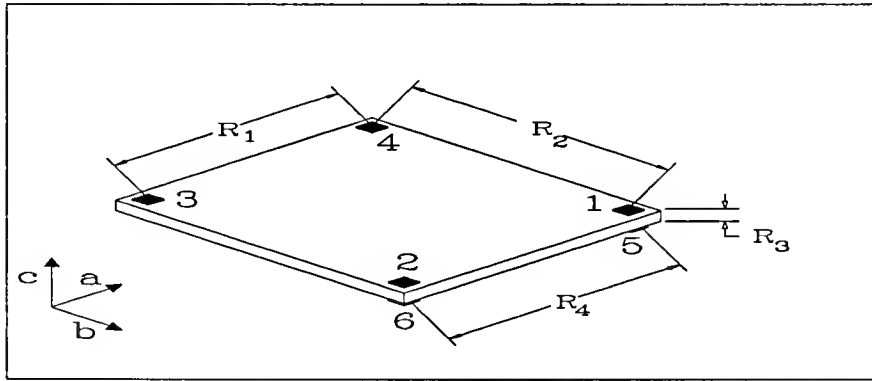


Fig. 66. Contact arrangements on sample one.

Table 4. Voltage-current ratios (V_n/I_n) for different contact configurations to obtain the R_n values on sample one.

R_n	I_n	V_n	axis
1	1,2	3,4	"a"
2	2,3	1,4	"b"
3	1,5	2,6	"c"
4	1,2	5,6	"a"

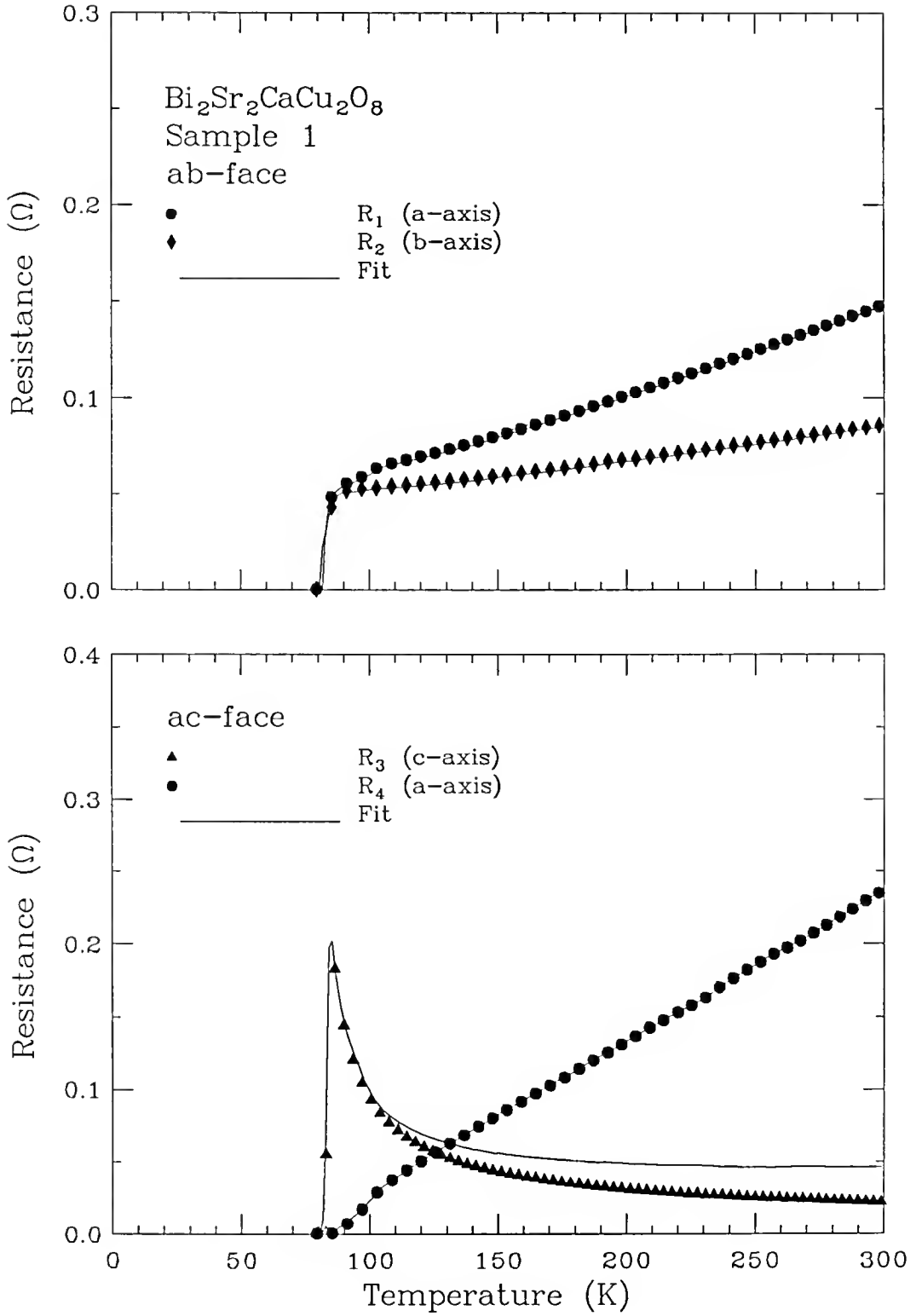


Fig. 67. Resistance measurements on the *ab* plane (top part) and the *ac* face (bottom part) of sample one.

The resistance measurements were obtained as voltage-current ratios ($R = V/I$) by using a standard ac phase-sensitive technique with an excitation current of $\sim 700\text{--}\mu\text{A}$ and a frequency of $f \sim 22\text{ Hz}$. The results were insensitive to the size of the current. The contact configuration on sample one allowed the measurement of voltage-current ratios on two faces of the crystal, *i.e.*, ab and ac faces, while for sample two we measured resistances for current mostly along the a - and b -axis directions. The results of the measurements on sample one are shown in Fig. 67, while the results on sample two are in Fig. 68. As an example, the R_1 shown in Fig. 67 corresponds to the ratio of a voltage that is taken from contacts 3,4 to an current applied through 1,2 on the ab face. The other current-voltage configurations are illustrated in Table 4. The bottom part of Fig. 67 shows the resistances obtained measured on the ac face. It can be seen in both figures, in spite of the fact that the c -axis dimension is much smaller compared to the a or b -axis dimensions the resistance measured across this direction (R_3) is comparable in magnitude to the resistance measured either along a or b . In addition, the increasing resistance as the temperature is lowered clearly points to semiconducting-like behavior for electronic conduction along the c axis. By contrast, when most of the current is limited to the a or b direction of the crystal, the resistance decreases as the temperature is lowered. There is some flattening in the ab plane results below 150 K that is due to the increasingly higher c -axis component of the resistivity. Since it is expected that $\rho_{ab} \ll \rho_c$, most of the current will be confined to a few layers on the surface. This is reflected in Fig. 67, where the magnitude of R_4 , which is obtained by applying the current on one side while the voltage is measured on the other, diminishes greatly even before the sample enters in the superconducting state. Hence, the measured resistances are influenced by the geometry of the contact configurations and they do not necessarily reflect the true behavior of the resistivity tensor along the principal axes of the sample. This will

become evident when describing the method used in extracting ρ_a , ρ_b , and ρ_c in the next section.

Resistivity Analysis for Anisotropic Materials

The electrical resistivity ρ is defined in terms of the vector electric field \mathbf{E} and the vector current density \mathbf{J} by the equation

$$\mathbf{E} = \rho \mathbf{J}, \quad (52)$$

where ρ is a geometrical invariant given by the formula

$$\rho = R \frac{A}{L}, \quad (53)$$

and R is the resistance measured on a solid by determining the voltage drop along the length L and with current flowing through the cross sectional area A . In anisotropic systems, ρ is a second-rank tensor. There are several methods to determine the components of the resistivity tensor for anisotropic conductors. Since the results of Fig. 67 suggest our crystal is electrically thick, the Montgomery analysis¹⁹² in its original form can not be used to extract the resistivities in the crystal. Instead, the transformation to the resistivity tensor from the voltage-current ratios that are obtained from the contact configurations shown in Fig. 66 are obtained by following the next two steps. The first one involves the use of a simple theorem based on work by van der Pauw¹⁹³ to map an anisotropic crystal of physical dimensions L_i into an equivalent isotropic block of scaled dimensions l_i . The mapping in the van der Pauw method is done through the expressions

$$l_i = L_i \left(\frac{\rho_i}{\rho} \right)^{1/2}, \quad (54)$$

$$\rho = (\rho_1 \rho_2 \rho_3)^{1/3}, \quad (55)$$

where ρ_i and ρ are the resistances of the anisotropy and equivalent isotropic crystals respectively. The second step involves solving the problem for the resistivity ρ of an

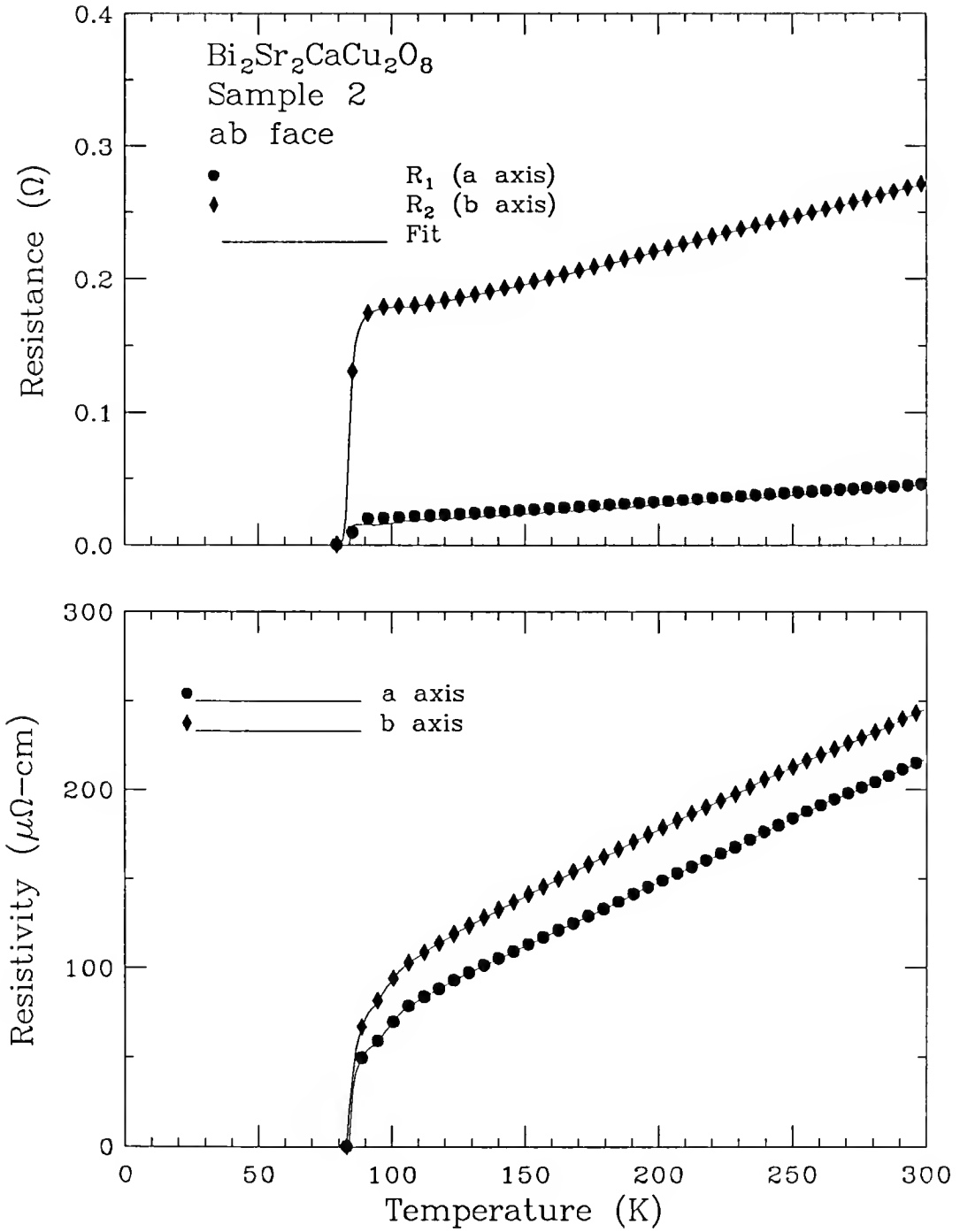


Fig. 68. Top part: Resistance measurements on the ab face of sample two. Bottom part: Component of the resistivity tensor along a and b axes for sample 2 derived from a fit to the resistance data.

isotropic rectangular block with dimensions l_i , l_j , and l_k . Let us consider the situation when a current I_i is injected in two corners of the ij face along the i direction and the voltage V_{ij} is read in two adjacent corners on the same face. This problem was first solved analytically by Logan, Rice and Wick.¹⁹⁴ In the solution, they found that the resistance defined by the voltage-current ratio

$$R_i^{ij} = \frac{V_{ij}}{I_i}, \quad (56)$$

can be written as

$$R_i^{ij} = \left(\frac{4}{\pi}\right) M_i^{ij} \rho, \quad (57)$$

where M_i^{ij} is a geometrical factor that only depends on the solid dimensions, l_i , l_j and l_k . It can be shown the calculation of M_i^{ij} is reduced to finding the sum of electrostatic potentials produced by a 3-dimensional array of plus and minus charges by using the method of images.¹⁹⁴ The result is

$$M_i^{ij} = \left(\frac{2l_i}{l_i l_k}\right) \sum_{m=1}^{\infty} \sum_{n=0}^{\infty} \frac{\epsilon_n}{S_{ijmn} \sinh(S_{ijmn})}, \quad (58)$$

where $\epsilon_0=1$; $\epsilon_n=2$ for $n \neq 0$ and

$$S_{ijmn}^2 = \pi^2 (2m+1)^2 \left(\frac{l_j}{l_i}\right)^2 + \pi^2 n^2 \left(\frac{l_j}{l_k}\right)^2. \quad (59)$$

Then, by substituting the van der Pauw's formulae (Eq. 54 and Eq. 55) for the mapping of the anisotropic crystal in the previous two equations, it is obtained

$$R_i^{ij} = \left(\frac{8L_j \rho_j}{L_i L_k}\right) \sum_{m=1}^{\infty} \sum_{n=0}^{\infty} \frac{\epsilon_n}{S_{ijmn} \sinh(S_{ijmn})}, \quad (60)$$

where now

$$S_{ijmn}^2 = \pi^2 (2m+1)^2 \left(\frac{L_j}{L_i}\right)^2 \left(\frac{\rho_j}{\rho_i}\right) + \pi^2 n^2 \left(\frac{L_j}{L_k}\right)^2 \left(\frac{\rho_j}{\rho_k}\right). \quad (61)$$

The problem has been reduced to finding the resistivities, ρ_i , that will satisfy these equations in term of the measured R_i^{ij} .

A non-linear fit to the data was done by using a grid-search method as described by Bevington *et al.*¹⁹⁵ The procedure is simply to select starting parameters, in this case the resistivities ρ_a , ρ_b , and ρ_c , and then to find the value of the resistivities that best fit the measured R_i values. The optimization of parameters was done by minimizing the value of χ^2 defined by the formula

$$\chi^2 = \sum \frac{(R^{fit} - R_i)^2}{\sigma_i^2}, \quad (62)$$

where the sum is over all the data points and σ_i is the uncertainty in the resistance measurements, which was estimated from the last significant digits in the current and voltage readings. The optimization of the parameters is performed cyclically until a best fit is found that minimizes χ^2 defined in Eq. 62. This procedure is repeated at each temperature until a set of resistivities (ρ_a, ρ_b, ρ_c) is generated. One aspect that we considered in this procedure is to ensure that each set of resistivities obtained at each temperature yield the absolute minimum for χ^2 . If the parameters are strongly correlated with variations of χ^2 , then the convergence to the “true” minimum will not be guaranteed and the convergence will be slow. The convergence in the method was tested by changing the starting parameters and letting the program to determine to best fit. We found the results were insensitive to this, only the time to determine a satisfactory fit changed depending on the initial parameters.

Figure 67 and the top part of Fig. 68 display the resistance measurements with the fitted value for sample one and two respectively. In fitting the results for sample two, we used the values of the resistivity ρ_c generated from sample one, and let the program to generate new values for ρ_a and ρ_b . Overall, we observe Eq. 60 provides reasonable good fits to the resistance data. There appears to be systematic differences of the measured and predicted values of the resistances in Fig. 67. There could be many reasons for this. One is a combination of the 2-dimensionality, *i.e.*, $\rho_c \gg \rho_{ab}$,

that causes the sample to be electrically thick and the very layered nature of the sample. Hence, small uncertainties in the thickness of the sample could translate into a relatively large difference in the measured resistance with respect to the predicted one. Other effects that could come into play to explain the systematic differences are inhomogeneity, finite size effects of the contacts, and slight misalignment of the contacts on the sample.

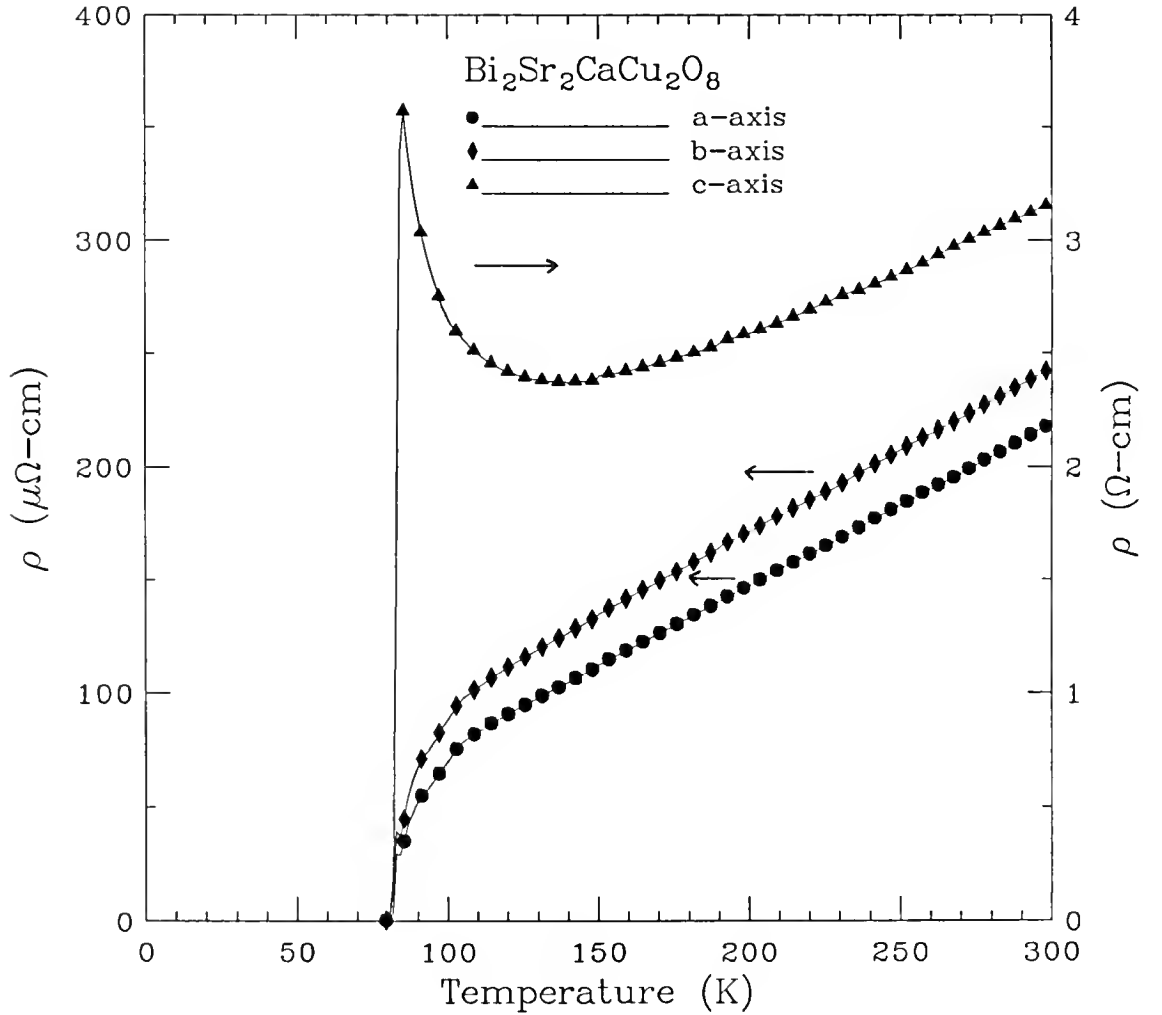


Fig. 69. Resistivity tensor for sample one derived from a fit to resistance data using Eq. 57.

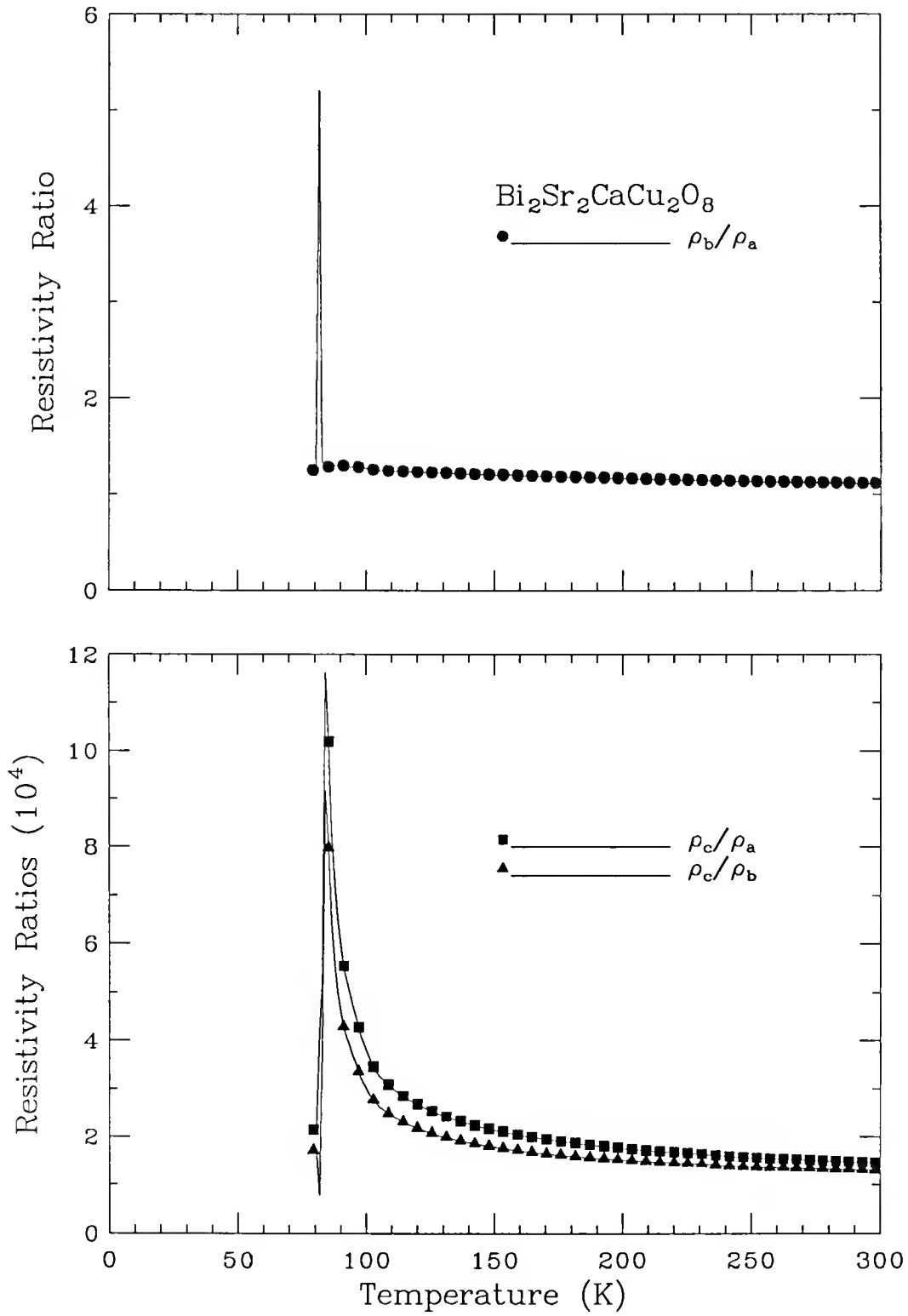


Fig. 70. Top part: Resistivity ratio ρ_b/ρ_a ; bottom part: Resistivity ratios ρ_c/ρ_a and ρ_c/ρ_b for sample one.

Resistivity Tensor

c-Axis Results

The results of the resistivities in the three principal axes are shown in Fig. 69. It is clear the resistivity in the c -direction is much higher, by a factor of 10^4 , when compared to the room temperature values in the ab -plane. This anisotropy grows even larger at low temperature as shown in the bottom part of Fig. 70. As results of this anisotropy, the $\text{Bi}_2\text{Sr}_2\text{CaCu}_2\text{O}_8$ material exhibits a much more pronounced 2-dimensional behavior in comparison to other copper-oxide superconductors. More evidence of this is seen in that ρ_c has a temperature dependence that shows a semiconducting-like behavior that is in sharp contrast to the linear temperature dependence that is observed in the resistivity along the a or b axis. To explain this behavior, Anderson and co-workers¹⁹⁶ have proposed a model in which the c -axis resistivity is assumed to contain a $1/T$ dependence term (in addition to a linear) that is related to the quasiparticle tunneling across the c -axis direction. Such picture will be consistent with a holon-spinon model for the transport of charge in the high- T_c systems. However, the validity of this model is challenged by the fact that in other copper-oxide superconductors, such as $\text{YBa}_2\text{Cu}_3\text{O}_{7-\delta}$, the temperature dependence of ρ_c is found to vary from semiconducting in reduced T_c samples to linear in fully oxygenated 90 K samples^{16,197}. Since similar changes in ρ_c with doping have been observed in other type of samples,²⁸ it is now thought that the c -axis resistivity in these materials is more sensitive to the presence of doping and/or impurities between the CuO_2 layers in the sample than to any intrinsic mechanism. The strong anisotropy that is observed in $\text{Bi}_2\text{Sr}_2\text{CaCu}_2\text{O}_8$ could be due to the fact that the entities that separate the CuO_2 planes in this material, the Bi_2O_2 layers, have an insulating character. However, this point has also been disputed by a photoemission study where it

has been shown the Bi_2O_2 layers can have metallic-like behavior in samples annealed in a high-oxygen pressure environment.¹⁹⁸

Anisotropy in the ab -Plane Resistivity

We now turn our attention to the anisotropy that was observed within the ab plane of the samples. From the ratios shown in the top of Fig. 70, it is clear the anisotropy in the ab -plane resistivity is not as strong as with respect to the c axis, the resistivity along the b axis is higher by about 20% in sample one, while it was found in sample two $\rho_b/\rho_a \sim 1.35$. The reasons for this could be due to a small contact misalignments in the two samples or a slightly different oxygen stoichiometry in sample two, since this sample was reannealed after it was cleaved. The close agreement in the anisotropy between the dc and far-infrared conductivity we measured on the same $\text{Bi}_2\text{Sr}_2\text{CaCu}_2\text{O}_8$ crystal gave us a consistency check in our transport measurements. Furthermore, these results are in agreement with the results of Yamaya *et al.*¹⁹¹ although they report a larger anisotropy with a resistivity that is several times lower along the a axis.

The enhanced conductivity that Friedmann *et al.*¹⁶ found along the b axis in $\text{YBa}_2\text{Cu}_3\text{O}_{7-\delta}$ single-domain crystals ($\rho_a/\rho_b \sim 2.2$) was attributed to the influence of the chains in the CuO_2 planes of this compound. This means the oxygen atoms that are presents in the CuO chains of this compound are providing some free carriers (preferentially along the b axis of the crystal) in addition to doping the CuO_2 planes.

If the anisotropy that is observed in $\text{Bi}_2\text{Sr}_2\text{CaCu}_2\text{O}_8$ is then due to the presence of the incommensurate superlattice modulation that is present along the b axis of this material, the results suggest this structure is providing a deleterious effect to the conduction of charge in the CuO_2 planes of this compound. For such interpretation to hold some validity, one possible explanation could be the incommensurate structure is providing an additional channel for scattering, due to possible disorder, for the

free carriers moving along this direction that is absent in the direction perpendicular. As was discussed in Chapter V, analysis of the far-infrared conductivity in the two-component picture suggested the temperature dependence in the free-carrier part scattering rate is anisotropic. At 100 K, $1/\tau$ is 20% higher along the b axis of the crystal. This picture would seem consistent with the interpretation expressed above. It should be noticed that such additional elastic scattering channel is also suppressed in the superconducting state.

Temperature Dependent ab -Plane Resistivity

Next, we turn our attention to the temperature dependence of the ab -plane resistivity. The high linearity in the temperature-dependent resistance is shown in Fig. 71, where a third sample was measured by using four probe contacts with current along the a axis of the sample. The configuration of the contacts was such that the c - and b -axis current paths were basically short-out by the Ag contacts. The numerical derivative of the curve is obtained by defining a power-law resistivity in the form

$$\rho(T) = AT^\alpha + B, \quad (63)$$

where A and B are constants and α is the exponent defined by

$$\alpha = \frac{T}{R} \frac{dR}{dT}. \quad (64)$$

The results of a numerical evaluation of Eq. 64 are shown in the bottom part of Fig. 71. It is seen here the exponent or the value of α is very close to 1.

Since the temperature dependence shows a high linearity for the results of sample one and two over the measured temperature range, we performed a fit to the data using the equation

$$\rho(T) = AT + B, \quad (65)$$

where A and B are the slope and intercept respectively. The results for the a axis yield a slope that is $A_a \sim 0.70 \mu\Omega\text{-cm/K}$ and an intercept that is nearly zero ($B_a \sim 3 - 6$

$\mu\Omega\text{-cm}$). The results for the b axis yield a slope that is slightly higher, $A_b \sim 0.73 \mu\Omega\text{-cm/K}$ and a finite intercept, $B_b \sim 25 - 30 \mu\Omega\text{-cm}$. These results are nearly the same in sample one and two (the slope for the a -axis results in sample three is $A_a \sim 0.60 \mu\Omega\text{-cm/K}$). As discussed in Chapter VII, the linear temperature dependence in the scattering rate allowed us to determine a coupling constant λ in the order $\lambda_a \sim 0.35$ and $\lambda_b \sim 0.31$. These results imply the coupling of the carriers to the excitations that are causing the scattering is in the weak-coupling limit.

Closer Look to the Transition Temperature

This section is devoted to results of a closer look to T_c in the $\text{Bi}_2\text{Sr}_2\text{CaCu}_2\text{O}_8$ samples that were studied as a function of current flow along each of the three principal axes of the sample. A closer look to the results shown in Fig. 67 and in Fig. 68 reveals the actual transition temperature at which zero resistance is obtained differs depending on which direction the current flows. There are examples in the literature of split superconducting transitions in the copper-oxide superconductors.^{19,199-202} In one of those studies, Bucher *et al.*²⁰¹ found a difference in T_c in single-domain crystals of $\text{YBa}_2\text{Cu}_3\text{O}_{7-\delta}$ in the order of 1–2 K higher along the a axis. However, these results were found reproducible in only one of the sample that was studied.

In what relates to the $\text{Bi}_2\text{Sr}_2\text{CaCu}_2\text{O}_8$ materials, Wan *et al.*¹⁹ reported the resistive transition of $\text{Bi}_2\text{Sr}_2\text{CaCu}_2\text{O}_8$ single crystals along the c -axis is found to be higher (by 2–3 K) in comparison to the results in the basal planes. In this study, which did not address anisotropy in the ab plane, the zero magnetic field upper T_c was interpreted as corresponding to Josephson coupling of parallel CuO_2 bilayers, and the lower T_c to a Kosterlitz-Thouless transition in the two-dimensional CuO_2 planes. It was found in other report²⁰² that the onset of superconductivity in iodine intercalated $\text{Bi}_2\text{Sr}_2\text{CaCu}_2\text{O}_8$ single crystals shows some anisotropy in the ab plane as well.

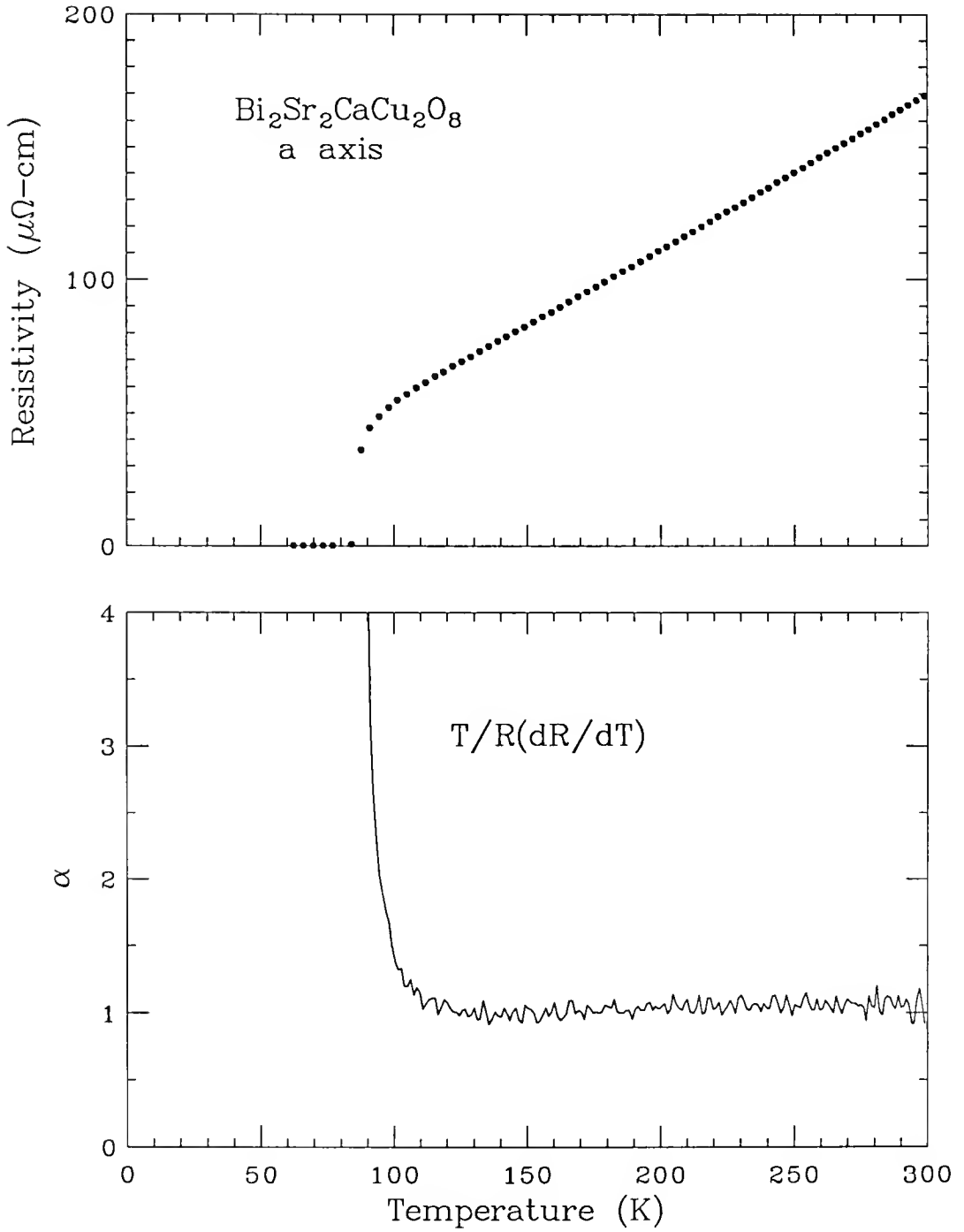


Fig. 71. Top part: Resistivity *vs.* temperature along *a* axis for a third $\text{Bi}_2\text{Sr}_2\text{CaCu}_2\text{O}_8$ sample. Bottom part: Result of numerical evaluation of exponent α using Eq. 64.

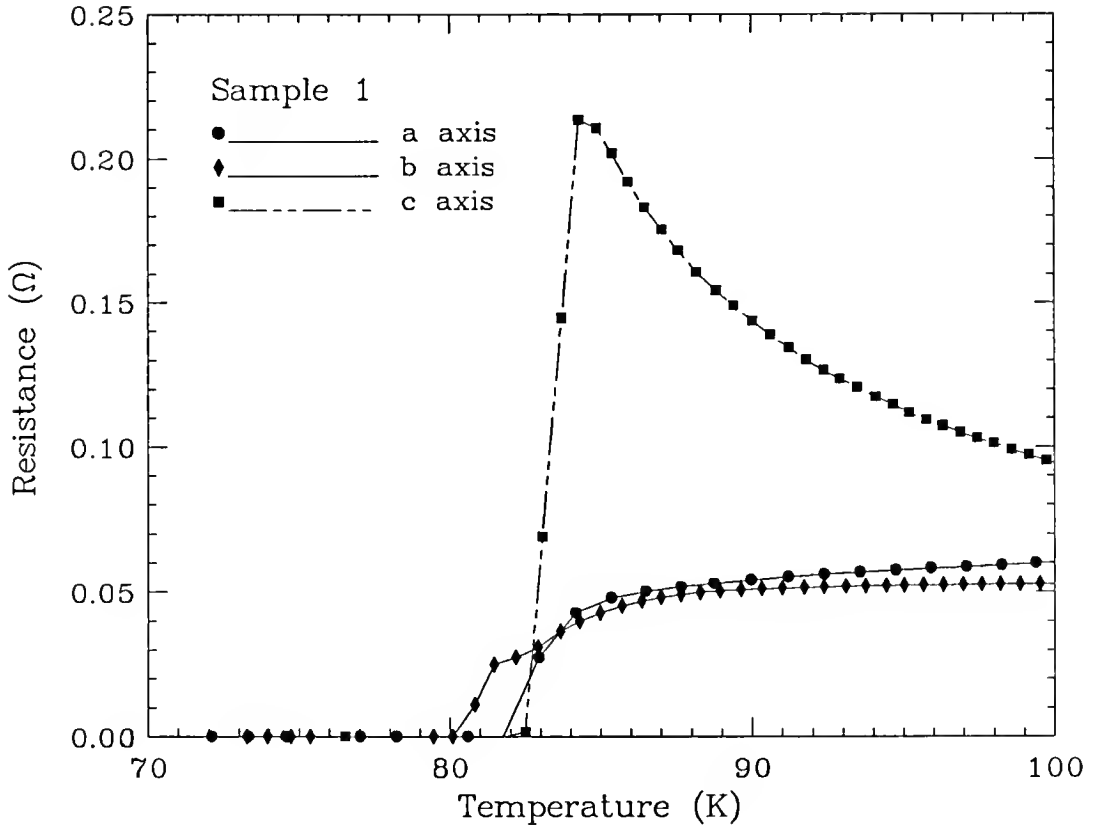


Fig. 72. Expanded view of the resistance *vs.* temperature near T_c for sample one.

Results and Discussion

A closer look of the transition to the superconducting state is shown in Fig. 72 and Fig. 73 for sample one and two respectively. In these results, we observed that, when measured on the same sample, the zero resistance value is different depending on the direction the current is applied. To rule out other possible effects such as heating effects by the current or thermal gradient on the sample the experiments were ran with lower currents (a factor of 10 smaller) and the sample was more carefully shielded from the room temperature outside. We finally became convinced of these results after reviewing earlier resistance *vs.* temperature measurements on samples that had “bad” contacts. In one of those samples, four gold strips were evaporated

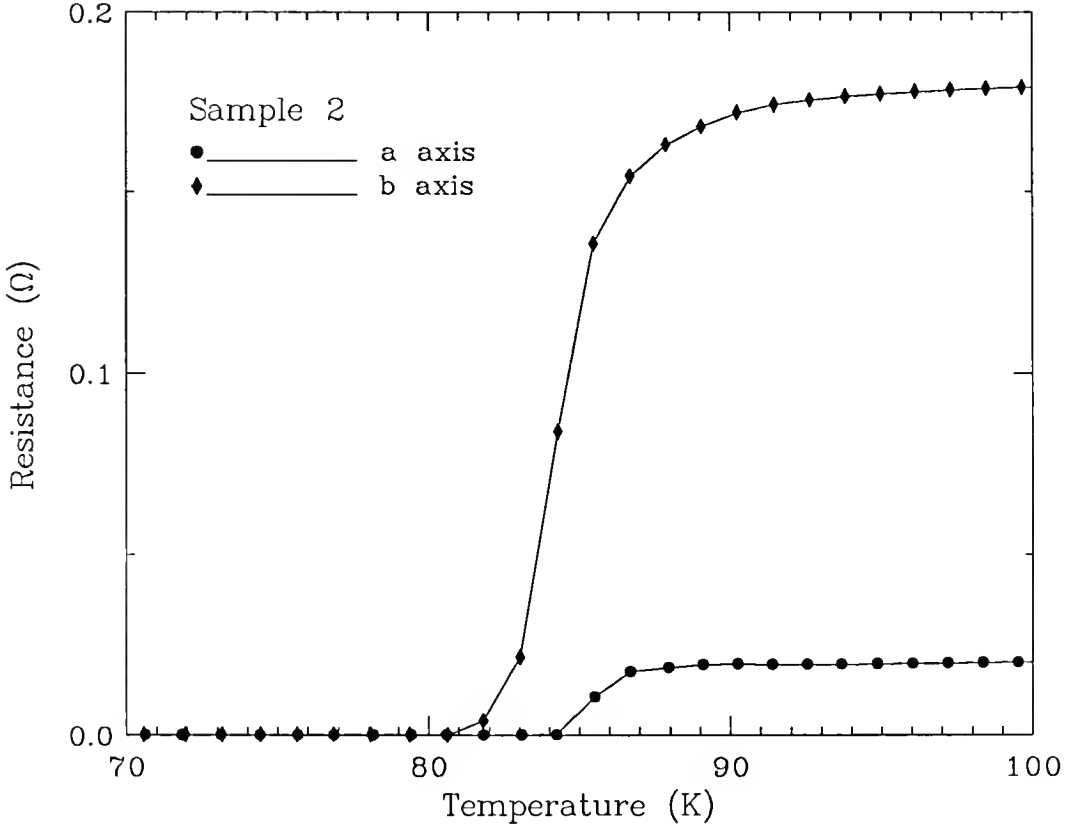


Fig. 73. Expanded view of resistance *vs.* temperature near T_c for sample two.

on a rectangular piece of the material to perform four-probe resistance measurements along the b axis of the crystal. The results of the resistance *vs.* temperature showed an upturn, typical of the c axis, followed by a two-step transition to the superconducting state. We initially discarded this data, since we were expecting a linear drop in the resistivity as function of temperature. A reannealing procedure of the sample in flowing oxygen at 600 °C for 12 hours and then in argon at 720 °C for 12 more hours did not change these results. It was later realized the current leads on this sample had a current path that included currents along the b and c axes of the sample. Hence, after repeated measurements with other samples, we finally realized the T_c is slightly higher (by as much as 2–3 K) when current flows along either the a or c direction in comparison to the result obtained along the b axis. So far, these results have

been found reproducible in one batch of samples. Measurements on another batch of samples from a different source, with some what poorer quality (determined by a broader transition) did not show differences in T_c . Attempts are being made, as of this writing to find reproducibility in these results by looking other samples with better qualities.

In explaining these results, the first thing that should be addressed is homogeneity of the sample. In general, the T_c in the copper-oxide superconductor is very sensitive to the amount of doping that is present in the sample. Hence, depending on the annealing history, the exact T_c might vary by a few degrees. This point is addressed in the results shown in Fig. 73. We observe that in this sample, which came from the one that was reannealed as mentioned above, the overall T_c hardly changed and the sample still shows two T_c in the ab plane.

The next question is what effect, if any, would have the superlattice modulation in the transport properties of the $\text{Bi}_2\text{Sr}_2\text{CaCu}_2\text{O}_8$ compound. Although the physical origin of the structure is not known, it is believed the superlattice is the result of partial substitution of some of the Bi sites in a way which is periodic along the b axis in the bismuth-rich layer.⁴⁷ The period of the structure is incommensurate with the crystallographic b -axis dimension in the unit cell and it is on the order of $4.7b$. A simple explanation of the two T_c observed in the sample could be done by considering pinning effects of the superlattice as a function of the current density direction along the three crystallographic axes in the sample. To provide a qualitative picture for this, we will address next the vortex state in type II superconductors.

Review of Flux-Flow Resistance and Kosterlitz-Thouless Transition

Two of the most fundamental lengths in a superconductor are the London penetration length λ_L and the coherence length ξ . The Ginzburg-Landau parameter κ , that is defined as $\kappa = \lambda_L/\xi$, gives an indication of the response of the superconductor

to a magnetic field. A superconductor is considered type I when $\kappa = \lambda_L/\xi < 1$. This means that when an external magnetic field is applied to the sample, it will be expelled from inside until the field reaches a critical value, called H_c , and the superconductivity is complete destroyed. In the opposite case, when $\kappa = \lambda_L/\xi > 1$, the superconductor is considered type II. In this case, there are two thresholds for the applied magnetic field. Initially, there will be a regime where not field can penetrate the sample. When the field exceeds a value called H_{c1} , the field is only partially exclude and the specimen remains electrically superconducting. Only at a much higher field, H_{c2} , does the flux penetrate completely and superconductivity vanishes. Hence, a type II superconductor in the mixed state is characterized by the circulation of superconducting currents in vortices throughout the bulk of the sample. The amount of field inside the core of a vortex is quantized in units of the flux quantum Φ_0 defined as

$$\Phi_0 = \frac{hc}{2e}, \quad (66)$$

where h and c are the Planck constant and the speed of light respectively and e is the elementary electronic charge. When a current is applied to a type II superconductor in the mixed state, there will be dissipation of energy due to a Lorentz force acting on each vortex flux, Φ_0 , that is threading the superconductor. The formula for the force density between the current in the superconductor and the flux threading through it is given by¹⁸⁸

$$\mathbf{F} = \mathbf{J} \times \frac{\Phi_0}{c}, \quad (67)$$

where Φ_0 is a vector in the direction of the magnetic field \mathbf{B} . Hence, flux lines tend to move transverse to the current due to this force. In the absent of pinning, if the flux lines move with a constant velocity \mathbf{v} , they essentially induce an electric field of magnitude

$$\mathbf{E} = \Phi_0 \times \frac{\mathbf{v}}{c}, \quad (68)$$

which is parallel to \mathbf{J} . This acts like a resistive voltage, and power is dissipated. From the above argument, it can be concluded that a type II superconductor in the vortex state will show some resistance unless there is a mechanism that prevents the Lorentz force from moving the vortices. The mechanism that has been found to be effective in preventing this is called the “pinning” force because it pins the vortices to fixed locations in the material providing a counter balance to the force described in Eq. 67. This pinning may result from inhomogeneity of the material.

All copper-oxide materials, including $\text{Bi}_2\text{Sr}_2\text{CaCu}_2\text{O}_8$, are all type II superconductors. The lower critical field, H_{c1} , in $\text{Bi}_2\text{Sr}_2\text{CaCu}_2\text{O}_8$ is in the order of 60–80 Gauss.¹¹ Therefore, the following scenario could explain the observed phenomenon of two T_c in the samples we studied. When current flows along the a axis, near T_c the material is close to the mixed or vortex state. The external current density will generate a Lorentz force on thermally generated vortex cores. The force is along the b axis. Then, the superlattice modulation provides pinning centers for the moving vortices and, hence, no resistive voltage should appear associated with the now fixed vortices. On the other hand, when current is along the b axis, the vortices will move within a range of temperatures near T_c and there would be a resistive voltage associated with the flux flow. Such phenomenon happens only for a narrow range of temperature, below which all the sample finally becomes superconductor. As pointed out by Wan *et al.*¹⁹ the lower T_c could be the results of a Kosterlitz-Thouless dissociation of bound vortex excitations. For this picture to have some validity there are certain criteria that must be met in the sample. The first one is that for the pinning centers to be effective, their distances must be on the scale of λ_L or ξ . Inhomogeneity on atomic scale or smaller will only cause electronic scattering which limits the mean-free path. The period of the superlattice, which is about 25 Å, is consistent with this picture. The next point is that this effect should only occur in samples

where the crystallographic structure is highly oriented. Sample with some disorder, will contain pinning centers randomly oriented all over the sample. The fact that we did not see this effect on a second batch of samples with a some what poorer quality is also consistent with this.

Concluding Remarks

In sum, we have determined the anisotropy in dc resistivity of $\text{Bi}_2\text{Sr}_2\text{CaCu}_2\text{O}_8$ single crystals. The results of anisotropy of the c axis *vs.* ab plane is $\rho_c/\rho_{ab} \sim 10^4$ at room temperature. This anisotropy is even larger at low temperatures on account of the fact the c -axis resistivity has a semiconducting-like behavior. In addition, the anisotropy in the ab plane is weak. The dc conductivity is lower along the b axis of the sample. This result is in good agreement with the observed anisotropy in the far-infrared conductivity obtained on similar samples by using polarized reflectance in the ab plane. A rather surprising result is that the transition to the superconducting state shows some anisotropy as well. It is found the T_c , determined from the temperature at which a first measurable resistance occurs, is higher when current flows along either the a or c axis (2–3 K) when compared to the result of current flowing along the b axis.

A final comment that should be made about these results is that if the finite resistance that is measured along the b axis, between T_{ca} and T_{cb} , is due to flux-flow motion there should be a voltage noise associated with it.²⁰³ The reasoning is that if vortices move across a conductor of width W with drift velocity $v = cE/B$, the voltage is the sum of a large number of square pulses of duration $\tau = W/v$ corresponding with each individual vortex. It can be shown²⁰⁴ that for a rectangular voltage pulse with duration τ , the rms noise is

$$\langle \delta V_f^2 \rangle = 2\Phi_0 V_{dc} \left(\frac{\sin \pi f \tau}{\pi f \tau} \right)^2 \delta f, \quad (69)$$

where δf is the bandwidth. Then, a model of crossing flux resistance will imply a noise with a cut-off frequency around $f \approx 1/\tau$. Evidence for this noise has already been measured in low- T_c samples made out of Mackay vanadium foils.¹⁹ It will be an important verification of crossing flux model to measure this noise in the present sample.

CHAPTER IX

CONCLUSIONS

This dissertation has been devoted to study the anisotropy in the infrared, optical, and transport properties of the copper-oxide superconductors. The single crystals that were studied and their corresponding critical temperatures are $\text{La}_2\text{CuO}_{4+\delta}$ ($T_c = 40$ K), $\text{YBa}_2\text{Cu}_3\text{O}_{7-\delta}$ ($T_c = 90$ K), and $\text{Bi}_2\text{Sr}_2\text{CaCu}_2\text{O}_8$ ($T_c = 85$ K). All these materials show a highly anisotropic crystal structure, which accounts for the anisotropy that is observed in their optical and transport properties. The feature common to all of these samples is the presence of the 2-dimensional CuO_2 planes that (with the appropriate doping) provide the metallic behavior and, hence, superconductivity in all these samples.

The first level of anisotropy is for transport of electric charge parallel (ab plane) and perpendicular (c axis) to the CuO_2 planes. The results of the optical reflectance of an oxygen-doped $\text{La}_2\text{CuO}_{4+\delta}$ single crystal indicate that for electric field parallel to the c axis the spectrum is typical of an insulator. The far-infrared spectrum is dominated by a total of four infrared-active phonons, one more than in the insulating parent compound. The extra mode at 492 cm^{-1} is a direct consequence of the additional oxygens in the structure. This is direct evidence the doped-oxygen atoms reside mostly in between the CuO_2 planes and nearby the apical-oxygen atoms. The insulating behavior in the c -axis direction is in sharp contrast to the spectrum in the ab plane, where metallic conductivity is observed. Evidence that electron-phonon interactions are important in the study of the optical properties of the copper-oxide materials is illustrated by showing ab -plane reflectance measurements obtained from the $\text{La}_2\text{CuO}_{4+\delta}$ single crystal when the propagation vector of the light \mathbf{q} is parallel

and perpendicular to the c axis of the sample. In this case, it is found the conductivity exhibits structures in the far infrared that are enhanced when \mathbf{q} is parallel to the c axis and the electric field vector is in the basal plane. Such structures appear to be the result of interactions between the ab -plane midinfrared carriers and the c -axis LO phonons.

Anisotropy along the two principal axes in the ab plane was addressed by measuring the reflectance of single-domain crystals of $\text{YBa}_2\text{Cu}_3\text{O}_{7-\delta}$ and $\text{Bi}_2\text{Sr}_2\text{CaCu}_2\text{O}_8$. The results indicate ab -plane anisotropy in the optical properties of both systems. In the normal state, the infrared conductivity in the $\text{YBa}_2\text{Cu}_3\text{O}_{7-\delta}$ single crystals is a factor of 2 larger along the CuO chain or b axis in comparison with the a axis. This is in agreement with the observed anisotropy in the dc resistivity that has been measured on samples from the same batch. Likewise, measurements on $\text{Bi}_2\text{Sr}_2\text{CaCu}_2\text{O}_8$ also show anisotropy along the principal axes in the ab plane. In this case, the infrared conductivity is higher along the a axis by about 20 % in comparison with the results along the b axis. Similar ab -plane anisotropy is observed in the normal-state dc resistivity of similar samples. By contrast, resistivity measurements along the c axis of $\text{Bi}_2\text{Sr}_2\text{CaCu}_2\text{O}_8$ single crystals indicate a semiconducting-like behavior. In this case, the estimated anisotropy between the c -axis and the ab -plane resistivities is $\rho_c/\rho_{ab} \sim 10^4$.

Regarding the dynamics of the infrared conductivity in the ab plane, we find all samples exhibit anomalous behavior. There is indication the normal-state conductivity exhibits a non-Drude behavior. This is characterized by a strong temperature dependence in the far infrared followed by a much weaker temperature variation at frequencies in the midinfrared. We find that, if the conductivity is analyzed in the frame work of the two-component picture, the low frequency part can be regarded as Drude-like in nature with a scattering rate that has a linear variation in temperature.

This is consistent with the linear temperature dependence observed in the dc resistivity. The coupling constant obtained in this analysis, assuming the linear temperature variation of the scattering rate is in the high-temperature limit, is in the order of $\lambda \sim 0.3 - 0.4$ in all samples.

The *ab*-plane anisotropy observed in the normal-state conductivity of these samples persists in the superconducting state as well. In both, $\text{YBa}_2\text{Cu}_3\text{O}_{7-\delta}$ and $\text{Bi}_2\text{Sr}_2\text{CaCu}_2\text{O}_8$, the conductivity at low frequencies is a factor of two larger along the *b*-axis in the superconducting state in comparison with the results along the *a*-axis. In $\text{YBa}_2\text{Cu}_3\text{O}_{7-\delta}$, most of this anisotropy is due to the presence of the chains along the *b* axis. For $\text{Bi}_2\text{Sr}_2\text{CaCu}_2\text{O}_8$, this suggests two possibilities. If a one-component analysis is applied to the measured $\sigma_1(\omega)$, the results suggest a highly anisotropic order parameter with a two-fold axis symmetry (C_{2v}) rather than a four-fold axis symmetry (C_{4v}) in this system. On the other hand, a two-component analysis can explain these results by assuming a second midinfrared component to the optical conductivity that is anisotropic.

Finally, estimates of the London penetration lengths, from the oscillator strength of the superfluid-carrier response, display some interesting anisotropy along the *a* and *b* axes. In $\text{YBa}_2\text{Cu}_3\text{O}_{7-\delta}$, the ratio in λ_L is $\lambda_a/\lambda_b \sim 1.3$. The fact that λ_L is lower along the *b* axis ($\lambda_b \sim 1200 \text{ \AA}$) suggests that the CuO chains can have a superconducting response in this compound. By contrast, in $\text{Bi}_2\text{Sr}_2\text{CaCu}_2\text{O}_8$ we find $\lambda_b/\lambda_a \sim 1.1$. This suggests some elastic scattering mechanism in the *b* axis of the crystal is resulting in some pair-breaking effect that is causing λ_L to be larger along this direction ($\lambda_b \sim 2000 \text{ \AA}$).

APPENDIX A

OPTICAL STUDY OF BEDT-TTF(ClO₄)₂

The organic donor *bis*(ethylenedithio) tetrathiafulvalene (BEDT-TTF), known also as the ET molecule, is the backbone of an important group of conducting and superconducting organic solids. The oxidation and formation of cation-radicals of this molecule is normally achieved by the incorporation of anions in a solidified structure that give this molecule different oxidation states. An indication of the considerable interest in the BEDT-TTF-based organic salts has been the many reports characterizing the properties of the neutral and cation-radical salts of this molecule.^{172,205-214} In particular, there have been optical investigations of the BEDT-TTF-based organic conductors (oxidation state between 0 and ⁺¹) and superconducting analogs with a formal charge of ⁺¹/2.^{172,211-214} Notably, there has not been much work done in the synthesis and characterization of cation-radical salts with oxidation states larger than ⁺¹. This appendix is devoted to results of an optical study of a double oxidized salt of BEDT-TTF(ClO₄)₂ that was prepared in the Chemistry Department of the University of Florida by Professor D. Talham and co-workers.

Crystal Structure of the BEDT-TTF(ClO₄)₂ Salt

A drawing of the BEDT-TTF²⁺ molecule with the different bond lengths in the molecule is shown in Fig. A-1. The two inner fulvalene rings (formed by carbon-sulfur atoms) are connected by a central C=C bond (labeled as bond A in Fig. A-1). This central portion forms part of the tetrathiafulvalene or TTF core. Attached to either side, there are two more rings composed of more carbon and sulfur atoms. In

addition, the molecule contains the CH_2 groups (not shown) that are connected to both carbon sites C4 and C5 to either side of the molecule. Structure and molecular analyses of several ET salts^{208,215,216} indicate the central $\text{C}=\text{C}$ double bond is the most affected by the oxidation of the molecule because the donated electronic charge is taken from this bond. For instance, in the oxidized molecule the $\text{C}=\text{C}$ double bond becomes longer, while the $\text{C}-\text{S}$ bonds become shorter.²⁰⁸

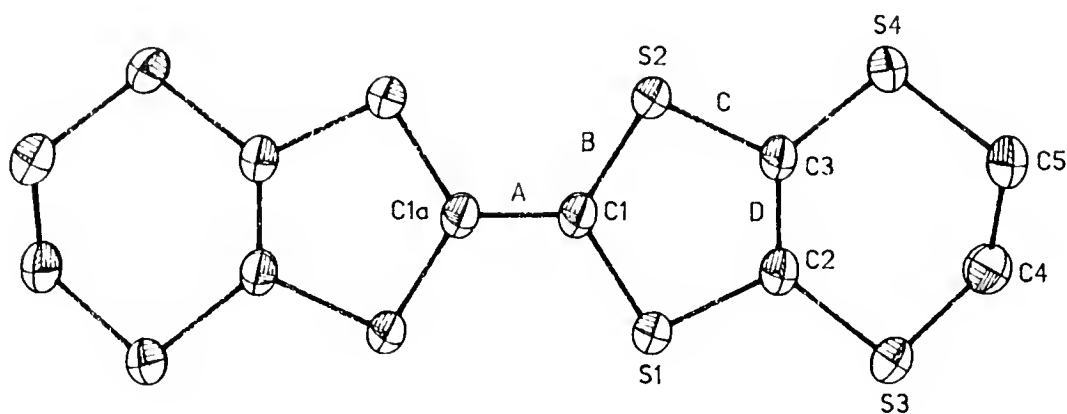


Fig. A-1. Thermal ellipsoid sketch of BEDT-TTF^{2+} in the salt $\text{BEDT-TTF}(\text{ClO}_4)_2$. The bond lengths are $A = 1.366 \text{ \AA}$, $B = 1.731 \text{ \AA}$, $C = 1.743 \text{ \AA}$, and $D = 1.345 \text{ \AA}$ (After Ref. 208).

X-ray investigations of the crystal structure of the $\text{BEDT-TTF}(\text{ClO}_4)_2$ salt revealed²¹⁶ that the structure crystallizes in the monoclinic space group P2_1 with unit cell dimensions $a = 5.867 \text{ \AA}$, $b = 9.579 \text{ \AA}$, $c = 17.669 \text{ \AA}$, and angle $\beta = 92.06^\circ$. In the structure shown in Fig. A-2, the BEDT-TTF^{2+} cations are surrounded by six counterions in a distorted octahedron. The relative orientation of the ET^{2+} cations is very similar to the one reported for the crystal structure of the neutral molecule.^{208,216} There are pairs of ET^{2+} cations ordered with the long axis nearly perpendicular to the

a axis, which is the stacking direction in the salt. Since this is the direction that provides the closest intermolecular contacts in the structure, the next larger dimension in the crystal, the *b* axis, contains a large projection of the long axis of the molecule. This will become important in the interpretation of the optical data that are going to be discussed later. The central C=C double bond, in the double oxidized molecule, becomes very weak and it can be regarded as a single bond with a distance of about 1.439 Å. The closest intermolecular contact is through the sulfur-sulfur atoms with a distance of 3.621 Å.

Experimental

Isolation²¹⁶ of the BEDT-TTF(ClO₄)₂ salt was achieved by placing ~ 10 mg of BEDT-TTF in one of the two working electrodes of an electrochemical H-cell with a solvent mixture of 10% CS₂ in ClCH₂COCl. A current density of 1 mA/cm² was maintained between the working electrodes for a period of 28 days. After the oxidation was completed, small and thin hexagonal plates of BEDT-TTF(ClO₄)₂ were formed that exhibit a blue tint in semitransparent samples.

Two samples of large enough area (~ 1 × 1 mm²) were selected for optical measurements. Identification of the optical principal axes in the (001) face was done by observation of the extinction point when rotating the sample under an Olympus microscope (model BHM) with crossed polarizers. The *a* and *b* axes in the crystal coincide with the directions of maximum optical anisotropy. Measurement of the polarized reflectance along these two axes was carried out in the frequency range of 3000–32,000 cm⁻¹ by using a Perkin-Elmer monochromator. Mounting of the sample was done by fixing it on to a frame with a hole of ~1 mm in diameter. A piece of Al-coated glass was mounted the same way as the sample and used as the reference. The surface of the sample was flat and smooth, giving a nearly specular reflectance. Due to the small thickness, the transmittance of one of the samples was measured in

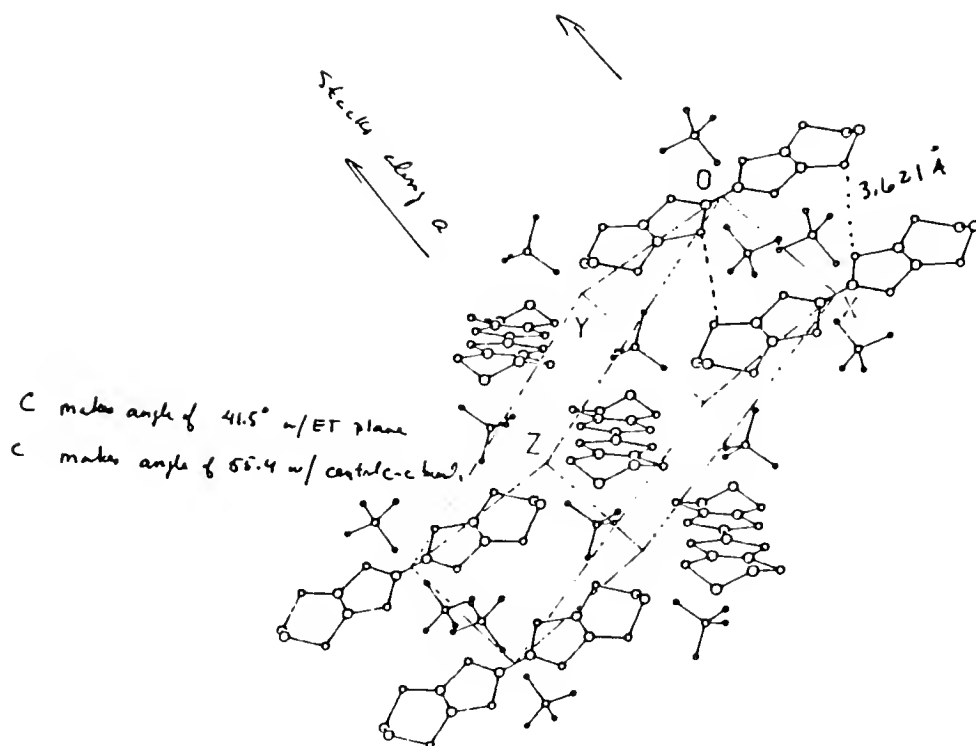


Fig. A-2. drawing of the crystal structure of the BEDT-TTF(ClO₄)₂ salt showing the orientation of the ET²⁺ ions in the crystal structure as determined from x-ray studies (After Ref. 216).

the far-infrared and midinfrared regions (100–4000 cm⁻¹) by using the fast-scanning Bruker IFS-113V Fourier interferometer.

Results and Discussion

Reflectance Measurements

Figure A-3 shows the room temperature reflectance parallel to the *a* and *b* axes in the BEDT-TTF(ClO₄)₂ salt. The spectra in the two samples measured were nearly

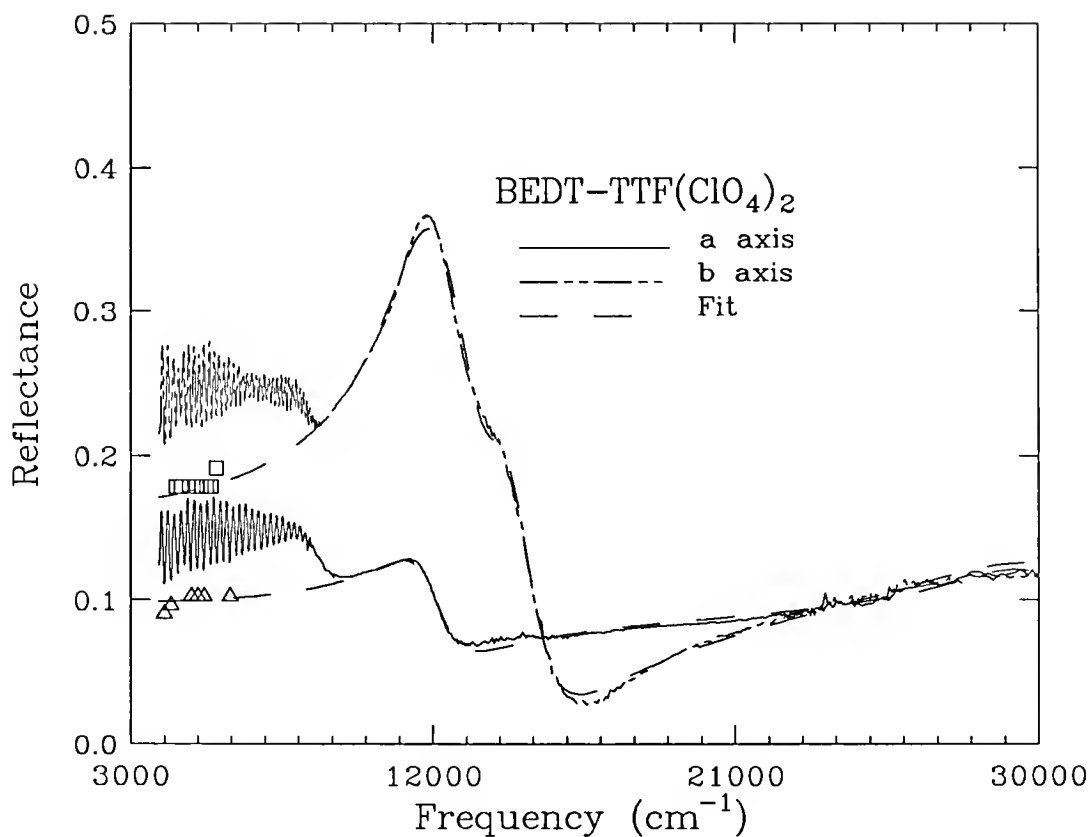


Fig. A-3. Reflectance of the BEDT-TTF(ClO₄)₂ salt for polarization of the light parallel to the *a* and *b* axes.

identical. One observation about these results is the appearance of fringes in the reflectance for frequencies just below 8000 cm⁻¹, caused by the very thin nature of the crystal studied ($\sim 13.5 \mu\text{m}$). The fringes pattern occurs due to successive constructive and destructive interferences between the beams reflected off the front and back surface of the sample. In addition, for nonabsorbing materials, the index of refraction (η) is purely real. In this case, the spacing of the fringes is given by the formula

$$\eta = \frac{1}{2d\Delta\nu}$$

where d and $\Delta\nu$ are the thickness of the sample and the period of the fringes respectively. The symbols (square and triangles) shown in Fig. A-3 are single-bounce

reflectance values calculated from the refractive index estimated from the fringes that are observed for frequencies below 8000 cm^{-1} . Clearly, η becomes complex in the region where the fringes disappear, *i.e.*, there is an onset of absorption as evidenced by the rising reflectance most notably in the direction of the electric field parallel to the b axis. It is evident in Fig. A-3 there are, at least, two bands that are more strongly polarized along this direction. A quantitative analysis of the reflectance is done by a Kramers-Kronig analysis and by fitting the reflectance (or $\epsilon(\omega)$) using the standard Lorentz formula:

$$\epsilon(\omega) = \sum_{j=1}^3 \frac{\omega_{pj}^2}{\omega_j^2 - \omega^2 - i\omega\gamma_j} + \epsilon_{\infty}, \quad (\text{A-1})$$

where ω_{pj} , ω_j , and γ_j are the oscillator strength, center frequency, and scattering rate of the j^{th} transition. Other higher frequency contributions are lumped into ϵ_{∞} . The results for the the optical conductivity obtained from the Kramers-Kronig analysis are shown in Fig. A-4, while the parameters obtained from a fit to the reflectance are listed in Table A-1. In general, the electronic transitions, which appear as broad peaks in the $\sigma_1(\omega)$ spectra, will fall into two classes. On the one hand, those at high energies generally are the results of localized-excitation bands (LE) in the molecule. On the other hand, transitions at lower energies that are along the stacking direction will in principle correspond to electronic transitions between cations or charge-transfer (CT) bands. The results of Fig. A-4 clearly show one electronic transition centered at $11,625\text{ cm}^{-1}$ that is more strongly polarized along the b axis (by a ratio of 3:1). In the structure, the long axis of the ET^{2+} cations is oriented parallel to this direction and hence any net dipole moment would be in the long direction of the cations (see Fig. A-2). The fact that the cations are oriented this way rules out this transition is a CT band, making it most likely due to a LE band. A second transition of this type is also resolved at $14,000\text{ cm}^{-1}$, although it is of much less intensity. It is clear

that the energies and oscillator strengths of these localized excitations are related to the electronic structure of the compound. Energetically, it will be more favorable to excite an electron within the molecule since the high oxidation state of the cation is expected to reduce the number of electrons that could make a transition between neighboring cations. Only in the situation when there are mixed valence states for the different ET cations in the structure, it will possible to have enough electrons to make a transitions to neighboring molecules.

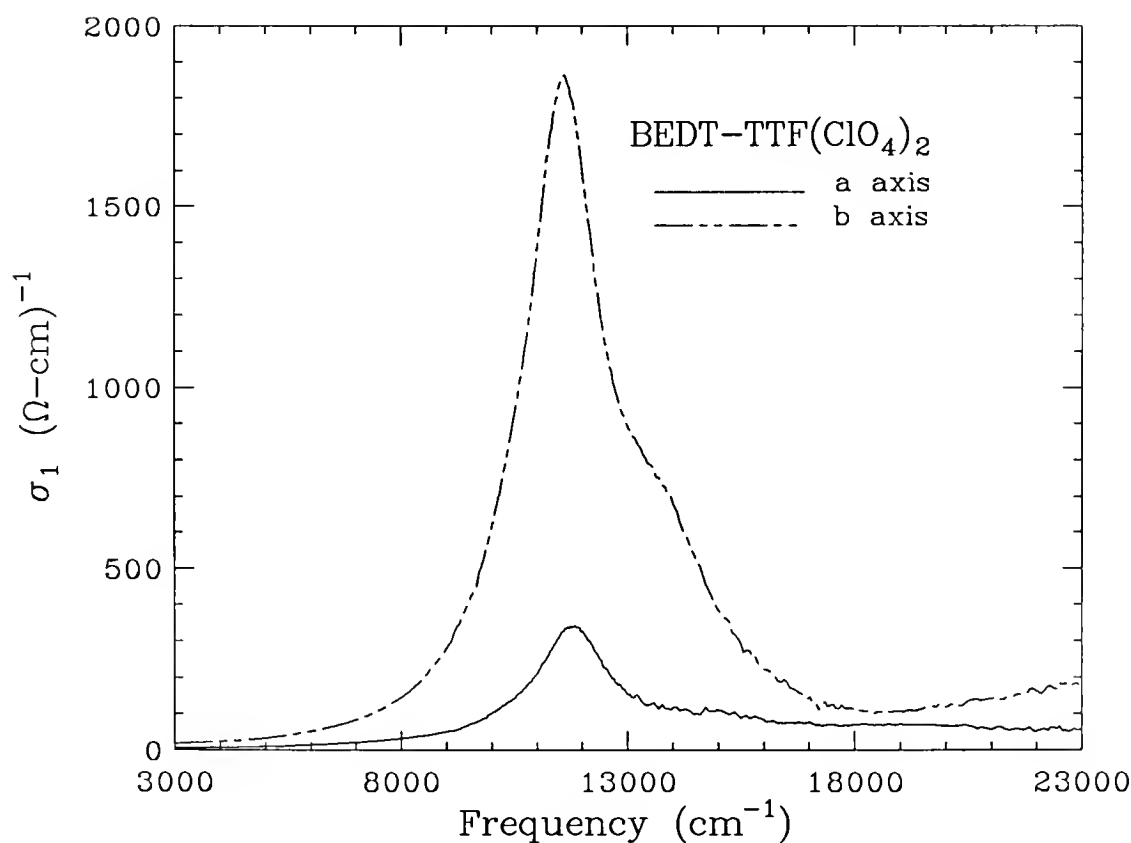


Fig. A-4. Conductivity of the BEDT-TTF(ClO₄)₂ salt for polarization of the light along the *a* and *b* axes.

Regarding the assignment of transitions occurring along the *a* axis, such as the one at 11,750 cm⁻¹, there are two considerations that should be made. In first place, this is the stacking direction of the molecule in the structure. On the other hand,

since the structure is monoclinic, there should be a small contribution of the c -axis direction as well. The fact that the intensity is not too strong weights against this to be a CT band in the molecule. A more definite conclusion would require an elaborate calculation of the energy levels in the cations. Finally, the band at $30,000\text{ cm}^{-1}$, which is isotropic in the ab plane of the salt, is most likely related to local intramolecular excitations (LE).

Table A-1. Parameters of a Lorentz fit for the measured $R(\omega)$ in the (001) face of BEDT-TTF(ClO₄)₂.

Oscillator#	ω_j (cm ⁻¹)	ω_{pj} (cm ⁻¹)	γ_j (cm ⁻¹)
$\vec{E} \parallel b$			
1	11625	15566	2283
2	13992	5918	1813
3	31000	22000	7500
$\epsilon_\infty = 3.1$			
$\vec{E} \parallel a$			
1	11810	6388	2189
2	30430	14914	4146
$\epsilon_\infty = 3.1$			

Transmittance Measurements

Next, we show in Fig. A-5 the transmittance in the far-infrared and midinfrared regions along the two principal axes in the (001) face. Both spectra show a series of

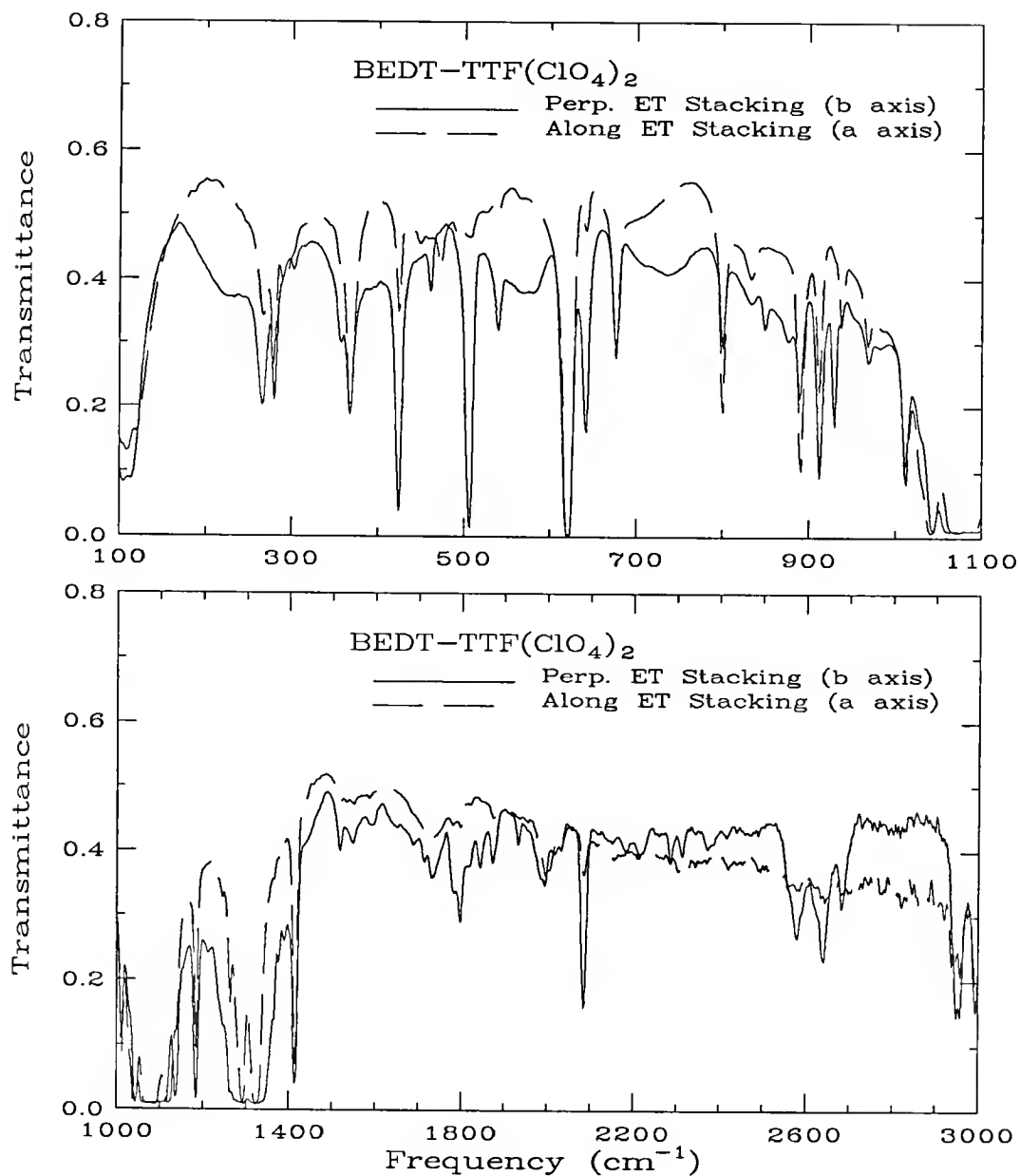


Fig. A-5. Transmittance of the BEDT-TTF(ClO₄)₂ salt for light polarized along the *a* and *b* axes.

strong phonon lines that are due to intramolecular vibrational modes of the ET^{2+} cations and the $(\text{ClO}_4)^-$ anions. No evidence of strong low-frequency metallic behavior is seen in these spectra. This is not surprising since metallic transport is only observed in the ET-based salt when the oxidation state of the ET cations is not an integer number. A tabulation of the center frequencies and relative intensities (with respect to the strongest band) of these absorptions is shown in Table A-2 and Table A-3 for the a and b axes respectively. In principle, analysis of these frequencies could be made by making a comparison with the measured and assigned frequencies in the phonon vibrational spectra of the neutral ET molecule and the ClO_4^- ion that have been reported.^{172,209,210,214,217} In the case of the ClO_4^- anion (tetrahedral point group symmetry) this molecule has two infrared active modes²¹⁷ at 620 cm^{-1} and $1170\text{--}1050\text{ cm}^{-1}$ (both with F_2 symmetry). The close correspondence between these frequencies and the two isotropic absorption lines in the spectra of Fig. A-5 indeed suggests these two absorptions are due to the ClO_4 ions.

Due to the planar nature of the central part, normal mode calculations^{172,209,210,214} of the neutral ET molecule usually assume the point group symmetry is D_{2h} . Hence, there will be symmetric vibrational modes, such as A_g , B_{1g} , B_{2g} , and B_{3g} that are Raman active, and the antisymmetric B_{1u} , B_{2u} , B_{3u} modes which are infrared actives. Complete assignment of the frequencies in the ET^{2+} cation by comparing them with the observed phonon lines in the neutral ET molecules is expected to be complicated for several reasons. In first place, the plane of the molecule in the structure is not oriented along neither of the principal axes that were measured in the crystal. This would explain the anisotropy that is seen in most of the modes associated the ET^{2+} cations. Secondly, there should be some frequency shifting of the modes in the oxidized molecule due to redistribution of charge and changes in bond lengths. Finally, there would be lifting of some degeneracies due to breaking of

some inversion symmetry in the lattice. In spite of these difficulties, some comparison with the modes that are expected to change could provide a general ideal of what is happening in the ET^{2+} cations. As it was mentioned before, the $\text{C}=\text{C}$ central double bond in the oxidized molecule is longer and weaker. Hence, it expected the resonant frequency associate with this mode will be redshifted. On the other hand, modes associated with the $\text{C}-\text{S}$ bonds and CH_2 groups should not show much change because there is only a slight shortening in these bond lengths in the ET^{2+} cation.

Vibrational frequencies associated with symmetrical and antisymmetrical TTF internal and external stretches of the $\text{C}-\text{S}$ bonds in the neutral molecule have been found around 507 and 495 cm^{-1} .²⁰⁹ At least, we find close correspondence between one of these frequencies and a strong line at 506 cm^{-1} in the spectrum of Fig. A-5 . This suggests this mode is related to stretch vibrations of the carbon-sulfur atoms. Moreover, the neutral molecule has symmetric (A_g) stretching of the central $\text{C}=\text{C}$ double bond at 1550 and 1494 cm^{-1} .^{209,210} We observe the spectra of Fig. A-5 have strong absorption lines at 1415 and ~ 1294 cm^{-1} . Since the central $\text{C}=\text{C}$ bond becomes a single bond in the oxidized molecule, it is expected the mode associated with vibrations of this central bond will be considerably redshifted in the oxidized molecule. Hence, it is quite plausible these vibrational frequencies are related to antisymmetric vibrations of this bond with B_{1u} symmetry. Other optical studies^{172,214} of ET-based salts with oxidation state of $1/2+$ have also shown a mode at 1300 cm^{-1} that is associated with symmetric vibrations of the central $\text{C}=\text{C}$ bond. The interpretation there has been that the strong coupling of this mode to the electronic background renders it infrared active at a substantially lower frequency.

Other modes in the neutral molecule that involve stretching of the outer CH_2 groups (B_{2u}) have been found at 2958 cm^{-1} , which is in agreement with the observed frequency at 2948 cm^{-1} in the b axis and 2958 cm^{-1} in the a axis in the present case.

Table A-2. Phonon frequencies and relative intensity for electric field polarized along a axis of BEDT-TTF(ClO₄)₂.

Freq. (cm ⁻¹)	Rel. Intensity %	Freq. (cm ⁻¹)	Rel. Intensity %
267	34	1012	85
279	42	1041	99
367	50	1088	99
424	32	1118	98
449	17	1184	82
473	22	1263	71
621	100	1292	97
677	49	1323	98
800	65	1415	87
833	27	1732	24
891	81	1955	19
912	59	2945	58
937	40	2958	62
968	46		

Concluding Remarks

In conclusion, we have presented a room temperature optical study of the BEDT-TTF(ClO₄)₂ salt. As expected, the spectra in the far infrared and midinfrared display an insulating character for this salt due to the double oxidized state of the ET molecule. Some of the phonon lines that are seen in the infrared spectrum can be attributed to either the ClO₄⁻ anions or the ET²⁺ cations. The results in the near infrared suggest there are two electronic transitions, centered at 11,600 and 14,000 cm⁻¹, that are more strongly polarized along the b axis. The fact that this is the

direction that contains a larger projection of the long axis of the molecule suggests these transitions are intramolecular in nature. It is also seen that higher electronic transitions do not show much anisotropy.

Table A-3. Phonon frequencies and relative intensity for electric field polarized along the b axis of BEDT-TTF(ClO₄)₂.

Freq. (cm ⁻¹)	Rel. Intensity %	Freq. (cm ⁻¹)	Rel. Intensity %
265	53	929	67
280	51	1012	79
357	35	1103	99
367	55	1136	96
424	82	1184	97
461	20	1294	99
506	92	1413	92
540	28	1798	44
621	100	1994	33
642	69	2084	69
677	44	2580	49
800	43	2640	56
890	59	2682	40
912	82	2948	72

APPENDIX B

MICROWAVE CAVITY APPARATUS

The use of microwave radiation to probe the physical properties in solids has been an important tool in studying the low-lying electronic excitations in organic metals^{218,219} as well as in superconducting materials.^{220,221} Since microwave techniques have been used with great success in the past to probe the superconducting state properties in conventional superconductors,¹⁸⁸ it is expected that such studies will be useful when performed in the copper-oxide superconductors. The study of microwave absorption in superconductors poses great challenges from the experimental point of view, since it requires the use of special techniques due to the low absorption these materials have in the presence of a microwave field.²²⁰ Normally, microwave cavities of very high Q -values are needed to achieve the required sensitivity, in addition to a set-up that allows temperature dependence measurements. This appendix is devoted to a description of a microwave apparatus that was built by this author in collaboration with Dr. G.L. Carr. The performance of the apparatus is tested by showing measurements of the microwave absorption as a function of temperature of $\text{Bi}_2\text{Sr}_2\text{CaCu}_2\text{O}_8$ single crystals.

Experimental Set-up

Microwave Apparatus

Figure B-1 shows a schematic of the microwave apparatus. A cylindrical cavity made out of oxygen-free high conductivity (OFHC) copper was built with inner dimensions 3.84-cm diameter \times 2.90-cm long. The cavity was actually fabricated in two pieces: the cylindrical walls and the bottom plate are all in one piece and the

removable top plate. The top plate had a central hole that was use for pumping and insertion of the sample and two coupling holes near the edge with a 90° angle separation between them. The cavity was contained inside a stainless-steel vacuum can, as shown in Fig. B-1, that was supported by four stainless-steel tubes hanging from the top plate of the cryostat unit. Three of the four tubes extended inside the vacuum can and provided support for the cavity by being soldered on to the three holes of the removable top plate. Indium metal seals were used so that both the cavity and the vacuum can were vacuum tight. Cooling of the cavity was achieved by placing the whole assembly inside a conventional liquid helium dewar with an outer bath of liquid nitrogen. Control of the cavity temperature was accomplished using an external temperature controller connected to a Si-diode sensor and heater attached to the top plate of the cavity.

Coupling of the microwaves in and out of the resonator was done from the top through two adjustable $50\text{-}\Omega$ cryogenic coaxial lines, each terminated in a loop. The coupling to the resonator could be changed by moving the lines (and the loops) in and out of the resonator. Operation of the cavity was done in the weakly coupled mode to achieve the maximum Q and, hence, maximum sensitivity without sacrificing in power signal strength.

Mounting of the sample was done by attaching it on a sapphire rod using a tiny dot of vacuum grease. At the same time, the sapphire was connected to a long rod that was inserted inside the cavity from the top of the cryostat unit. The lengths of the long rod and piece of sapphire were cut so that the sample attached to the end will lie right at the center when inserted in the cavity. Uniform temperature inside the cavity (and sample) was ensured by keeping a He gas pressure of 50 mm of Hg during the cool down.

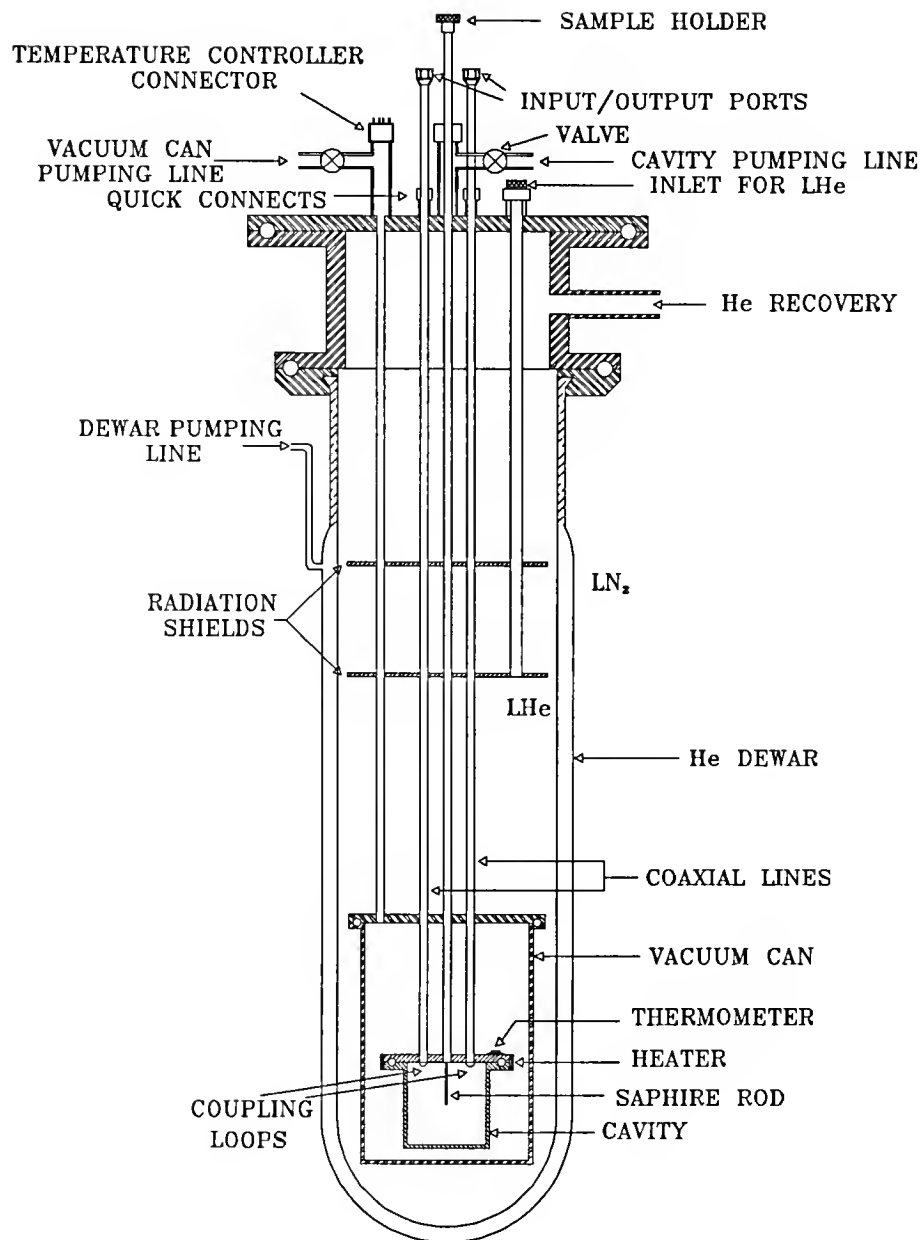


Fig. B-1. Diagram of the apparatus showing the microwave cavity with the cryostat.

Instrumentation Control and Data Acquisition

Figure B-2 shows a block diagram of the experimental set up that was used for data acquisition. As illustrated in Fig. B-2, the cavity was run in transmission mode. The microwave signal that was generated at the microwave source (Hewlett Packard model 8359-8350A) was amplitude modulated (AM) with an audio oscillator (~ 1 kHz) and was fed into the cavity through a coaxial line. A crystal diode detector was connected at the exit port that converted the microwave power into a voltage signal that was sent to a lock-in amplifier for phase-sensitive amplification. This amplified voltage was later digitized by using a Keithley digital voltmeter (model 195). A frequency counter in phase-lock mode was used to monitor the frequency and to ensure frequency stability in the ~ 1 kHz range. All instruments, except the lock-in amplifier, were remotely controlled by a personal computer through a IEEE board. The Q of the cavity was determined in the following way: The resonant frequency f_0 was determined by finding the frequency at which maximum power was transmitted through the cavity circuitry. Then, a computer program recorded the output power at a few frequencies around f_0 and the results was stored in a file that was later used to find the full-width at half the maximum power (FWHM) or Γ . Using the parameter Γ , the Q was determined from the relation $Q = f_0/\Gamma$. Figure B-3 shows an example of a trace obtained at room temperature with the determined parameters by doing a fit using a standard Lorentzian line shape. The measured room-temperature value for the Q was $\sim 10,500$.

All measurements were done by coupling the cavity to the TM_{010} mode (transverse magnetic field). In this mode, the electric field is uniform along the symmetry axis and had maximum amplitude at the center of the cavity. This configuration is appropriate to probe the microwave response for small and needle-like samples that are centrally located with the long axis along the symmetry axis of the cavity. This, combined

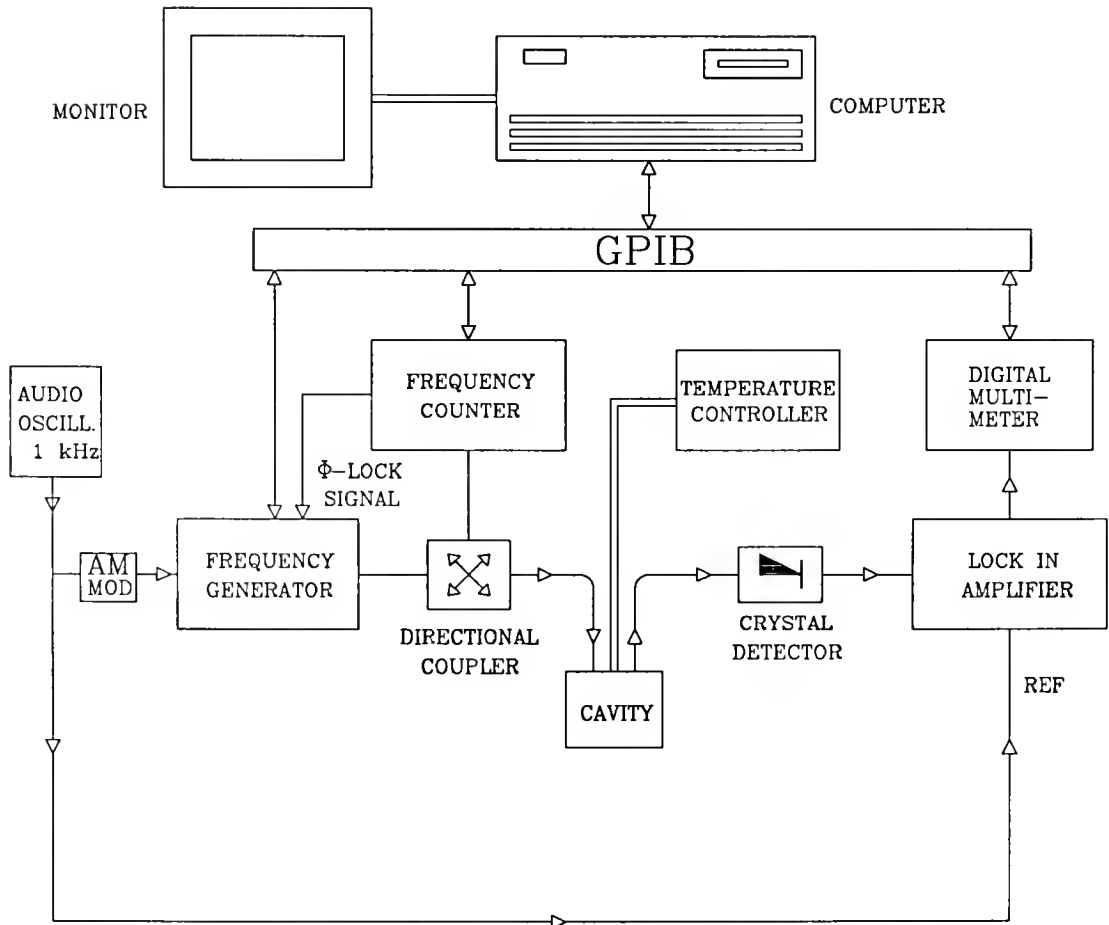


Fig. B-2. Sketch of the instruments connection in the experimental set-up.

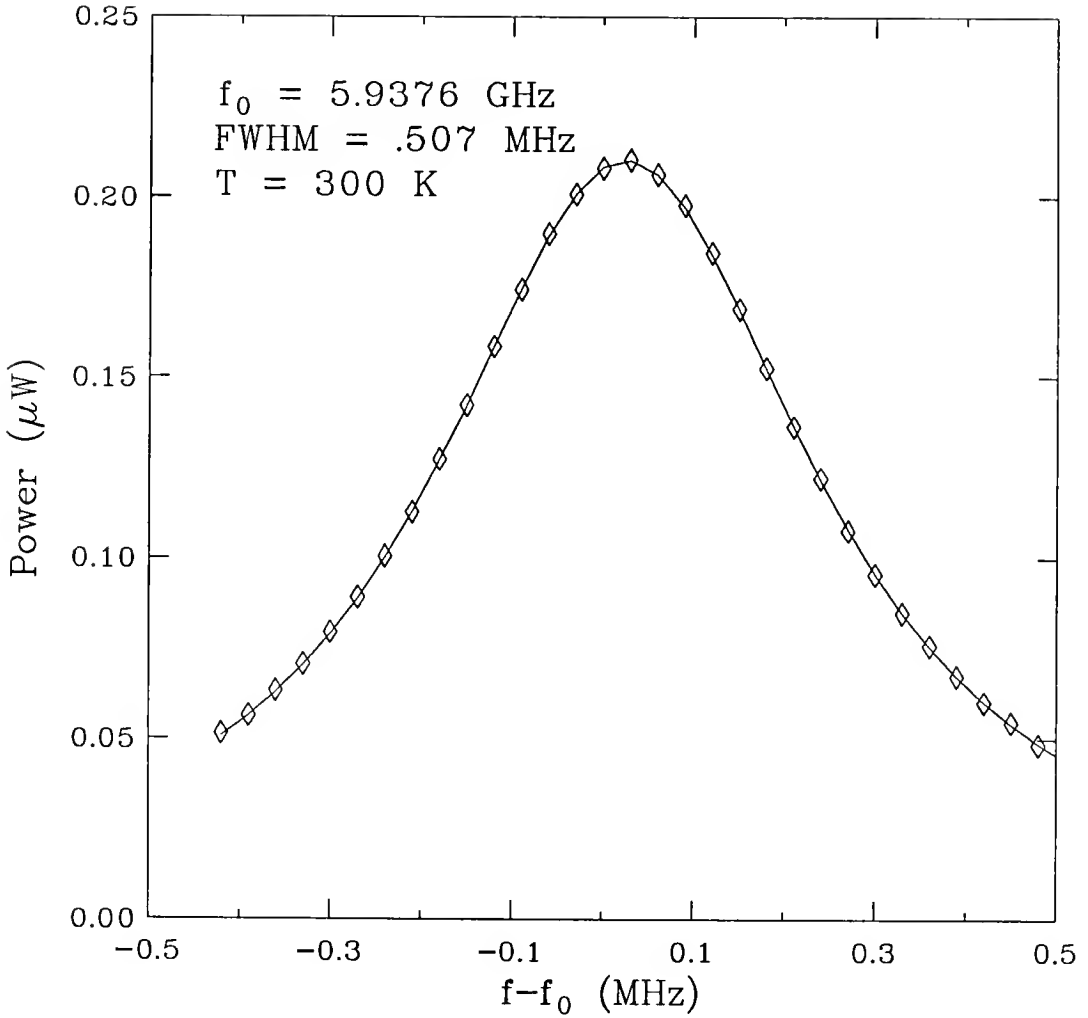


Fig. B-3. Example of a trace obtained in the experiment to determine the Q and center frequency of the cavity.

with the fact that the depolarizing factor of the sample is minimum in this geometry, ensured that only the microwave properties in the long axis were probed by virtue of the electric field being oriented along the long dimension of the sample.

For a cylindrical cavity, the resonant frequency (f) for the TM_{010} mode is only a function of the radius R . The formula²²² that relates these two is $f = 2.504c/R$, where c is the speed of light. Hence, the fundamental TM_{010} mode for the present cavity ($R = 1.92 \text{ cm}$) is 5.95 GHz. An initial run was taken to test the cavity

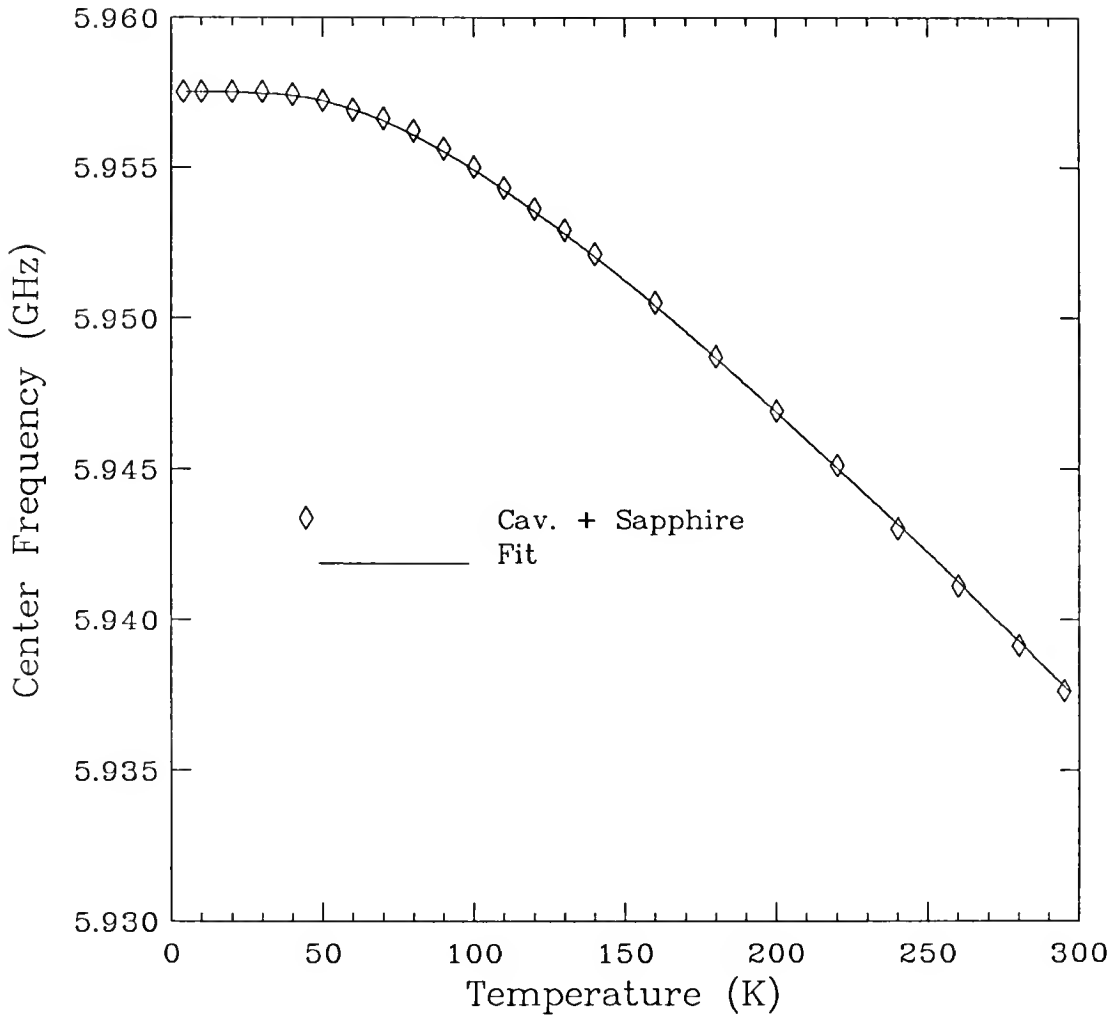


Fig. B-4. Plot of the change of resonance frequency vs. temperature.

performance at low temperatures. Figure B-4 shows the change of the resonance frequency in the cavity as a function of temperature between 4.2 K and 300 K. The increase in the resonance frequency that is observed as the temperature is lowered, is due to the contraction of the cavity radius. This is corroborated by showing (solid line) a calculation of the predicted resonance frequency from the known²²³ thermal coefficient of expansion for Cu. It should also be noticed that below 50–60 K there is not much temperature dependence.

Likewise, the Q of the cavity has considerable temperature dependence as well. It goes from 10,500 at room temperature to 27,000 at 4.2 K. For a cylindrical cavity tuned in the TM_{010} the expected Q is given by the formula²²²

$$Q = \frac{L}{R + L} \frac{R}{\delta_c}, \quad (B-1)$$

where L is the cavity length and δ_c is the skin-depth penetration of the electromagnetic field in copper metal. This is given by

$$\delta_c = \sqrt{\frac{2}{\mu_c \omega \sigma_c}}, \quad (B-2)$$

where μ_c and σ_c are the permeability and conductivity of copper respectively and ω is the resonance frequency. Hence, any temperature dependence in Q is related to the temperature dependence of σ_c . A numerical evaluation of Eq. B-1 ($T = 300K$) yielded a predicted Q_0 in the order of $\sim 13,500$. Thus, there is a discrepancy of at least 20% with the measured Q . Although some loss might occur as leakage at the coupling holes, most of it can be accounted for by micron-size imperfections in the cavity walls (such losses are usually minimized by polishing the cavity). At liquid helium temperature, where the conductivity of copper is dominated by the anomalous skin effect (ASE), the skin depth is given by¹⁴³

$$\delta_{ASE} = 2.8 \times 10^{-5} \left(\frac{GHz}{f} \right)^{1/3}, \quad (B-3)$$

Hence, we find the agreement between the predicted and measured Q is even less 40%, since δ_{ASE} is much smaller compared to the room temperature value. This makes the microwave radiation even more susceptible to the imperfections mentioned above.

The introduction of the sample in the cavity will produce changes in both the resonance frequency and the Q or quality factor. In the limit that the sample only occupies a small fraction of the cavity volume these changes are considered a small perturbation. Hence, we can define a frequency shift that is written as

$$\delta = \frac{f' - f}{f}, \quad (\text{B-4})$$

and the loss or absorption by the sample

$$\Delta \left(\frac{1}{Q} \right) = \frac{1}{Q'} - \frac{1}{Q}, \quad (\text{B-5})$$

where primed and unprimed refer to parameters measured with and without the sample respectively. In low-loss materials $\Delta \left(\frac{1}{Q} \right) \sim 0$.

Given the parameters of the cavity with and without the sample, it is possible to estimate the conductivity by considering the sample will only cause a small perturbation to the electric field in the cavity. For example, in the limit $V_s/V \ll 1$ it is possible to define a filling factor α as

$$\alpha = \frac{V_s E_{0,max}^2}{2 \int_V |E_0|^2 dV}, \quad (\text{B-6})$$

where $E_{0,max}^2$ is the maximum unperturbed electric field at the sample site and V_s and V are the sample and cavity volumes respectively. The integral in Eq. B-6 depends on the configuration of the electric field inside the cavity. It can be shown²²¹ that for a cylindrical cavity tuned in the TM_{010} mode the filling factor is just $\alpha \approx 1.86 V_s/V$.

Cohen *et al.*²¹⁸ and Ong²²⁴ derived expressions for the conductivity of a needle-like spheroid in the skin-depth regime, *i.e.*, when the electric field does not penetrate completely in the sample. The formulae are

$$1 + \frac{N_z}{\alpha} \frac{\Delta f}{f} = \frac{N_z}{\alpha} \frac{\Delta}{2}, \quad (\text{B-7})$$

$$\frac{\Delta}{2} = \frac{9\epsilon_0\pi b}{64\alpha} \left(\frac{\alpha}{N_z}\right)^2 \sqrt{\frac{\omega^3\mu_0}{2\sigma_1}}, \quad (\text{B-8})$$

where

$$N_z \approx \left(\frac{b}{a}\right) [\ln(2a/b - 1)], \quad (\text{B-9})$$

is the depolarizing factor of a needle-like spheroid, α is defined in Eq. B-6, b and a are the short and long principal axes and μ_0 and ϵ_0 are the vacuum permeability and permittivity. The conductivity of the sample is denoted σ_1 . It was shown by Ong²²⁴ that in a highly conducting sample the depolarizing factor can be independently obtained from

$$N_{exp} = \frac{\alpha}{\delta}, \quad (\text{B-10})$$

where δ and α are defined in Eq. B-4 and Eq. B-6 respectively.

These equations were initially tested using different pieces of copper wire alloy (radius $\sim .06$ mm) as the sample to determine their applicability in the present set-up. Table B-1 shows a summary of the results. There is good agreement between the depolarization factor N_{th} obtained from Eq. B-9 and the one obtained from the frequency shift in Eq. B-10. A comparison of the conductivity obtained from Eq. B-8 with the direct dc value ($\sigma_{dc} \sim 1.4 \times 10^6 (\Omega - m)^{-1}$) gives an uncertainty in the order of 5–15%. It is noted that the experimental value is somewhat smaller. This is consistent with the fact that sharp edges on the right cylinder enhance the losses compared to a true spheroid.²¹⁹ Nonetheless, Eq. B-8 appears to give an adequate

Table B-2. Conductivity of different pieces of copper wires using the microwave cavity perturbation method in the skin-depth regime.

Length	$\Delta\left(\frac{1}{Q}\right)$	δ	α	N_{exp}	N_{th}	$\sigma(\Omega\text{-m})^{-1}$
(cm)	10^{-6}	10^{-3}	10^{-6}	10^{-3}	10^{-3}	10^6
0.50	5.24	1.85	3.50	1.89	2.17	.5
0.70	9.64	4.04	4.91	1.21	1.22	.95
0.80	26.9	6.99	5.60	.802	.996	.82
0.90	52.9	1.07	6.31	.590	.778	.91

description of the cavity perturbation in the skin-depth regime. The differences in shape between an spheroid of revolution and a right cylinder do not appear to be of major importance.

Results for $\text{Bi}_2\text{Sr}_2\text{CaCu}_2\text{O}_8$ Single Crystal

This section will discuss results and the analysis of data taken on a $\text{Bi}_2\text{Sr}_2\text{CaCu}_2\text{O}_8$ sample in the frame work of the cavity perturbation method. The results for $1/Q$ vs. T (TM_{010} mode) for the empty cavity (but with the sapphire rod) and with a rectangular $\text{Bi}_2\text{Sr}_2\text{CaCu}_2\text{O}_8$ sample ($T_c \approx 85\text{K}$) are shown in Fig. B-5. The sample dimensions (length-width-thickness) were $3.6 \times 0.60 \times 0.02\text{mm}^3$. It were estimated from these numbers the sample was in the skin-depth regime.

The data in Fig. B-5 show there is higher absorption (low Q -value) when the sample is inserted in the cavity. This happens for temperatures above the transition temperature. Below T_c , both curves merge together signaling the sample has entered the superconducting state. This marked reduction in the absorption is due to the fact that when a superconductor is cooled below T_c , most electrons condense into pairs.

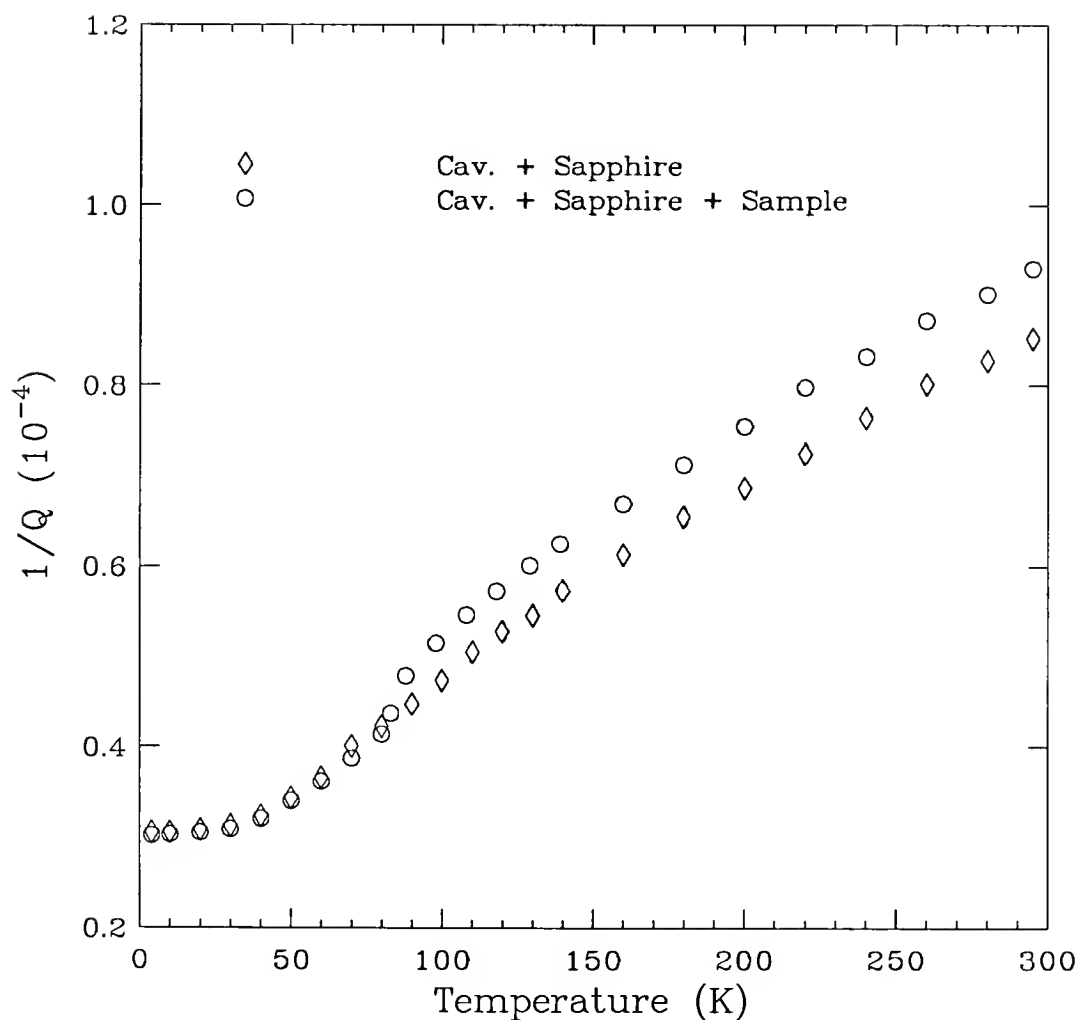


Fig. B-5. The loss ($1/Q$) for the cavity with and without $\text{Bi}_2\text{Sr}_2\text{CaCu}_2\text{O}_8$ sample as a function of temperature (microwave electric field in the ab plane).

This is possible since the pairs are effective in shielding the applied fields causing a reduced penetration inside the sample.

Visible in Fig. B-5 is that just below T_c , the loss due to the sample appears to be smaller than the loss of the empty cavity. This was reproducible in two samples that were measured. This can be explained by noticing that the resonant frequencies in both set of data are not quite the same. The $\text{Bi}_2\text{Sr}_2\text{CaCu}_2\text{O}_8$ sample was cut in a reasonable size as to produce a measurable change in the Q when the sample was

inserted in the cavity. It turned out the change in the resonant frequency (in the order of 7.7 MHz) was large enough to show differences in the absorption due to the cavity walls, specially in the temperature range where the sample became superconducting. In this respect, a true “background” would have been to measure the Q of the cavity at the same frequency as it was measured with the sample inside. Since this was not done, the microwave resistivity data (obtained from Eq. B-8 by replacing the factor πb for the cross sectional perimeter of the rectangle width+thickness) that are shown in Fig. B-6 can be considered as a lower bound for the $\text{Bi}_2\text{Sr}_2\text{CaCu}_2\text{O}_8$ sample that was measured. These numbers show a good agreement with the reported resistivities in the literature.¹³ The temperature dependence in ρ vs. T shows a linear variation, within the systematic uncertainty in the data that was due to error in determining the parameters of the cavity with and without the sample at exactly the same temperature.

Summary

In sum, the technique discussed above can be applied to study the microwave power absorption in the high- T_c superconductors. The sensitivity in this set-up is adequate to measure the absorption above T_c . For measurements below T_c , there are a couple of improvements that could be made to increase the sensitivity. In first place, the substitution method can be applied to account for the frequency dependence in the absorption of the cavity wall. Secondly, since the sensitivity is ultimately dominated by the Q -value of the cavity, a substantial improvement is possible by operating the cavity at 4.2 K and having the inner wall coated with a material such as Pb or Nb that is superconducting at this temperature. Then, the sample temperature could be controlled by thermally isolate the sapphire rod from the cavity walls and installing a small heater and a second thermometer nearby.

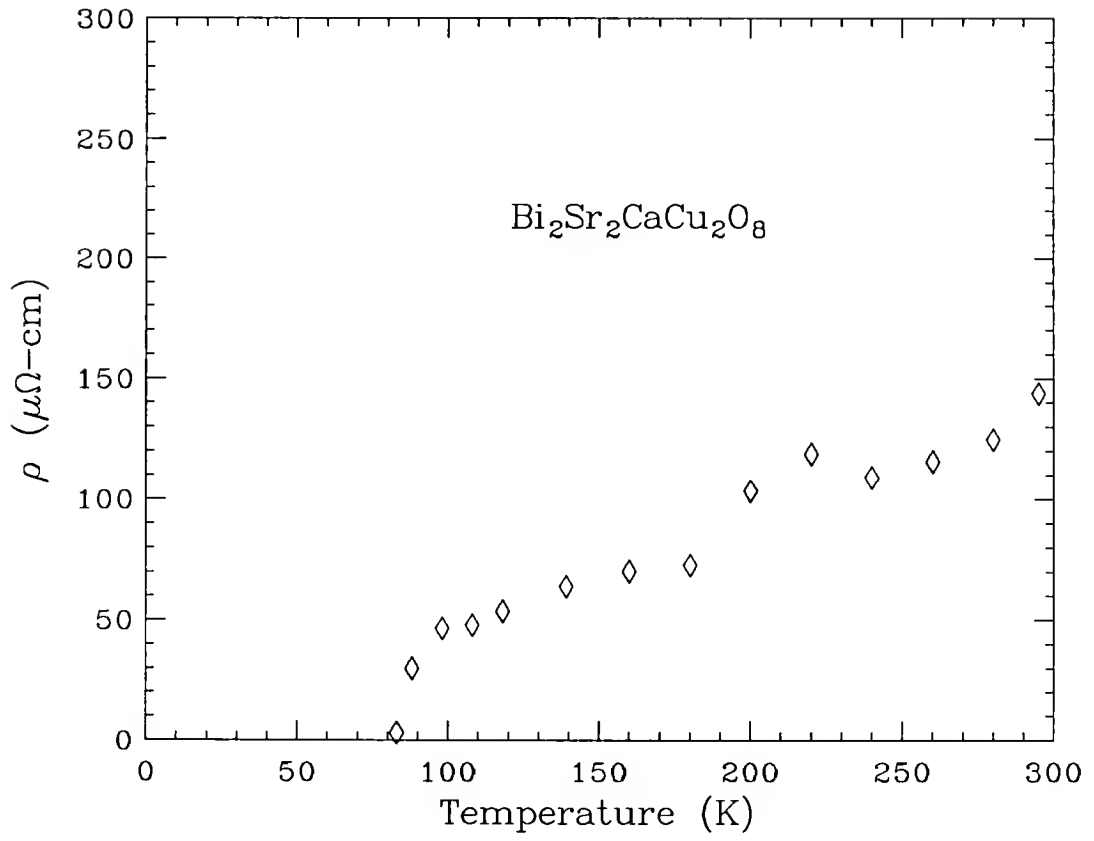


Fig. B-6. Microwave resistivity ($1/\sigma$) at 5.95 GHz in the ab plane of $\text{Bi}_2\text{Sr}_2\text{CaCu}_2\text{O}_8$ crystal.

REFERENCES

1. J.G. Bednorz and K.A. Müller, *Z. Phys. B* **64**, 189 (1986).
2. J. Bardeen, L.N. Cooper, and J.R. Schrieffer, *Phys. Rev.* **108**, 1175 (1957).
3. C.E. Gough, M.S. Colclough, E.M. Forgan, R.G. Jordan, M. Keene, C.M. Muirhead, A.I.M. Rae, N. Thomas, J.S. Abell, and S. Sutton, *Nature* **326**, 855 (1987).
4. R.H. Koch, C.P. Umbach, G.J. Clark, P. Chaudhari, and R.B. Laibowitz, *Appl. Phys. Lett.* **51**, 200 (1987).
5. Z.-X. Shen, D.S. Dessau, B.O. Wells, D.M. King, W.E. Spicer, A.J. Arko, Marshall, L.W. Lombardo, A. Kapitulnik, P. Dickinson, S. Doniach, J. DiCarlo, T. Loeser, *Phys. Rev. Lett.* **70**, 1553 (1993).
6. Y. Hwu, L. Lozzi, M. Marsi, S. La Rosa, M. Winokur, P. Davis, M. Onellion, H. Berger, F. Gozzo, F. Levy, and G. Margaritondo *Phys. Rev. Lett.* **67**, 2573 (1991).
7. R. Kelley, J. Ma, G. Margaritondo, and M. Onellion, *Phys. Rev. Lett* (in press).
8. H.J. Tao, A. Chang, F. Lu, and E.L. Wolf, *Phys. Rev. B* **45**, 10622 (1992).
9. D. Mandrus, L. Forro, D. Koller, and L. Mihaly, *Nature* **351**, 460 (1991).
10. M.K Wu, J.R. Ashburn, C.J. Torng, P.H. Hu, R.L. Meng, L. Gao, Z.J. Huang, Y.Q. Wang, and C.W. Chu, *Phys. Rev. Lett.* **58**, 908 (1987).
11. Y. Tanaka, M. Fukutomi, and T. Asano, *Jpn. J. Appl. Phys.* **27**, L209 (1988).
12. T. Siegrist, S. Sunshine, D.W. Murphy, R.J. Cava, and S.M. Zahurak, *Phys. Rev. B* **35**, 7137 (1987).
13. S.A. Sunshine, T. Siegrist, L.F. Schneemeyer, D.W. Murphy, R.J. Cava, B. Batlogg, R.B. van Dover, R.M. Fleming, S.H. Glarum, S. Nakahara, R. Farrow, J.J. Krajewski, S.M. Zahurak, J.V. Waszczak, J.H. Marshall, P. Marsh, L.W. Rupp Jr., and W.F. Peck *Phys. Rev. B* **38**, 893 (1988).
14. S.A. Wolf and V.Z. Kresin, *IEEE Trans. Magnetics* **27**, 852 (1991).

15. A. Umezawa, G.W. Crabtree, J.Z. Liu, T.J. Moran, S.K. Malik, L.H. Nunez, W.L. kwok, and C.H. Sowers, *Phys. Rev. B* **38**, 2843 (1988).
16. T.A. Friedmann, M.W. Rabin, J. Giapintzakis, J.P. Rice, and D.M. Ginsberg, *Phys. Rev. B* **42**, 6217 (1990).
17. J.P. Rice, D.M. Ginsberg, and M.W. Rabin, *Phys. Rev. B* **42**, 6217 (1990).
18. S.Martin, A.T. Fiory, R.M. Fleming, L.F. Schneemeyer, and J.V. Waszczak, *Phys. Rev. Lett.* **60**, 2194 (1988).
19. Y.M. Wan, S.E. Hennoul, D.C. Harris, and J.C. Garland, *Phys. Rev. Lett.* **71**, 157 (1993).
20. K.E. Gray and D.H. Kim, *Phys. Rev. Lett.* **70**, 1693 (1993).
21. H.M. Duan, W. Kiehl, C. Dong, A.W. Cordes, M.J. Saeed, D.L. Viar, and A.M. Hermann, *Phys. Rev. B* **43**, 12925 (1991).
22. T. Timusk and D.B. Tanner, in *Physical Properties of High Temperature Superconductors I*, edited by D.M. Ginsberg (World Scientific Press, Singapore, 1989) p. 339.
23. D.B. Tanner and T. Timusk, in *Physical Properties of High Temperature Superconductors I*, edited by D.M. Ginsberg (World Scientific Press, Singapore, 1992) p. 363.
24. G.A. Thomas, in *Proceedings of the Thirty-Ninth Scottish Universities Summer School in Physics of High-Temperature Superconductivity*, edited by D.P. Tunstall and W. Barford (Adam Hilger, Bristol, Philadelphia and New York, 1991) p. 169.
25. R.T. Collins, Z. Schlesinger, F. Holtzberg, and C. Feild, *Phys. Rev. Lett.* **63**, 801 (1990).
26. M.P. Petrov, A.I. Grachev, M.V. Krasin'kova, A.A. Nechitailov, V.V. Prokofiev, V.V. Poborchy, S.I. Shagin, and N.F. Kartenko, *Solid State Commun.* **67**, 1197 (1989).
27. J.K. Kim, I. Bozovic, D.B. Mitzi, and A. Kapitulnik, *Phys. Rev. B* **41**, 7251 (1990).
28. S. Uchida, T. Ido, H. Takagi, T. Arima, Y. Tokura, and S. Tajima, *Phys. Rev. B* **43**, 7942 (1991).

29. C.C. Homes, T. Timusk, R. Liang, D.A. Bonn, and W.N. Hardy, *Phys. Rev. Lett.* **71**, 1645 (1993).
30. T. Pham, M.W. Lee, H.D. Drew, U. Welp, and Y. Fang *Phys. Rev. B* **44**, 5377 (1991).
31. Z. Schlesinger, R.T. Collins, F. Holtzberg, C. Feild, S.H. Blanton, U. Welp, G.W. Crabtree, and Y. Fang, *Phys. Rev. Lett.* **65**, 801 (1990).
32. EI. Takagi, S. Uchida, K. Kitazawa, and S. Tanaka, *Jpn. J. Appl. Phys.* **26**, L123 (1987).
33. C. Chaillout, S-W. Cheong, Z. Fisk, M.S. Lehmann, M. Marezio, B. Morosin, and J.E. Schirber, *Physica C* **158**, 183 (1989).
34. P.M. Grant, S.S.P. Parkin, V.Y. Lee, E.M. Engler, M.L. Ramirez, J.E. Vazquez, G. Lim, and R.D. Jacowitz, *Phys. Rev. Lett.* **58**, 2482 (1987).
35. C. Chaillout, J. Chenevas, S-W. Cheong, Z. Fisk, M. Marezio, and B. Morosin, *Physica C* **170**, 87 (1990).
36. J.D. Jorgensen, B. Dabrowski, S. Pei, D.R. Richards, and D.G. Hinks, *Phys. Rev. B* **40**, 2187 (1989).
37. P.G. Radaelli, J.D. Jorgensen, A.J. Shultz, B.A Hunter, J.L. Wagner, F.C. Chou, and D.C. Johnston, *Phys. Rev. B* **48**, 499 (1993).
38. R.J. Birgeneau and G. Shirane, in *Physical Properties of High Temperature Superconductors I*, edited by D.M. Ginsberg (World Scientific Press, Singapore, 1989) p. 198.
39. F. Beech, S. Miraglia, A. Santoro, and R.S. Roth, *Phys. Rev. B* **35**, 8778 (1987).
40. J.P. Rice and D.M. Ginsberg, *J. Crystal Growth* **109**, 432 (1991).
41. R.J. Cava, B. Batlogg, S.A. Sunshine, T. Siegrist, R.M. Fleming, K. Rabe, L.F. Schneemeyer, D.W. Murphy, R.B. van Dover, P.K. Gallagher, S.H. Glarum, S. Nakahara, R. Farrow, J.J. Krajewski, S.M. Zahurak, J.V. Waszczak, J.H. Marshall, P. Marsh, L.W. Rupp Jr., W.F. Peck, and E.A. Rietman *Physica C* **153-155**, 560 (1988).
42. C. Michel, M. Hervieu, M.M. Borel, A. Grandin, F. Deslandes, J. Provost, and B. Raveau, *Z. Phys. B* **68**, 421 (1987).

43. R.M. Hazen, C.T. Prewitt, R.J. Angel, N.L. Ross, L.W. Finger, C.G. Hadidiacos, D.R. Veblen, P.J. Heaney, P.H. Hor, R.L. Meng, Y.Y. Sun, Y.Q. Wang, Y.Y. Xue, Z.J. Huang, L. Gao, J. Bechtold, and C.W. Chu, *Phys. Rev. Lett.* **60**, 1174 (1988).
44. A. W. Sleight, *Physics Today* **44**, 24 (1991).
45. T.M. Shaw, S.A. Shivashnskar, S.J. La Placa, J.J. Cuomo, T.R. McGuire, R.A. Roy, K.H. Kelleher, and D.S. Yee, *Phys. Rev. B* **37**, 9856 (1988).
46. P. Bordet, J.J. Capponi, C. Chaillout, J. Chenavas, A.W. Hewat, E.A. Hewat, J.L. Hodeau, M. Marezio, J.L. Tholence, and D. Tranqui, *Proc. Interlaken Physica C* **153-155**, 623 (1988).
47. C.H. Chen, D.J. Werder, S.H. Liou, H.S. Chen, and M. Hong, *Phys. Rev. B* **37**, 9834 (1988).
48. E.A. Hewat, J.J. Capponi, and M. Marezio, *Physica C* **157**, 502 (1989).
49. A.K. Cheetham, A.M. Chippindale, and S.J. Hibble, *Nature* **333**, 21 (1988).
50. Y. Gao, P. Lee, P. Coppens, M.A. Subramanian, and A.W. Sleight, *Science* **241**, 954 (1988).
51. M.D. Kirk, J. Nogami, A.A. Baski, D.B. Mitzi, A. Kapitulnik, T.H. Geballe, and C.F. Quate, *Science* **242**, 1673 (1988).
52. F. Gervais, P. Echegut, J.M. Bassat, and P. Odier, *Phys. Rev. B* **37**, 9364 (1988).
53. P.C. Eklund, A. M. Rao, G.W. Lehman, G.L. Doll, M.S. Dresselhaus, P.J. Picone, D.R. Gabbe, H.P. Jenssen, and G. Dresselhaus, *J. Opt. Soc. Am. B* **6**, 389 (1989).
54. R.T. Collins, Z. Schlesinger, G.V. Chandrashekhar, and M.W. Shafer, *Phys. Rev. B* **39**, 2251 (1989).
55. D.A. Bonn, R. Liang, T.M. Riseman, D.J. Baar, D.C. Morgan, K. Zhang, P. Dosanjh, T.L. Duty, A. Macfarlane, G.D. Morris, J.H. Brewer, W.N. Hardy, C. Kallin, and A.J. Berlinsky, *Phys. Rev. B* **47**, 11314 (1993).
56. S.L. Herr, K. Kamaras, C.D. Porter, M.G. Doss, D.B. Tanner, D.A. Bonn, J.E. Greedan, C.V. Stager, and T. Timusk, *Phys. Rev. B* **36**, 733 (1987).
57. A. Zibold, M. Durrler, A. Gaymann, H.P. Geserich, N. Nucker, V.M. Burlakov, and P. Müller, *Physica C* **193**, 171 (1992).

58. K. Tamasaku, Y. Nakamura, and S. Uchida, *Phys. Rev. Lett.* **69**, 1455 (1992).
59. A. Fujimori, E. Takajama-Muromachi, Y. Uchida, and B. Okai, *Phys. Rev. B* **35**, 8814 (1987).
60. S. Sugai, T. Kobayashi, and J. Akimitsu, *Phys. Rev. B* **40**, 2686 (1989).
61. J.D. Perkin, J.M. Graybeal, M.A. Kastner, R.J. Birgeneau, J.P. Falck, and M. Greven, *Phys. Rev. Lett.* **71**, 1621 (1993).
62. G.A. Thomas, D.H. Rapkine, S.L. Cooper, S-W. Cheong, A.S. Cooper, L.F. Schneemeyer, and J.V. Waszczak, *Phys. Rev. B* **45**, 2474 (1992).
63. Xiang-Xin Bi and Peter C. Eklund, *Phys. Rev. Lett.* **70**, 2625 (1993).
64. J.P. Falck, A. Levy, M.A. Kastner, and R.J. Birgeneau, *Phys. Rev. B* **48**, 4043 (1993).
65. J. Orenstein, G.A. Thomas, A.J. Milis, S.L. Cooper, D.H. Rapkine, T. Timusk, L.F. Schneemeyer, and J.V. Waszczak, *Phys. Rev. B* **42**, 6342 (1990).
66. Y.H. Kim, S-W. Cheong, and Z. Fisk, *Phys. Rev. Lett.* **67**, 2227 (1991).
67. C.M. Foster, A.J. Heeger, G. Stuckey, and N. Heron, *Solid State Commun.* **71**, 945 (1989).
68. K. Kamaras, S.L. Herr, C.P. Porter, N. Tache, D.B. Tanner, S. Etemad, T. Venhatesan, E. Chase, A. Inam, X.D. Wu, M.S. Hegde, and B. Dutta, *Phys. Rev. Lett.* **64**, 84 (1990).
69. M. Shimada, M. Shimizu, and J. Tanaka, *Physica C* **193**, 277 (1992).
70. S.L. Cooper, D. Reznik, A.L. Kotz, M.A. Kalow, R. Liu, M.V. Klein, W.C. Lee, J. Giapintzakis, and D.M. Ginsberg, *Phys. Rev. B* **47**, 8233 (1993).
71. D.B. Romero, C.D. Porter, D.B. Tanner, L. Forro, D. Mandrus, L. Mihalý, G.L. Carr, and G.P. Williams, *Phys. Rev. Lett.* **68**, 1590 (1992).
72. F. Gao, D.B. Romero, D.B. Tanner, J. Talvacchio, and M.G. Forrester, *Phys. Rev. B* **47**, 1036 (1993).
73. H. Schmid, E. Burkhardt, B.N. Sun, and J.P. Rivera, *Physica C* **157**, 555 (1989).
74. B. Koch, H.P. Geserich, and T. Wolf, *Solid State Commun.* **71**, 495 (1989).

75. S.L. Cooper, A.L. Kotz, M.V. Klein, W.C. Lee, J. Giapintzakis, and D.M. Ginsberg, *Phys. Rev. B* **45**, 2549 (1992).
76. S.L. Cooper, G. A. Thomas, J. Orenstein, D.H. Rapkine, A.J. Millis, S-W. Cheong, A.S. Cooper, and Z. Fisk *Phys. Rev. B* **41**, 11605 (1990).
77. Y. Tokura, H. Takagi, T. Arima, S. Koshihara, T. Ido, S. Ishibashi, and S. Uchida, *Physica C* **162-164**, 1231 (1989).
78. L.D. Rotter, Z. Schlesinger, R.T. Collins, F. Holtzberg, and C. Feild, *Phys. Rev. Lett.* **67**, 2741 (1991).
79. D. Mandrus, M.C. Martin, C. Kendziora, D. Koller, L. Forro, and L. Mihaly, *Phys. Rev. Lett.* **70**, 2629 (1993).
80. K. Kamaras, S.L. Herr, C.D. Porter, J.S. Kim, B. Andracka, G.R. Stewart, D.B. Tanner, M. Reedyk, D.A. Bonn, and T. Timusk, unpublished.
81. I. Bozovic, K. Char, S.J.B. Yoo, A. Kapitulnik, M.R. Beasley, T.H. Geballe, Z.Z. Wang, S. Hagen, N.P. Ong, D.E. Aspnes, and M.K. Kelly, *Phys. Rev. B* **38**, 5077 (1988).
82. Y-Y. Wang and A.L. Ritter, *Phys. Rev. B* **43**, 1241 (1991).
83. J. Humlíček, E. Schmidt, L. Bočánek, M. Garriga, and M. Cardona, *Solid State Commun.* **73**, 127 (1990).
84. M. Reedyk, D.A. Bonn, J.D. Garrett, J.E. Greedan, C.V. Stager, T. Timusk, K. Kamaras, and D.B. Tanner, *Phys. Rev. B* **38**, 11981 (1988).
85. M.K. Kelly, P. Barboux, J.M. Tarascon, D.E. Apnes, P.A. Morris, and W.A. Bonner, *Physica C* **162-164**, 1123 (1989).
86. D.B. Romero, G.L. Carr, D.B. Tanner, L. Forro, D. Mandrus, L. Mihaly, and G.P. Williams, *Phys. Rev. B* **44**, 2818 (1991).
87. D.B. Romero, C.D. Porter, D.B. Tanner, L. Forro, D. Mandrus, L. Mihaly, G.L. Carr, and G.P. Williams, *Solid State Commun.* **68**, 1590 (1992).
88. W.A. Harrison, *Novel Mechanism of Superconductivity*, edited by S.A. Wolf and V.Z. Kresin (Plenum, New York, 1987).
89. V.J. Emery, *Phys. Rev. Lett.* **58**, 2794 (1987).
90. V.J. Emery and G. Reiter, *Phys. Rev. B* **38**, 4547 (1988).

91. C.M. Varma, S. Schmitt-Rink, and Elihu Abrahams, *Solid State Commun.* **62**, 681 (1987).
92. M. Hybertsen, M. Schlüter, and N.E. Christensen, *Phys. Rev. B* **39**, 9028 (1989).
93. F. Mila, *Phys. Rev. B* **38**, 11358 (1988).
94. P.W. Anderson, *Science*, **235**, 1196 (1987).
95. J.E. Hirsch, *Phys. Rev. Lett.* **54**, 1317 (1985).
96. C. Gros, R. Joynt, and T.M. Rice, *Phys. Rev. B* **36**, 381 (1987).
97. F.C. Zhang and T.M. Rice, *Phys. Rev. B* **37**, 3759 (1988).
98. A. Moreo and E. Dagotto, *Phys. Rev. B* **42**, 4786 (1990).
99. W. Stephan and P. Horsch, *Phys. Rev. B* **42**, 8736 (1990).
100. E. Dagotto, *Physica C* **185-189**, 1629 (1991).
101. C. Lanczos, *J. Res. Natl. Bur. Stand* **45**, 255 (1950).
102. C.-X. Chen and H.-B. Schüttler, *Phys. Rev. B* **43**, 3771 (1991).
103. T. Timusk and D.B. Tanner, *Physica C* **169**, 535 (1990).
104. H. Krakauer and W.E. Pickett, *Phys. Rev. Lett.* **60**, 1665 (1988).
105. J.W. Allen and J.C. Mikkelsen, *Phys. Rev. B* **15**, 2952 (1977).
106. C.M. Varma, P.B. Littlewood, S. Schmitt-Rink, E. Abrahams, and A.E. Ruckenstein, *Phys. Rev. Lett.* **63**, 1996 (1989).
107. P.B. Littlewood and C.M. Varma, *J. Appl. Phys.* **69**, 4979 (1991).
108. A. Virosztek and J. Ruvalds, *Phys. Rev. B* **42**, 4064 (1990).
109. F. Slakey, S.L. Cooper, M.V. Klein, J.P. Rice, E.D. Bukowsky, and D.M. Ginsberg *Phys. Rev. B* **38**, 11934 (1989).
110. R.E. Glover and M. Tinkham, *Phys. Rev. B* **107**, 844 (1956); *ibid*, *Phys. Rev. B* **108**, 1175 (1957)
111. J.F. Annett, *Adv. Phys.* **39**, 83 (1990).

112. V.I. Marchenko, *Sov. Phys. JETP* **66**, 331 (1987).
113. J.F. Annet, N. Goldenfeld, and S.R. Renn, in *Physical Properties of High Temperature Superconductors I*, edited by D.M. Ginsberg (World Scientific Press, Singapore, 1992) p. 571.
114. M. Sgrist and T.M. Rice, *Z. Phys. B* **68**, 9 (1987).
115. E. Dagotto and J. Riera, *Phys. Rev. Lett.* **70**, 682 (1993).
116. W.N. Hardy, D.A. Bonn, D.C. Morgan, R. Liang, and K. Zhang, *Phys. Rev. Lett.* **70**, 3999 (1993).
117. T. Barnes, A.E. Jacobs, M.D. Kovarik, and W.G. Macready, *Phys. Rev. B* **45**, 256 (1992).
118. H. Fehske, V. Wass, H. Roder, and H. Buttner, *Phys. Rev. B* **44**, 8473 (1991).
119. J. Riera and A.P. Young, *Phys. Rev. B* **39**, 9697 (1989).
120. V.J. Emery, S.A. Kivelson, and H.Q. Lin, *Phys. Rev. Lett.* **64**, 475 (1990).
121. F.E. Nori, E. Abrahams, and G. Zimanyi, *Phys. Rev. B* **41**, 7277 (1991).
122. M. Frick, P.C. Pattnaik, I. Morgenstern, D.M. Newsn, and W. von der Linden, *Phys. Rev. B* **42**, 2665 (1990).
123. R.T. Scalettar, S.R. White, D.J. Scalapino, and R.L. Sugar, *Phys. Rev. B* **44**, 770 (1991).
124. D.R. Harshman, G. Aeppli E.J. Ansaldo, B. Batlogg, J.H. Brewer, J.F. Carolan, R.J. Cava, M. Celio, and A.C.D. Chaklader, *Phys. Rev. B* **36**, 2386 (1987).
125. D.R. Harshman, L.F. Schneemeyer, J.V. Waszczak, G. Aeppli, R.J. Cava, B. Batlogg, L.W. Rupp, E.J. Ansaldo, and D.L. Williams, *Phys. Rev. B* **39**, 851 (1989).
126. L. Kruisin, R.L. Greene, F. Holtsberg, A.P. Malosemoff, and Y. Yeshurun, *Phys. Rev. Lett.* **62**, 217 (1989).
127. A.T. Fiory, A.F. Hebard, P.M. Mankiewich, and R.E. Howard, *Phys. Rev. Lett.* **61**, 1419 (1988).
128. J.F. Annet, N. Goldenfeld, and S.R. Renn, *Phys. Rev. B* **43**, 2778 (1991).

129. J.F. Annet and N. Goldenfeld, *J. Low Temp. Phys.* **89**, 197 (1992).
130. Z. Ma, R.C. Taber, L.W. Lombardo, A. Kapitulnik, M.R. Beasley, P. Merchant, C.B. Eom, S.Y. Hou, and J.M. Phillips, *Phys. Rev. Lett.* **71**, 781 (1993).
131. P.J. Hirschfeld and N. Goldenfeld, *Phys. Rev. B* **48**, 4219 (1993).
132. prohammer+peterprb87 to be supplied.
133. G.A. Thomas, J. Orenstein, D.H. Rapkine, M. Capizzi, A.J. Milis, R.N. Bhatt, L.F. Schneemeyer, and J.V. Waszczak, *Phys. Rev. Lett.* **61**, 1313 (1988).
134. L.C. Brunel, S. G. Louie, G. Martinez, S. Labdi, and H. Raffy, *Phys. Rev. Lett.* **66**, 1346 (1991).
135. M. Reedyk, Ph.D. Thesis, McMaster University (1992).
136. M. Reedyk and T. Timusk, *Phys. Rev. Lett.* **69**, 2705 (1992).
137. K.S. Krane, *Modern Physics* (John Wiley & Sons, New York, 1983).
138. R.J. Bell, *Introductory Fourier Transform Spectroscopy* (Academic Press, New York, 1972).
139. P. Fellgett, *J. Phys. Radium* **19**, 187 (1958).
140. C.D. Porter and D.B. Tanner, *Intern. J. Infrared and Millimeter Waves* **4**, 273 (1983).
141. D.B. Tanner and R.P. McCall, *Applied Optics* **23**, 2363 (1984).
142. K.D. Cummings, Ph.D. Thesis, Ohio State University (1981).
143. F. Wooten, *Optical Properties of Solids* (Academic Press, New York, 1972).
144. J.I. Pankove, *Optical Processes in Semiconductors* (Dover Publications Inc., New York, 1971).
145. J.P. Rice, B.G. Pazol, D.M. Ginsberg, T.J. Moran, and M.B. Weissman, *J. Low Temp. Phys.* **72**, 345 (1988).
146. J. Giapintzakis, D.M. Ginsberg, and P.D. Han, *J. Low Temp. Phys.* **77**, 155 (1989).
147. J.P. Rice, E.D. Bukowski, and D.M. Ginsberg, *J. Low Temp. Phys.* **72**, 345 (1989).

148. F. Slakey, S.L. Cooper, M.V. Klein, J.P. Rice, and D.M. Ginsberg *Phys. Rev. B* **39**, 2781 (1989).
149. P.D. Han and D.A. Payne, *J. Crystal Growth* **104**, 201 (1990).
150. S-W. Cheong, Z. Fisk, J.O. Willis, S.E. Brown, J.D. thompson, J.P. Remeika, A.S. Cooper, R.M. Aikin, D. Schiferl, and G. Gruner, *Solid State Commun.* **65**, 111 (1988).
151. F.C. Chou, J.H. Cho, and D.C. Johnston, *Physica C* **197**, 303 (1992).
152. F.C. Chou, D.C. Johnston, S-W. Cheong, and P.C. Canfield, *Physica C* **216**, 66 (1993).
153. A.V. Bazhenov, T.N. Fursova, V.B. Timofeev, A.S. Cooper, J.P. Remeika, and Z. Fisk, *Phys. Rev. B* **40**, 4413 (1989).
154. S. Tajima, T. Ido, S. Ishibashi, T. Itoh, H. Eisaki, Y. Mizuo, H. Takagi, and S. Uchida, *Phys. Rev. B* **43**, 10496 (1991).
155. J.P. Falck, A. Levy, M.A. Kastner, and R.J. Birgeneau, *Phys. Rev. Lett.* **69**, 1109 (1992).
156. Z. Schlesinger, R.T. Collins, M.W. Shafer, and E.M. Engler, *Phys. Rev. B* **36**, 5275 (1987).
157. A. Wattiaux, J.C. Park, J.C. Grenier, and M. Pouchard, *C.R. Acad. Sci. Ser. B* **310**, 1047 (1990).
158. S. Uchida, *J. Phys. Chem. Solids* **53**, 1603 (1992).
159. D. van der Marel, H-U. Habermeier, D. Heitmann, W. König, and A. Wittlin, *Physica C* **176**, 1 (1991).
160. M. Mostoller, J. Zhang, A.M. Rao, and P.C. Eklund, *Phys. Rev. B* **41**, 6488 (1990).
161. F.E. Bates and J.E. Eldridge, *Solid State Commun.* **72**, 187 (1989).
162. J.F. Scott, *Phys. Rev. B* **4**, 1360 (1971).
163. I. Ohana, M.S. Dresselhaus, Y.C. Liu, P.J. Picone, D.R. Gabbe, H.P. Jenssen, and G. Dresselhaus, *Phys. Rev. B* **39**, 2293 (1989).
164. S. Sugai, *Phys. Rev. B* **39**, 4306 (1989).

165. M. Čopič, D. Mihailović, M. Zgonik, M. Prester, K. Biljaković, B. Orel, and N. Brničević, *Solid State Commun.* **64**, 297 (1987).
166. P. Böni, J.D. Axe, G. Shirane, R.J. Birgeneau, D.R. Gabbe, H.P. Jenssen, M.A. Kastner, C.J. Peters, P.J. Picone, and T.R. Thurston, *Phys. Rev. B* **38**, 185 (1988).
167. W.E. Pickett, R.E. Cohen, and H. Krakauer, *Phys. Rev. Lett.* **67**, 228 (1991).
168. S. Tajima, H. Ishii, T. Nakahashi, T. Takagi, S. Uchida, M. Seki, S. Suga, Y. Hidaka, M. Suzuki, T. Murakami, K. Oka, and H. Unoki, *J. Opt. Soc. Am. B* **6**, 475 (1989).
169. G.A. Thomas, D.H. Rapkine, S.L. Cooper, S-W. Cheong, and A.S. Cooper, *Phys. Rev. Lett.* **67**, 2906 (1991).
170. B. Renker, F. Gompf, E. Gering, D. Ewert, H. Rietschek, and A. Dianoux, *Z. Phys. B* **73**, 309 (1988).
171. W. Reichard, N. Pyka, L. Pintschovius, B. Hennion, and G. Collin, *Physica C* **162-164**, 464 (1989).
172. K. Kornelsen, J.E. Eldridge, H.H. Wang, and J.M. Williams, *Phys. Rev. B* **44**, 5235 (1991).
173. M.J. Rice, *Phys. Rev. Lett.* **37**, 36 (1976).
174. T. Timusk, C.D. Porter, and D. B. Tanner, *Phys. Rev. Lett.* **66**, 663 (1991).
175. J. Schützmann, B. Gorshunov, J. Münzel, A. Zibold, H.P. Geserich, A. Erb, and Müller-Vogt, *Phys. Rev. B* **46**, 512 (1992).
176. H.P. Geserich, B. Koch, M. Durrler, and Th. Wolf, in *Electronic Properties of high T_c superconductors and Related Compounds*, edited by H. Kuzmany, M. Mehring, and J. Fink (Springer-Verlag, Series of Solid State Science, Berlin, 1990).
177. S. Lupi, P. Calvani, M. Capizzi, P. Maselli, W. Sadowski, and E. Walker, *Phys. Rev. B* **45**, 12470 (1992).
178. G.A. Thomas, M. Capizzi, J. Orenstein, D.H. Rapkine, A.J. Millis, P. Gammel, L.F. Schneemeyer, and J.V. Waszczak, in *Proceedings of the International Symposium on the Electronic Structure of High T_c Superconductors*, edited by A. Bianconi (Pergamon Press, Oxford, 1988) p. 169.

179. P.B. Allen, T.B. Beaulac, F.S. Khan, W.H. Butler, F.J. Pinski, and J.H. Swihart, *Phys. Rev. B* **34**, 4331 (1986).
180. E.J. Nicol and J.P. Carbotte, *Phys. Rev. B* **44**, 7741 (1991).
181. F.A. Miranda, W.L. Gordon, K.B. Bhasin, V.O. Heinen, and J.D. Warner, *J. Appl. Phys.* **70**, 5450 (1991).
182. M.C. Nuss, P.M. Mankiewich, M.L. O'Malley, E.H. Westerwick, and P.B. Littlewood, *Phys. Rev. Lett.* **66**, 3305 (1991).
183. P.K. Holczer, L. Forro, L. Mihaly, and G. Gruner, *Phys. Rev. Lett.* **67**, 152 (1991).
184. P.B. Allen, W.E. Pickett, and H. Krakauer, *Phys. Rev. B* **36**, 3926 (1987).
185. J.R. Cooper, L. Forró, and B. Keszei, *Nature* **343**, 444 (1990).
186. D.S. Dessau, Ph.D. Dissertation, Stanford University (1992).
187. D.C. Mattis and J. Bardeen, *Phys. Rev.* **111**, 412 (1958).
188. M. Tinkham, *Introduction to Superconductivity* (McGraw Hill, New York, 1975).
189. P.J. Hirschfeld, P. Wölfle, J.A. Sauls, D. Einzel, and W.O. Putikka, *Phys. Rev. B* **40**, 6695 (1989).
190. U. Welp, S. Fleshler, W.K. Kwok, J. Downey, Y. Fang, G.W. Crabtree, and J.Z. Liu, *Phys. Rev. B* **42**, 10189 (1990).
191. K. Yamaya, T. Haga, T. Honma, Y. Abe, F. Minami, S. Takekawa, Y. Tajima, and Y. Hidaka, *Physica C* **162-164**, 1009 (1989).
192. H.C. Montgomery, *J. Appl. Phys.* **42**, 2971 (1971).
193. L.J. van der Pauw, *Philips Res. Repts.* **16**, 187 (1961).
194. B.F. Logan, S.O. Rice, and R.F. Wick, *J. Appl. Phys.* **42**, 2975 (1971).
195. P.R. Bevington and D.K. Robinson, *Data Reduction and Error Analysis for the Physical Science*, 2nd Ed. (McGraw Hill, New York, 1992).
196. P.W. Anderson and Z. Zou *Phys. Rev. Lett.* **60**, 132 (1988).
197. T. Ito, H. Takagi, S. Ishibashi, and S. Uchida, *Nature* **350**, 596 (1991).

- 198. B.O. Wells, Z.-X. Shen, D.S. Dessau, W.E. Spicer, C.G. Olson, D.B. Mitzi, A. Kapitulnik, R.S. List, and A. Arko, *Phys. Rev. Lett.* **66**, 3056 (1991).
- 199. Y. Nakazawa, T. Takabatake, A. Kishi, R. Kato, and A. Maesono, *Solid State Commun.* **66**, 201 (1988).
- 200. R.A. Butera, *Phys. Rev. B* **37**, 5909 (1988).
- 201. B. Bucher, J. Karpinski, E. Kaldis, and P. Wachter, *Physica C* **199**, 337 (1991).
- 202. D. Pooke, K. Kishio, H.J. Trodahl, Y. Kotaka, S. Kitao, M. Seto, and Y. Maeda, in *Proceedings of the 6th International Symposium on Superconductivity* (Springer-Verlag, Tokyo, 1993).
- 203. D.J. Van Ooijen and G.J. Van Grup, *Physics Letters* **17**, 231 (1965).
- 204. D.K.C. MacDonald, *Noise and Fluctuations* (John Wiley, New York, 1962).
- 205. J.B. Torrance, B.A. Scott, B. Welber, F.B. Kaufman, and P.E. Seiden, *Phys. Rev. B* **19**, 730 (1979).
- 206. B.A. Scott, S.J. La Placa, J.B. Torrance, B.D. Silverman, and B. Weber, *J. Am. Chem. Soc.* **99**, 6631 (1977).
- 207. T. Sugano, K. Yakushi, and H. Kuroda, *Bull. Chem. Soc. Jpn.* **51**, 1041 (1978).
- 208. H. Kobayashi, A. Kobayashi, Y. Sasaki, G. Saito, and H. Inokuchi, *Bull. Chem. Soc. Jpn.* **59**, 301 (1986).
- 209. M. Meneghetti, R. Bozio, and C. Pecile, *J. Physique* **47**, 1377 (1986).
- 210. M.E. Kozlov, K.I. Pokhodnia, and A.A. Yurchenko, *Spectrochimica Acta* **43A**, 323 (1987).
- 211. A. Ugawa, G. Ojima, K. Yakushi, and H. Kuroda, *Phys. Rev. B* **38**, 5122 (1988).
- 212. R. Zamboni, D. Schweitzer, and H.J. Kellier, *Solid State Commun.* **73**, 41 (1990).
- 213. R.M. Vlasova, S. Ya. Prieve, V.N. Semkin, R.N. Lyubovskaya, E. I. Zhilyaeva, E.B. Yagubskii, and V.M. Yartsen, *Synthetic Metals* **48**, 129 (1992).
- 214. S. Sugai, H. Mori, H. Yamochi, and G. Saito, *Phys. Rev. B* **47**, 14374 (1993).

- 215. T. Mori, A. Kobayashi, Y. Sasaki, H. Kobayashi, G. Saito, H. Inokuchi, *Chem. Lett.* **1963**, 001 (1982).
- 216. K.A. Abboud, M.B. Clevenger, G.F. De Oliveira, and D.R. Talham, submitted.
- 217. K. Nakamoto, *Infrared and Raman Spectra of Inorganic and Coordination Compounds*, 3rd Edition (John Wiley & Sons, New York, 1978).
- 218. M. Cohen, S.K. Khanna, W.J. Gunning, A.F. Garito, and A.J. Heeger, *Solid State Commun.* **17**, 367 (1975).
- 219. S.K. Khanna, Ph.D. Dissertation, University of Pennsylvania (1974).
- 220. H. Piel and G. Muller, *IEEE Trans. Magn.* **27**, 854 (1991).
- 221. W.P. Beyermann, J.P. Carini, and G. Grüner, preprint.
- 222. J.D. Jackson, *Classical Electrodynamics* (John Wiley & Sons, New York, 1975).
- 223. T. Rubin, H.W. Altman, and H.L. Johnston, *J. Am. Chem. Soc.* **76**, 5289 (1954).
- 224. N.P. Ong, *J. Appl. Phys.* **48**, 2935 (1977).

BIOGRAPHICAL SKETCH

Manuel A. Quijada was born in the city of Santiago, Dominican Republic, in 1962. After attending elementary and the first year of secondary school in that country, he and his parents moved to reside permanently on the island of Puerto Rico where he finished high school and attended the University of Puerto Rico to pursue a career in physics. He obtained a B.S. degree in 1984, and a M.S. degree in 1987 with Dr. Lesser Blum as his thesis advisor. The topic of his master's thesis was statistical mechanics of charge transfer in metal-electrolite interfaces.

After living for 6 six months in the city of New York, Manuel came to the University of Florida to pursue a doctoral degree in physics. He joined Professor Tanner's group in 1989 to conduct experiments in the microwave and later optical properties of high temperature superconductors.

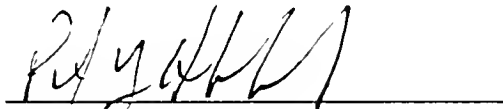
Manuel married Zunilda in 1986 and they have a daughter Melissa, who was born in 1989. His recreational interests are listening to music, playing softball, and jogging.

I certify that I have read this study and that in my opinion it conforms to acceptable standards of scholarly presentation and is fully adequate, in scope and quality, as a dissertation for the degree of Doctor of Philosophy.



David B. Tanner, Chairman
Professor of Physics

I certify that I have read this study and that in my opinion it conforms to acceptable standards of scholarly presentation and is fully adequate, in scope and quality, as a dissertation for the degree of Doctor of Philosophy.




Peter J. Hirschfeld
Assistant Professor of Physics

I certify that I have read this study and that in my opinion it conforms to acceptable standards of scholarly presentation and is fully adequate, in scope and quality, as a dissertation for the degree of Doctor of Philosophy.



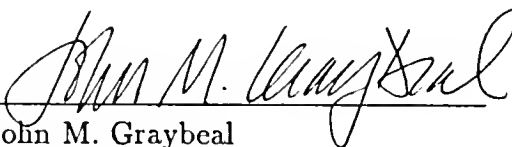
Charles F. Hooper Jr.
Professor of Physics

I certify that I have read this study and that in my opinion it conforms to acceptable standards of scholarly presentation and is fully adequate, in scope and quality, as a dissertation for the degree of Doctor of Philosophy.



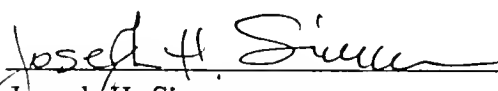
Neil S. Sullivan
Professor of Physics

I certify that I have read this study and that in my opinion it conforms to acceptable standards of scholarly presentation and is fully adequate, in scope and quality, as a dissertation for the degree of Doctor of Philosophy.



John M. Graybeal
Associate Professor of Physics

I certify that I have read this study and that in my opinion it conforms to acceptable standards of scholarly presentation and is fully adequate, in scope and quality, as a dissertation for the degree of Doctor of Philosophy.



Joseph H. Simmons
Professor of Materials Science and
Engineering

This dissertation was submitted to the Graduate Faculty of the Department of Physics in the College of Liberal Arts and Sciences and to the Graduate School and was accepted as partial fulfillment of the requirements for the degree of Doctor of Philosophy.

April 1994

Dean, Graduate School

LD
1780
1994
- 26

UNIVERSITY OF FLORIDA



3 1262 08557 1130